
Collisions in an ultracold gas of $^{23}\text{Na}^{39}\text{K}$ molecules

Von der Fakultät für Mathematik und Physik
der Gottfried Wilhelm Leibniz Universität Hannover

zur Erlangung des akademischen Grades

Doktor der Naturwissenschaften

-Dr. rer. nat.-

genehmigte Dissertation

von

M.Sc. Philipp Gersema

geboren am 29.05.1992 in Westerstede

2022

Referentin: Prof. Dr. Silke Ospelkaus
Institut für Quantenoptik
Leibniz Universität Hannover

Korreferent: Prof. Dr. Luis Santos
Institut für theoretische Physik
Leibniz Universität Hannover

Korreferent: Prof. Dr. Dajun Wang
Department of Physics
The Chinese University of Hong Kong

Tag der Promotion: 13.07.2022

Abstract

The creation of a quantum degenerate ensemble of heteronuclear molecules with dominant dipole-dipole interactions, is considered to be instrumental for studying and understanding strongly correlated many-body systems. The latter might reveal new quantum states of matter and substantially advance quantum metrology, computation and ultracold chemistry.

A handful of experiments have been successful in creating ultracold bialkali molecular ensembles with large phase-space densities, assembled from different fermionic or bosonic alkali constituents. Every new species promises to improve the knowledge about molecular many-body systems interacting through anisotropic long-range dipole-dipole interactions. Nevertheless, only recently two groups succeeded in observing a degenerate gas of fermionic molecules, while a Bose-Einstein condensate is yet to be demonstrated. A substantial obstacle is the unexpected two-body loss rate close to the universal limit, observed in every experiment. New theoretical concepts attempted to explain them by introducing so-called sticky collisions and subsequent photo-excitation. Providing experimental data on ultracold molecule and also atom-molecule collisions is crucial for the understanding of the yet unknown and complicated molecular collision processes.

This thesis reports on the progress achieved in the development of a new bialkali molecular platform. New Feshbach resonances in $^{23}\text{Na}+^{39}\text{K}$ collisions are revealed, which enable the production of weakly bound molecules. Spectroscopic measurements of $^{23}\text{Na}^{39}\text{K}$ are performed and possible pathways to the rovibronic ground state discussed. Finally, for the first time, an ultracold ensemble of $^{23}\text{Na}^{39}\text{K}$ ground-state molecules is created.

To study the possible photoexcitation of metastable complexes, a chopped optical dipole trap has been realized. A large parameter space of different modulation frequencies, laser intensities and wavelengths as well as dark to bright time ratios has been probed. As the key findings of this thesis, surprisingly, the expected decrease of molecular losses has not been observed. Instead, all measurements show a null result. Together with similar results from a group in Hong Kong working with $^{23}\text{Na}^{87}\text{Rb}$ this suggests that the current theory describing ultracold molecular collisions is incomplete.

Subsequent studies of collisions between ^{39}K atoms prepared in different hyperfine states, with $^{23}\text{Na}^{39}\text{K}$ molecules in a single hyperfine state, show intriguing scattering properties. In particular, the non spin-stretched state $|F = 1, m_F = -1\rangle$ exhibits a strong suppression of the two-body losses far below the universal limit.

Keywords: Electronic structure of atoms & molecules, Atomic & molecular collisions
Ultracold collisions, Bose gases, Cold and ultracold molecules

Contents

1	Introduction	1
1.1	Dipole-Dipole interactions	2
1.2	Ultracold polar molecules	3
1.3	Ultracold molecular collisions	5
1.4	This thesis	6
2	List of publications and own contributions	9
3	Feshbach resonances and molecules	11
3.1	Feshbach resonances in $^{23}\text{Na}+^{39}\text{K}$ mixtures and refined molecular potentials for the NaK molecule [A1]	11
3.2	Beyond Born-Oppenheimer approximation in ultracold atomic collisions [A2]	27
3.3	Formation of ultracold weakly bound dimers of bosonic $^{23}\text{Na}^{39}\text{K}$ [A3]	39
4	From Feshbach molecules to ground-state molecules	53
4.1	A pathway to ultracold bosonic $^{23}\text{Na}^{39}\text{K}$ ground state molecules [A4]	53
4.2	Ultracold Gas of Bosonic $^{23}\text{Na}^{39}\text{K}$ Ground-State Molecules [A5]	65
5	Molecule-molecule and atom-molecule collisions	83
5.1	Probing photoinduced two-body losses [A6]	83
5.2	Spin dependent atom-molecule collisions [A7]	95
6	Conclusion and outlook	105
	Bibliography	I

1 Introduction

Since the development of quantum mechanics in the early 20th century, this theory has pushed the boundaries of our understanding of the world around us and led to the development of many technologies that improve the standard of living in our modern world. For example, advancements in quantum optics, the study of the interactions between light and matter within quantum mechanics, led to, among other things, the development of the laser [1], which can be found in almost every aspect of day to day life, from supermarket checkouts to surgery. The invention of the atomic clock [2] is a necessity for global satellite navigation (e.g., GPS, Galileo), or nowadays, the construction of quantum computers, which promises to revolutionize modern computer science [3].

The implementation and improvement of these developments requires a deep understanding of the underlying physics and many years of fundamental research. Systems with ultracold atoms, operating at temperatures in the sub μK regime, have proven to be a versatile platform for these studies. They allow to decompose complex problems into theoretically and practically accessible experiments, with precise control over all relevant physical parameters. These systems have enabled the study of degenerate quantum states of matter, such as Bose-Einstein condensates (BEC) in 1995 [4, 5, 6] or the Fermi gas in 1999 [7]. Spurred by these successes, this branch of physics has received much attention and subsequent experiments have been able, for example, to study the Bardeen-Cooper-Schrieffer(BCS)-BEC transition [8, 9, 10], simulate crystal-like structures in optical lattices [11], observe the transition from superfluid to Mott insulator [12], or generate entangled states of matter [13, 14].

The possibilities for new exciting experiments with ultracold atoms are far from exhausted. However, they are fundamentally limited by the fact that most neutral atomic systems interact only through short-range Van der Waals dominated contact interactions that scale with r^{-6} , where r denotes the interatomic distance. This is true for the most commonly used atomic species, the alkali atoms. These are often used because of their relatively simple energy structure, the resulting efficient cooling methods and experimentally straightforward manipulation of internal states. Due to the limitation of these atomic systems to short range contact interactions, there is a growing interest in expanding the field of research to increase the explorable quantum states of matter and to reveal new exotic quantum phenomena through the introduction of long-ranged dipole-dipole interactions (DDI), for example with ultracold heteronuclear molecules [15].

1.1 Dipole-Dipole interactions

The potential of particles interacting via DDI with all dipoles aligned in the same direction can be described by

$$V_{dd}(r) = \frac{C_{dd}}{4\pi} \cdot \frac{1 - 3 \cos^2(\theta)}{r^3}, \quad (1.1)$$

where C_{dd} is the magnetic or electric coupling constant and θ is the angle between the direction of polarization and the relative position of the particles [15]. As can be seen from equation 1.1 the DDI is not only long-ranged in a three dimensional system ($\frac{1}{r^3}$) but also anisotropic, as it can exhibit attractive or repulsive forces dependent on the angle θ .

There are different possible candidates to introduce DDIs, most commonly magnetic atoms [15], Rydberg atoms [16] or polar molecules [15]. These systems have advantages and disadvantages in comparison to each other.

Magnetic atoms possess a permanent magnetic dipole moment that originates from the magnetic moment of electrons in non-closed shell structures. The resulting dipole moment is weak compared to many polar molecules [17] but these systems exhibit a good stability and long lifetime. Several atomic species have already been cooled to quantum degeneracy [18, 19, 20, 21] and enabled, for example, fascinating studies of roton modes [22], quantum droplets [23, 24], or two-dimensional supersolidity [25].

Rydberg atoms are created through laser excitation of atoms to states near the ionisation threshold. The result is a highly excited atom with a large principle quantum number n that can be as high as $n \approx 100$ [16]. The highly excited electron has a large separation from the nucleus and therefore produces a large electric dipole moment that is proportional to n^2 [26] and exceeds that of magnetic atoms or polar molecules. On the other side these states are metastable and have comparatively low lifetimes on the order of $100 \mu\text{s}$ [27]. Nevertheless, Rydberg atoms have drawn substantial attention since the observation of the effect of Rydberg blockade [28], which allowed to entangle two atoms with each other [29, 30] and gave rise to the observation of Rydberg molecules [31].

Polar molecules combine, in some ways, the best of these two worlds, as they can possess a large electric dipole moment [17] and can have comparable lifetimes to atoms. In addition, the DDI is also tunable in strength through the application of external electric fields [32]. If an appropriate molecule is chosen, the electric dipole moment can be large enough to make DDI the dominant interaction in such quantum gases, even if the molecules are placed inside an optical lattice, with spacings that are typically on the order of 532 nm [15, 33]. An appropriate molecule is a heteronuclear molecule with a dipole moment around 1 Debye, that is cooled down and prepared in the lowest electronic and a low rovibrational state, most preferably the absolute ground state [15].

In the following section, I will discuss the challenges in creating ultracold polar molecules and their properties.

1.2 Ultracold polar molecules

Obtaining ensembles of polar molecules with high phase-space densities (PSDs) requires efficient cooling or slowing methods, such as laser or evaporative cooling techniques, like the Zeeman slower, a magneto-optical trap (MOT), sub-Doppler polarization gradient cooling, or microwave evaporation in a magnetic trap and forced dipole trap evaporation [34].

The cooling techniques used for atoms are not easily applicable to molecules. Molecules, in contrast to atoms, exhibit rotational and vibrational degrees of freedom. This can be both an advantage and a disadvantage, an advantage as it opens up even more new research fields, such as quantum chemistry [35, 36] and a disadvantage as to date there are no direct cooling methods efficient enough to create quantum degenerate samples of polar molecules. Laser cooling relies on closed cycling transitions, otherwise the scattering rate is not high enough and the final quantum state is not defined. Evaporative cooling methods cool the ensembles by removing the constituents with highest energy and rely on subsequent rethermalisation due to elastic scattering processes. With some exceptions [37, 38], the complex internal structure of molecules does not support (closed) cooling transitions and makes rethermalization by purely elastic collisions difficult to achieve. Faced with these obstacles, physicists developed new cooling schemes to directly cool or slow molecules, such as cryogenic buffer gas cooling [39], Stark [40] and Zeeman deceleration [41, 42], centrifugal cooling [43], a molecular MOT [44] or molecular Zeeman slowing [45]. Even though direct cooling of molecules has made significant progress in the past and promise to do so in the future, current ensembles still lack the extremely low temperatures and high phase-space densities reached in atomic ensembles [46].

In a different approach, physicists prepare an ultracold atomic mixture, for example with the well known alkali atoms, and then associate these atoms to molecules. This concept was first introduced at JILA in 2009 with the production of an ultracold $^{40}\text{K}^{87}\text{Rb}$ molecular cloud, with high phase-space density [47, 48]. First they prepare ultracold atomic mixtures with high phase-space densities, and then create weakly bound molecules utilizing Feshbach resonances, so-called Feshbach molecules [49]. In a following step these weakly bound molecules are coherently transferred to the rovibronic ground state utilizing Stimulated Raman Adiabatic Passage (STIRAP).

With the exception of radioactive Francium, there are five different long-living or stable alkali atoms (and their isotopes) to choose from. Fig. 1.1 shows all possible combinations of alkali atoms and their isotopes. Dashed lines represent fermionic, solid lines bosonic molecules, whereas faint lines represent the currently not investigated combinations. To date, a few groups have been able to produce ultracold bialkali molecules in their rovibronic ground state, fermionic $^{40}\text{K}^{87}\text{Rb}$ [48], $^{23}\text{Na}^{40}\text{K}$ [50, 51, 52], $^6\text{Li}^{23}\text{Na}$ (prepared in the rovibronic triplet ground state) [50] and bosonic $^{87}\text{Rb}^{133}\text{Cs}$ [53, 54], $^{23}\text{Na}^{87}\text{Rb}$ [55] and $^{23}\text{Na}^{133}\text{Cs}$ (single molecules in optical tweezers) [56].

The work within this dissertation has led to the preparation of a new molecular species at temperatures of around 300 nK, bosonic $^{23}\text{Na}^{39}\text{K}$ molecules [57].

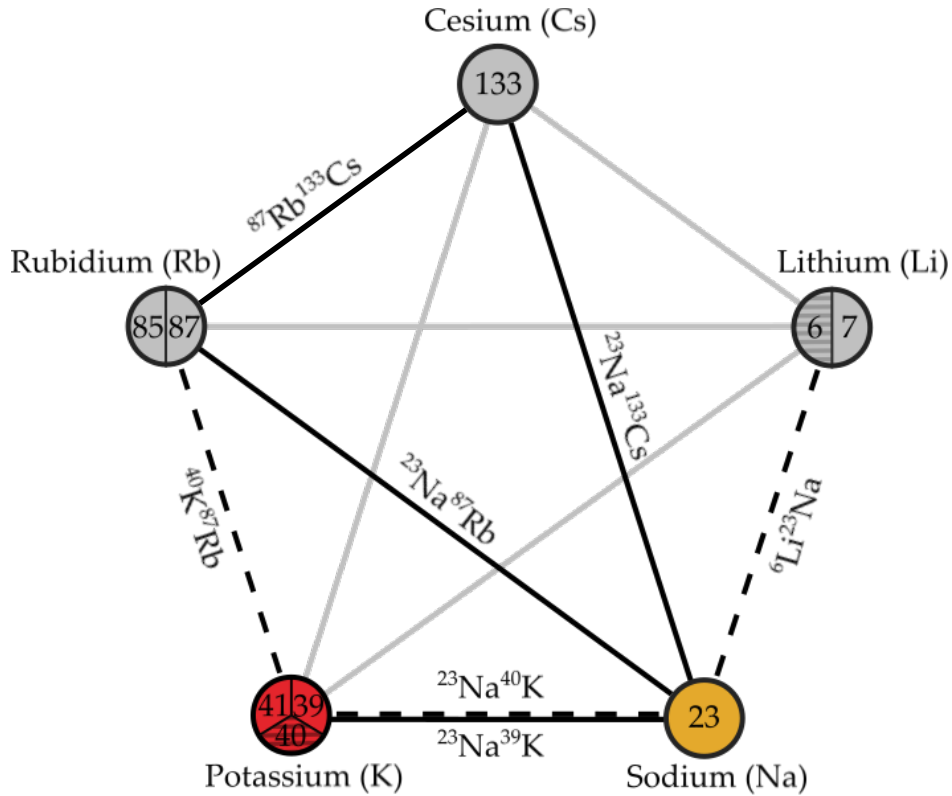


Figure 1.1: Possible combinations of alkali atoms and their isotopes to create heteronuclear bialkali molecules, excluding radioactive elements/isotopes. Solid (dashed) black lines represent bosonic (fermionic) molecules, faint lines denote not yet demonstrated combinations. The striped regions show the fermionic isotopes, the non-striped ones the bosonic ones. Image adopted from [58].

To study long-range DDIs in these systems, an electric dipole moment must first be induced, since the ground-state wave function of these molecules is isotropic and therefore has no permanent dipole moment in the laboratory frame. This must be done by either external DC electric or microwave (MW) fields that mix the ground state with higher rotational states [32]. This in turn gives rise to tunable induced dipole moments with defined orientations along the electric field axis. Outside of a degenerate molecular gas, dipole-dipole interactions have already been observed, such as dipolar spin-exchange interactions in a 3D optical lattice [59] or resonant dipolar collisions [60]. In 2020 the JILA group at the University of Colorado Boulder evaporatively cooled KRb molecules to a Fermi degenerate sample, exploiting the anisotropic nature of DDIs in a one-dimensional lattice [61]. This was done shortly after they have been able to create a three-dimensional molecular Fermi gas starting from two highly degenerate atomic ensembles [62]. Recently, a group in Munich was also able to create quantum degenerate ensembles of fermionic polar ground-state molecules [63]. These impressive achievements lay the groundwork for the exploration of new quantum states of matter [15, 63].

Nevertheless, the production of degenerate ultracold molecular ensembles remains a challenge. A molecular BEC is not yet within reach and although the first preparation of a quantum gas of fermionic KRb molecules goes back to 2009, it took until 2019 to create a Fermi gas [48, 62]. This raises the following question: What were the difficulties responsible for this considerable delay? This will be discussed in the following section.

1.3 Ultracold molecular collisions

After the first ultracold molecular cloud in the ground state was created, a rapid two-body decay of the molecules at a rate close to the universal scattering limit (every collision leads to a loss) was observed, even though the molecules were prepared in the rovibronic ground state [48, 64, 65]. This was later attributed to the fact that KRb molecules undergo exothermic exchange reactions during a collision, $2\text{KRb} \rightarrow \text{K}_2 + \text{Rb}_2$ [64, 66, 67]. Indeed, all alkali molecule combinations containing a lithium atom and KRb can pass through this reaction channel [66].

Following experiments therefore concentrated their efforts on chemically stable alkali molecules. Interestingly and surprisingly, these molecules also exhibit two-body loss rates close to the universal limit [53, 55, 50, 57, 68]. Also the direct comparison of reactive and non-reactive collisions of $^{23}\text{Na}^{87}\text{Rb}$, by preparing the molecules in their first vibrational level which in turn allowed reactions to take place, showed very similar loss rates [69].

For this reason, direct evaporative cooling of the molecules into the quantum degenerate region is not possible. In addition, if one polarizes the molecular ensemble in a three-dimensional trap through the use of an external electric field even higher loss rates are observed due to the long-range anisotropic nature of the DDIs [70, 71, 72].

It became clear that a deeper understanding of the physics of ultracold molecule-molecule or atom-molecule mixtures is required to allow for the creation of quantum degenerate ensembles of polar molecules.

Collisional studies led, for example, to the observation of atom-molecule Feshbach resonances [73, 74] or the exploration of controlled chemical reactions [35, 75, 76, 77]. In addition, a possible explanation for the surprising two-body losses was introduced by the concept of long-lived metastable four-body complexes that form in the short-range potential during so-called sticky collisions [78]. These complexes might be subsequently excited by light from the optical dipole trap (ODT) [79]. This hypothesis was recently both supported [80, 81] and refuted [82, 83] by experimental findings, possibly depending on the molecular mass or the chemical reactivity and is still part of a lively debate. Collisional shielding concepts have been suggested, that utilize electrical, MW or optical fields [84, 85, 86], to avoid chemical reactions or the formation of complexes from the start by preventing the molecules from reaching the short-range potential. Electrical and MW shielding concepts have already been successfully implemented [87, 88, 63] and enabled the production of a degenerate Fermi gas [63].

1.4 This thesis

The aim of the POLAR experiment at the Leibniz University Hanover is to create and investigate bosonic ultracold polar $^{23}\text{Na}^{39}\text{K}$ molecules and therefore to add a new molecular species to the vibrant field of ultracold polar molecules. In particular, the molecular scattering properties are of crucial importance, as they could deliver much needed insight into the ongoing debate about the unexplained molecular losses. The investigation of these properties is the main focus of this thesis. Detailed descriptions of the capabilities and techniques utilized in this experiment can be found in the PhD theses of Dr. M. W. Gempel [33], Dr. T. A. Schulze [17], Dr. T. Hartmann [89] and Dr. K. K. Voges [58].

Within my thesis, I now describe the story from the start of my studies in 2017, where the experiment had just produced dual-species BECs of ^{23}Na and ^{39}K in a three dimensional crossed ODT (cODT) utilizing previously unknown interspecies Feshbach resonances [90], to the end of my work, where collisional studies with ultracold $^{23}\text{Na}^{39}\text{K}$ molecules have been performed. This thesis is structured as follows.

Chapter 3 focuses on Feshbach resonance spectroscopy and Feshbach molecule production. After the successful production of dual-species BECs, the main objective of the experiment was on the exploration of yet unknown Feshbach resonances, since the interspecies scattering properties in different spin-channels have not yet been known at that time, this is detailed in the paper [A1] (**Hartmann *et al.***), see section 3.1. These studies are a prerequisite for the future generation of Feshbach molecules and refined the molecular potentials of the $^{23}\text{Na}^{39}\text{K}$ molecule. A detailed description of this paper can be found in the PhD thesis of Dr. T. Hartmann [89]. This paper is followed by measurements on homonuclear potassium Feshbach resonances in section 3.2. As the POLAR experiment generates ultracold atomic quantum gases, it can be used not only as a platform for molecular experiments, but also for experiments with ultracold ^{23}Na and ^{39}K atoms. In a theory collaboration with Prof. Dr. E. Tiemann three previously unknown potassium *d*-wave Feshbach resonances have been measured. This improved the understanding of the potassium interatomic potentials and showed that corrections beyond the Born-Oppenheimer approximation are necessary for a detailed description of these ([A2]; **Tiemann, Gersema *et al.***).

Afterwards, in section 3.3, an appropriate $^{23}\text{Na}+^{39}\text{K}$ Feshbach resonance is chosen to create weakly bound dimers by the use of resonant radiofrequency (RF) pulses ([A3]; **Voges, Gersema *et al.***).

Chapter 4 details the pathway from Feshbach molecules to the rovibronic molecular ground state, in particular the implementation of the STIRAP, and culminates in the first preparation of a quantum gas of rovibronic ground-state polar $^{23}\text{Na}^{39}\text{K}$ molecules.

To create molecules by a STIRAP, detailed knowledge of the molecular energy structure, transition

strengths and singlet/triplet admixtures is required to identify the best possible pathways to the rovibronic ground state. This was accomplished by spectroscopic measurements ([A4]; **Voges, Gersema *et al.***), see section 4.1.

In section 4.2, this spectroscopic data allowed for an efficient STIRAP transfer of the Feshbach molecules to the rovibronic ground state of $^{23}\text{Na}^{39}\text{K}$ ([A5]; **Voges, Gersema *et al.***). A single-pass efficiency of 70% was achieved, resulting in roughly 4000 molecules at 300 nK with a PSD of up to 0.14. A detailed description of the papers [A3],[A4] and [A5] can be found in the PhD thesis of Dr. K. K. Voges [58].

Finally, in Chapter 5, molecule-molecule and atom-molecule collisions are investigated. Soon after the $^{23}\text{Na}^{39}\text{K}$ molecules have been created, the concept of light excitation of metastable complexes by the trapping light was discussed and ways to test this hypothesis were sought out. Section 5.1 gives a detailed summary of this topic and the performed measurements in collaboration with the group of Prof. Dr. D. Wang from the Department of Physics at the Chinese University of Hong Kong ([A6]; **Gersema, Voges, Lin, He *et al.***).

In addition, first collisional experiments in atom-molecule mixtures have been performed and revealed intriguing scattering properties ([A7]; **Voges, Gersema *et al.***), this is discussed in more detail in section 5.2.

2 List of publications and own contributions

- [A1] Torsten Hartmann, Torben A. Schulze, Kai K. Voges, Philipp Gersema, Matthias W. Gempel, Eberhard Tiemann, Alessandro Zenesini, and Silke Ospelkaus. Feshbach resonances in $^{23}\text{Na}+^{39}\text{K}$ mixtures and refined molecular potentials for the NaK molecule. *Phys. Rev. A* 99, 032711 (2019)

I contributed to the experiments, took part in the interpretation of the data and contributed to the manuscript.

- [A2] Eberhard Tiemann, Philipp Gersema, Kai K. Voges, Torsten Hartmann, Alessandro Zenesini, and Silke Ospelkaus. Beyond Born-Oppenheimer approximation in ultracold atomic collisions. *Phys. Rev. Research* 2, 013366 (2020)

In this theory collaboration with Prof. Tiemann, I led the experiments for the measurements of the d -wave resonances, took part in the interpretation of the data in the context of the Born-Oppenheimer approximation and contributed to the manuscript.

- [A3] Kai K. Voges, Philipp Gersema, Torsten Hartmann, Torben A. Schulze, Alessandro Zenesini, and Silke Ospelkaus. Formation of ultracold weakly bound dimers of bosonic $^{23}\text{Na}^{39}\text{K}$. *Phys. Rev. A* 101, 042704 (2020)

Together with Kai K. Voges, I planned, set-up and performed the experiments, took part in the interpretation of the data and contributed to the manuscript.

- [A4] Kai K. Voges, Philipp Gersema, Torsten Hartmann, Torben A. Schulze, Alessandro Zenesini, and Silke Ospelkaus. A pathway to ultracold bosonic $^{23}\text{Na}^{39}\text{K}$ ground-state molecules. *New J. Phys.* 21 123034 (2019)

Together with Kai K. Voges, I set-up and performed the experiments, took part in the interpretation of the data and contributed to the manuscript.

2 List of publications and own contributions

- [A5] Kai K. Voges, Philipp Gersema, Mara Meyer zum Alten Borgloh, Torben A. Schulze, Torsten Hartmann, Alessandro Zenesini, and Silke Ospelkaus. Ultracold Gas of Bosonic $^{23}\text{Na}^{39}\text{K}$ Ground-State Molecules. *Phys. Rev. Lett.* 125, 083401 (2020)

Together with Kai K. Voges, I planned, set-up and performed the experiments, took part in the interpretation of the data and had a major role in the preparation of the manuscript.

- [A6] Philipp Gersema, Kai K. Voges, Mara Meyer zum Alten Borgloh, Leon Koch, Torsten Hartmann, Alessandro Zenesini, Silke Ospelkaus, Junyu Lin, Junyu He, and Dajun Wang. Probing Photoinduced Two-Body Loss of Ultracold Nonreactive Bosonic $^{23}\text{Na}^{87}\text{Rb}$ and $^{23}\text{Na}^{39}\text{K}$ Molecules. *Phys. Rev. Lett.* 127, 163401 (2021)

I led the planning, set-up and data acquisition of the experiments, had a major role in the interpretation and the analysis of the data and wrote the manuscript.

- [A7] Kai K. Voges, Philipp Gersema, Torsten Hartmann, Silke Ospelkaus and Alessandro Zenesini. Hyperfine dependent atom-molecule loss analyzed by the analytic solution of few-body loss equations. arXiv:2109.03605v2. accepted in *Phys. Rev. Research*

Together with Kai K. Voges, I planned, set-up and performed the experiments, had a major role in the interpretation and the analysis of the data, as well as the writing of the manuscript.

3 Feshbach resonances and molecules

Within this chapter, I summarize our experiments on Feshbach resonances and Feshbach molecule creation. This includes the measurement and analysis of $^{23}\text{Na}^{39}\text{K}$ resonances [A1] and the preparation of $^{23}\text{Na}^{39}\text{K}$ Feshbach molecules [A3]. This is supplemented by a detailed investigation of homonuclear ^{39}K d -wave Feshbach resonances [A2].

3.1 Feshbach resonances in $^{23}\text{Na}+^{39}\text{K}$ mixtures and refined molecular potentials for the NaK molecule [A1]

As mentioned in the introduction, there are three steps involved in the successful preparation of ultracold ground-state molecules. These are the creation of an ultracold atomic mixture, the association of weakly bound molecules from it, and the subsequent two-photon STIRAP to the rovibronic ground state [48]. In this section, a detailed analysis of Feshbach resonances in a mixture of ultracold $^{23}\text{Na}+^{39}\text{K}$ atoms is presented. This lays the foundation for a future generation of weakly bound molecules close to a Feshbach resonance. In the following, I will give a short introduction to the physics of Feshbach resonances.

At a Feshbach resonance, a molecular state, typically with a high vibrational quantum number, crosses the energy of the scattering channel of two unbound atoms at a given magnetic field strength B_{Res} [89, 91]. This requires a differential magnetic moment between these two states, resulting in a magnetic field dependent energy shift. The potential energy curve (PEC) of the scattering atoms is also called the open channel, as the scattering energy E_{scat} is larger than the continuum energy, which is the potential energy at infinite separation R of the two atoms. The PEC of the bound molecular state is called the closed channel, as it can support a bound molecular state at the kinetic energy of the scattering channel. In Fig. 3.1 a schematic of a Feshbach resonance is shown.

For a Feshbach resonance, there needs to be a coupling between the molecular and the diatomic state. This can originate from Coulomb, dipole-dipole or spin-orbit interactions [89]. Close to the resonance the states mix, dependent on the coupling strength and energy difference $\Delta E(B)$ between the scattering channel and the bound molecular state.

Feshbach resonances are often labelled with the partial wave of the incoming scattering channel, such as s -, p - or d -waves. Higher partial wave resonances are generally weak and narrow compared to s -wave resonances in bosonic quantum gases at ultracold temperatures due to the centrifugal barrier. In section (3.2, [A2]), potassium d -wave resonances are studied. Note that, homonuclear p -wave collisions and all higher partial waves with odd angular momentum l , can not occur in a

3 Feshbach resonances and molecules

spin-polarized bosonic gas, as the total wavefunction, comprised of spin and spatial wavefunction, needs to be symmetric.

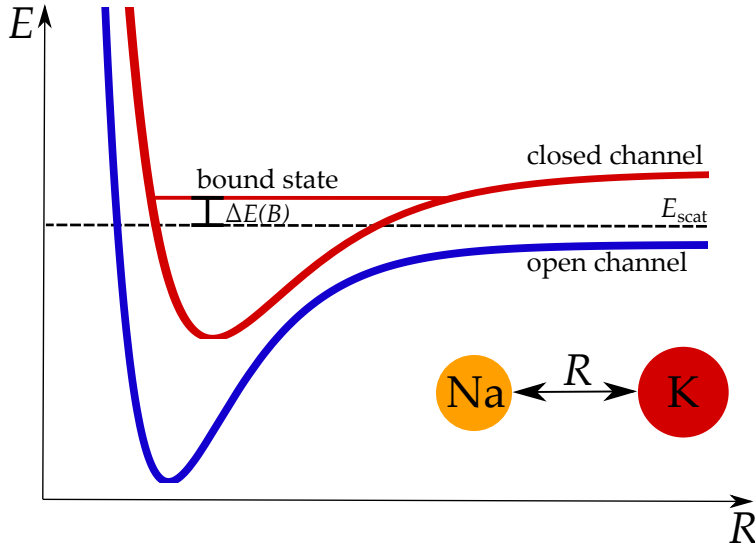


Figure 3.1: Schematic of a Feshbach resonance. R is the interatomic distance and E the energy of the system. During a collision in the open channel a bound molecular state might be close to the energy of the scattering channel. If these couple, the atomic and the molecular states mix, dependent on the coupling strength and the energy difference $\Delta E(B)$.

In general, a Feshbach resonance can also occur from a differential electric moment. However, an electric dipole moment is usually not present for atomic or weakly bound molecular states and is therefore not considered in the following.

Knowing the exact location of the interatomic Feshbach resonances in $^{23}\text{Na}^{39}\text{K}$ is valuable for the refinement of the molecular potentials [A1], but also for two other reasons.

First, close to a resonance, the molecular and the atomic states mix. This enables the creation of weakly bound molecules (Feshbach molecules), for example with a magnetic field sweep across the resonance at B_{Res} or with resonant RF or MW pulses, magnetic field modulations or optical Raman transitions, see section 3.3[A3] [58]. This is a prerequisite for a successful creation of a high phase-space density molecular gas, following the pioneering three-step pathway from JILA in 2009 with KRb [48].

Second, due to the coupling of the scattering channel to the molecular state, the scattering length is altered, dependent on the applied external magnetic field. The s -wave scattering length is given by

$$a(B) = a_{\text{bg}} \left(1 - \frac{\Delta}{B - B_{\text{Res}}} \right), \quad (3.1)$$

where a_{bg} is the background scattering length associated with the PEC of the open channel, B the

applied external magnetic field, B_{Res} the resonance position and Δ the width of the resonance, which is the distance from the resonance to the zero crossing of the scattering length [91]. The background scattering length a_{bg} as well as the width Δ can be positive or negative. A positive/negative scattering length denotes repulsive/attractive interactions between the atoms. Note that, the width of the resonance is not to be confused with the coupling strength, as the width is also dependent on the background scattering length and the differential magnetic moment. If the differential magnetic moment is very small, even a weak coupling might lead to a large width.

As can be seen from this formula, the scattering length is heavily modified close to the resonance. This is depicted in Fig. (3.2).

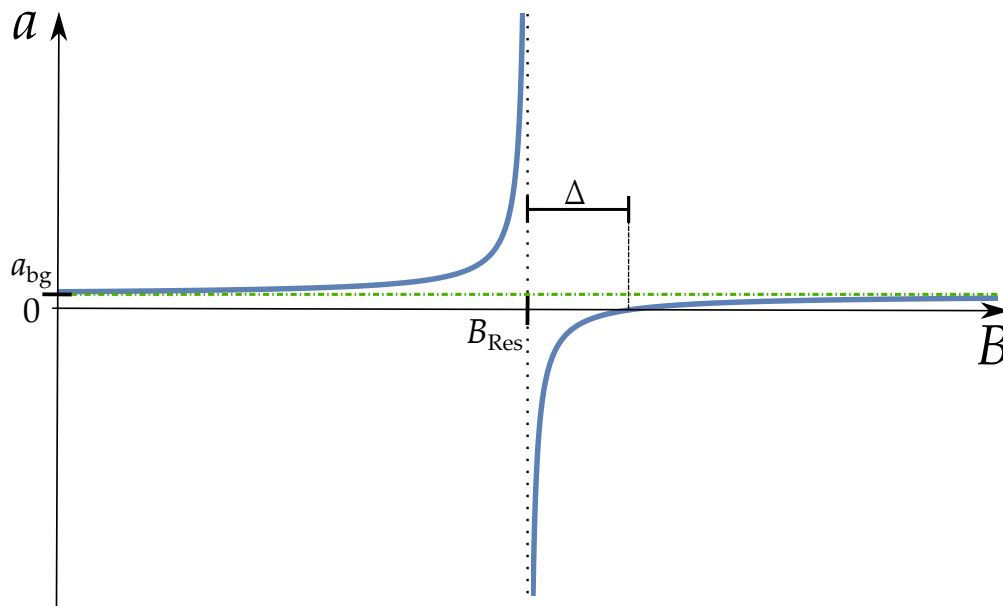


Figure 3.2: Schematic of the s -wave scattering length at a Feshbach resonance. At the resonance the scattering length diverges and switches its sign, at large detunings it approaches again its background scattering value a_{bg} . At the distance Δ from the resonance the scattering length becomes zero.

At the position of the resonance the scattering length diverges and switches its sign. This behaviour allows to change the scattering length between the atoms by choosing a magnetic field. Therefore this is a convenient knob to fine-tune the rethermalization rate of an ultracold gas, for example for efficient evaporation schemes in an optical dipole trap [90]. For the production of a stable BEC it is important to work at a positive scattering length, as a negative scattering length can lead to its collapse [92].

Another important feature is the zero crossing. At this magnetic field, the interaction between the two atoms vanishes, effectively halting atomic losses through, for example, three-body collisions, with the three-body loss rate coefficient $L_3 \propto a^4$ [17].

In the following paper, extensive studies of previously unknown Feshbach resonances between

3 Feshbach resonances and molecules

ultracold ^{23}Na and ^{39}K atoms, prepared in different hyperfine states with adiabatic RF sweeps over avoided crossings utilizing the Zeeman structure of ^{23}Na and ^{39}K , are presented. These are detected via atomic loss measurements. The resulting new resonance positions are used to refine the singlet and triplet ground-state potentials of NaK.

3.1 Feshbach resonances in $^{23}\text{Na}+^{39}\text{K}$ mixtures and refined molecular potentials for the NaK molecule [A1]

Reprinted with permission from Hartmann *et al.*, Feshbach resonances in $^{23}\text{Na}+^{39}\text{K}$ mixtures and refined molecular potentials for the NaK molecule, Phys. Rev. A 99, 032711, 2019

Copyright © 2022 by the American Physical Society (APS).

DOI <http://dx.doi.org/10.1103/PhysRevA.99.032711>

Feshbach resonances in $^{23}\text{Na} + ^{39}\text{K}$ mixtures and refined molecular potentials for the NaK molecule

Torsten Hartmann, Torben A. Schulze, Kai K. Voges, Philipp Gersema, Matthias W. Gempel,
Eberhard Tiemann, Alessandro Zenesini, and Silke Ospelkaus*
Institut für Quantenoptik, Leibniz Universität Hannover, 30167 Hannover, Germany



(Received 24 September 2018; published 27 March 2019)

We present a detailed study of interspecies Feshbach resonances of the bosonic $^{23}\text{Na} + ^{39}\text{K}$ mixture for magnetic fields up to 750 G in various collision channels. A total of 14 Feshbach resonances are reported, as well as four zero crossings of the scattering length and three inelastic two-body loss features. We use the observed magnetic-field locations of the resonant features together with the known data on $^{23}\text{Na} + ^{40}\text{K}$ to refine the singlet and triplet ground-state potentials of NaK and achieve a consistent description of Feshbach resonances for both the Bose-Bose mixture of $^{23}\text{Na} + ^{39}\text{K}$ and the Bose-Fermi mixture of $^{23}\text{Na} + ^{40}\text{K}$. We also discuss the influence of the interplay between inelastic two-body and three-body processes on the observation of a Feshbach resonance.

DOI: [10.1103/PhysRevA.99.032711](https://doi.org/10.1103/PhysRevA.99.032711)

I. INTRODUCTION

Mixtures of ultracold atoms have recently attracted great interest as they enable the study of exciting quantum many-body effects [1]. Furthermore, molecules in their rovibrational ground state are promising candidates for the study of dipolar many-body physics [2–4]. Ensembles of Na + K feature several predicted interspecies Feshbach resonances [5] and their heteronuclear molecules possess a large electric dipole moment of 2.72 D [6], the freedom to prepare both bosonic and fermionic NaK molecules, and chemical stability in molecular two-body collisions [7].

Up to now, Feshbach resonances for the mixture of bosonic ^{23}Na and fermionic ^{40}K have been reported [8,9] and fermionic ground-state $^{23}\text{Na}^{40}\text{K}$ molecules have been prepared by association of Feshbach molecules [10] and, subsequently, by following two different stimulated Raman adiabatic passage (STIRAP) paths [7,11]. Thanks to these results and to previously obtained spectroscopic data [12,13], the interatomic molecular potentials of the singlet and triplet ground states have been refined [9], leading to predictions for Feshbach resonances in the bosonic mixtures by isotope mass rescaling. However, the very different hyperfine coupling between ^{23}Na and ^{40}K compared to that of ^{23}Na and ^{39}K leads to different singlet-triplet mixing within the Feshbach manifold. The accuracy of the predictions strongly depends on residual correlations in the determination of the singlet and triplet potentials from measured $^{23}\text{Na} + ^{40}\text{K}$ Feshbach resonances. A direct measurement of the Feshbach resonance positions in the bosonic mixture is necessary to further refine the potentials for NaK and, in particular, to minimize correlations between the singlet and triplet molecular potentials.

Experimental investigations of the Feshbach resonance spectrum of the bosonic pair $^{23}\text{Na} + ^{39}\text{K}$ have started recently. The identification of Feshbach resonances in the

$|f = 1, m_f = -1\rangle_{\text{Na}} + |f = 1, m_f = -1\rangle_{\text{K}}$ channel has been the basis for the preparation of a dual-species Bose-Einstein condensate of ^{23}Na and ^{39}K atoms in the vicinity of a Feshbach resonance at about 247 G [14]. Here, f denotes the total angular momentum of the respective atom, and m_f denotes the projection onto the quantization axis. By comparing the measured resonance positions with predictions by Viel and Simoni [5] significant deviations become apparent, whereas predictions making use of the recent evaluation in [9], including measured d -wave resonances of $^{23}\text{Na} + ^{40}\text{K}$, reduce these deviations. Since the Feshbach resonances observed in the $|1, -1\rangle_{\text{Na}} + |1, -1\rangle_{\text{K}}$ mixture are only a small subset of the many possible resonances, the observed deviations have motivated a thorough search for the remaining structures in order to further improve the potential-energy curves (PECs).

In this paper we present a detailed study of Feshbach resonances in a variety of hyperfine combinations in the ground-state manifold of $^{23}\text{Na} + ^{39}\text{K}$ for a magnetic-field range from 0 to 750 G. Our approach follows the iterative procedure of prediction, measurement and model refinement that is typical for molecular spectroscopy. The paper is structured accordingly:

In Sec. II we first give a brief summary of Feshbach resonance predictions for the bosonic $^{23}\text{Na} + ^{39}\text{K}$ mixture, which have been derived from molecular potentials obtained by conventional spectroscopy of the NaK molecule and measurements of Feshbach resonances in the Bose-Fermi mixture of $^{23}\text{Na} + ^{40}\text{K}$ by isotope mass rescaling. In the second part of the section the experimental sequence for the measurements is described.

In Sec. III we present our measurements of loss features arising from elastic and inelastic scattering resonances.

In Sec. IV we describe and discuss the updated molecular potentials and how they improve the current knowledge of the scattering properties of both the Bose-Bose and Bose-Fermi mixtures.

In Sec. V a brief discussion of an inelastic loss feature observed in the $|1, 1\rangle_{\text{Na}} + |1, -1\rangle_{\text{K}}$ channel and its influence

*silke.ospelkaus@iqo.uni-hannover.de

on the possible observation of a close-lying Feshbach resonance is given.

II. THEORETICAL AND EXPERIMENTAL OVERVIEW

A. Theoretical predictions from known molecular potentials and a brief discussion of atom-loss spectroscopy

Molecular potentials for the $X^1\Sigma^+$ state and the $a^3\Sigma^+$ state, correlating to the atomic ground-state asymptote, have been derived from extensive classical spectroscopy [12,13] and refined by measurements of Feshbach resonances of the atom pair $^{23}\text{Na} + ^{40}\text{K}$ [8,9]. These can be used to predict Feshbach resonances for the pair $^{23}\text{Na} + ^{39}\text{K}$ if the Born-Oppenheimer approximation is assumed to remain valid and by incorporating the proper hyperfine and Zeeman interactions of ^{39}K . Details about the potential representations and the interpretation of the coupled-channel calculations are given in Sec. IV.

From the potentials we predict 32 resonances in the magnetic-field region from 0 to 750 G with coupled-channel calculations for atom pairs with magnetic quantum numbers $f_{\text{Na}} = 1$, $m_{f_{\text{Na}}} = \{-1, 0, +1\}$ and $f_{\text{K}} = 1$, $m_{f_{\text{K}}} = \{-1, 0, +1\}$. Additionally, resonances for $f = 2$, $m_{f_{\text{Na,K}}} = -2$ are predicted. The calculations are done for an ensemble temperature of $1 \mu\text{K}$, and therefore, only s -wave resonances are considered. Comparing theoretical and experimental results in [14], the accuracy of our predictions is expected to be on the order of a few Gauss, significantly simplifying the search in the experiment.

We locate Feshbach resonance positions by atom-loss spectroscopy, making use of the strongly enhanced scattering length and associated large on-resonance three-body loss in the atomic ensemble [15]. The detected losses are referred to as an elastic loss signal throughout this paper. Atom loss is also observed in the case of inelastic two-body collisions, where the energy released by the spin exchange is sufficiently high to lead to a two-body loss process in the trapped sample. In both cases we identify the local maximum of the atom loss with a resonance position. Typically, three-body processes require higher particle densities than two-body processes to obtain comparable loss rates. Thus, in our case inelastic loss processes are expected to elapse on a shorter timescale than the three-body loss and will therefore lead to strong losses already for short hold times.

Care has to be taken when investigating a zero crossing of the scattering length as a function of magnetic field. The minimum of the detected losses is, in general, not identical to the zero of the scattering length [16], and a measurement similar to that in Sec. IIB can give misleading results. We instead localize this magnetic-field position by exploiting the two-body losses that appear during optical evaporation, similar to the work in [14]. In this procedure the magnetic-field strength is set to the target value before the start of the optical evaporation. Because the optical trapping potential depth ratio is $U_{\text{K}} \approx 2.51U_{\text{Na}}$, predominantly, ^{23}Na is ejected from our crossed optical dipole trap (cODT), while ^{39}K is sympathetically cooled. On a zero crossing two-body collisions are suppressed and therefore also losses resulting from the evaporation process [17].

B. Experimental procedure

The experimental setup is described in detail in [18,19]. The experimental sequence is based on the experiences of [14]. Since precise knowledge of the generated magnetic-field strength is necessary, calibration was performed repetitively in the course of the measurement campaign. The calibration method is the same as already described in [14]. We use microwave spectroscopy on a sample of ^{23}Na with a temperature of $\sim 800 \text{ nK}$ confined in the cODT. For a defined electric current we measure the microwave frequency of the $|f = 1, m_f = -1\rangle \rightarrow |f = 2, m_f = 0\rangle$ transition using the atom loss in the $|f = 1, m_f = -1\rangle$ state as a signal and calculate the corresponding magnetic field using the Breit-Rabi formula. The transition frequency is determined with an uncertainty of about 10 kHz, leading to uncertainty on the value for the magnetic-field strength on the order of 30 mG. This is typically small compared to the statistical uncertainty originating from the resonance loss measurements. In the following we give a brief summary of the experiment sequence and explain the applied modifications in comparison to [14].

First, an optically plugged magnetic quadrupole trap is loaded from a dual-species magneto-optical trap (MOT). The atoms are then transferred to a cODT where we prepare an ultracold mixture of ^{23}Na and ^{39}K , both in $|f = 1, m_f = -1\rangle$, by optical evaporation. The temperature is $\sim 1 \mu\text{K}$ for both species, as measured by time-of-flight (TOF) expansions.

After the evaporation in the cODT has been completed, we transfer ^{23}Na and ^{39}K to the spin-state combination of interest, making use of rapid-adiabatic-passage [20] sequences. Their efficiency is close to unity, and neither heating the sample nor atom loss due to the transfers is observed in our experiment.

For the atom-loss spectroscopy, we vary the atom numbers of the two species, preparing one species as the majority component and the other one as the minority component. The peak densities in the cODT are between 1.5×10^{12} and $7.4 \times 10^{14} \text{ cm}^{-3}$ for ^{23}Na and between 3.9×10^{13} and $1.6 \times 10^{15} \text{ cm}^{-3}$ for ^{39}K . Detected loss within the minority component provides the primary signal. We use different tuning knobs in the experimental sequence to adjust the atom numbers. The first one is given by the loading times of the dual-species MOT. The second tuning knob is the depth of the forced microwave evaporation we perform in our optically plugged magnetic quadrupole trap. Due to the smaller repulsion of ^{39}K by the blue-detuned plug laser light, a deeper evaporation and thereby colder atomic sample lead to an increased ^{39}K density close to the magnetic trap center compared to ^{23}Na . This increases losses in the ^{39}K cloud. Hence, the deeper the evaporation is performed, the more the atom ratio inside the cODT is shifted towards a prevalence of ^{23}Na .

We ramp the magnetic-field strength in a few milliseconds to the target value. The loss measurement is repeated multiple times for every magnetic-field value. For every resonance under investigation we experimentally determine the appropriate holding time, ensuring that the minority cloud is not depleted completely at the minimum but the loss feature is clearly visible. The holding time varies between 10 and 1000 ms and its magnitude can be an indication of whether inelastic two-body or inelastic three-body processes dominate the losses.

The number of remaining atoms is recorded by absorption imaging of the majority component in the cODT and of the minority component after a short TOF. Where possible, we ramp down the magnetic field to zero in 5 to 40 ms (depending on the initial magnetic-field value) and image both species at zero magnetic field.

For some spin-state combinations we find that low-field Feshbach resonances and/or high-background-scattering lengths lead to sizable losses, rendering imaging both species at zero magnetic field unfavorable. To circumvent these additional losses, we perform high-field imaging on the ^{39}K D_2 line. For magnetic-field strengths beyond 200 G the Paschen-Back regime is reached for ^{39}K , where the electron angular momentum (j, m_j) and the nuclear spin (i, m_i) decouple from each other in both electronic states and instead align directly relative to the external magnetic field. With this, f is no longer a good quantum number. Together with the selection rule $\Delta m_i = 0$, it is always possible to find a transition with $\Delta m_j = \pm 1$, which then serves as a closed imaging transition. We choose a magnetic field for which no other resonance has to be crossed and for which the scattering rate of the state combination under investigation is low. We then image ^{39}K as the majority component in the cODT and follow the scheme above for the ^{23}Na detection.

To improve the signal-to-noise ratio of the atomic cloud pictures, especially for low atom numbers, the absorption images of ^{23}Na and ^{39}K are postprocessed. The background of every picture is reconstructed using an algorithm based on principal-component analysis [21], and this background is subtracted from the picture. The pictures taken at equal magnetic-field values are then averaged, and the resulting image is fitted with a two-dimensional Gaussian. From the fit, the atom number is derived. The errors on the atom number result from the standard deviations of the fit. They vary between the different resonance measurements because they incorporate shot-to-shot atom-number fluctuations which can originate from the different required spin preparation steps and the number of resonances which need to be crossed to reach the magnetic-field value under investigation. For lucidity they are shown only for two exemplary measurements in Fig. 1. The errors are propagated to the profile fit of the loss feature and therefore contribute to the uncertainties of the resonance positions (see Table I).

III. LOSS RESONANCES AND ZERO CROSSINGS

We have located 21 features, including the ones already presented in [14]. Fourteen features are assigned to predicted Feshbach resonances, resulting in three-body loss; three result from inelastic loss channels, and four are assigned to zero crossings of the two-body scattering length. Figure 1 shows the measured features. To determine the resonance positions we do a weighted fit to our data with a phenomenological Gaussian function. For every measurement the atom number is normalized on the baseline of the fit. In Fig. 1, the normalized atom numbers of the different measurements for every channel are set equal to 1. This leads to an artificial increase in the atom number above 1 in case of a measured zero crossing. The resulting positions of all measured features are summarized in Table I. In cases of loss features being clearly

visible for both species, the position of the resonance is the weighted average of the center positions from the two fits. The error estimate of the experimentally determined resonance positions, given in Table I, includes the uncertainty in the profile fit (which includes the errors from the atom number determination as explained above) as well as the uncertainty in the calibration of the magnetic-field strength.

As summarized in Table I, some calculated resonances remain undetected. The main reasons are as follows:

(i) Some of the state combinations experience a very high background scattering rate over the complete investigated magnetic-field range. For these spin mixtures, the resonances are hidden since the atomic samples experience large losses already during the state preparation and/or the ramp to the target magnetic field.

(ii) While pure ^{23}Na does not show significant loss features in the investigated range of the magnetic-field strength, ^{39}K exhibits several Feshbach resonances in different spin channels. We remeasured the ^{39}K resonances relevant for our investigations and found all resonance positions to be within the experimental uncertainties of previous publications [22,23]. Some of them are critical for our heteronuclear measurements since they are located near or even overlap the resonance positions predicted for $^{23}\text{Na} + ^{39}\text{K}$. These cases are mentioned in Table I. Additionally, the ^{39}K Feshbach resonances are indicated in Fig. 1 as vertical blue dashed lines.

IV. THEORY AND CALCULATIONS

The theoretical modeling of two-body collisions of two alkali atoms in their electronic ground state is well established and described in many publications (see, for example, [24]).

The Hamiltonian contains the conventional kinetic and potential energies for the relative motion of the two particles and needs, for the coupling of the molecular states $X^1\Sigma^+$ and $a^3\Sigma^+$, the hyperfine and Zeeman terms. For finer details of the partial waves with $l \geq 1$, one also needs the spin-spin interaction. The molecular PECs are represented in a power expansion of an appropriate function $\xi(R)$ of the internuclear separation R ,

$$\xi(R) = \frac{R - R_m}{R + b R_m}, \quad (1)$$

to describe the anharmonic form of the potential function for $R \rightarrow \infty$ or $R \rightarrow 0$. R_m is an internuclear separation close to the minimum of the respective PEC, and b is a parameter to optimize the potential slopes left and right of R_m with few terms in the power expansion. The full PECs are extended by long-range terms and short-range repulsive ones (see [24] and the Supplemental Material of this paper [25]).

We calculate the two-body collision rate at the kinetic energy that corresponds to the temperature of the prepared ensemble. Thermal averaging is not performed, which would need significant computing time, but more importantly, for a complete description we would have to consider the two cases of two- and three-body effects in the modeling. Here, we take the calculated maximum in the two-body collision rate constant to be equal to the observed Feshbach resonance and the calculated minimum to be equal to the observed loss minimum in optical evaporation.

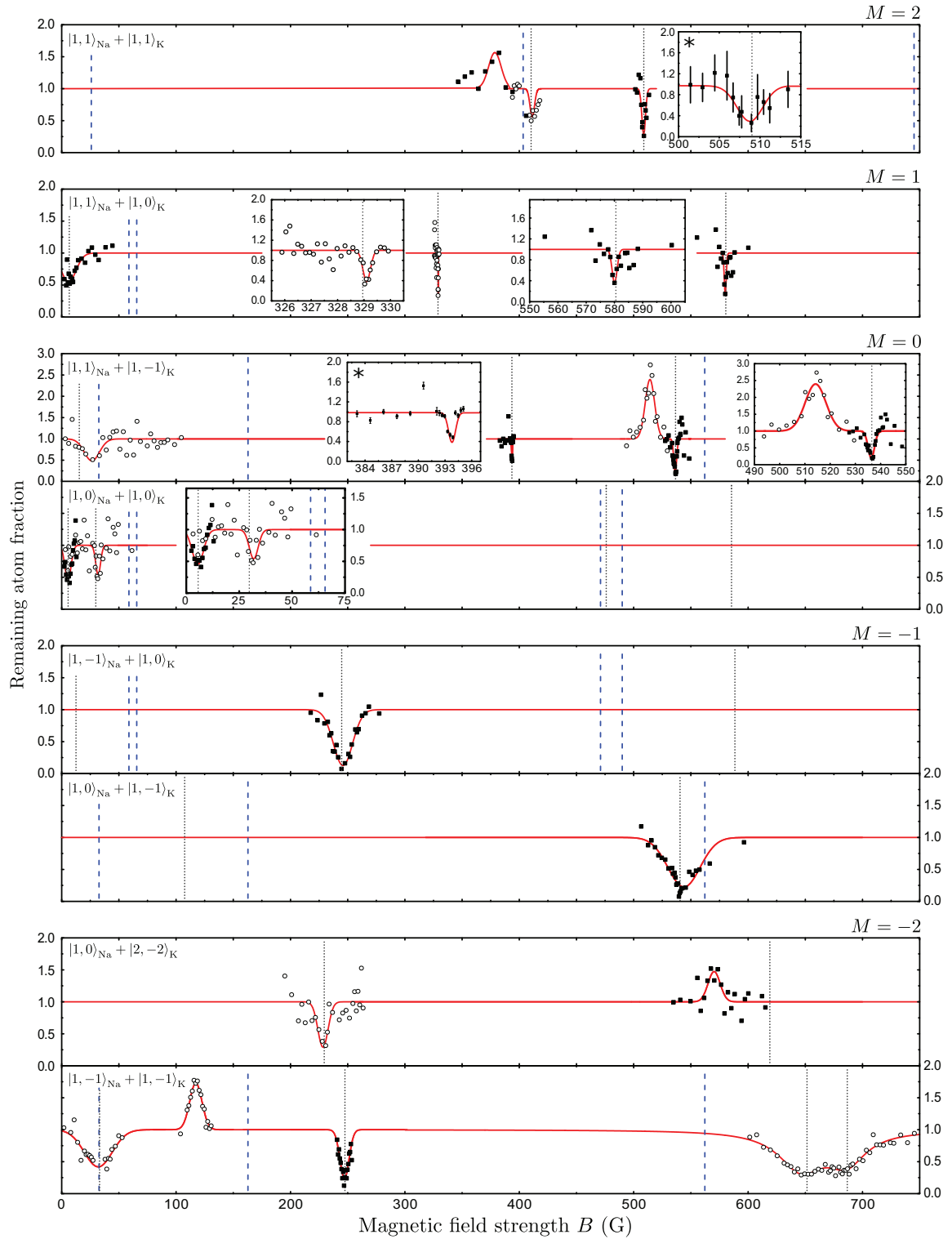


FIG. 1. Collection of resonant features in different spin mixtures of $^{23}\text{Na} + ^{39}\text{K}$. M is the total magnetic quantum number of the pair $|f, m_f\rangle_{\text{Na}} + |f, m_f\rangle_{\text{K}}$, and f is for increasing magnetic-field strength B only an approximate quantum number. Open circles and solid squares correspond to resonances observed by loss of ^{23}Na and of ^{39}K , respectively. Insets show zooms of the detected narrow-resonance features. For two measurements, in $|1, 1\rangle_{\text{Na}} + |1, 1\rangle_{\text{K}}$ and $|1, 1\rangle_{\text{Na}} + |1, -1\rangle_{\text{K}}$, marked with an asterisk, error bars are given, representing the variation in the errors for different loss measurements (for details, see text). For each recording, the holding time and the initial atom numbers are independently optimized. The data are normalized according to the respective phenomenological Gaussian fit (red solid line) of the feature with a baseline set to 1. Zero crossings therefore appear artificially as an enhancement of the atom number. Vertical gray dotted lines indicate the calculated positions of $^{23}\text{Na} + ^{39}\text{K}$ Feshbach resonances as listed in Table I. Vertical dashed blue lines mark the positions of ^{39}K resonances, taken from [22,23]. The trace for the $|1, -1\rangle_{\text{Na}} + |1, -1\rangle_{\text{K}}$ mixture corresponds to data from Ref. [14].

TABLE I. Measured magnetic-field positions B_{exp} and uncertainties (\pm) together with calculated positions B_{th} , applying the improved potentials. M is the total magnetic quantum number of the pair $|f, m_f\rangle_{\text{Na}} + |f, m_f\rangle_{\text{K}}$; f is, in most cases, only an approximate quantum number. Subscripts res and ZC stand for resonance and zero crossing, respectively. KK res. indicates an intraspecies ^{39}K Feshbach resonance in the respective scattering channel. In some cases, maxima of the elastic (el.) and inelastic (in.) scattering rate are listed. A.1 marks the inelastic loss feature discussed in Sec. V.

M	Na_{f,m_f}	K_{f,m_f}	$B_{\text{exp,ZC}}$ (G)	$B_{\text{th,ZC}}$ (G)	$B_{\text{exp,res}}$ (G)	$B_{\text{th,res}}$ (G)
2	1,1	1,1	380.88 (3.83)	381.43 507.0	411.33 (1.28) 508.73 (0.83)	410.1 508.81
1	1,1	1,0		328.5 442.5 577.5	6.72 (2.09) 329.12 (0.77) close to KK res. 579.94 (0.88)	6.6 328.96 467 580.49
	1,0	1,1		336.0	close to KK res.	7.5 (in.) 9.0 (el.) 419.0 508.5 (in.) 512.0 (el.)
0	1,1	1, -1		393.0 516.4	26.34 (3.31) A.1 393.61 (0.76) 536.07 (0.94)	15.4 (el.) 28.2 (in.) 393.59 536.67
	1,0	1,0	515.85 (1.68)	4.25 407	5.47 (1.01) 31.86 (1.69) close to KK res.	5.6 29.8 475.5 (in.) 476.0 (el.) 581.5 (in.) 585.5 (el.) 516.0 (el.) 522.5 (in.)
-1	1, -1	1,1				13.0 244.75 588.5 (el.) 593.0 (in.)
	1, -1	1,0			245.76 (1.45)	107.5 540.5 88.5 (in.) 134.0 (in.) 138.0 (el.) 471
	1,0	1, -1			541.09 (1.50)	272.5 (in., weak) 314.5 (in.) 465.5 (in.) 473.5 (el.)
	1,1	2, -2				
	2, -2	1,1				
-2	1, -1	1, -1		117.08	32.5 (0.8) ^a 247.1 (0.2) ^a 646.6 (1.5) ^a 686.2 (1.5) ^a 228.48 (1.49)	33.13 247.57 651.5 (el./in.) 686.7 (in.) 229.5 619.0
	1,0	2, -2	570.29 (2.55)	574.3		358.5 (in.) 528.0 (in.) 533.0 (el.)
	2, -2	1,0				

^aMeasurement previously presented in [14].

The most recent fit of Feshbach resonances was reported for $^{23}\text{Na} + ^{40}\text{K}$ in [9], and the present evaluation starts from that result. Calculating the resonances for the observed cases with those derived PECs, we find significant deviations between observation and theory, thus requiring new fits. They include all former observations and, additionally, the measured Feshbach resonances and zero crossings presented in this paper, in total 82 independent data points from Feshbach spectroscopy. This allows us to further reduce correlations in the determination of the triplet and singlet potentials. The improved molecular potentials lead to a higher consistency between the measured and theoretically predicted resonance features for the bosonic $^{23}\text{Na} + ^{39}\text{K}$ mixture as well as the Bose-Fermi mixture of $^{23}\text{Na} + ^{40}\text{K}$. The sum of squared

residuals of calculated and experimentally determined resonance positions, weighted by the experimental uncertainties, improved from 337.0 to 255.31. We give a full listing of the data points and the evaluation with the different potential approaches in the Supplemental Material. Furthermore, we find that no inclusion of Born-Oppenheimer correction is needed to achieve this improvement. The parameters of the refined PECs can be found in the Supplemental Material.

Table I lists the calculated resonance positions which are derived using the updated potential-energy curves. In several channels, the calculations show maxima for the elastic and inelastic scattering rates appear close to each other. Such a constellation can lead to a shifted minimum in the atom-loss measurement. For one resonance a remarkable shift was

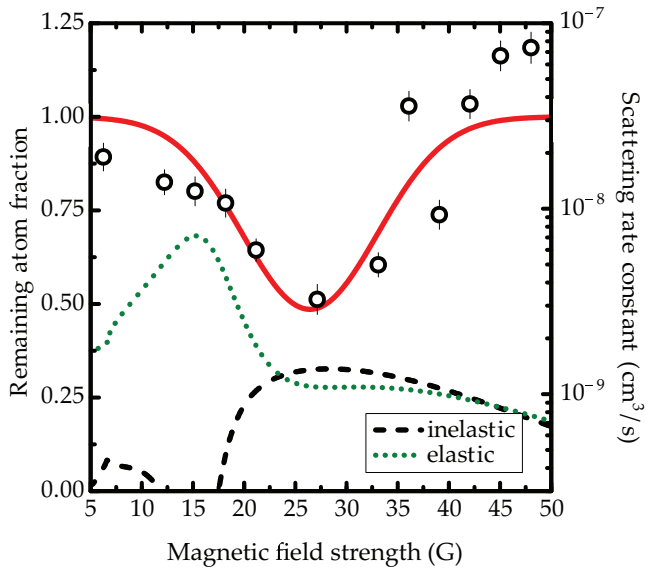


FIG. 2. Remaining atom fraction of ^{23}Na (open circles) and Gaussian fit (red curve) as well as elastic (green dotted line) and inelastic (black dashed line) collision rate constants for the $|1, 1\rangle_{\text{Na}} + |1, -1\rangle_{\text{K}}$ channel. The rate constants are calculated for a kinetic energy of $1 \mu\text{K}$. The peak densities in the cODT for this measurement were $2.2 \times 10^{12} \text{ cm}^{-3}$ for ^{23}Na and $4.4 \times 10^{13} \text{ cm}^{-3}$ for ^{39}K .

observed in our experiment and will be discussed in the following section. Note that closely located maxima of elastic and inelastic scattering rates can also lead to asymmetric broadening of loss signals. This could be an additional reason why for several measurements of Feshbach resonances shifts and asymmetric broadening of the loss signals were reported [26–31].

V. INELASTIC LOSS FEATURE IN $|1, 1\rangle_{\text{Na}} + |1, -1\rangle_{\text{K}}$

Our theoretical model predicts a Feshbach resonance at 15 G for the $|1, 1\rangle_{\text{Na}} + |1, -1\rangle_{\text{K}}$ channel. However, our measurements show a broad loss signal at 26.34 G (see Fig. 1 and Table I). The large deviation can be explained by looking at both elastic and inelastic loss contributions. Figure 2 shows the atom-loss measurement together with the elastic loss rate, which has a maximum at 15.4 G and an enhancement of the inelastic loss rate at 28.2 G. The inelastic part is due to the coupling to the $|1, 0\rangle_{\text{Na}} + |1, 0\rangle_{\text{K}}$ channel and gains strength through a Feshbach resonance at 29.8 G for the latter channel. The inelastic two-body losses occur on a shorter timescale and dominate the three-body losses invoked by the elastic part

of the scattering rate. This is confirmed by a relatively short hold time of 100 ms for the measurement presented in Fig. 2, in comparison to up to an order of magnitude larger hold times for the measurements of three-body losses at a Feshbach resonance. The elastic peak might be hidden in the shoulder of the recorded profile. To pinpoint the Feshbach resonance position with higher accuracy, a binding energy measurement should be performed [32], which is left for future investigation. Similar findings on the interplay of inelastic two-body and three-body processes have been reported in [9].

VI. CONCLUSION AND OUTLOOK

In this paper we presented a detailed study of Feshbach resonances in many possible hyperfine combinations of the ground-state manifold of $^{23}\text{Na} + ^{39}\text{K}$ in a magnetic-field range from 0 to 750 G. We compared these measurements to theoretical predictions based on the currently available data for NaK molecular potentials and used our data to refine those potentials. The improved potentials lead to a higher consistency between the experimental data and theoretical predicted resonance features for both the bosonic $^{23}\text{Na} + ^{39}\text{K}$ mixture and the Bose-Fermi mixture of $^{23}\text{Na} + ^{40}\text{K}$. With the incorporation of the experimental data of the bosonic Feshbach resonances and the finding that the Born-Oppenheimer approximation remains valid for the investigated partial waves, reliable predictions based on the new potentials will also be possible for the other, still unexplored bosonic mixture of $^{23}\text{Na} + ^{41}\text{K}$.

Moreover, the observation of the inelastic loss feature deviating significantly from the corresponding elastic peak indicates that careful theoretical investigation is recommended in case unexpected deviations appear in an analysis of a performed Feshbach resonance atom-loss measurement.

The measurements and refined molecular potentials will greatly aid the future investigation of interspin phenomena such as droplet formation [33] as well as in producing stable $^{23}\text{Na}^{39}\text{K}$ molecules in their absolute ground state via a STIRAP process [34].

ACKNOWLEDGMENTS

We gratefully acknowledge financial support from the European Research Council through ERC Starting Grant POLAR and from the Deutsche Forschungsgemeinschaft (DFG) through CRC 1227 (DQ-mat), project A03, and FOR2247, project E5. K.K.V. thanks the Deutsche Forschungsgemeinschaft for financial support through Research Training Group 1991.

- [1] C. Chin, R. Grimm, P. Julienne, and E. Tiesinga, *Rev. Mod. Phys.* **82**, 1225 (2010).
- [2] M. Baranov, *Phys. Rep.* **464**, 71 (2008).
- [3] T. Lahaye, C. Menotti, L. Santos, M. Lewenstein, and T. Pfau, *Rep. Prog. Phys.* **72**, 126401 (2009).
- [4] M. A. Baranov, M. Dalmonte, G. Pupillo, and P. Zoller, *Chem. Rev.* **112**, 5012 (2012).
- [5] A. Viel and A. Simoni, *Phys. Rev. A* **93**, 042701 (2016).
- [6] M. Aymar and O. Dulieu, *J. Chem. Phys.* **122**, 204302 (2005).
- [7] J. W. Park, S. A. Will, and M. W. Zwierlein, *Phys. Rev. Lett.* **114**, 205302 (2015).
- [8] J. W. Park, C.-H. Wu, I. Santiago, T. G. Tiecke, S. Will, P. Ahmadi, and M. W. Zwierlein, *Phys. Rev. A* **85**, 051602 (2012).
- [9] M.-J. Zhu, H. Yang, L. Liu, D.-C. Zhang, Y.-X. Liu, J. Nan, J. Rui, B. Zhao, J.-W. Pan, and E. Tiemann, *Phys. Rev. A* **96**, 062705 (2017).
- [10] C.-H. Wu, J. W. Park, P. Ahmadi, S. Will, and M. W. Zwierlein, *Phys. Rev. Lett.* **109**, 085301 (2012).

- [11] F. Seeßelberg, N. Buchheim, Z.-K. Lu, T. Schneider, X.-Y. Luo, E. Tiemann, I. Bloch, and C. Gohle, *Phys. Rev. A* **97**, 013405 (2018).
- [12] A. Gerdes, M. Hobein, H. Knöckel, and E. Tiemann, *Eur. Phys. J. D* **49**, 67 (2008).
- [13] I. Temelkov, H. Knöckel, A. Pashov, and E. Tiemann, *Phys. Rev. A* **91**, 032512 (2015).
- [14] T. A. Schulze, T. Hartmann, K. K. Voges, M. W. Gempel, E. Tiemann, A. Zenesini, and S. Ospelkaus, *Phys. Rev. A* **97**, 023623 (2018).
- [15] T. Weber, J. Herbig, M. Mark, H.-C. Nägerl, and R. Grimm, *Phys. Rev. Lett.* **91**, 123201 (2003).
- [16] Z. Shotan, O. Machtay, S. Kokkelmans, and L. Khaykovich, *Phys. Rev. Lett.* **113**, 053202 (2014).
- [17] This procedure is most efficient for a low ^{39}K intraspecies scattering length because self-evaporation is suppressed in this case.
- [18] M. W. Gempel, Ph.D. thesis, Leibniz University Hannover, 2016.
- [19] T. A. Schulze, Ph.D. thesis, Leibniz University Hannover, 2018.
- [20] J. C. Camparo and R. P. Frueholz, *J. Phys. B* **17**, 4169 (1984).
- [21] X. Li, M. Ke, B. Yan, and Y. Wang, *Chin. Opt. Lett.* **5**, 128 (2007).
- [22] C. D'Errico, M. Zaccanti, M. Fattori, G. Roati, M. Inguscio, G. Modugno, and A. Simoni, *New J. Phys.* **9**, 223 (2007).
- [23] S. Roy, M. Landini, A. Trenkwalder, G. Semeghini, G. Spagnolli, A. Simoni, M. Fattori, M. Inguscio, and G. Modugno, *Phys. Rev. Lett.* **111**, 053202 (2013).
- [24] S. Knoop, T. Schuster, R. Scelle, A. Trautmann, J. Appmeier, M. K. Oberthaler, E. Tiesinga, and E. Tiemann, *Phys. Rev. A* **83**, 042704 (2011).
- [25] See Supplemental Material at <http://link.aps.org/supplemental/10.1103/PhysRevA.99.032711> for the parameters of the refined singlet and triplet potentials of NaK given with respect to the Na(3s)+K(4s) asymptote, as well as for a table which lists 82 different resonance features of Na+K, comparing their experimentally determined positions with those calculated with different molecular potentials, including the potentials presented in this paper.
- [26] K. Dieckmann, C. A. Stan, S. Gupta, Z. Hadzibabic, C. H. Schunck, and W. Ketterle, *Phys. Rev. Lett.* **89**, 203201 (2002).
- [27] T. Bourdel, J. Cubizolles, L. Khaykovich, K. M. F. Magalhães, S. J. J. M. F. Kokkelmans, G. V. Shlyapnikov, and C. Salomon, *Phys. Rev. Lett.* **91**, 020402 (2003).
- [28] C. Weber, G. Barontini, J. Catani, G. Thalhammer, M. Inguscio, and F. Minardi, *Phys. Rev. A* **78**, 061601 (2008).
- [29] O. Machtay, D. A. Kessler, and L. Khaykovich, *Phys. Rev. Lett.* **108**, 130403 (2012).
- [30] S. Zhang and T.-L. Ho, *New J. Phys.* **13**, 055003 (2011).
- [31] A. Y. Khramov, A. H. Hansen, A. O. Jamison, W. H. Dowd, and S. Gupta, *Phys. Rev. A* **86**, 032705 (2012).
- [32] J. Ulmanis, S. Häfner, R. Pires, E. D. Kuhnle, M. Weidemüller, and E. Tiemann, *New J. Phys.* **17**, 055009 (2015).
- [33] D. S. Petrov, *Phys. Rev. Lett.* **115**, 155302 (2015).
- [34] U. Gaubatz, P. Rudecki, M. Becker, S. Schieman, M. Kütz, and K. Bergmann, *Chem. Phys. Lett.* **149**, 463 (1988).

Feshbach resonances in $^{23}\text{Na}+^{39}\text{K}$ mixtures and refined molecular potentials for the NaK molecule

Torsten Hartmann, Torben A. Schulze, Kai K. Voges, Philipp Gersema,
Matthias W. Gempel, Eberhard Tiemann, Alessandro Zenesini, and Silke Ospelkaus*

Institut für Quantenoptik, Leibniz Universität Hannover, 30167 Hannover, Germany

(Dated: February 11, 2019)

I. MOLECULAR POTENTIAL CURVES

The parametrization of the molecular potentials is described for example in [1]. The potentials are represented in three parts: the repulsive short-range part $U_{\text{SR}}(R)$, the intermediate range $U_{\text{IR}}(R)$ and the asymptotic long range part $U_{\text{LR}}(R)$, which are given by the following expressions:

$$U_{\text{SR}}(R) = A + \frac{B}{R^q} \quad \text{for} \quad R < R_i, \quad (1)$$

$$U_{\text{IR}}(R) = \sum_{k=0}^n a_k \xi(R)^k \quad \text{for} \quad R_i \leq R \leq R_o, \quad (2)$$

$$\text{with } \xi(R) = \frac{R - R_m}{R + bR_m}, \quad (3)$$

and

$$U_{\text{LR}}(R) = -\frac{C_6}{R^6} - \frac{C_8}{R^8} - \frac{C_{10}}{R^{10}} - \dots \pm E_{\text{ex}} \quad \text{for} \quad R < R_o, \quad (4)$$

where the exchange energy is given by

$$E_{\text{ex}} = A_{\text{ex}} R^\gamma \exp(-\beta R). \quad (5)$$

It is negative for the singlet and positive for the triplet potential.

The parameters of the refined NaK singlet and triplet molecular potential curves are listed in Tab. I. A computer code in FORTRAN for calculating the potential functions can be found in the supplement of [2].

II. EVALUATION OF FESHBACH SPECTROSCOPY

We present a detailed evaluation of 82 independent data points obtained in Feshbach spectroscopy and taken from different publications. The quality of four different PEC-representations is compared in terms of the sum of weighted squared deviations in Tab. II. Note that the reference [3] only takes a subset of the given scattering features into account. Therefore, a sum of weighted squared deviations is only calculated for the last three columns of Tab. II.

* silke.ospelkaus@iqo.uni-hannover.de

-
- [1] A. Gerdes, M. Hobein, H. Knöckel, and E. Tiemann, *Eur. Phys. J. D* **49**, 67 (2008).
 [2] R. Pires, M. Repp, J. Ulmanis, E. D. Kuhnle, M. Weidemüller, T. G. Tiecke, C. H. Greene, B. P. Ruzic, J. L. Bohn, and E. Tiemann, *Phys. Rev. A* **90**, 012710 (2014).
 [3] A. Viel and A. Simoni, *Phys. Rev. A* **93**, 042701 (2016).
 [4] I. Temelkov, H. Knöckel, A. Pashov, and E. Tiemann, *Phys. Rev. A* **91**, 032512 (2015).
 [5] M.-J. Zhu, H. Yang, L. Liu, D.-C. Zhang, Y.-X. Liu, J. Nan, J. Rui, B. Zhao, J.-W. Pan, and E. Tiemann, *Phys. Rev. A* **96**, 062705 (2017).
 [6] This work..
 [7] T. A. Schulze, T. Hartmann, K. K. Voges, M. W. Gempel, E. Tiemann, A. Zenesini, and S. Ospelkaus, *Phys. Rev. A* **97**, 023623 (2018).
 [8] J. W. Park, C.-H. Wu, I. Santiago, T. G. Tiecke, S. Will, P. Ahmadi, and M. W. Zwierlein, *Phys. Rev. A* **85**, 051602 (2012).
 [9] J. Rui, H. Yang, L. Liu, D.-C. Zhang, Y. Liu, J. Nan, B. Zhao, and J.-W. Pan, *Nature Physics* (2017).

TABLE I. Potential parameters of the $X^1\Sigma^+$ and $a^3\Sigma^+$ states of NaK given with respect to the Na(3s)+K(4s) asymptote.

$X^1\Sigma^+$		$a^3\Sigma^+$	
For $R < R_i = 2.617\text{\AA}$		For $R < R_i = 4.60\text{\AA}$	
A	$-0.7205185 \times 10^4 \text{ cm}^{-1}$	A	$-0.13272988 \times 10^4 \text{ cm}^{-1}$
B	$0.696124608 \times 10^6 \text{ cm}^{-1} \text{\AA}^q$	B	$0.212875317 \times 10^5 \text{ cm}^{-1} \text{\AA}^q$
q	4.92948	q	1.844150
For $R_i \leq R \leq R_o$		For $R_i \leq R \leq R_o$	
b	-0.4	b	-0.27
R_m	3.49901422 \AA	R_m	5.4478206 \AA
a_0	$-5273.62315 \text{ cm}^{-1}$	a_0	$-207.81119 \text{ cm}^{-1}$
a_1	$-0.239542348630413837 \times 10^1 \text{ cm}^{-1}$	a_1	$-0.474837907736683607 \text{ cm}^{-1}$
a_2	$0.145382657416013644 \times 10^5 \text{ cm}^{-1}$	a_2	$0.178992974113576133 \times 10^4 \text{ cm}^{-1}$
a_3	$0.114848641509625941 \times 10^5 \text{ cm}^{-1}$	a_3	$-0.159602468357546013 \times 10^4 \text{ cm}^{-1}$
a_4	$-0.393070200439200050 \times 10^3 \text{ cm}^{-1}$	a_4	$-0.948541718924311908 \times 10^3 \text{ cm}^{-1}$
a_5	$-0.169145814548076414 \times 10^5 \text{ cm}^{-1}$	a_5	$-0.135179373273532747 \times 10^4 \text{ cm}^{-1}$
a_6	$-0.374171063602873910 \times 10^5 \text{ cm}^{-1}$	a_6	$-0.183565449370861752 \times 10^5 \text{ cm}^{-1}$
a_7	$0.106844724280541472 \times 10^6 \text{ cm}^{-1}$	a_7	$0.124501710356527314 \times 10^6 \text{ cm}^{-1}$
a_8	$0.549571543607791886 \times 10^6 \text{ cm}^{-1}$	a_8	$-0.163160543217713166 \times 10^5 \text{ cm}^{-1}$
a_9	$-0.216398544375193026 \times 10^7 \text{ cm}^{-1}$	a_9	$-0.199688039882199257 \times 10^7 \text{ cm}^{-1}$
a_{10}	$-0.101610099703415297 \times 10^8 \text{ cm}^{-1}$	a_{10}	$0.617100814516823366 \times 10^7 \text{ cm}^{-1}$
a_{11}	$0.221444819359695017 \times 10^8 \text{ cm}^{-1}$	a_{11}	$0.588039077124197735 \times 10^6 \text{ cm}^{-1}$
a_{12}	$0.109959157819038272 \times 10^9 \text{ cm}^{-1}$	a_{12}	$-0.391885588318469822 \times 10^8 \text{ cm}^{-1}$
a_{13}	$-0.154974082312119037 \times 10^9 \text{ cm}^{-1}$	a_{13}	$0.881312470507461876 \times 10^8 \text{ cm}^{-1}$
a_{14}	$-0.782460601529465795 \times 10^9 \text{ cm}^{-1}$	a_{14}	$-0.839469806952623278 \times 10^8 \text{ cm}^{-1}$
a_{15}	$0.764737042077244759 \times 10^9 \text{ cm}^{-1}$	a_{15}	$0.307023775214641131 \times 10^8 \text{ cm}^{-1}$
a_{16}	$0.381868029858328533 \times 10^{10} \text{ cm}^{-1}$		
a_{17}	$-0.270560975156805658 \times 10^{10} \text{ cm}^{-1}$		
a_{18}	$-0.130777134652790947 \times 10^{11} \text{ cm}^{-1}$		
a_{19}	$0.693123967590401554 \times 10^{10} \text{ cm}^{-1}$		
a_{20}	$0.317969910129808044 \times 10^{11} \text{ cm}^{-1}$		
a_{21}	$-0.127583274381506557 \times 10^{11} \text{ cm}^{-1}$		
a_{22}	$-0.547443981078124619 \times 10^{11} \text{ cm}^{-1}$		
a_{23}	$0.164038438389521656 \times 10^{11} \text{ cm}^{-1}$		
a_{24}	$0.653485806778233261 \times 10^{11} \text{ cm}^{-1}$		
a_{25}	$-0.139350456346844196 \times 10^{11} \text{ cm}^{-1}$		
a_{26}	$-0.514892853898448334 \times 10^{11} \text{ cm}^{-1}$		
a_{27}	$0.700668473929830647 \times 10^{10} \text{ cm}^{-1}$		
a_{28}	$0.240948997045685349 \times 10^{11} \text{ cm}^{-1}$		
a_{29}	$-0.157575108054349303 \times 10^{10} \text{ cm}^{-1}$		
a_{30}	$-0.507254397888037300 \times 10^{10} \text{ cm}^{-1}$		
For $R > R_o = 11.30\text{\AA}$		For $R > R_o = 11.3\text{\AA}$	
C_6	$0.1184012 \times 10^8 \text{ cm}^{-1} \text{\AA}^6$	C_6	$0.1184012 \times 10^8 \text{ cm}^{-1} \text{\AA}^6$
C_8	$0.3261886 \times 10^9 \text{ cm}^{-1} \text{\AA}^8$	C_8	$0.3261886 \times 10^9 \text{ cm}^{-1} \text{\AA}^8$
C_{10}	$0.6317249 \times 10^{10} \text{ cm}^{-1} \text{\AA}^{10}$	C_{10}	$0.6317249 \times 10^{10} \text{ cm}^{-1} \text{\AA}^{10}$
A_{ex}	$0.41447134 \times 10^4 \text{ cm}^{-1} \text{\AA}^{-\gamma}$	A_{ex}	$0.41447134 \times 10^4 \text{ cm}^{-1} \text{\AA}^{-\gamma}$
γ	5.25669	γ	5.25669
β	2.11445 \AA^{-1}	β	2.11445 \AA^{-1}

TABLE II. Listed are 82 scattering features measured with Feshbach spectroscopy by different groups (see column "ref"). The "note" column contains information about the scattering feature. *ZC* refers to a zero crossing of the scattering length, *in* to a loss feature which results from an inelastic two-body collision process, *ov* indicates the presence of two overlapping structures and an empty entry refers to a Feshbach resonance. M is the total magnetic quantum number of the entrance channel listed in column $|f, m_f\rangle$. l and l_{max} give the partial waves considered in the calculation of the feature position. B_{exp} gives the experimentally determined position of the scattering feature and σ_{exp} the error. The difference Δ of experimentally determined and calculated positions of the features for four different representations for the PECs are compared in the last four columns of the table. Subscripts indicate the publications the PECs are taken from. The question mark in the $\Delta_{[3]}(G)$ column indicates that the correct assignment is unknown for that specific data point.

Isotope		note	M	$ f, m_f\rangle$		l	l_{max}	$B_{exp}(G)$	$\sigma_{exp}(G)$	ref	$\Delta_{[3]}(G)$	$\Delta_{[4]}(G)$	$\Delta_{[5]}(G)$	$\Delta_{[6]}(G)$
Na	K			Na	K									
23	39		2.0	(1,1)	(1,1)	0	0	411.334	1.276	[6]	-31.18	-1.334	1.206	1.245
23	39		2.0	(1,1)	(1,1)	0	0	508.730	0.831	[6]	-27.27	-2.486	-0.330	-0.079
23	39	<i>ZC</i>	2.0	(1,1)	(1,1)	0	0	380.88	3.83	[6]	-24.14	-2.439	-0.614	-0.545
23	39		1.0	(1,1)	(1,0)	0	0	6.716	2.089	[6]	-28.98	-0.889	1.082	0.103
23	39		1.0	(1,1)	(1,0)	0	0	329.115	0.772	[6]	-27.10	-2.043	-0.019	0.157
23	39		1.0	(1,1)	(1,0)	0	0	579.940	0.880	[6]	-26.58	-2.841	-0.778	-0.550
23	39		0.0	(1,0)	(1,0)	0	0	5.473	1.011	[6]	-	-0.741	0.396	-0.124
23	39		0.0	(1,0)	(1,0)	0	0	31.860	1.685	[6]	-1.74	-0.850	4.468	2.030
23	39	<i>in</i>	0.0	(1,1)	(1,-1)	0	0	26.340	3.311	[6]	-	-3.500	-0.820	-1.860
23	39		0.0	(1,1)	(1,-1)	0	0	393.608	0.759	[6]	-28.90	-2.372	-0.182	0.019
23	39		0.0	(1,1)	(1,-1)	0	0	536.066	0.940	[6]	-29.99	-3.007	-0.702	-0.608
23	39	<i>ZC</i>	0.0	(1,1)	(1,-1)	0	0	515.854	1.684	[6]	-23.95	-2.490	-0.669	-0.558
23	39		-1.0	(1,-1)	(1,0)	0	0	245.764	1.446	[6]	-	1.046	0.550	1.015
23	39		-1.0	(1,0)	(1,-1)	0	0	541.087	1.496	[6]	-	-2.657	0.751	0.564
23	39		-2.0	(1,0)	(2,-2)	0	0	228.481	1.492	[6]	-129?	-2.831	-0.285	-1.026
23	39	<i>ZC</i>	-2.0	(1,0)	(2,-2)	0	0	570.286	2.546	[6]	-29.15	-5.947	-4.033	-4.021
23	39		-2.0	(1,-1)	(1,-1)	0	0	32.475	0.830	[7]	30.47	1.043	-1.643	-0.663
23	39		-2.0	(1,-1)	(1,-1)	0	0	247.108	0.230	[7]	5.71	-0.329	-0.969	-0.460
23	39	<i>ZC</i>	-2.0	(1,-1)	(1,-1)	0	0	117.189	0.150	[7]	41.48	3.405	0.024	0.109
23	39	<i>ov</i>	-2.0	(1,-1)	(1,-1)	0	0	646.600	1.500	[7]	-	-	-3.800	-4.585
23	40		-3.5	(1,1)	(9/2,-9/2)	0	0	78.320	0.150	[8]	0.54	0.008	-0.066	-0.024
23	40		-3.5	(1,1)	(9/2,-9/2)	0	0	89.700	0.250	[8, 9]	1.02	0.692	0.596	-0.084
23	40		-2.5	(1,1)	(9/2,-7/2)	0	0	81.620	0.160	[8]	0.20	-0.108	-0.160	-0.032
23	40		-2.5	(1,1)	(9/2,-7/2)	0	0	89.780	0.460	[8]	-0.04	-0.594	-0.672	-0.609
23	40		-2.5	(1,1)	(9/2,-7/2)	0	0	108.600	3.000	[8]	-0.31	-0.606	-0.719	-1.694
23	40		-1.5	(1,1)	(9/2,-5/2)	0	0	96.540	0.090	[8]	0.15	-0.091	-0.141	0.002
23	40		-1.5	(1,1)	(9/2,-5/2)	0	0	106.920	0.270	[8]	0.38	-0.155	-0.234	-0.152
23	40		-1.5	(1,1)	(9/2,-5/2)	0	0	138.560	1.000	[8, 9]	1.74	1.518	1.384	0.042
23	40		-0.5	(1,1)	(9/2,-3/2)	0	0	116.910	0.150	[8]	-0.28	-0.350	-0.388	-0.226
23	40		-0.5	(1,1)	(9/2,-3/2)	0	0	130.640	0.030	[8, 9]	0.28	-0.127	-0.199	-0.100
23	40		-0.5	(1,1)	(9/2,-3/2)	0	0	175.000	5.000	[8]	-2.44	-2.520	-2.674	-4.531
23	40		-4.5	(1,1)	(9/2,-9/2)	1	1	6.350	0.030	[8]	-0.15	-0.034	-0.042	-0.030
23	40		-2.5	(1,1)	(9/2,-9/2)	1	1	6.410	0.030	[8]	-0.16	0.003	-0.008	-0.002
23	40		-3.5	(1,1)	(9/2,-9/2)	1	1	6.470	0.030	[8]	-0.16	0.006	-0.004	-0.002
23	40		-3.5	(1,1)	(9/2,-9/2)	1	1	6.680	0.030	[8]	-0.17	0.013	0.005	0.010
23	40		-2.5	(1,1)	(9/2,-9/2)	1	1	19.100	0.100	[8]	-0.22	-0.056	-0.060	-0.052
23	40		-4.5	(1,1)	(9/2,-9/2)	1	1	19.200	0.100	[8]	-0.19	0.016	0.012	0.008
23	40		-3.5	(1,1)	(9/2,-9/2)	1	1	19.300	0.100	[8]	-0.17	0.048	0.044	0.036
23	40		-3.5	(1,1)	(9/2,-7/2)	1	1	7.320	0.140	[8]	-0.30	-0.119	-0.133	-0.134
23	40		-1.5	(1,1)	(9/2,-7/2)	1	1	7.540	0.040	[8]	-0.36	-0.148	-0.160	-0.156
23	40		-2.5	(1,1)	(9/2,-7/2)	1	1	7.540	0.040	[8]	-0.36	-0.164	-0.176	-0.168
23	40		-3.5	(1,1)	(9/2,-7/2)	1	1	7.540	0.040	[8]	-0.34	-0.138	-0.150	-0.144
23	40		-2.5	(1,1)	(9/2,-7/2)	1	1	23.190	0.040	[8]	-0.30	-0.048	-0.048	-0.048
23	40		-3.5	(1,1)	(9/2,-7/2)	1	1	23.290	0.040	[8]	-0.31	-0.012	-0.012	-0.024
23	40	<i>in</i>	-2.5	(1,1)	(9/2,-5/2)	1	1	9.230	0.340	[8]	-0.11	0.108	0.092	0.096
23	40		-1.5	(1,1)	(9/2,-5/2)	1	1	9.600	0.040	[8]	-0.29	0.032	0.016	0.028
23	40		-2.5	(1,1)	(9/2,-5/2)	1	1	9.600	0.040	[8]	-0.28	0.004	-0.012	-0.004
23	40		-0.5	(1,1)	(9/2,-5/2)	1	1	9.600	0.040	[8]	-0.29	-0.004	-0.016	-0.012
23	40		-1.5	(1,1)	(9/2,-5/2)	1	1	29.200	0.090	[8]	-0.41	-0.080	-0.072	-0.064

Isotope		note	M	$ f, m_f\rangle$		l	l_{max}	$B_{exp}(G)$	$\sigma_{exp}(G)$	ref	$\Delta_{[3]}(G)$	$\Delta_{[4]}(G)$	$\Delta_{[5]}(G)$	$\Delta_{[6]}(G)$
Na	K			Na	K									
23	40		-2.5	(1,1)	(9/2,-5/2)	1	1	29.520	0.090	[8]	-0.41	0.041	0.046	0.024
23	40		-0.5	(1,1)	(9/2,-5/2)	1	1	29.450	0.090	[8]	-0.43	-0.002	0.004	-0.008
23	40		-0.5	(1,1)	(9/2,-3/2)	1	1	12.510	0.050	[8]	-0.53	-0.171	-0.183	-0.159
23	40		0.5	(1,1)	(9/2,-3/2)	1	1	12.680	0.050	[8]	-0.52	-0.096	-0.113	-0.108
23	40		-0.5	(1,1)	(9/2,-3/2)	1	1	39.390	0.040	[8]	-0.48	0.059	0.080	0.100
23	40		0.5	(1,1)	(9/2,-3/2)	1	1	39.850	0.040	[8]	-0.52	0.192	0.215	0.188
23	40		0.5	(1,1)	(9/2,-1/2)	0	0	146.700	0.200	[5]	-	-0.251	-0.245	-0.065
23	40		0.5	(1,1)	(9/2,-1/2)	0	0	165.340	0.300	[5]	-	-0.340	-0.383	-0.269
23	40		0.5	(1,1)	(9/2,-1/2)	0	0	233.000	1.800	[5]	-	-4.994	-5.126	-7.722
23	40		1.5	(1,1)	(9/2, 1/2)	0	0	190.500	0.200	[5]	-	-0.620	-0.513	-0.319
23	40		1.5	(1,1)	(9/2, 1/2)	0	0	218.400	0.200	[5]	-	-0.667	-0.622	-0.505
23	40		1.5	(1,1)	(9/2, 1/2)	0	0	308.100	3.220	[5]	-	-19.413	-19.588	-23.114
23	40		2.5	(1,1)	(9/2, 3/2)	0	0	256.600	0.200	[5]	-	-0.965	-0.619	-0.423
23	40		2.5	(1,1)	(9/2, 3/2)	0	0	299.900	0.400	[5]	-	-1.900	-1.630	-1.522
23	40		0.5	(1,1)	(9/2,-1/2)	1	1	18.810	0.100	[5]	-	-0.024	-0.031	0.012
23	40		1.5	(1,1)	(9/2,-1/2)	1	1	19.150	0.100	[5]	-	0.112	0.107	0.116
23	40		0.5	(1,1)	(9/2,-1/2)	1	1	58.320	0.100	[5]	-	-0.103	-0.036	-0.012
23	40		1.5	(1,1)	(9/2,-1/2)	1	1	59.100	0.100	[5]	-	0.184	0.249	0.200
23	40		1.5	(1,1)	(9/2, 1/2)	1	1	35.170	0.100	[5]	-	-0.156	-0.116	-0.025
23	40		2.5	(1,1)	(9/2, 1/2)	1	1	35.830	0.100	[5]	-	0.047	0.084	0.112
23	40		1.5	(1,1)	(9/2, 1/2)	1	1	100.360	0.100	[5]	-	-0.104	0.111	0.112
23	40		2.5	(1,1)	(9/2, 1/2)	1	1	101.310	0.100	[5]	-	0.171	0.381	0.285
23	40		-3.5	(1,1)	(9/2,-9/2)	0	2	204.520	0.200	[5]	-	-3.75	0.084	0.116
23	40		-3.5	(1,1)	(9/2,-9/2)	0	2	279.800	0.200	[5]	-	-5.99	-0.202	0.024
23	40	<i>in</i>	-2.5	(1,1)	(9/2,-7/2)	0	2	202.680	0.200	[5]	-	-3.51	0.105	0.112
23	40	<i>in</i>	-2.5	(1,1)	(9/2,-7/2)	0	2	276.300	0.200	[5]	-	-5.50	-0.040	0.113
23	40	<i>in</i>	-1.5	(1,1)	(9/2,-5/2)	0	2	201.660	0.200	[5]	-	-3.29	0.117	0.096
23	40	<i>in</i>	-1.5	(1,1)	(9/2,-5/2)	0	2	274.600	0.200	[5]	-	-5.14	0.026	0.115
23	40	<i>in</i>	-0.5	(1,1)	(9/2,-3/2)	0	2	201.440	0.200	[5]	-	-3.06	0.124	0.076
23	40	<i>in</i>	-0.5	(1,1)	(9/2,-3/2)	0	2	274.800	0.200	[5]	-	-4.67	0.223	0.251
23	40	<i>in</i>	0.5	(1,1)	(9/2,-1/2)	0	2	202.100	0.200	[5]	-	-2.77	0.168	0.096
23	40	<i>in</i>	0.5	(1,1)	(9/2,-1/2)	0	2	276.200	1.300	[5]	-	-4.67	-0.048	-0.079
23	40	<i>in</i>	1.5	(1,1)	(9/2, 1/2)	0	2	278.800	0.400	[5]	-	-5.02	-0.711	-0.795
23	40	<i>in</i>	2.5	(1,1)	(9/2, 3/2)	0	2	283.700	0.900	[5]	-	-3.98	0.003	-0.160
sum of weighted squared deviations:											-	5240.5	337.0	255.31

3.2 Beyond Born-Oppenheimer approximation in ultracold atomic collisions [A2]

The Born-Oppenheimer approximation (BOA) takes into account the fact that the mass of an electron is about three orders of magnitude less than the mass of a proton, and thus much less than the mass of the nucleus that the electron surrounds. The atomic nucleus is inert compared to the electron. If the electron position changes, the position of the nucleus will only slowly adjust to the new equilibrium position. Therefore one can make the approximation of treating the total wavefunction Ψ_{tot} as a product of decoupled wavefunctions that describe the motion of the electron and the nucleus separately, $\Psi_{\text{tot}} = \Psi_{\text{electron}} \cdot \Psi_{\text{nucleus}}$. This reduces the complexity of the system, which in turn reduces the computational effort. In molecular spectroscopy, for example, this allows to use the same interatomic potentials for different isotopes by a simple rescaling of the nuclear motion according to the reduced molecular mass [A2]. Deviations from this approach are in the order of the electron-to-proton mass ratio and therefore correspond to energy shifts in the order of $\Delta E/E \approx 10^{-4}$ [A2]. However, for a precise description of the molecular potentials, beyond BOA effects might be necessary. As Feshbach resonances carry information of the molecular short-range potential to the atomic threshold, a detailed study of the position of Feshbach resonances across all potential isotopes of a chosen element might reveal these effects.


In the following paper, it is shown that for an optimal description of the positions of Feshbach resonances across different potassium isotopes, beyond BOA effects must be taken into account, which therefore refine the molecular potentials. For this, all previously known potassium Feshbach resonance positions were gathered. In addition three new d -wave resonances for ^{39}K - ^{39}K in the $|F = 2, m_F = -2\rangle$ hyperfine state, with F the total angular momentum and m_F its projection on the magnetic field axes, have been measured. This is done through the identification of atomic loss features. With this ^{39}K - ^{39}K is the only isotope combination where a large number of s -wave as well as d -wave resonances are known. As this fixes the asymptotic branch of the molecular potentials, this isotope combination is used as a reference for the model.

3 *Feshbach resonances and molecules*

Copyright © 2022 The Author(s), Originally published by Physical Review Research from the American Physical Society (APS), CC BY 4.0.

DOI <https://link.aps.org/doi/10.1103/PhysRevResearch.2.013366>

Beyond Born-Oppenheimer approximation in ultracold atomic collisions

Eberhard Tiemann ^{*}, Philipp Gersema , Kai K. Voges , Torsten Hartmann , Alessandro Zenesini , and Silke Ospelkaus[†]
Institut für Quantenoptik, Leibniz Universität Hannover, 30167 Hannover, Germany



(Received 17 December 2019; accepted 4 March 2020; published 26 March 2020)

We report on deviations beyond the Born-Oppenheimer approximation in potassium interatomic potentials. Identifying three previously unknown d -wave Feshbach resonances, we significantly improve the understanding of the ^{39}K interatomic potentials. Combining these observations with the most recent data on known inter- and inraisoisotope Feshbach resonances, we show that Born-Oppenheimer corrections can be determined from atomic collisional properties alone and that significant differences between the homo- and heteronuclear cases appear.

DOI: [10.1103/PhysRevResearch.2.013366](https://doi.org/10.1103/PhysRevResearch.2.013366)

I. INTRODUCTION

In quantum chemistry and molecular physics, the assumption that the electronic and nuclear motions can be separately treated is well justified by the three orders of magnitude separating the proton and the electron masses. The nuclei are considered as fixed objects at relative distance R when solving the eigenvalue problem of the electron motion, resulting in a R -dependent electronic energy, which is taken as the potential for the nuclear motion. This approximation leads to large simplifications when solving the Schrödinger equation for molecules and is named *Born-Oppenheimer approximation* (BOA) [1]. The BOA is extremely powerful in matching theoretical predictions and spectroscopic results, particularly concerning the understanding of diatomic molecules. One major aspect within the BOA is that the same interatomic potential (BO potential) is used for different isotopes by simply rescaling the nuclear motion according to the reduced molecular mass. Deviations from this assumption lead to perturbative corrections to the BOA on the order of the electron-to-proton mass ratio. The isotopic dependence of corrections has been discussed in many papers; see, for example, Refs. [2–4]. These deviations from the BO-potential approach correspond to shifts in energy levels on the order of $\Delta E/E \approx 10^{-4}$ or less and they have been observed in spectroscopy experiments like Refs. [5–7] and in the dissociation energy of different isotope combinations of hydrogen diatomic molecules [8].

Effects of the corrections to the BOA are much weaker at the collisional threshold of atom pairs as the long-range behavior of the interatomic potential is weakly affected by short-range variations. Recent developments in molecule cooling and molecule association from ultracold atoms have considerably increased the experimental resolution, giving access

to study effects beyond the BOA. Corrections to the triplet and singlet scattering lengths are indeed predicted to be on the order of a few tenths of the Bohr radius a_0 [7] and are practically undetectable. However, Feshbach resonances are an effective passkey as they carry important information of the short-range potential to the atomic threshold [9]. A particular interesting case is given by the collisional properties of ultracold potassium atoms. Potassium features two stable bosonic isotopes (^{39}K and ^{41}K) and a very long living fermionic one (^{40}K). All these isotopes have been cooled to quantum degeneracy both in single- and two-isotope experiments and collisional data for five (^{39}K - ^{39}K , ^{40}K - ^{40}K , ^{41}K - ^{41}K , ^{39}K - ^{41}K , ^{40}K - ^{41}K) of the six possible combinations are available in literature [10–14]. The comparison of Feshbach resonance positions for different isotope combinations is a promising way to reveal corrections to the BOA. First hints of such corrections were obtained by Falke *et al.* [7] studying the two cases ^{39}K - ^{39}K and ^{40}K - ^{40}K available at that time. In this paper, we present the experimental observation of previously unmeasured d -wave Feshbach resonances of ^{39}K and show how this allows us to improve the knowledge of $^{39}\text{K}_2$. We combine this result with the published literature on potassium Feshbach resonances and we determine corrections to the BOA from collisional data alone.

The paper is structured as follows. In Sec. II, we explain how to reveal effects from beyond BOA corrections in atomic collisional properties. In Sec. III, we present the observation of three new Feshbach resonances for ^{39}K , which enhances the knowledge on $^{39}\text{K}_2$ to use this dimer as reference for the full isotope analysis. In Sec. IV, we quantify the corrections to the BOA thanks to a multiparameter fit of the new and already known Feshbach resonance positions.

II. THEORY ASPECTS

To treat the collision of an atom pair of alkali atoms at low kinetic energy, we set up the Hamiltonian of the coupled system of the two lowest molecular states $X^1\Sigma_g^+$ and $a^3\Sigma_u^+$, because the product state of two ground-state atoms is generally a mixture of singlet and triplet states. The appropriate Hamiltonian is presented in many papers, e.g., Refs. [7,9], and will not be repeated here. It contains the hyperfine

^{*}tiemann@iqo.uni-hannover.de

[†]silke.ospelkaus@iqo.uni-hannover.de

Published by the American Physical Society under the terms of the [Creative Commons Attribution 4.0 International license](https://creativecommons.org/licenses/by/4.0/). Further distribution of this work must maintain attribution to the author(s) and the published article's title, journal citation, and DOI.

interaction, also responsible for the singlet-triplet mixing, the atomic Zeeman interaction, and the effective spin-spin interaction of the two atoms in their doublet states. The nuclear motion is governed by the molecular potentials of the two interacting molecular states.

The potential functions within the Born-Oppenheimer approximation (BO potentials) are represented in analytic form as described in detail in Ref. [7] in three R sections divided by an inner R_{in} and outer radius R_{out} .

In the intermediate range around the minimum, it is described by a finite power expansion

$$U_{\text{IR}}(R) = \sum_{i=0}^n a_i \xi(R)^i \quad (1)$$

with a nonlinear variable function ξ of internuclear separation R :

$$\xi(R) = \frac{R - R_m}{R + bR_m}. \quad (2)$$

In Eq. (1), the $\{a_i\}$ are fitting parameters and b and R_m are chosen such that only few parameters a_i are needed for describing the steep slope at the short internuclear separation side and the smaller slope at the large R side by the analytic form of Eq. (1). R_m is normally close to the value of the equilibrium separation.

The potential is extrapolated for $R < R_{\text{in}}$ with

$$U_{\text{SR}}(R) = A + B/R^{N_s} \quad (3)$$

by adjusting the A and B parameters to get a continuous transition at R_{in} ; the final fit uses N_s equal to 12 and 6 for $X^1\Sigma_g^+$ and $a^3\Sigma_u^+$ states, respectively, as adequate exponents.

For large internuclear distances ($R > R_{\text{out}}$), we adopt the standard long-range form of molecular potentials:

$$U_{\text{LR}}(R) = U_\infty - \frac{C_6}{R^6} - \frac{C_8}{R^8} - \frac{C_{10}}{R^{10}} \pm E_{\text{exch}}(R), \quad (4)$$

where the exchange contribution is given by

$$E_{\text{exch}}(R) = A_{\text{ex}} R^\gamma \exp(-\beta R) \quad (5)$$

and U_∞ is set to zero, which fixes the energy reference of the total potential scheme.

The BO potentials are extended by correction functions $U_{\text{ad}}(R)$, which make the full potentials mass dependent. These correction functions [3,4,15] contain matrix elements of the nuclear momentum operators over the electronic wave functions of the considered electronic state and other ones with $\Delta\Omega = 0$, where Ω is the projection of the total electronic angular momentum onto the molecular axis. $U_{\text{ad}}(R)$ is the so-called adiabatic correction to the BO-potential function, and it contains the interaction of the considered electronic state with all states according the selection rule $\Delta\Omega = 0$ by the nuclear vibrational motion. We do not include nonadiabatic correction with the selection rule $\Delta\Omega = \pm 1$ because it will be negligibly small for collisions with low partial waves as s , p , or d .

Watson [3] shows that in the lowest order the mass dependence of these corrections for a molecule AB will be of the form $U_A(R) \frac{m_e}{M_A} + U_B(R) \frac{m_e}{M_B}$, where $M_{A(B)}$ is the atomic mass of atom $A(B)$ and m_e is the electron mass. For true heteronuclear molecules, the coefficients $U_A(R)$ and $U_B(R)$ will be different; for homonuclear cases in the electronic

system such as K_2 both coefficients will be equal and thus the isotope dependence of the correction function will be inversely proportional to the reduced mass μ of the molecule. Van Vleck [15] considered the mass dependence of the heteronuclear cases in the hydrogen-deuterium (HD) molecule and found that the corrections should be extended by a term $(M_A - M_B)^2 / (M_A + M_B)^2$. Thus, in our case with the nuclei like ^{39}K - ^{41}K , the representation of the correction functions should read

$$U_{\text{ad}}(R) = U_{\text{gen}}(R) \frac{m_e}{\mu} + U_{\text{asym}}(R) m_e \left(\frac{M_A - M_B}{M_A + M_B} \right)^2, \quad (6)$$

where μ is the reduced mass for the molecular rovibrational motion. $U_{\text{gen}}(R)$ and $U_{\text{asym}}(R)$ are functions of the internuclear separation R . The subscripts refer to the general and asymmetric contributions.

III. d -WAVE FESHBACH RESONANCES IN ^{39}K

In our setup, ultracold samples of ^{39}K atoms are prepared by sympathetic cooling in a bath of evaporatively cooled Na atoms as explained in Refs. [16,17]. Compared to the experimental sequence used in our previous works, the mixture here is heavily unbalanced toward ^{39}K and the Na atom number is practically negligible. During evaporation in a crossed optical dipole trap, the ^{39}K atoms are initially in the $|f = 1, m_f = -1\rangle$ state and are transferred to the target $|f = 2, m_f = -2\rangle$ state by rapid adiabatic passage. f is the total angular momentum of the atom and m_f is its projection. The transfer is based on a 1-ms radio frequency sweep performed at an external magnetic field of about 199 G. At this magnetic field, losses are small in both the initial and final states and during the transfer. The sample contains up to 3×10^5 atoms at 650 nK in a trap with an average frequency of $2\pi \times 114(5)$ Hz.

To locate the d -wave resonances, we observe that the atom number decreased due to inelastic two-body losses in the proximity of the Feshbach resonance. We ramp the magnetic field strength in 10 ms to the target value. After a fixed holding time, chosen to not lead to complete depletion of the atoms at resonance, the magnetic field is ramped back to the magnetic field strength where high-field absorption imaging of the remaining atoms is performed [17]. Figure 1 shows the remaining atom fraction at different values of the magnetic field strength in the vicinity of the predicted d -wave Feshbach resonances. By fitting the loss data with phenomenological Gaussian curves, we obtain the following three resonance positions: 125.94(14), 188.72(5), and 227.71(60) G. The predicted width of the resonance at 188.72 G is far below our magnetic field stability of about 30 mG and leads to experimental points not following a Gaussian profile; see Fig. 1(b).

We also measure the remaining atom number at the resonance positions for variable holding time. The data are shown in Figs. 1(d)–1(f) for the 125.94, 188.72, and 227.71 G resonances, respectively. The inelastic loss rate coefficients are obtained from a fit to the data according to the two-body loss differential equation including the effects of antievaporation heating [18,19] and background lifetime (about 17 s). The loss rate coefficients are summarized in Fig. 1(g) and confirm the expected large difference between fast [Fig. 1(e)] and slow [Figs. 1(d) and 1(f)] losses despite the same d -wave character

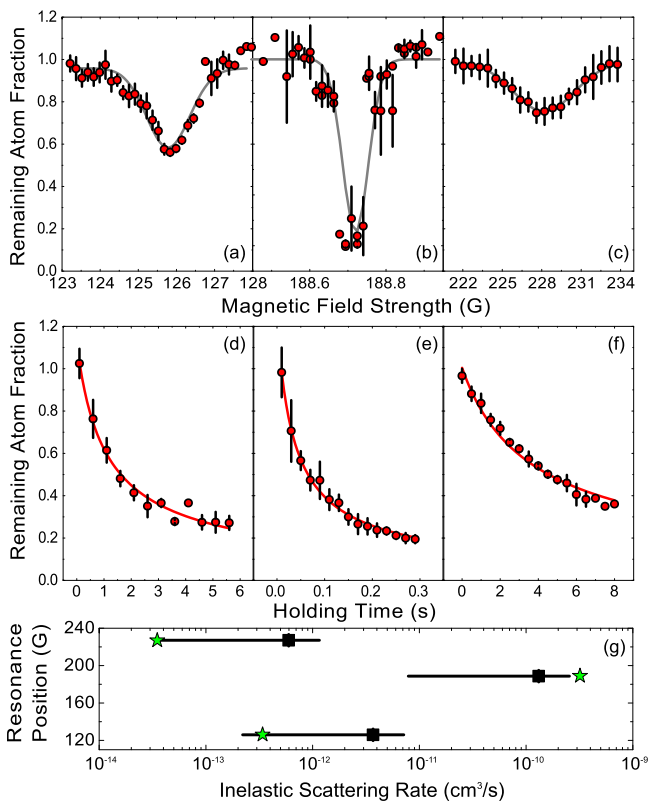


FIG. 1. ^{39}K d -wave Feshbach resonances in the hyperfine state $|f = 2, m_f = -2\rangle$. [(a)–(c)] The remaining fraction of ^{39}K atoms is measured for different values of the magnetic field. The holding times for the three measurements are 1 s, 470 ms, and 4 s, respectively. Gray lines are the phenomenological Gaussian fit curves. Error bars are the standard deviation of different experimental runs. [(d)–(f)] Remaining atom fraction as a function of time for the d -wave Feshbach resonances in panels (a), (b), and (c), respectively. The measurements are performed at the magnetic fields where losses are maximal. The lines are fits according to the two-body loss rate equation; see text. (g) Comparison between the measured (black squares) and predicted (green stars) inelastic loss rates. For the uncertainties on the loss rate, see text.

of the resonances. The values are in good agreement with theoretical predictions using the results of Sec. IV within the error bars, which include statistical uncertainties and the uncertainties on the calibration of temperature, trap frequency, and atom number. The values for the 125.94 G [Figs. 1(a) and 1(d)] and 227.71 G [Figs. 1(c) and 1(f)] resonances are larger than predicted, probably because of other loss contributions not included in the fit. The measured value for the 188.7 G [Figs. 1(b) and 1(e)] resonance is instead smaller than expected as the narrow resonance width and the magnetic field jitter do not allow to remain exactly at resonance.

The resonance measurements were only performed for one sample temperature. We checked with the derived potential system; see Sec. IV for the temperature dependence of the resonance positions. Changing the kinetic energy from 1 to $0.5\ \mu\text{K}$ results in a shift of the positions by less than 5 mG, which is much smaller than the present experimental uncertainty.

IV. ANALYSIS

We start our analysis from potential functions of the two lowest electronic states $X^1\Sigma_g^+$ and $a^3\Sigma_u^+$ derived from spectroscopic observation which have been described in detail in [7]. We refit the spectroscopic data with a smaller set of potential parameters to reduce the risk of obtaining unphysical tiny oscillatory behavior of the potential function. In Ref. [7], state $X^1\Sigma_g^+$ was described by 31 parameters, but now 22 are sufficient. For state $a^3\Sigma_u^+$, we use 14 parameters, compared to 22 in the previous work. The resulting potentials form the starting point for a fit of 49 Feshbach resonances and a comparison of the experimentally determined Feshbach resonance positions with the ones resulting from the coupled channel calculation. We identify the Feshbach resonance position by the maximum scattering rate coefficient at the kinetic energy given by the experimental conditions. We base our analysis on Feshbach resonance data for the isotope combinations ^{39}K - ^{39}K from D’Errico *et al.* [11] and Refs. [14,20], ^{40}K - ^{40}K from Regal *et al.* [21,23], ^{39}K - ^{41}K from Tanzi *et al.* [14], ^{41}K - ^{41}K from Chen *et al.* [13] and Tanzi *et al.* [14], and ^{40}K - ^{41}K from Wu *et al.* [12]. We summarize the data in Table I with their quantum numbers and the reported experimental uncertainty. As quantum numbers, we use the projection M of the total angular momentum onto the field axis, the atom pair labels for dressed states, and the interval $l_{\min} - l_{\max}$ of the partial waves. The labels of the atomic dressed states are given by $|f, m_f\rangle$. The column “type” indicates that for “el” the peak of the elastic part of the rate coefficient is taken and for “in” the sum of the inelastic contributions.

The evaluation uses atomic hyperfine and g factors from Ref. [24]. We fit the data in Table I to the BO potentials, adjusting the branches at small ($R < R_{\text{in}}$) and large ($R > R_{\text{out}}$) internuclear separations. After a few trials, it became clear that the three data points for the ^{40}K - ^{41}K isotope combination show significant deviations (several times the experimental uncertainty) compared to all other isotope combinations. In the following, we thus exclude these resonances from the analysis and report only their resulting deviations in the final conclusion [25]. Refitting all remaining resonances, we obtain a normalized standard deviation of $\sigma = 0.977$. These results are given in Table I in column “o-c(1)” (observed-calculated) and in row 1 of Table II [labeled model (1)]. Analyzing the obtained fit for the different isotope combinations [see Table II, model (1)] reveals that the main part of the sum of squared weighted deviations stems from the isotope combination ^{39}K - ^{41}K , resulting in $\sigma = 1.235$, whereas the other isotope combinations show values below 0.72. A separate fit to the data of the isotope combination ^{39}K - ^{41}K only emphasizes the consistency of these observations with a resulting normalized standard deviation of $\sigma = 0.753$ [see Table II, model (^{39}K ^{41}K)_a]. We thus started an additional fit in an attempt to optimize the result for the isotope combination ^{39}K - ^{41}K by applying the potentials from the separate fit of ^{39}K - ^{41}K above as initial values. Note that nonlinear fits regularly give slightly different results depending on initial values since it is hard to find the global minimum of the sum of squared weighted deviations. In this second fit, we obtain almost the same overall fit quality with a normalized standard deviation of $\sigma = 0.993$ but now the main deviation

TABLE I. Feshbach resonances and their theoretical modeling. Column o-c gives the difference of observed field value [obs] and experimental uncertainty [unc] to calculated one (not listed). The number indicates the model of evaluation as in Table II: (1) pure BO potentials, (2) adding BO correction BO_{gen} for the general case, and (3) adding BO corrections BO_{gen} and BO_{asym} for the homo- and heteronuclear cases.

Isotope	M	Atom pair	l_{\min}	l_{\max}	Type	Obs [G]	Unc [G]	o-c(1) [G]	o-c(2) [G]	o-c(3) [G]	Ref.
39/39	2	1, 1⟩ 1, 1⟩	0	0	el	403.4	0.7	0.958	0.876	0.849	[11]
	2	1, 1⟩ 1, 1⟩	0	0	el	752.3	0.1	0.104	0.024	0.039	
	2	1, 1⟩ 1, 1⟩	0	0	el	25.85	0.1	0.016	-0.033	-0.024	
	0	1, 0⟩ 1, 0⟩	0	2 ^a	el	59.3	0.6	0.400	0.315	0.320	
	0	1, 0⟩ 1, 0⟩	0	0	el	66.0	0.9	0.491	0.421	0.430	
	-2	1, -1⟩ 1, -1⟩	0	0	el	32.6	1.5	-1.006	-0.979	-0.982	
	-2	1, -1⟩ 1, -1⟩	0	0	el	162.8	0.9	0.503	0.460	0.467	
	-2	1, -1⟩ 1, -1⟩	0	0	el	562.2	1.5	1.383	1.301	1.274	
	-2	1, -1⟩ 1, -1⟩	0	2	in	395.1	1.0	-0.020	-0.122	-0.160	[20]
	-1	1, 0⟩ 1, -1⟩	0	0	el	113.76	0.1	0.062	-0.002	0.007	[14]
	-4	2, -2⟩ 2, -2⟩	0	2	in	125.94	0.14	-0.097	-0.125	-0.120	present
	-4	2, -2⟩ 2, -2⟩	0	2	in	188.72	0.05	0.033	-0.008	0.000	
	-4	2, -2⟩ 2, -2⟩	0	2	in	227.71	0.60	-0.150	-0.170	-0.130	
	40/40	-8	9/2, -9/2⟩ 9/2, -7/2⟩	0	0	el	202.10	0.07	0.003	-0.014	0.005
-7		9/2, -9/2⟩ 9/2, -5/2⟩	0	0	el	224.21	0.05	-0.001	-0.018	0.003	
-6		9/2, -7/2⟩ 9/2, -5/2⟩	0	0	el	174.0	2.0	-0.280	-0.155	-0.130	
-7		9/2, -7/2⟩ 9/2, -7/2⟩	1	1	el	198.81	0.05	-0.010	-0.044	-0.024	[22]
-8		9/2, -7/2⟩ 9/2, -7/2⟩	1	1	el	198.34	0.05	0.030	-0.006	0.014	
7	9/2, 7/2⟩ 9/2, 7/2⟩	1	1	el	436.3	0.5	-0.484	-0.444	-0.440	[21]	
39/41	-1	1, -0⟩ 1, -1⟩	0	0	el	228.88	0.08	-0.091	-0.036	-0.035	[14]
	-2	1, -1⟩ 1, -1⟩	0	0	el	149.84	0.06	0.100	0.083	0.082	
	-3	1, -1⟩ 2, -2⟩	0	0	el	649.6	0.6	0.564	0.535	0.343	
	3	1, 1⟩ 2, 2⟩	0	0	el	341.5	0.20	-0.018	0.097	0.101	
	3	1, 1⟩ 2, 2⟩	0	0	el	353.8	0.20	-0.092	0.017	0.023	
	2	1, 1⟩ 1, 1⟩	0	0	el	139.27	0.04	-0.072	-0.020	-0.016	
	2	1, 1⟩ 1, 1⟩	0	0	el	146.24	0.07	-0.109	-0.057	-0.056	
	2	1, 1⟩ 1, 1⟩	0	0	el	338.12	0.07	-0.057	0.032	0.024	
	2	1, 1⟩ 1, 1⟩	0	0	el	500.2	0.3	0.276	0.242	0.051	
	2	1, 1⟩ 1, 1⟩	0	0	el	518.4	0.1	0.072	0.049	-0.124	
	1	1, 1⟩ 1, 0⟩	0	0	el	88.2	0.1	-0.212	-0.157	-0.160	
	1	1, 1⟩ 1, 0⟩	0	0	el	160.05	0.06	-0.020	0.034	0.037	
	1	1, 1⟩ 1, 0⟩	0	0	el	165.80	0.05	-0.069	-0.016	-0.015	
	1	1, 1⟩ 1, 0⟩	0	0	el	344.4	0.1	-0.006	0.073	0.053	
	1	1, 1⟩ 1, 0⟩	0	0	el	522.6	0.2	0.246	0.217	0.028	
	1	1, 1⟩ 1, 0⟩	0	0	el	553.1	0.1	0.243	0.229	0.069	
	0	1, 1⟩ 1, -1⟩	0	0	el	189.88	0.05	-0.053	0.000	0.001	
	0	1, 1⟩ 1, -1⟩	0	0	el	348.4	0.1	0.040	0.110	0.076	
	0	1, 1⟩ 1, -1⟩	0	0	el	384.91	0.07	-0.044	0.049	0.049	
	0	1, 1⟩ 1, -1⟩	0	0	el	553.5	0.2	0.249	0.223	0.044	
	-1	1, 0⟩ 1, -1⟩	0	0	el	228.88	0.08	-0.091	-0.036	-0.035	
	-2	1, -1⟩ 1, -1⟩	0	0	el	149.84	0.06	0.100	0.083	0.082	
	-3	1, -1⟩ 2, -2⟩	0	0	el	649.6	0.6	0.564	0.535	0.343	
41/41	-2	1, -1⟩ 1, -1⟩	0	0	el	51.1	0.2	-0.021	-0.100	-0.101	[14]
	-1	1, -1⟩ 1, 0⟩	0	0	el	51.92	0.08	0.022	-0.077	-0.081	
	2	1, 1⟩ 1, 1⟩	0	0	el	409.2	0.2	-0.160	0.053	0.068	[23]
	2	1, 1⟩ 1, 1⟩	0	0	el	660.6	0.2	-0.015	0.000	0.059	
40/41	11/2	9/2, 9/2⟩ 1, 1⟩	0	2	el	472.6	0.3	-2.150	-1.922	-1.906	[12]
	11/2	9/2, 9/2⟩ 1, 1⟩	1	1	el	432.9	0.3	-2.651	-2.280	-2.252	
	11/2	9/2, 9/2⟩ 1, 1⟩	0	0	el	542.7	1.0	0.167	0.402	0.416	

^aThis *s*-wave resonance is influenced by a *d*-wave resonance at 59.9 G.

lies in the ⁴⁰K - ⁴⁰K isotope combination with its individual value $\sigma = 1.566$ as given in the third line of Table II, model (³⁹K ⁴¹K)_b. Since the reduced masses of ³⁹K ⁴¹K and ⁴⁰K - ⁴⁰K are almost equal, the different behavior of these two

isotope combinations in the two different fits [model (1) and model (³⁹K ⁴¹K)_b] give a strong hint that mass effects beyond the simple mass scaling of the rovibrational motion should be considered.

TABLE II. Overview of obtained standard deviations at different evaluation steps. The column “model” gives the same numbers as in Table I. Columns labeled by isotope combinations show the contribution of that combination: (1) BOA; (39/41)_a, fit restricted to ³⁹K-⁴¹K; (39/41)_b, as (1) using (39/41)_a as starting guess; (2), BOA with BO_{gen} corrections; (3), BOA with BO_{gen} and BO_{asym} corrections.

Model	σ				
	Total	³⁹ K - ⁴¹ K	⁴⁰ K - ⁴⁰ K	³⁹ K - ³⁹ K	⁴¹ K - ⁴¹ K
(1)	0.977	1.235	0.476	0.718	0.428
(39/41) _a		0.753			
(39/41) _b	0.993	0.867	1.566	0.991	0.394
(2)	0.786	0.952	0.541	0.593	0.556
(3)	0.651	0.737	0.428	0.584	0.607

In the next step, we thus include beyond BO corrections proportional to the reduced mass for the general case [i.e., part U_{gen} from Eq. (6)]. Because we can only study the small variations between the naturally existing isotope combinations, it is advantageous to define one isotope combination as a reference. This results in a parametrization of the full potentials with BO corrections for molecule AB given by

$$U(R) = U_{\text{BO}}(R) + \text{BO}_{\text{gen}}(R) \left(1 - \frac{\mu_{\text{ref}}}{\mu_{AB}}\right) + \text{BO}_{\text{asym}}(R) \left(\frac{M_A - M_B}{M_A + M_B}\right)^2, \quad (7)$$

where the factor of the electron mass in Eq. (6) is incorporated in the new functions BO_{gen} and BO_{asym} and μ_{ref} is the reduced mass of the reference combination. Here we apply ³⁹K - ³⁹K as a reference. For this combination, we have a large number of s -wave resonances and additionally also d -wave resonances. Both together fix the asymptotic branch of the potentials. This is different for the ³⁹K - ⁴¹K isotope combination where only s -wave resonances have been measured. In principle, BO_{gen} is a function of R , but the present data set is too small to derive such function from a fit with acceptable significance. Thus, we simplify the condition by assuming correction functions to be proportional to the BO potential and Eq. (7) reads now

$$U(R) = U_{\text{BO}}(R) \left[1 + \text{BO}_{\text{gen}} \left(1 - \frac{\mu_{\text{ref}}}{\mu_{AB}}\right) + \text{BO}_{\text{asym}} \left(\frac{M_A - M_B}{M_A + M_B}\right)^2 \right], \quad (8)$$

where now BO_{gen} and BO_{asym} are fit parameters for the amplitude of the BO corrections. A crude justification of this assumption is that the normal mass effect in atomic physics, e.g., the Rydberg constant and its nuclear mass dependence, show a similar form of the correction for the binding energy. Furthermore, a molecular potential describes the variation of the kinetic energy within the nuclear vibrational motion as function of R and is therefore a measure of the coupling to the electron motion.

Starting with BO_{gen} for states $X^1\Sigma_g^+$ and $a^3\Sigma_u^+$ we perform a fit of all resonances, adding the parameter for both electronic

TABLE III. Born-Oppenheimer corrections, according to Eq. (8). The number indicates the model of evaluation: (2) adding BO correction BO_{gen} for the general case and (3) adding BO corrections BO_{gen} and BO_{asym} for the general and heteronuclear cases. Values in brackets are not significantly determined and effectively zero.

Parameter	$X^1\Sigma_g^+$	$a^3\Sigma_u^+$
BO _{gen} (2)	(-0.00003)	-0.00046
BO _{gen} (3)	(-0.00006)	-0.00046
BO _{asym} (3)	0.0057	(-0.000001)

states, and obtain a normalized standard deviation of $\sigma = 0.786$ (the individual deviations are shown in column “o-c(2)” in Table I). This value should be compared with the one from a fit of the pure BO potentials $\sigma = 0.977$. Including beyond Born-Oppenheimer corrections apparently leads to a significantly better fit.

Looking again at details of the fit for the different isotope combinations in Table II model (2), we see that the combination ³⁹K - ⁴¹K is described with $\sigma = 0.952$ whereas the other three show values below 0.6. Since we removed the isotope combination ⁴⁰K - ⁴¹K from the evaluation already earlier for another reason (see also Ref. [26]), the former one is the only heteronuclear case remaining for which the standard deviation is significantly larger than the value seen in a separate fit (comp. above 0.753). Keeping in mind that the isotope combination with almost equal reduced mass, namely ⁴⁰K - ⁴⁰K, is well represented by the introduced BO correction, we complement our model by the heteronuclear extension of the BO correction, which is already contained in Eq. (8) by the parameter BO_{asym}. The new fit results now in a standard deviation of $\sigma = 0.651$ [see Table II model (3)] and thus a further improvement compared to 0.786 from model (2). Additionally, all individual standard deviations are almost equal to the values obtained by separated fits. The deviations of observation to calculation from the new fit are shown in column “o-c(3)” of Table I. The sequential improvement of the fit quality including beyond Born-Oppenheimer terms underlines the significance of corrections beyond Born-Oppenheimer for the precise description of molecular potentials and the precision derivation of atomic scattering properties [27].

In Table III, we give the magnitude of the BO corrections for the two electronic states $X^1\Sigma_g^+$ and $a^3\Sigma_u^+$. The uncertainty of the significantly determined parameters is about 20%. For better insight into the BO correction, we calculate the highest vibrational levels with the correction and compare them with the level energy, setting the correction to zero. For the heaviest isotope ⁴¹K - ⁴¹K and thus the largest difference to the reference isotope ³⁹K - ³⁹K, we obtain for the level $v = 27$, $N = 0$ of the state $a^3\Sigma_u^+$ a difference of 220 kHz and for the state $X^1\Sigma_g^+$ ($v = 87$, $N = 0$) it is effectively zero, because here the influence by BO correction appears only for heteronuclear isotope combinations.

V. DISCUSSION

From the different models, we calculated the scattering lengths for the pure singlet and triplet states. The results are

TABLE IV. Scattering lengths in units of a_0 of all natural isotope combinations of K derived from the different potential models.

Isotope	(1) $X^1\Sigma_g^+$	(3) $X^1\Sigma_g^+$	(1) $a^3\Sigma_u^+$	(3) $a^3\Sigma_u^+$
39/39	138.801	138.759(20)	-33.376	-33.413(25)
39/40	-2.669	-2.707(15)	-2031	-2026(10)
39/41	113.094	113.036(20)	176.600	176.688(25)
40/40	104.416	104.410(20)	169.204	169.288(25)
40/41	-54.447	-54.479(25)	97.139	97.186(20)
41/41	85.400	85.409(18)	60.266	60.317(18)

summarized in Table IV for the different isotope combinations using model (1) (BO approximation) and (3) (including all beyond BO corrections). Because we choose the isotope combination ^{39}K - ^{39}K as reference, one might expect no difference for the resulting scattering lengths for this isotope pair when using model (1) or (3) respectively. However, we do observe corrections (see Table IV). Equal values for ^{39}K - ^{39}K would result if the evaluation in case (3) would only vary the BO-correction parameters and anything else would be kept constant. This will not be the optimal fit strategy, because in case (1), i.e., no BO corrections, existing significant BO corrections are distributed over the deviations of the fit over all isotopes and thus also the reference isotope is influenced. One can see such different distribution from the standard deviations of ^{39}K - ^{39}K given for models (1) and (3) in Table II, the former one is larger than the latter one. Because of this influence, we only give error estimates for the complete model including BO corrections in Table IV and the differences between models (1) and (3) do not show the true magnitude of the BO correction. See also the calculation of the energy shift by the BO correction as given at the end of Sec. IV.

A complete list of scattering lengths was reported in Ref. [7]. The new values show a significant improvement by roughly a factor 5 of the error limit. The values agree in most cases within uncertainty limits despite the fact that the former evaluation could only incorporate Feshbach resonances for ^{39}K - ^{39}K and ^{40}K - ^{40}K . The paper stated that a weak indication of BO corrections could be obtained from the resonances. We believe the present evaluation shows this clearly. Additionally, we were able to study the difference between the homonuclear and heteronuclear cases, resulting in the values of BO_{gen} and BO_{asym} .

We obtained a significant contribution for the triplet state $a^3\Sigma_u^+$ by BO_{gen} for both fit cases but for the singlet state $X^1\Sigma_g^+$ only for the heteronuclear isotope pairs. This is probably related to the fact that the closest singlet state, namely $A^1\Sigma_u^+$, has u symmetry compared to g symmetry for the singlet ground state. These two can only couple by the symmetry breaking part of the Hamiltonian responsible for the BO correction [28]. The situation for the triplet state is different, where the energetically closest is $b^3\Pi_u$ and has u symmetry as the triplet ground state. We should note that the magnitudes of both effects, BO_{gen} and BO_{asym} cannot be directly compared, because the former one is referenced to ^{39}K - ^{39}K and thus describes only the difference between the isotope pairs whereas the latter indicates the total effect.

We evaluated the isotope dependence by using the precise Feshbach spectroscopy and checked finally that the obtained

BO corrections have little influence in the deep rovibrational levels measured by molecular spectroscopy, e.g., in Refs. [7,29,30], which have an uncertainty in the order of few thousands of cm^{-1} or about 100 MHz compared to 1 MHz or better for the Feshbach spectroscopy. For this purpose, we went back to the full data set from the spectroscopy for iterating the fit for obtaining the consistent description of the complete data set from molecular and Feshbach spectroscopy. The final parameter sets of the potentials are given in the Appendix; see Tables V–VII.

VI. CONCLUSION AND OUTLOOK

We use an analysis of the complete set of all known Feshbach resonances in different K isotope combinations to derive potential energy curves for states $X^1\Sigma_g^+$ and $a^3\Sigma_u^+$ and find clear signatures of beyond BO corrections. We base our work on the discussion of H_2 and HD molecules by van Vleck [15] and find correction terms for the homonuclear and heteronuclear cases when analyzing homo- and heteronuclear isotope combinations of K respectively. Unfortunately, our analysis of heteronuclear cases is restricted to the ^{39}K - ^{41}K isotope combination, although, in principle, more isotope combinations exist. However, available Feshbach resonance data of the ^{40}K - ^{41}K [12] isotope combination show very large deviations which are beyond a realistic description [25]. We therefore excluded this isotope combination from the analysis given in Sec. IV. To allow for an extended analysis of heteronuclear beyond BO corrections, it would be very much desirable to revisit observed Feshbach resonances in the $|9/2, 9/2\rangle + |1, 1\rangle$ channel of the ^{40}K - ^{41}K isotope combination and extend measurements to resonances within other collision channels such as $|9/2, -9/2\rangle + |1, 1\rangle$. In the same context, the ^{39}K - ^{40}K isotope is of great interest. Here, it would be particularly favorable to study collisions in the $|9/2, -7/2\rangle + |1, 1\rangle$ and $|9/2, -5/2\rangle + |1, 1\rangle$ channels. In these channels, well-separated Feshbach resonances in a magnetic field region below 200 G should be found, whereas sharp resonances in the $|9/2, -9/2\rangle + |1, 1\rangle$ channel will be overlapped by a very broad resonance. Furthermore, the above-mentioned channels will show sharp Feshbach resonances in the range of 800 to 850 G. We believe that such studies will settle the discussion of the importance of BO corrections in cases of homo- and heteronuclear pairs of homopolar molecules.

In the same spirit, it would be very interesting to analyze Feshbach resonances in the different isotope combinations of the homopolar molecule Li_2 . There exists a detailed analysis [31] of spectroscopic data of the $X^1\Sigma_g^+$ - $A^1\Sigma_u^+$ transition in the Li_2 considering homonuclear BO corrections [$\text{BO}_{\text{gen}}(R)$ from Eq. (7)]. The study includes data from ^7Li - ^6Li isotopologue; however, the authors do not mention any need to distinguish between homo- and heteronuclear corrections. The data set for the ^7Li - ^6Li molecule is small compared to that of both homonuclear molecules ^7Li - ^7Li and ^6Li - ^6Li , and thus it could be not sufficiently significant for the above mentioned distinction. For Li_2 there exist also measurements of Feshbach resonances for the homonuclear cases (see the latest report by Gerken *et al.* [32]), but nothing on ^7Li - ^6Li . Thus, studies of Feshbach resonances of Li-Li would be worthwhile

TABLE V. Parameters of the analytic representation of the $X^1\Sigma_g^+$ state potential with adiabatic Born-Oppenheimer correction and reference isotopologue ^{39}K - ^{39}K . The energy reference is the dissociation asymptote. Parameters with * are set for continuous extrapolation of the potential.

$R < R_{\text{in}} = 2.87 \text{ \AA}$	
A^*	$-0.2600158561 \times 10^4 \text{ cm}^{-1}$
B^*	$0.8053173040 \times 10^9 \text{ cm}^{-1} \text{ \AA}^{12}$
N_s	12
$R_{\text{in}} \leq R \leq R_{\text{out}} = 12.000 \text{ \AA}$	
b	-0.39
R_m	3.9243617 \AA
a_0	$-4450.9007703 \text{ cm}^{-1}$
a_1	$0.159877863995326747 \text{ cm}^{-1}$
a_2	$0.141337574101676037 \times 10^5 \text{ cm}^{-1}$
a_3	$0.107669620493846905 \times 10^5 \text{ cm}^{-1}$
a_4	$-0.331314023322698995 \times 10^4 \text{ cm}^{-1}$
a_5	$-0.163943210499613087 \times 10^5 \text{ cm}^{-1}$
a_6	$-0.216334200177141829 \times 10^5 \text{ cm}^{-1}$
a_7	$-0.384655804768731250 \times 10^5 \text{ cm}^{-1}$
a_8	$-0.768229889574501722 \times 10^5 \text{ cm}^{-1}$
a_9	$0.157896664088991121 \times 10^6 \text{ cm}^{-1}$
a_{10}	$0.833691806464401074 \times 10^6 \text{ cm}^{-1}$
a_{11}	$-0.115890452663354226 \times 10^7 \text{ cm}^{-1}$
a_{12}	$-0.653607110081680864 \times 10^7 \text{ cm}^{-1}$
a_{13}	$0.487172809603480622 \times 10^7 \text{ cm}^{-1}$
a_{14}	$0.308101362964722812 \times 10^8 \text{ cm}^{-1}$
a_{15}	$-0.863340173933527432 \times 10^7 \text{ cm}^{-1}$
a_{16}	$-0.8118046377488166609 \times 10^8 \text{ cm}^{-1}$
a_{17}	$0.492251670364311151 \times 10^7 \text{ cm}^{-1}$
a_{18}	$0.121156746090629265 \times 10^9 \text{ cm}^{-1}$
a_{19}	$0.280059277888290165 \times 10^7 \text{ cm}^{-1}$
a_{20}	$-0.968951931944736689 \times 10^8 \text{ cm}^{-1}$
a_{21}	$-0.314874358611015789 \times 10^7 \text{ cm}^{-1}$
a_{22}	$0.324661526246530302 \times 10^8 \text{ cm}^{-1}$
BO_{gen}	(-0.00006)
BO_{asym}	0.00566

to investigate both homonuclear and heteronuclear beyond BO corrections.

We conclude that very interesting Feshbach spectroscopy is ahead of us to work out and highlight the importance of BO corrections in the understanding of cold collisions.

Recently, we became aware that in the doctoral thesis of Antje Ludewig, University Amsterdam [33], a large number of unpublished Feshbach resonances of ^{40}K are reported and that in Liu *et al.* [34] *d*-wave resonances for ^{41}K are reported. We checked these data with our model and found complete consistency for the data from Antje Ludewig after reassignment of some *p*-wave resonances. For the resonances in Liu *et al.*, we find mainly consistency for the high-field data but the low-field data deviate systematically due to their strong temperature dependence, the analysis of which would require the inclusion of the kinetic energy dependence of the collision rates and the thermal distribution in the actual experiment. The description by a single-channel approximation for so-called ‘‘broad’’ resonances assumed by Liu *et al.* is not justified because the resonances show strong inelastic con-

TABLE VI. Parameters of the long-range part of the potentials for both states $X^1\Sigma_g^+$ and $a^3\Sigma_u^+$.

$R_{\text{out}} < R$	
U_∞	0.0 cm^{-1}
C_6	$0.1892338370 \times 10^8 \text{ cm}^{-1} \text{ \AA}^6$
C_8	$0.5706799528 \times 10^9 \text{ cm}^{-1} \text{ \AA}^8$
C_{10}	$0.1853042723 \times 10^{11} \text{ cm}^{-1} \text{ \AA}^{10}$
A_{ex}	$0.90092159 \times 10^4 \text{ cm}^{-1} \text{ \AA}^{-\gamma}$
γ	5.19500
β	2.13539 \AA^{-1}

tributions. Details of these calculations are contained in the Appendix.

ACKNOWLEDGMENTS

We gratefully acknowledge financial support from the European Research Council through ERC Starting Grant POLAR and from the Deutsche Forschungsgemeinschaft (DFG) through CRC 1227 (DQ-mat), Project No. A03, and FOR 2247, Project No. E5. K.K.V. and P.G. thank the Deutsche Forschungsgemeinschaft for financial support through Research Training Group 1991.

TABLE VII. Parameters of the analytic representation of the $a^3\Sigma_u^+$ state potential with adiabatic Born-Oppenheimer correction and reference isotopologue $^{39}\text{K}_2$. The energy reference is the dissociation asymptote. Parameters with * are set for continuous extrapolation of the potential.

$R < R_{\text{in}} = 4.755 \text{ \AA}$	
A^*	$-0.7009379657 \times 10^3 \text{ cm}^{-1}$
B^*	$0.80690073665 \times 10^7 \text{ cm}^{-1} \text{ \AA}^6$
N_s	6
$R_{\text{in}} \leq R \leq R_{\text{out}} = 12.000 \text{ \AA}$	
b	-0.40
R_m	5.7347289 \AA
a_0	$-255.0214692 \text{ cm}^{-1}$
a_1	$-0.013405598929310479 \text{ cm}^{-1}$
a_2	$0.153940442323125171 \times 10^4 \text{ cm}^{-1}$
a_3	$-0.626944977828736569 \times 10^3 \text{ cm}^{-1}$
a_4	$-0.147039918194012284 \times 10^4 \text{ cm}^{-1}$
a_5	$0.238628331428504282 \times 10^3 \text{ cm}^{-1}$
a_6	$-0.121465057044283844 \times 10^4 \text{ cm}^{-1}$
a_7	$-0.131024472517054273 \times 10^5 \text{ cm}^{-1}$
a_8	$0.410390478256789502 \times 10^5 \text{ cm}^{-1}$
a_9	$0.585609645570106004 \times 10^5 \text{ cm}^{-1}$
a_{10}	$-0.316660644987405278 \times 10^6 \text{ cm}^{-1}$
a_{11}	$0.178579875710784399 \times 10^6 \text{ cm}^{-1}$
a_{12}	$0.690085326716458891 \times 10^6 \text{ cm}^{-1}$
a_{13}	$-0.116538893384502688 \times 10^7 \text{ cm}^{-1}$
a_{14}	$0.541518493723396794 \times 10^6 \text{ cm}^{-1}$
BO_{gen}	-0.000465
BO_{asym}	(-0.000001)

TABLE VIII. Feshbach resonances taken from Ref. [33] and their theoretical modeling. Columns o-c give the difference of observed field value (obs) and experimental uncertainty (unc) to the calculated one (not listed). The number indicates the model of evaluation as in Table II: (3) both BO corrections BO_{gen} and BO_{asym} for the homo- and heteronuclear cases.

Isotope	M	Atom pair	l_{min}	l_{max}	Type	Obs [G]	Unc [G]	o-c(3) [G]	
40/40	-6	9/2, -7/2> 9/2, -5/2>	0	0	el	228.8	0.4	0.131	
	-5	9/2, -7/2> 9/2, -3/2>	0	0	el	168.5	0.4	-0.467	
	-5	9/2, -7/2> 9/2, -3/2>	0	0	el	260.3	0.6	-0.128	
	-4	9/2, -5/2> 9/2, -3/2>	0	0	el	22.1	0.3	0.140	
	-4	9/2, -5/2> 9/2, -3/2>	0	0	el	178.0	1.0	-0.017	
	-4	9/2, -5/2> 9/2, -3/2>	0	0	el	254.8	0.9	-0.188	
	-2	9/2, -3/2> 9/2, -1/2>	0	0	el	37.2	0.3	-0.199	
	-2	9/2, -3/2> 9/2, -1/2>	0	0	el	102.1	0.1	-0.065	
	-2	9/2, -3/2> 9/2, -1/2>	0	0	el	138.2	0.1	0.034	
	-2	9/2, -3/2> 9/2, -1/2>	0	0	el	219.1	0.1	-0.367	
40/40	-2	9/2, -3/2> 9/2, -1/2>	0	0	el	292.3	0.4	-0.180	
	6	9/2, 7/2> 9/2, 5/2>	0	0	el	312.0	1.8	-0.164	
	-7	9/2, -9/2> 9/2, -5/2>	1	1	in	215.0	5.0	-1.060	
	-8	9/2, -9/2> 9/2, -5/2>	1	1	in	215.0	5.0	-0.020	
	-6	9/2, -5/2> 9/2, -5/2>	1	1	in	232.8	0.2	-0.141	
	-5	9/2, -5/2> 9/2, -5/2>	1	1	in	233.5	0.2	-0.100	
	-5	9/2, -5/2> 9/2, -5/2>	1	1	in	245.3	0.4	0.019	
	-5	9/2, -5/2> 9/2, -3/2>	1	1	in	262.2	0.2	0.059	
	-4	9/2, -5/2> 9/2, -3/2>	1	1	in	262.6	0.2	0.140	
	-3	9/2, -3/2> 9/2, -3/2>	1	1	in	287.0	1.8	-0.580	
	-3	9/2, -3/2> 9/2, -3/2>	1	1	in	311.8	0.4	0.090	
	-2	9/2, -3/2> 9/2, -1/2>	1	1	in	338.0	1.8	-0.320	
	-1	9/2, -1/2> 9/2, -1/2>	1	1	in	373.0	1.8	-0.654	
	5	9/2, 5/2> 9/2, 5/2>	1	1	in	68.0	1.8	0.195	
	5	9/2, 5/2> 9/2, 5/2>	1	1	in	102.0	1.8	-0.581	
	5	9/2, 5/2> 9/2, 5/2>	1	1	in	139.0	1.8	2.517	
	5	9/2, 5/2> 9/2, 5/2>	1	1	in	324.0	1.8	0.238	
	7	9/2, 5/2> 9/2, 9/2>	1	1	in	44.0	1.8	-0.900	
	6	9/2, 7/2> 9/2, 7/2>	1	1	in	43.8	0.2	-0.011	reassigned
	7	9/2, 7/2> 9/2, 7/2>	1	1	in	43.8	0.2	0.075	reassigned
8	9/2, 7/2> 9/2, 7/2>	1	1	el	44.7	0.2	0.100	reassigned	
7	9/2, 7/2> 9/2, 7/2>	1	1	in	45.2	0.2	0.079	reassigned	
7	9/2, 7/2> 9/2, 7/2>	1	1	in	46.4	0.2	-0.254		

APPENDIX

Tables V–VII show the potential parameters [defined in Eqs. (1), (3), and (4)] for the two states $X^1\Sigma_g^+$ and $a^3\Sigma_u^+$, as derived during the evaluation. These results are improved potentials compared to the published ones [7], not only because the Feshbach data have been largely extended but also the number of potential parameters is significantly reduced, leading to a more stringent potential form with less danger of showing tiny oscillatory unphysical effects.

We analyzed the Feshbach resonances for ^{40}K reported by Ludwig [33] using the derived potential system and the full beyond Born-Oppenheimer correction, model labeled by (3). The s -wave resonances are described consistently but some of the p -wave resonances needed a reassignment related to the assumed total magnetic quantum number M . The results are given in Table VIII. The s -wave resonances are dominated by the elastic channel but the p -wave resonances show mainly inelastic contributions as indicated in the column type by

labels “el” or “in,” respectively. The overall agreement is very good and confirms our analysis of the previously known resonances.

Furthermore, we analyzed the resonances given by Liu *et al.* [34]. With our model we confirm the positions of the three groups of d -wave Feshbach resonances; see Table IX. Our theoretical approach includes the effective spin-spin interaction, and thus we checked the splitting within the multiplet according the projection of rotational angular momentum m_l and found that the expected splitting in the case of $|1, 1\rangle + |1, 0\rangle$ at 544 G is too small to resolve the resonances $m_l = 0$ and ± 1 in the study by Liu *et al.* [34]. This case is marked as “reassigned” in the table.

For the four reported groups of shape resonances, we see a systematic deviation from our predictions; compare the upper part of Table IX. The profile of these observed resonances is significantly asymmetric and highly dominated by the thermal distribution of the ensemble. Hence, a precise analysis of the resonance positions would require detailed knowledge of the experimental condition and the inclusion of their significant

TABLE IX. Feshbach resonances taken from Ref. [34] and their theoretical modeling. Columns o-c give the difference of observed field value (obs) and experimental uncertainty (unc) to calculated one (not listed). The number indicates the model of evaluation as in Table II: (3) both BO corrections BO_{gen} and BO_{asym} for the homo- and heteronuclear cases. The upper panel summarizes the shape resonances (assuming 50 nK) and the lower one shows the Feshbach resonances (with 310 nK according to Ref. [34]).

Isotope	M	Atom pair	l_{min}	l_{max}	Type	Obs [G]	Unc [G]	o-c(3) [G]	
41/41	2	1, 1⟩ 1, 1⟩	0	2	el	16.83	0.04	0.539	
	3	1, 1⟩ 1, 1⟩	2	2	el	17.19	0.04	0.381	
	4	1, 1⟩ 1, 1⟩	2	2	el	18.75	0.04	0.333	
	1	1, 1⟩ 1, 0⟩	0	2	in	25.31	0.04	0.685	
	2	1, 1⟩ 1, 0⟩	2	2	in	25.41	0.23	0.642	
	3	1, 1⟩ 1, 0⟩	2	2	in	25.74	0.04	0.542	
	0	1, 0⟩ 1, 0⟩	0	2	in	63.30	0.04	0.806	
	1	1, 0⟩ 1, 0⟩	2	2	in	63.69	0.08	0.731	
	2	1, 0⟩ 1, 0⟩	2	2	in	65.16	0.06	0.694	
	-2	1, -1⟩ 1, -1⟩	0	2	in	104.47	0.04	0.445	
	-1	1, -1⟩ 1, -1⟩	2	2	in	104.95	0.04	0.475	
	0	1, -1⟩ 1, -1⟩	2	2	in	106.27	0.04	0.401	
	41/41	2	1, 1⟩ 1, 1⟩	0	2	el	530.48	0.04	0.122
3		1, 1⟩ 1, 1⟩	2	2	el	530.40	0.04	0.114	
4		1, 1⟩ 1, 1⟩	2	2	el	530.18	0.04	0.131	
1		1, 1⟩ 1, 0⟩	0	2	el	544.93	0.04	0.130	
3		1, 1⟩ 1, 0⟩	2	2	in	544.79	0.04	0.140	reassigned
3		1, 1⟩ 1, 0⟩	2	2	in	544.34	0.11	-0.310	doubtful
1		1, 0⟩ 1, 0⟩	0	2	in	565.23	0.04	0.053	
2		1, 0⟩ 1, 0⟩	2	2	in	565.05	0.04	0.058	
3		1, 0⟩ 1, 0⟩	2	2	in	564.53	0.04	0.106	

kinetic energy dependence, which is not discussed in Liu *et al.* The authors applied an asymmetric line profile for the fit, which leads us to the assumption that the reported resonance positions are extrapolated to lower energies than

the average value of 310 nK. We find better agreement with our predictions when the kinetic energy for our calculations is lowered to 50 nK; see Table IX. A conclusive analysis would require full access to the originally recorded spectra.

- [1] M. Born and R. Oppenheimer, *Ann. Phys.* **389**, 457 (1927).
[2] R. Herman and A. Asgharian, *J. Mol. Spectrosc.* **19**, 305 (1966).
[3] J. K. G. Watson, *J. Mol. Spectrosc.* **80**, 411 (1980).
[4] P. R. Bunker, *J. Mol. Spectrosc.* **68**, 367 (1977).
[5] L. Che, Z. Ren, X. Wang, W. Dong, D. Dai, X. Wang, D. H. Zhang, X. Yang, L. Sheng, G. Li *et al.*, *Science* **317**, 1061 (2007).
[6] H. Knöckel, B. Bodermann, and E. Tiemann, *Eur. Phys. J. D* **28**, 199 (2004).
[7] S. Falke, H. Knöckel, J. Friebe, M. Riedmann, E. Tiemann, and C. Lisdat, *Phys. Rev. A* **78**, 012503 (2008).
[8] M. Färnik, S. Davis, M. A. Kostin, O. Polyansky, J. Tennyson, and D. Nesbitt, *J. Chem. Phys.* **116**, 6146 (2002).
[9] C. Chin, R. Grimm, P. Julienne, and E. Tiesinga, *Rev. Mod. Phys.* **82**, 1225 (2010).
[10] C. A. Regal, C. Ticknor, J. L. Bohn, and D. S. Jin, *Phys. Rev. Lett.* **90**, 053201 (2003).
[11] C. D’Errico, M. Zaccanti, M. Fattori, G. Roati, M. Inguscio, G. Modugno, and A. Simoni, *New J. Phys.* **9**, 223 (2007).
[12] C.-H. Wu, I. Santiago, J. W. Park, P. Ahmadi, and M. W. Zwierlein, *Phys. Rev. A* **84**, 011601(R) (2011).
[13] H.-Z. Chen, X.-C. Yao, Y.-P. Wu, X.-P. Liu, X.-Q. Wang, Y.-X. Wang, Y.-A. Chen, and J.-W. Pan, *Phys. Rev. A* **94**, 033408 (2016).
[14] L. Tanzi, C. R. Cabrera, J. Sanz, P. Cheiney, M. Tomza, and L. Tarruell, *Phys. Rev. A* **98**, 062712 (2018).
[15] J. H. van Vleck, *J. Chem. Phys.* **4**, 327 (1936).
[16] T. A. Schulze, T. Hartmann, K. K. Voges, M. W. Gempel, E. Tiemann, A. Zenesini, and S. Ospelkaus, *Phys. Rev. A* **97**, 023623 (2018).
[17] T. Hartmann, T. A. Schulze, K. K. Voges, P. Gersema, M. W. Gempel, E. Tiemann, A. Zenesini, and S. Ospelkaus, *Phys. Rev. A* **99**, 032711 (2019).
[18] T. Weber, J. Herbig, M. Mark, H.-C. Nägerl, and R. Grimm, *Phys. Rev. Lett.* **91**, 123201 (2003).
[19] P. D. Gregory, M. D. Frye, J. A. Blackmore, E. M. Bridge, R. Sawant, J. M. Hutson, and S. L. Cornish, *Nat. Commun.* **10**, 3104 (2019).
[20] L. Fouché, A. Boissé, G. Berthet, S. Lepoutre, A. Simoni, and T. Bourdel, *Phys. Rev. A* **99**, 022701 (2019).
[21] C. A. Regal and D. S. Jin, *Phys. Rev. Lett.* **90**, 230404 (2003).
[22] C. Ticknor, C. A. Regal, D. S. Jin, and J. L. Bohn, *Phys. Rev. A* **69**, 042712 (2004).
[23] C. A. Regal, M. Greiner, and D. S. Jin, *Phys. Rev. Lett.* **92**, 040403 (2004).
[24] E. Arimondo, M. Inguscio, and P. Violino, *Rev. Mod. Phys.* **49**, 31 (1977).

- [25] By sharing our manuscript with M. Zwierlein [35], we learned that for the two resonances at lower fields, the authors extrapolated the field values from low-field calibrations and therefore an error of 2 G is not unlikely. For the broad resonance at 542.7 G, an uncertainty of 0.5 G would be a good estimate because an improved calibration was applied.
- [26] At the bottom of Table I we give the deviations for the removed isotope combination derived from the three fit models. The magnitude of the deviations does not show a significant difference between the three models described, thus it is independent of type of modeling and not related to BO corrections.
- [27] Note that within our many trials of nonlinear fitting we found one solution excluding BO corrections in which the $\sigma(^{39}\text{K} - ^{39}\text{K}) = 0.924$ and $\sigma(^{39}\text{K} - ^{41}\text{K}) = 0.988$ from the main body of data are almost equally distributed, but both are significantly larger than the ones derived from separate fits of the isotope combinations, namely 0.593 and 0.753. Thus, also this fit shows the need for BO corrections.
- [28] P. R. Bunker, *J. Mol. Spectrosc.* **46**, 119 (1973).
- [29] C. Amiot, J. Vergès, and C. Fellows, *J. Chem. Phys.* **103**, 3350 (1995).
- [30] A. Pashov, P. Popov, H. Knöckel, and E. Tiemann, *Eur. Phys. J. D* **46**, 241 (2008).
- [31] R. J. LeRoy, N. S. Dattani, J. A. Coxon, A. J. Ross, P. Crozet, and C. Linton, *J. Chem. Phys.* **131**, 204309 (2009).
- [32] M. Gerken, B. Tran, S. Häfner, E. Tiemann, B. Zhu, and M. Weidemüller, *Phys. Rev. A* **100**, 050701(R) (2019).
- [33] A. Ludewig, Ph.D. thesis, 2012, <https://hdl.handle.net/11245/1.369033>.
- [34] X.-P. Liu, X.-C. Yao, R. Qi, X.-Q. Wang, Y.-X. Wang, Y.-A. Chen, and J.-W. Pan, *Phys. Rev. A* **98**, 022704 (2018).
- [35] M. Zwierlein (private communication).

3.3 Formation of ultracold weakly bound dimers of bosonic $^{23}\text{Na}^{39}\text{K}$ [A3]

As detailed in section 3.1 the preparation of weakly bound molecules near a Feshbach resonance can be accomplished through either a magnetic field sweep across the resonance or resonant RF/MW pulses, magnetic field modulations or two-photon Raman pulses.

A magnetic field sweep has the advantage that it is robust, does not demand a high magnetic field stability and promises high conversion efficiencies of up to 60 % for highly degenerate samples [93]. Such a sweep has to start on the negative and has to end on the positive scattering length side [58]. In addition the sweep over the resonance has to be fast, as on or close to the resonance position large three-body losses occur. This turned out to be a problem for $^{23}\text{Na}^{39}\text{K}$, as the feasible Feshbach resonances, with regard to easy accessibility of the hyperfine states and magnetic field strength, have a large width Δ , demanding large and fast magnetic field sweeps on the order of ≈ 100 G/ms. The POLAR experiment generates its homogeneous magnetic fields through coils in Helmholtz configuration. Up to 250 A flow through the coils generating a magnetic field of roughly 750 G. The large inductance of these coils aggravates fast sweeps over large field ranges. Small offset coils mounted on top of the main coils with lower inductance and therefore higher speed, did not have enough range and gave rise to inductive currents in the main coils, demanding a damping time before the following production of ground-state molecules. Since it turned out that the lifetime of the Feshbach molecules is only on the order of a few hundred microseconds, see [A3], this approach is ultimately not feasible.

Instead, as antennas were easily implementable and sources as well as amplifiers already available, a resonant RF pulse was realized. This has the advantage of an already settled magnetic field and therefore enables an immediate STIRAP after the Feshbach molecule production. For an efficient and stable creation, this resonant RF pulse requires a stable and low-noise magnetic field.

3.3.1 Magnetic field stability

In the POLAR experiment the homogenous magnetic field is produced with a current flowing through two coils in Helmholtz configuration. Therefore for a stable magnetic field the current through the coils needs to be stabilized. A possibility for a stable, fast and low noise current supply is the use of batteries. These can give an extremely small root-mean-square (rms) noise well below 1 mA at 100 A [94]. However, handling batteries at high currents and power levels is quite challenging and poses a major fire hazard. In the POLAR experiment an rms noise of around 10 mA (roughly 30 mG) at 70 A was sufficient to create weakly bound molecules, see [A3]. This is achievable with DC power supplies, in this case two *SM30-200* from *Delta Elektronik* connected in parallel, which are additionally stabilized with feedback from a current transducer *IT 400-S ULTRASTAB* from *LEM*.

The rms noise of 10 mA was later further improved to around 3 mA (10 mG) which in turn enhanced

3 Feshbach resonances and molecules

the molecular conversion efficiency to slightly above 10% with regard to the potassium atom number (in contrast to 6% as noted in [A3]). The implementation of this improved low-noise current-control circuit is shown in Fig. 3.3.

Note that, the Helmholtz coils can also be used to apply quadrupole and Stern-Gerlach fields. A detailed overview of this coil circuit and the implementation and control of high current switches can be found in [89].

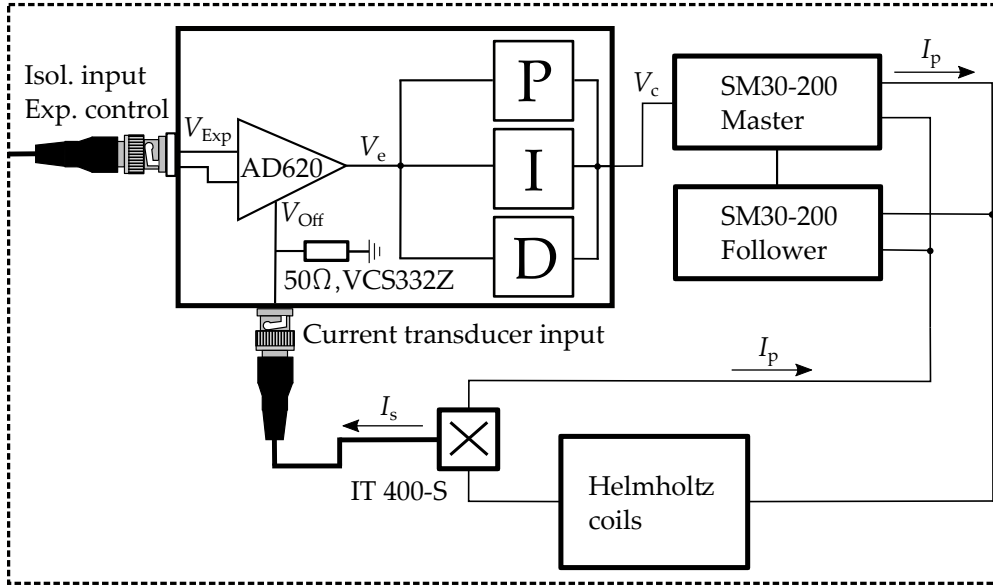


Figure 3.3: Schematic of the current control circuit. The experimental control voltage used to set the desired current value I_p is supplied to a proportional-integral-derivative (PID) controller. An instrumental amplifier compares this experiment control voltage V_{Exp} to an offset voltage V_{Off} . This voltage originates from the current transducer that converts the primary current I_p into a secondary current I_s , with a conversion ratio of $I_s/I_p = 1/2000$. This current is then converted into the offset voltage through a $50\ \Omega$ resistance with an ultra-low temperature coefficient of $0.05\ \text{ppm/K}$. The error signal is equal to $V_e = V_{\text{Exp}} - V_{\text{Off}}$. The resulting control voltage V_c sets the output current of the *Delta* power supplies. This current flows through the Helmholtz coils generating a homogenous magnetic field.

The primary current I_p of the *Delta* power supplies is set with the control voltage V_c , which is generated from a proportional-integral-derivative (PID) controller. The error signal V_e of this PID controller originates from an instrumental amplifier *AD620*, which has a relatively low offset drift and noise, with $V_e = V_{\text{Exp}} - V_{\text{Off}}$. The experiment analog control voltage V_{Exp} is generated from an *ADwin Pro II board* (*Jaeger Messtechnik GmbH*). This voltage can be set between $\pm 10\ \text{V}$ with a 16 bit resolution and is electrically isolated from the rest of the current control circuit to prevent ground loops. The offset voltage V_{Off} originates from the *IT 400-S*. The current transducer converts the current I_p into a secondary current I_s with a ratio of $I_s/I_p = 1/2000$. This current is then converted into a voltage using *VCS332Z* resistances from *Vishay*. These possess an extremely

low temperature coefficient of around 0.05 ppm/K, which is necessary to prevent current drifts as during operation the resistances heat up. This would change the resistance, thus the offset voltage and consequently the applied primary current. Both the PID controller and the current transducer are powered by the same power supply whose output voltage is additionally stabilized and filtered. In addition, to avoid RF-induced noise, the entire current control loop in the laboratory is located as far away as possible from the RF emitting antennas at the main chamber.

The residual rms noise is measured by an atomic hyperfine transfer utilizing RF pulses. For this, an ultracold atomic cloud is prepared in a homogeneous magnetic field, a 100 ms long RF pulse applied and its frequency scanned over the resonance position. As the transition has a negligible linewidth and is probed at low RF intensities, the width of the resulting curve can be converted to a magnetic field noise using the Breit-Rabi-formula. This relatively simple setup provides a magnetic field stability of 3 mA (10 mG) at 70 A for the production of Feshbach molecules with resonant RF pulses.

With a stable magnetic field configuration, a Feshbach resonance in the $|F = 1, m_F = -1\rangle_{\text{Na}} + |F = 2, m_F = -2\rangle_{\text{K}}$ hyperfine state at roughly 196 G is used to populate a weakly bound molecular state [A3]¹. This resonance has a few advantages. Initially both atomic clouds are prepared in the $|F = 1, m_F = -1\rangle$ hyperfine state. Therefore a single RF pulse is enough to access this Feshbach resonance. In addition, this magnetic field is easily accessible without crossing many Feshbach resonances and has feasible inter- and intraspecies scattering lengths in the initial hyperfine states [90]. Lastly, the $|F = 2, m_F = -2\rangle_{\text{K}}$ hyperfine state enables a sensitive high field potassium absorption imaging, capable of resolving the few thousand Feshbach molecules with high signal-to-noise ratio. It should be noted, that a sodium or potassium high field image also images the weakly bound Feshbach molecules. This is possible, as the molecular state is heavily mixed with the atomic one and only a few 100 kHz away. This is far smaller than the natural linewidth of the D_2 line of sodium and potassium, used for the absorption imaging, of roughly $2\pi \cdot 10$ MHz and $2\pi \cdot 6$ MHz respectively. The weakly bound molecules are destroyed after the first photon is absorbed and afterwards the resulting atomic $^{39}\text{K} + ^{23}\text{Na}$ clouds are imaged. In the next section, a high-field imaging technique for ^{23}Na and ^{39}K atoms is presented.

3.3.2 High-field imaging of ^{23}Na and ^{39}K

For an absorption imaging, the shadow cast by an atomic cloud by a resonant laser beam is detected on a camera. Sensitive imaging schemes rely on closed cycling transitions where the atoms always remain in the bright state. For example at zero magnetic field, in the case of ^{23}Na and ^{39}K this can be realized with a laser driving the transition from the $|^2\text{S}_{1/2}, F = 2\rangle$ state to the $|^2\text{P}_{3/2}, F = 3\rangle$ state. However, off-resonant scattering on the $|^2\text{P}_{3/2}, F = 2\rangle$ state reduces the signal-to-noise ratio and requires a subsequent repumping back to the $|^2\text{S}_{1/2}, F = 2\rangle$ state. This is especially relevant for potassium due to a small hyperfine constant $a_{\text{hf}}/h \approx 6$ MHz, with h being the Planck constant,

¹Note that, unless otherwise specified, atomic states are always written as their corresponding state in the low magnetic field basis that would be achieved by an adiabatic downward ramp of the magnetic field.

3 Feshbach resonances and molecules

of the $|4^2P_{3/2}\rangle$ manifold.

At low magnetic fields, the total angular momentum F and its projection m_F on the magnetic field axis are good quantum numbers. This is called the Zeeman region. At high magnetic field strengths the nuclear spin I and the total electronic angular momentum J decouple and precess individually around the magnetic field axis. This is the Paschen-Back region. Therefore the basis $|J, m_J, I, m_I\rangle$, with m_J and m_I denoting the projection of J and I on the magnetic field axis, can be used to describe the energy levels.

The Feshbach molecules are prepared at roughly 200 G. At this magnetic field strength the atoms are neither in the Zeeman nor in the Paschen-Back region, although potassium is close to the latter due to a smaller hyperfine constant, see Fig. 3.5. Written in the high- or low-field basis each level might therefore be in a mixture of these states. Please note, referring to the image as high-field is therefore strictly speaking not correct, but makes sense in an experimental context and is therefore commonly used in the field.

The sodium atoms initially populate the $|F = 1, m_F = -1\rangle$ hyperfine state. Starting from this state, no closed cycling transition can be found, at least with a single laser frequency. Therefore a hyperfine state manipulation with an adiabatic RF sweep prior to the high-field image would be beneficial. However, as will be described in detail in [A5], the sodium atoms should be removed as quickly as possible directly after the Feshbach molecule and following ground-state molecule formation, due to unfavourable scattering properties. This removal can be achieved with a high-field imaging pulse. Therefore, a hyperfine state manipulation prior to the high-field image turned out to be too slow and an imaging for the $|F = 1, m_F = -1\rangle$ hyperfine state at 200 G needs to be implemented, as shown in Fig. 3.4.

At 200 G the initial $|F = 1, m_F = -1\rangle$ hyperfine state is adiabatically transferred to $|\Psi\rangle \approx 0.8|J = 1/2, m_J = 1/2, I = 3/2, m_I = -3/2\rangle + 0.6|J = 1/2, m_J = -1/2, I = 3/2, m_I = -1/2\rangle$. This state can be coupled to the $|J = 3/2, m_J = -3/2, I = 3/2, m_I = -1/2\rangle$ state in the $|4^2P_{3/2}\rangle$ manifold, using σ^- -polarized light. The excited state can decay back to the initial state but also to $|\Psi'\rangle \approx -0.6|J = 1/2, m_J = 1/2, I = 3/2, m_I = -3/2\rangle + 0.8|J = 1/2, m_J = -1/2, I = 3/2, m_I = -1/2\rangle$ and therefore requires an additional laser that couples this state back to the excited state. This scheme can lead to the problem of sodium atoms falling into a coherent dark state, though this was never observed. This is probably because the MW sources used for the acousto-optic modulators to shift the lasers to the desired frequencies are noisy (around 1 MHz), which constantly destabilizes the dark state that is formed.

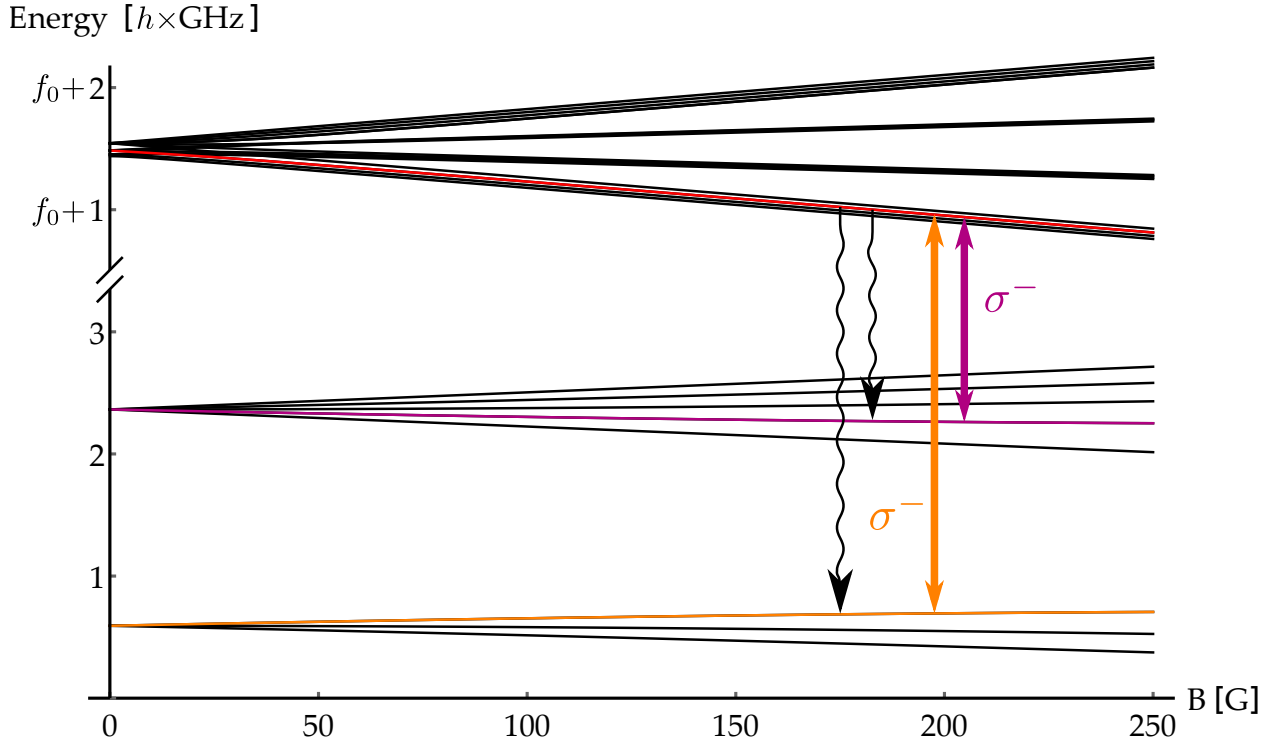


Figure 3.4: Sodium high-field imaging scheme. The energy level splitting of the $|3^2\text{S}_{1/2}\rangle$ (lower levels) and the $|3^2\text{P}_{3/2}\rangle$ (higher levels) manifolds of the ^{23}Na atom in an external magnetic field is shown. f_0 is the frequency of a photon bridging these manifolds. The orange line shows the initial state of the atoms $|\Psi\rangle$. This is coupled with σ^- polarized light to the $|J = 3/2, m_J = -3/2, I = 3/2, m_I = -1/2\rangle$ state in the $|4^2\text{P}_{3/2}\rangle$ manifold (orange arrow, red line). This excited state can decay into two states, the initial state $|\Psi\rangle$ and the state $|\Psi'\rangle$ (purple line). An additional laser couples this state again with the same excited state (purple arrow). Image adopted from [95].

For the potassium high-field image, one can take advantage of the fact, that the atomic hyperfine state $|F = 2, m_F = -2\rangle$ is a stretched state. In this case, the nuclear as well as the total electronic angular momentum are maximally stretched along the magnetic field axis and can therefore always be written in both basis sets with a single contribution, in this case $|J = 1/2, m_J = -1/2, I = 3/2, m_I = -3/2\rangle$. From this stretched state there exists a closed σ^- -transition to another spin stretched state in the $|4^2\text{P}_{3/2}\rangle$ manifold, $|J = 3/2, m_J = -3/2, I = 3/2, m_I = -3/2\rangle$, see Fig. 3.5. This transition is closed regardless of the applied magnetic field. With this absorption imaging scheme and a single lens focusing the shadow cast of the atomic cloud on a *PF-M-QE-PIV pco.pixelfly* camera, with a magnification of 2.66, the signal-to-noise ratio is good enough to reliably resolve 200-300 atoms or Feshbach molecules in a single shot.

3 Feshbach resonances and molecules

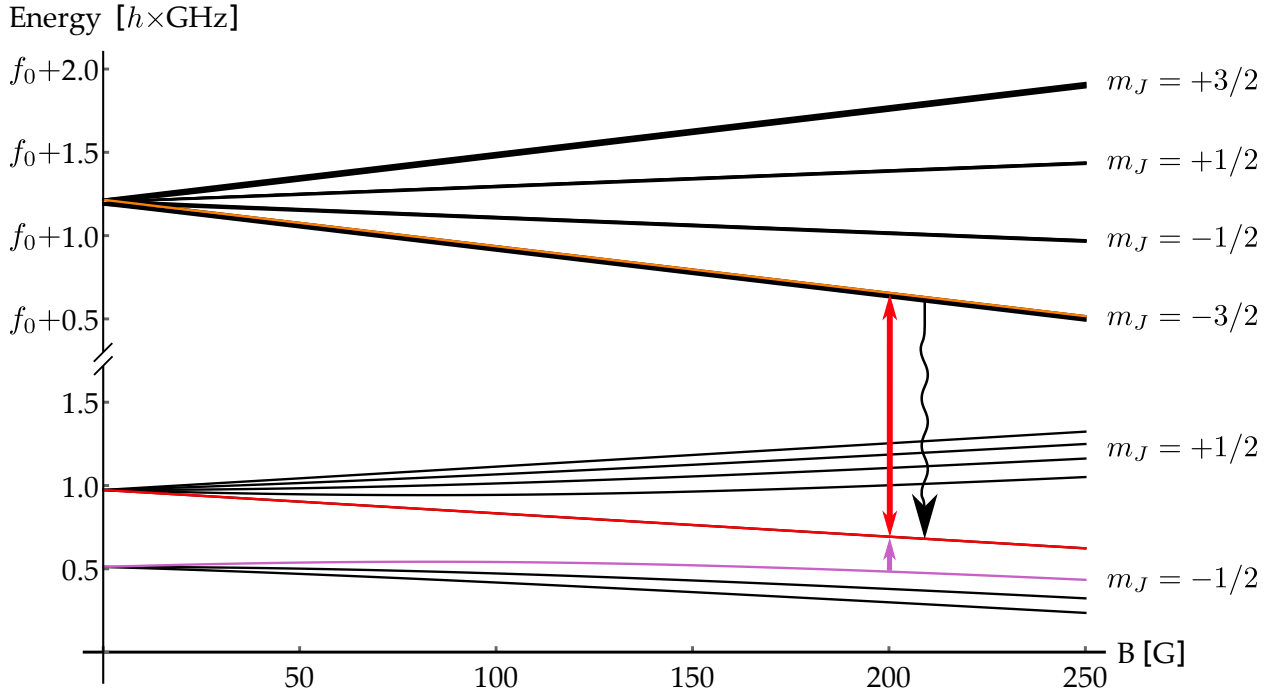


Figure 3.5: Potassium high-field imaging scheme. The energy level splitting of the $|4^2S_{1/2}\rangle$ (lower levels) and the $|4^2P_{3/2}\rangle$ (higher levels) manifolds of the ^{39}K atom in an external magnetic field is shown. f_0 is the frequency of a photon bridging these manifolds. Initially the potassium atoms are prepared in the $|F = 1, m_F = -1\rangle$ hyperfine state (purple line). Through either a resonant RF pulse or a sweep across the atomic resonance, Feshbach molecules or potassium atoms in the $|F = 2, m_F = -2\rangle$ (red line), are prepared (purple arrow). For the absorption imaging a closed cycling transition from this state to $|F = 2, m_F = -2\rangle$ is utilized (red arrow). Through stimulated or spontaneous decay the atoms can only fall back to $|F = 2, m_F = -2\rangle$ (black arrow). Image adopted from [95].

For the potassium high-field image only one resonant scattering cross section is needed to determine the scattering rate of the resonant laser with the atomic cloud. This makes the atom number determination more reliable compared to all other imaging schemes implemented in the POLAR experiment. Therefore, the atom numbers derived from the other absorption imaging schemes are calibrated to the high-field potassium image. For a comparison of the low-field and high-field atom number, one can simply switch between these two imaging techniques and compare the derived atom numbers. For the calibration of the sodium atom number, one can take advantage of the fact that the Feshbach molecule number must be the same for the sodium and potassium high-field images. The sodium high-field image is too noisy to resolve the Feshbach molecules in a single image. Therefore, to achieve a reliable calibration, we allowed the system to average for more than 1 hour and collected about 120 data points. In the end, this enabled a calibration of the sodium atom number.

3.3 Formation of ultracold weakly bound dimers of bosonic $^{23}\text{Na}^{39}\text{K}$ [A3]





In the following paper, the formation of weakly bound dimers of bosonic $^{23}\text{Na}^{39}\text{K}$ at roughly 200 G, close to a Feshbach resonance in the $|F = 1, m_F = -1\rangle_{\text{Na}} + |F = 2, m_F = -2\rangle_{\text{K}}$ hyperfine state, with a resonant RF pulse is shown. The transfer efficiency is investigated, with respect to atom number ratios and pulse duration. Additionally the lifetime of the Feshbach molecules embedded in the atomic sample is measured. This successful creation enables the production of ground-state molecules with a subsequent STIRAP, as shown in section 4.2.

3 Feshbach resonances and molecules

Reprinted with permission from Voges *et al.*, Formation of ultracold weakly bound dimers of bosonic $^{23}\text{Na}^{39}\text{K}$, Phys. Rev. A 101, 042704, 2020

Copyright © 2022 by the American Physical Society (APS).

DOI <https://link.aps.org/doi/10.1103/PhysRevA.101.042704>

Formation of ultracold weakly bound dimers of bosonic $^{23}\text{Na}^{39}\text{K}$ Kai K. Voges , Philipp Gersema , Torsten Hartmann ,* Torben A. Schulze, Alessandro Zenesini , and Silke Ospelkaus[†]
Institut für Quantenoptik, Leibniz Universität Hannover, 30167 Hannover, Germany

(Received 6 November 2019; revised manuscript received 28 February 2020; accepted 9 March 2020; published 20 April 2020)

We create weakly bound bosonic $^{23}\text{Na}^{39}\text{K}$ molecules in a mixture of ultracold ^{23}Na and ^{39}K . The creation is done in the vicinity of a so far undetected Feshbach resonance at about 196 G which we identify in this work by atom-loss spectroscopy. We investigate the involved molecular state by performing destructive radio-frequency binding-energy measurements. For the constructive molecule creation we use radio-frequency pulses with which we assemble up to 6000 molecules. We analyze the molecule creation efficiency as a function of the radio-frequency pulse duration and the atom number ratio between ^{23}Na and ^{39}K . We find an overall optimal efficiency of 6 % referring to the ^{39}K atom number. The measured lifetime of the molecules in the bath of trapped atoms is about 0.3 ms.

DOI: [10.1103/PhysRevA.101.042704](https://doi.org/10.1103/PhysRevA.101.042704)**I. INTRODUCTION**

Feshbach molecule creation from ultracold atomic gases has led to exciting developments ranging from the observation of the BCS-BEC crossover [1,2] to Efimov physics [3] and state-to-state chemistry [4]. Furthermore, Feshbach molecules constitute an important steppingstone for the creation of deeply bound molecules by means of stimulated Raman adiabatic passage (STIRAP). For heteronuclear molecules, this was first demonstrated for fermionic KRb molecules starting from a heteronuclear K and Rb quantum gas mixture [5]. Heteronuclear ground-state molecules are of special interest because of their large electric dipole moment. The anisotropic and tunable dipole-dipole interaction can be used for the control of ultracold chemical reactions [6], quantum simulation [7], and quantum computing [8].

In recent years different alkali heteronuclear ground-state molecules have been produced by association of weakly bound dimers and subsequent STIRAP to the ground state. So far, fermionic KRb [5,9], LiNa [10,11], NaK [12,13], and bosonic RbCs [14,15] and NaRb [16,17] have been created in different experiments. Up to now the bosonic molecule $^{23}\text{Na}^{39}\text{K}$ has been missing, although it might enable an interesting comparison to its fermionic counterpart, such as the exploration of atom-molecule trimer potential energy surfaces [18] or molecule-molecule collisions in rotational excited states [19]. NaK ground-state molecules have an intrinsic dipole moment of 2.72 D and are known to be chemically stable against two-body exchange reactions [20].

In our experiment we aim for the creation of $^{23}\text{Na}^{39}\text{K}$ ground-state molecules. Therefore, a detailed investigation of weakly bound dimers is mandatory for an efficient ground-state molecule production. Recently, Feshbach resonances and refined molecular potentials for the $^{23}\text{Na} + ^{39}\text{K}$ mixture have been reported and a quantum-degenerate Bose-Bose

mixture has been produced [21,22]. Additionally, to transfer the dimers to the ground state, possible STIRAP pathways have been investigated theoretically [23] and experimentally [24].

Weakly bound Feshbach molecules have mainly been created using two different approaches. First of all, magnetic field ramps have been used mostly in the vicinity of Feshbach resonances with small widths. Second, direct state transfer methods have been implemented mostly in the vicinity of Feshbach resonances with a large width. In this case, the bound molecular state is directly populated starting from a nonresonant scattering channel using radio frequencies, microwave radiation, magnetic field modulation [25], or optical Raman transitions [18,26].

Here we report the formation of weakly bound $^{23}\text{Na}^{39}\text{K}$ dimers from an ultracold mixture of bosonic ^{23}Na and ^{39}K by means of rf association. In our experiment we make use of an up-to-now undetected Feshbach resonance in the $|f = 1, m_f = -1\rangle_{\text{Na}} + |f = 2, m_f = -2\rangle_{\text{K}}$ scattering channel at approximately 196 G. Here f is the hyperfine quantum number and m_f its projection on the magnetic field axis. We locate the Feshbach resonance by magnetic-field-dependent atom-loss spectroscopy. We also measure the binding energy of the involved molecular state and characterize the efficiency of the molecule creation process.

In the following we describe our experimental procedure in Sec. II. Characterization measurements of the Feshbach resonance are summarized in Sec. III. Finally, we discuss the formation of weakly bound dimers and the efficiency of the creation process in Sec. IV.

II. EXPERIMENTAL PROCEDURES

For the presented experiments the atomic mixture is prepared following the procedure described in [21,22]. We start with two precooled atomic beams, the one for ^{23}Na produced by a Zeeman slower and the one for ^{39}K produced by a two-dimensional magneto-optical trap (MOT). Atoms from both beams are captured in a three-dimensional MOT. Afterwards

*torben.alexander@icloud.com

†silke.ospelkaus@iqo.uni-hannover.de

both species are individually molasses cooled before they are optically pumped to the $f = 1$ state and loaded into an optically plugged magnetic quadrupole trap. In the trap ^{23}Na atoms are cooled by forced microwave evaporation. ^{39}K atoms are sympathetically cooled in the bath of ^{23}Na atoms. The cold atomic mixture is loaded from the magnetic trap to a 1064-nm crossed-beam optical dipole trap (cODT). The cODT intensity is increased while the quadrupole field is switched off and a homogeneous magnetic field of about 150 G is applied, yielding favorable inter- and intraspecies scattering lengths. A final optical evaporation step is performed by lowering the intensity in both beams of the cODT. For the experiments both species are cooled to temperatures below $1\ \mu\text{K}$. The atom number ratio between the two species is adjusted by the depth of the magnetic trap evaporation before the mixture is loaded to the cODT. During the sympathetic cooling process the phase-space density of ^{39}K atoms increases and hence three-body losses on ^{39}K occur [27], reducing drastically the atom number. We can vary the atom number ratio $N_{\text{Na}}/N_{\text{K}}$ in the $|f = 1, m_f = -1\rangle_{\text{Na}} + |f = 1, m_f = -1\rangle_{\text{K}}$ channel in the final cODT between 0.3 and 18.

III. FESHBACH RESONANCE IN THE $|1, -1\rangle_{\text{Na}} + |2, -2\rangle_{\text{K}}$ STATE

The newly found Feshbach resonance in the $|1, -1\rangle_{\text{Na}} + |2, -2\rangle_{\text{K}}$ state possesses several advantages for the creation of the weakly bound molecules. For ^{39}K this state is a stretched one which allows for a state-selective imaging of atoms or molecules by utilizing a single laser frequency (see Sec. IV A). In addition, the molecular state can be directly populated using a single rf transfer from a long-lived mixture in the initial $|1, -1\rangle_{\text{Na}} + |1, -1\rangle_{\text{K}}$ state. The transition itself also is relatively insensitive to magnetic field noise [28].

For a successful creation of weakly bound dimers by rf pulses precise knowledge of the involved molecular state is essential. The Feshbach resonance and therefore the molecular state used here have never been observed before. We first investigate the Feshbach resonance by means of atom-loss spectroscopy (see Sec. III A). For the precise determination of the resonance position we perform destructive binding-energy measurements as a function of magnetic field (see Sec. III B).

A. Atom-loss spectroscopy

In the vicinity of Feshbach resonances the atoms experience an increased scattering rate which enhances two- and three-body losses. To determine the position of the Feshbach resonance we use this effect and perform atom-loss spectroscopy. The Feshbach resonance of interest is predicted to be located at a magnetic field of about 196 G in the $|f = 1, m_f = -1\rangle_{\text{Na}} + |f = 2, m_f = -2\rangle_{\text{K}}$ scattering channel [29]. We prepare the atomic mixture as explained above and finally transfer the ^{39}K atoms to the $|f = 2, m_f = -2\rangle_{\text{K}}$ state at 137 G using rapid adiabatic passage (RAP) [21,30]. In this specific case we apply a rf of 256 MHz and sweep the magnetic field by approximately 1 G within 100 ms. At about 137 G the inter- and intraspecies scattering rates for the $^{23}\text{Na} + ^{39}\text{K}$ mixture for all involved

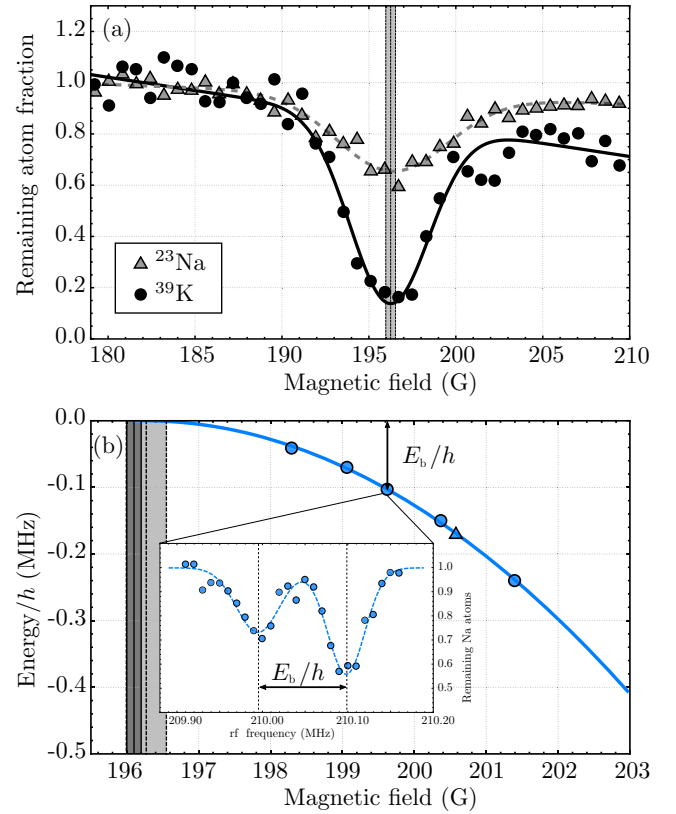


FIG. 1. Feshbach resonance characterization. (a) Atom-loss spectroscopy in the $|f = 1, m_f = -1\rangle_{\text{Na}} + |f = 2, m_f = -2\rangle_{\text{K}}$ channel. The remaining atom fraction of ^{23}Na and ^{39}K for different magnetic field strengths with a holding time of 40 ms. The remaining atom number is normalized to the initial atom number for each species, respectively. Open gray triangles and the dashed gray line refer to the remaining ^{23}Na atom fraction and solid black circles and the solid black line refer to the ^{39}K atom number fraction. The vertical lines and corresponding shaded area indicate the resonance position and the standard deviation obtained from the two Gaussian fits. (b) Binding energy of the weakly bound state as obtained from rf spectroscopy. The continuous blue line is a fit to the destructive measurements (blue circles) according to universal binding energy [Eq. (1)]. The triangle is the binding energy extracted from the constructive signal from Fig. 2. The vertical lines are the resonance position with the standard deviation; dashed lines for the atom-loss measurement in (a), and solid lines for the binding-energy measurement. The inset shows a sample rf scan for a binding energy of $h \times 103\ \text{kHz}$ with a double-Gaussian fit (dashed blue line). The arrows indicate the binding energy. Error bars in both figures are smaller than the plot markers and are not shown.

state combinations are low enough to allow for sufficient long holding time for the RAP [29].

To start atom-loss spectroscopy of the Feshbach resonance, we perform a fast magnetic field ramp to different magnetic field values in the vicinity of the resonance. We hold the mixture at each magnetic field value for 40 ms so that the enhanced scattering rate leads to atom losses. We record the remaining atom number after the hold time resulting in a loss feature as shown in Fig. 1(a). Using a phenomenological Gaussian fit to the data of ^{23}Na and ^{39}K , respectively, we

determine the resonance position to be at 196.27(28) G. The value is in good agreement with predictions obtained from our most recent available NaK ground-state potentials [29].

B. Molecular binding energy

At the position of a Feshbach resonance a molecular state enters from the diatomic continuum into the scattering threshold. As both states are highly coupled close to the Feshbach resonance, the molecular state becomes spectroscopically accessible. To observe the bound state, we perform destructive binding-energy measurements starting from a free diatomic state. We start with the atomic mixture in the $|f = 1, m_f = -1\rangle_{\text{Na}} + |f = 1, m_f = -1\rangle_{\text{K}}$ state (see Sec. II) and apply rf radiation to bridge the energy gap to the resonant $|f = 1, m_f = -1\rangle_{\text{Na}} + |f = 2, m_f = -2\rangle_{\text{K}}$ state and the energetically lower-lying bound molecular state. The rf radiation in this experiment is switched on for 40 ms. This ensures that atoms, which are transferred to the resonant $|f = 2, m_f = -2\rangle_{\text{K}}$ state and which experience a high number of scattering events, are significantly depleted from the trap. The particles transferred to the weakly bound molecular state also experience strong losses (see inset in Fig. 1(b)). The obtained data for different magnetic field strengths is shown in Fig. 1(b). The inset shows an example of a single binding-energy measurement at 199.62 G, where the atom-loss feature (at about 210.1 MHz) serves as a magnetic field calibration and the difference from the molecule-loss feature (at about 210.0 MHz) as binding energy E_b/h . The smaller depth of the loss signal for the molecular transition can be attributed to a weaker coupling between atoms and molecules than between atoms.

Close to the resonance position and on the positive scattering length side of the Feshbach resonance the binding energy $E_b(B)$ can be described by the universal formula

$$E_b(B) = \frac{\hbar^2}{2\mu a(B)^2}, \quad (1)$$

with

$$a(B) = a_{\text{bg}} \left(1 - \frac{\Delta}{B - B_0} \right), \quad (2)$$

where a is the interspecies scattering length, a_{bg} the background scattering length of the entrance channel, and Δ and B_0 the width and position of the Feshbach resonance, respectively. μ is the reduced mass of the molecular system. The solid blue line in Fig. 1(b) is a fit according to Eq. (1). Using a background scattering length of $a_{\text{bg}} = -38.1a_0$, a_0 being the Bohr radius, as obtained from coupled-channel calculation [31], we determine the resonance width to the zero crossing to be $\Delta = 105.8(1.6)$ G and the position to be $B_0 = 196.10(10)$ G, in good agreement with the results from the loss measurement (see Sec. III A).

IV. WEAKLY BOUND DIMERS

With the knowledge of the exact resonance position and molecular binding energy, the molecular state can be selec-

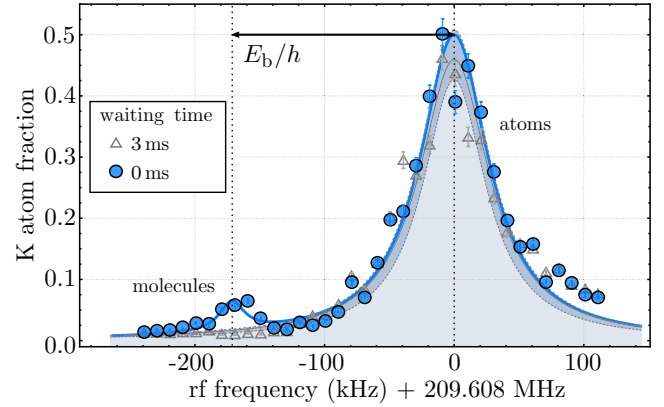


FIG. 2. Constructive molecular signal. ^{39}K atom number as a function of the applied rf radiation. The blue circles are the detected atom number directly after the rf pulse. Fitting a phenomenological double-Lorentzian function (solid blue line) the atomic transition occurs at 209.608(3) MHz, corresponding to a magnetic field of 200.58(3) G. The extracted binding energy is $h \times 171(4)$ kHz, shown as the black arrow. The value is displayed also in Fig. 1(b) as a blue triangle. Open gray triangles are the measured background atoms after an additional waiting time of 3 ms (see text) and the solid gray line with the underlying shaded gray area is a Lorentzian fit with the standard error as a darker shaded area. The atom number is normalized to the total number of ^{39}K atoms. Error bars are the standard deviation and come from different experimental runs.

tively populated by rf radiation. This process requires precisely determined experimental parameters, which are characterized in this section. Also a direct imaging of the molecules is mandatory.

A. Creation process

We start with an atomic mixture in the $|f = 1, m_f = -1\rangle_{\text{Na}} + |f = 1, m_f = -1\rangle_{\text{K}}$ state at a temperature of 500 nK and an atom number ratio of $N_{\text{Na}}/N_{\text{K}} = 3$. Applying a rf pulse we associate molecules immediately followed by a state-selective imaging of the atoms in the $|f = 2, m_f = -2\rangle_{\text{K}}$ state. For this purpose the laser frequency for the ^{39}K imaging is shifted to be on resonance with the $|S_{1/2}, f = 2, m_f = -2\rangle_{\text{K}} \leftrightarrow |P_{3/2}, f = 3, m_f = -3\rangle_{\text{K}}$ transition for a given magnetic field, which is a closed transition from the Zeeman to the Paschen-Back regime and allows high-field imaging of ^{39}K atoms at arbitrary magnetic field values. As long as the molecular binding energy is smaller than the linewidth of the atomic transition, this cycling transition can be used to also image weakly bound dimers.

For molecule creation, we switch on the rf source 75 ms before the actual molecule creation takes place with a frequency detuned by -120 kHz with respect to the molecular transition. We then jump the rf frequency for 0.6 ms to the frequency required for molecule creation followed by a hard switch-off. We found this method to be more reliable and stable than a simple switch on and off, accounting for less disturbance of the rf to our magnetic field stabilization system. We populate selectively the atomic and the molecular states as shown in Fig. 2. Both peaks reveal an asymmetric shape on the

positive frequency side originating from this pulse application technique (see Fig. 2). The creation pulse is followed by ^{39}K imaging as explained above. With this method molecule creation efficiency can be as high as 6% at a binding energy of $E_b = h \times 100$ kHz. For smaller binding energies the atomic and molecular peaks start to overlap. In this case it is not possible to prepare pure samples of bound dimers and distinguish them from free atoms in a single experimental cycle. In a separated experimental cycle we introduce a waiting time of 3 ms between molecule creation and imaging to distinguish the short-living molecules from atoms (see triangle symbols in Fig. 2).

B. Characterization and optimization

For an efficient molecule association the duration of the rf pulse as well as the atom number ratio between ^{23}Na and ^{39}K is critical.

The dependence on the pulse duration is shown in Fig. 3(a). The maximum appears when the molecule creation is overcome by losses of the molecules due to collisions with atoms. The dynamic is modeled by a set of three differential equations for the time-dependent populations N_{mol} , N_{Na} , and N_{K} :

$$\begin{aligned} \frac{dN_{\text{mol}}}{dt} &= k_{\text{mol}} g_{\text{Na,K}} N_{\text{Na}} N_{\text{K}} \\ &\quad - k_a (g_{\text{Na,mol}} N_{\text{Na}} + g_{\text{K,mol}} N_{\text{K}}) N_{\text{mol}} \\ \frac{dN_{\text{Na}}}{dt} &= -k_{\text{mol}} g_{\text{Na,K}} N_{\text{Na}} N_{\text{K}} - k_a g_{\text{Na,mol}} N_{\text{Na}} N_{\text{mol}} \\ \frac{dN_{\text{K}}}{dt} &= -k_{\text{mol}} g_{\text{Na,K}} N_{\text{Na}} N_{\text{K}} - k_a g_{\text{K,mol}} N_{\text{K}} N_{\text{mol}}, \end{aligned} \quad (3)$$

where N_{mol} , N_{Na} , and N_{K} are the particle numbers for molecules, ^{23}Na atoms, and ^{39}K atoms, respectively; $g_{i,j}$ is the two-body overlap integral [32]; and k_{mol} is the molecular creation coefficient and k_a the loss coefficient for atom-molecule collisions. The loss coefficient k_a is set equal for the case of a colliding molecule either with a ^{23}Na atom or a ^{39}K atom. Collisions between molecules are excluded from the model as they are expected to be negligibly small. The solid line in Fig. 3(a) shows a fit using the rate model system [Eqs. (3)] with k_{mol} and k_a as free parameters. According to the fit, $k_{\text{mol}} = 1.18(16) \times 10^{-9} \text{ cm}^3 \text{ s}^{-1}$ and $k_a = 4.54(45) \times 10^{-9} \text{ cm}^3 \text{ s}^{-1}$. The maximal creation efficiency is found at a pulse duration of about $350 \mu\text{s}$. By accounting for the initial atom numbers the loss rate obtained from the second line in Eq. (3) is $k_a (g_{\text{Na,mol}} N_{\text{Na}}(0) + g_{\text{K,mol}} N_{\text{K}}(0))$, corresponding to a calculated lifetime of $184(23) \mu\text{s}$.

We have also measured the molecule formation efficiency as a function of the atom number ratio. We find the highest efficiency at $N_{\text{Na}}/N_{\text{K}} \approx 3$ (see Fig. 3(b)). We use the parameter from the fit in Fig. 3(a) and the specific atom number ratios and total atom number for each experimental data point to calculate the maximal associated molecule fraction. The results are plotted as bars in Fig. 3(b) for a direct comparison to the experimental data. Despite the model not accounting for temperature effects such as antievaporation or temperature disequilibrium, the predictions are in good agreement with the observed dependence on the atom number ratio.

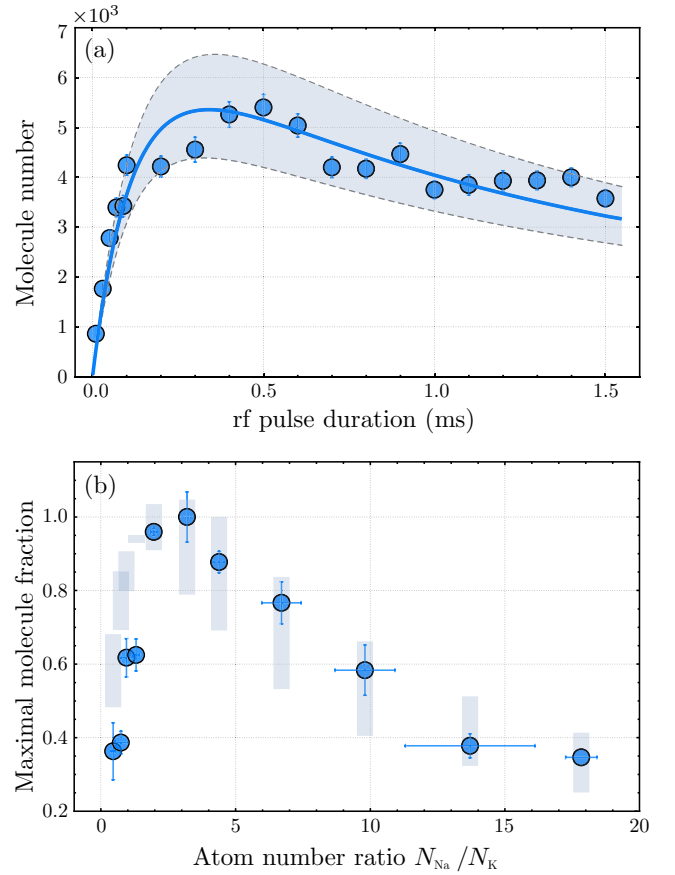


FIG. 3. Characterization of the association process. (a) The molecule number is plotted as a function of the rf pulse duration. The molecules are imaged directly after switching off the rf. The best creation efficiency is reached at a pulse duration around $350 \mu\text{s}$. The solid blue line is the fit modeled with the set of differential equations [Eqs. (3)]. The dashed lines with the enclosed shaded area refer to the fit uncertainties. (b) Normalized molecule number as function of the atom number ratio at a creation time of $500 \mu\text{s}$. The bars represent the predictions from the fit results in (a) taking the individual starting conditions for each point as well as the fit uncertainties into account. The normalization is done according to the maximal created molecule number. Error bars in both figures are the standard deviation and come from different experimental runs.

C. Molecule lifetime

We measure the lifetime for molecules immersed in the bath of residual atoms. This measurement is done by introducing a hold time between the rf pulse and the imaging. Figure 4 shows a typical measurement. For this experiment the creation pulse duration is set to $500 \mu\text{s}$. During the hold time the rf is set back to the offset detuning to stop molecule creation during the hold time. Using the model from Eq. (3), we determine a lifetime of $299(17) \mu\text{s}$, which differs from the one obtained in Sec. IV B. We suggest that the observed difference in lifetime originates from the presence of the resonant rf radiation. For the off-resonant case in Sec. IV C we do not see a difference with or without applied rf. The model from Eqs. (3) does

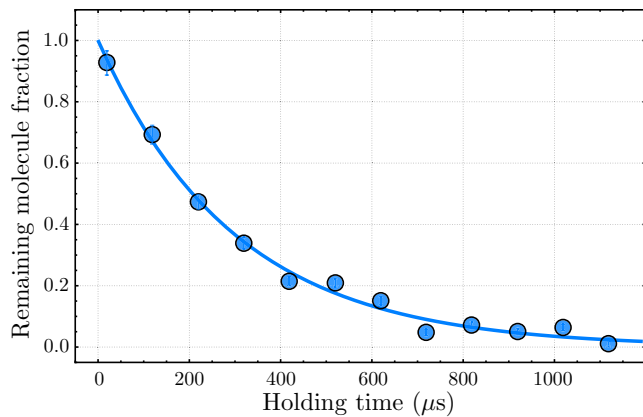


FIG. 4. Lifetime measurement of the molecules in the cODT. The molecule number is normalized to the value of zero waiting time. For this measurement ^{23}Na and ^{39}K atoms are not removed. A fit to the data (solid line) results in a lifetime of $\tau = 299(17) \mu\text{s}$. Error bars are the standard deviation and come from different experimental runs.

not elucidate or account for the pulse shape and frequency detuning of the rf.

A lifetime of several hundred microseconds is sufficient for subsequent STIRAP transfer of the Feshbach molecules to the molecular ground state, which takes typically 10–20 μs [33,34].

V. CONCLUSION AND OUTLOOK

In summary we have investigated a Feshbach resonance for the bosonic $^{23}\text{Na} + ^{39}\text{K}$ mixture in the $|f = 1, m_f = -1\rangle_{\text{Na}} + |f = 2, m_f = -2\rangle_{\text{K}}$ channel around 196 G. We located the Feshbach resonance using atom-loss spectroscopy as well as destructive binding-energy measurements on the bound molecular state. By applying rf pulses we have been able to populate the bound molecular state and distinguish the dimers from free atoms. We have further characterized and optimized the Feshbach molecule creation efficiency with respect to rf pulse duration and atom number ratio. We have been able to create up to 6000 weakly bound molecules per experimental cycle. The lifetime of the dimers in the presence of background atoms is about 0.3 ms, which is sufficiently long to perform a STIRAP transfer. These dimers serve as an ideal starting point for efficient creation of so far unobserved ultracold chemically stable bosonic $^{23}\text{Na}^{39}\text{K}$ molecules in their absolute electronic and rovibrational ground state.

ACKNOWLEDGMENTS

We thank E. Tiemann for enlightening discussions and theory support. We gratefully acknowledge financial support from the European Research Council through ERC Starting Grant POLAR and from the Deutsche Forschungsgemeinschaft (DFG) through CRC 1227 (DQ-mat), project A03, and FOR 2247, project E5. K.K.V. and P.G. thank the DFG for financial support through Research Training Group 1991.

- [1] C. Chin, M. Bartenstein, A. Altmeyer, S. Riedl, S. Jochim, J. H. Denschlag, and R. Grimm, Observation of the pairing gap in a strongly interacting Fermi gas, *Science* **305**, 1128 (2004).
- [2] C. A. Regal, M. Greiner, and D. S. Jin, Observation of Resonance Condensation of Fermionic Atom Pairs, *Phys. Rev. Lett.* **92**, 040403 (2004).
- [3] T. Kraemer, M. Mark, P. Waldburger, J. G. Danzl, C. Chin, B. Engeser, A. D. Lange, K. Pilch, A. Jaakkola, H.-C. Nägerl, and R. Grimm, Evidence for Efimov quantum states in an ultracold gas of caesium atoms, *Nature (London)* **440**, 345 (2006).
- [4] J. Rui, H. Yang, L. Liu, D.-C. Zhang, Y.-X. Liu, J. Nan, Y.-A. Chen, B. Zhao, and J.-W. Pan, Controlled state-to-state atom-exchange reaction in an ultracold atom-dimer mixture, *Nat. Phys.* **13**, 699 (2017).
- [5] K.-K. Ni, S. Ospelkaus, M. H. G. de Miranda, A. Peer, B. Neyenhuis, J. J. Zirbel, S. Kotochigova, P. S. Julienne, D. S. Jin, and J. Ye, A high phase-space-density gas of polar molecules, *Science* **322**, 231 (2008).
- [6] S. Ospelkaus, K.-K. Ni, D. Wang, M. H. G. de Miranda, B. Neyenhuis, G. Quemener, P. S. Julienne, J. L. Bohn, D. S. Jin, and J. Ye, Quantum-state controlled chemical reactions of ultracold potassium-rubidium molecules, *Science* **327**, 853 (2010).
- [7] B. Yan, S. Moses, B. Gadway, J. Covey, K. Hazzard, A. Rey, D. Jin, and J. Ye, Observation of dipolar spin-exchange interactions with lattice-confined polar molecules, *Nature (London)* **501**, 521 (2013).
- [8] D. DeMille, Quantum Computation with Trapped Polar Molecules, *Phys. Rev. Lett.* **88**, 067901 (2002).
- [9] C. Ospelkaus, S. Ospelkaus, L. Humbert, P. Ernst, K. Sengstock, and K. Bongs, Ultracold Heteronuclear Molecules in a 3D Optical Lattice, *Phys. Rev. Lett.* **97**, 120402 (2006).
- [10] M.-S. Heo, T. T. Wang, C. A. Christensen, T. M. Rvachov, D. A. Cotta, J.-H. Choi, Y.-R. Lee, and W. Ketterle, Formation of ultracold fermionic NaLi Feshbach molecules, *Phys. Rev. A* **86**, 021602(R) (2012).
- [11] T. M. Rvachov, H. Son, A. T. Sommer, S. Ebadi, J. J. Park, M. W. Zwierlein, W. Ketterle, and A. O. Jamison, Long-Lived Ultracold Molecules with Electric and Magnetic Dipole Moments, *Phys. Rev. Lett.* **119**, 143001 (2017).
- [12] C.-H. Wu, J. W. Park, P. Ahmadi, S. Will, and M. W. Zwierlein, Ultracold Fermionic Feshbach Molecules of $^{23}\text{Na}^{40}\text{K}$, *Phys. Rev. Lett.* **109**, 085301 (2012).
- [13] J. W. Park, S. A. Will, and M. W. Zwierlein, Ultracold Dipolar Gas of Fermionic $^{23}\text{Na}^{40}\text{K}$ Molecules in Their Absolute Ground State, *Phys. Rev. Lett.* **114**, 205302 (2015).
- [14] T. Takekoshi, M. Debatin, R. Rameshan, F. Ferlaino, R. Grimm, H.-C. Nägerl, C. R. Le Sueur, J. M. Hutson, P. S. Julienne, S. Kotochigova, and E. Tiemann, Towards the production of ultracold ground-state RbCs molecules: Feshbach resonances, weakly bound states, and the coupled-channel model, *Phys. Rev. A* **85**, 032506 (2012).
- [15] T. Takekoshi, L. Reichsöllner, A. Schindewolf, J. M. Hutson, C. R. Le Sueur, O. Dulieu, F. Ferlaino, R. Grimm, and H.-C. Nägerl, Ultracold Dense Samples of Dipolar RbCs Molecules in the Rovibrational and Hyperfine Ground State, *Phys. Rev. Lett.* **113**, 205301 (2014).

- [16] F. Wang, X. He, X. Li, B. Zhu, J. Chen, and D. Wang, Formation of ultracold NaRb Feshbach molecules, *New J. Phys.* **17**, 035003 (2015).
- [17] M. Guo, B. Zhu, B. Lu, X. Ye, F. Wang, R. Vexiau, N. Bouloufa-Maafa, G. Quémener, O. Dulieu, and D. Wang, Creation of an Ultracold Gas of Ground-State Dipolar $^{23}\text{Na}^{87}\text{Rb}$ Molecules, *Phys. Rev. Lett.* **116**, 205303 (2016).
- [18] H. Yang, D.-C. Zhang, L. Liu, Y.-X. Liu, J. Nan, B. Zhao, and J.-W. Pan, Observation of magnetically tunable Feshbach resonances in ultracold $^{23}\text{Na}^{40}\text{K} + ^{40}\text{K}$ collisions, *Science* **363**, 261 (2019).
- [19] S. A. Will, J. W. Park, Z. Z. Yan, H. Loh, and M. W. Zwierlein, Coherent Microwave Control of Ultracold $^{23}\text{Na}^{40}\text{K}$ Molecules, *Phys. Rev. Lett.* **116**, 225306 (2016).
- [20] P. S. Zuchowski and J. M. Hutson, Reactions of ultracold alkali-metal dimers, *Phys. Rev. A* **81**, 060703(R) (2010).
- [21] T. Hartmann, T. A. Schulze, K. K. Voges, P. Gersema, M. W. Gempel, E. Tiemann, A. Zenesini, and S. Ospelkaus, Feshbach resonances in $^{23}\text{Na} + ^{39}\text{K}$ mixtures and refined molecular potentials for the NaK molecule, *Phys. Rev. A* **99**, 032711 (2019).
- [22] T. A. Schulze, T. Hartmann, K. K. Voges, M. W. Gempel, E. Tiemann, A. Zenesini, and S. Ospelkaus, Feshbach spectroscopy and dual-species Bose-Einstein condensation of ^{23}Na - ^{39}K mixtures, *Phys. Rev. A* **97**, 023623 (2018).
- [23] T. A. Schulze, I. I. Temelkov, M. W. Gempel, T. Hartmann, H. Knöckel, S. Ospelkaus, and E. Tiemann, Multichannel modeling and two-photon coherent transfer paths in NaK, *Phys. Rev. A* **88**, 023401 (2013).
- [24] K. K. Voges, P. Gersema, T. Hartmann, T. A. Schulze, E. Tiemann, S. Ospelkaus, and A. Zenesini, A pathway to ultracold bosonic $^{23}\text{Na}^{39}\text{K}$ ground state molecules, *New J. Phys.* **21**, 123034 (2019).
- [25] C. Chin, R. Grimm, P. Julienne, and E. Tiesinga, Feshbach resonances in ultracold gases, *Rev. Mod. Phys.* **82**, 1225 (2010).
- [26] Z. Fu, L. Huang, Z. Meng, P. Wang, L. Zhang, S. Zhang, H. Zhai, P. Zhang, and J. Zhang, Production of Feshbach molecules induced by spin-orbit coupling in Fermi gases, *Nat. Phys.* **10**, 110 (2014).
- [27] T. A. Schulze, Quantum degenerate mixtures of ^{23}Na - ^{39}K and coherent transfer paths in NaK molecules, Ph.D. thesis, Leibniz Universität Hannover, 2018.
- [28] The magnetic field stability in our experimental setup is about 20 mG. For the transition in ^{39}K at 200 G this corresponds to a stability of 10 kHz.
- [29] T. Hartmann, An experiment apparatus for the production of ultracold bosonic dipolar ground state $^{23}\text{Na}^{39}\text{K}$ molecules and Feshbach spectroscopy in a cold mixture of ^{23}Na and ^{39}K , Ph.D. thesis, Leibniz Universität Hannover, 2018.
- [30] J. C. Camparo and R. P. Frueholz, A dressed atom interpretation of adiabatic rapid passage, *J. Phys. B* **17**, 4169 (1984).
- [31] E. Tiemann (private communication).
- [32] For calculating the two-body overlap integral we use the equation $g_{i,j} = \frac{1}{N_i N_j} \int_V n_i n_j dV$, where i and j denote the atom species or molecules and V the volume. We assume the densities n follow a Gaussian distribution.
- [33] N. V. Vitanov, A. A. Rangelov, B. W. Shore, and K. Bergmann, Stimulated Raman adiabatic passage in physics, chemistry, and beyond, *Rev. Mod. Phys.* **89**, 015006 (2017).
- [34] Removing residual atoms before applying the STIRAP is not feasible in our system as any removal would take longer than the molecule lifetime would allow for, resulting in a drastic decrease of the number of ground-state molecules.

4 From Feshbach molecules to ground-state molecules

This chapter summarizes our successful experimental endeavour to prepare rovibronic ground state polar molecules. Starting from Feshbach molecules a two-photon transfer scheme is worked out to convert an ensemble of Feshbach molecules into rovibronic ground state molecules [A4]. Finally we report on the successful creation of these molecules [A5].

4.1 A pathway to ultracold bosonic $^{23}\text{Na}^{39}\text{K}$ ground state molecules [A4]

In this section, a STIRAP is prepared by identifying a pathway to the $^{23}\text{Na}^{39}\text{K}$ ground state through spectroscopic studies.

In attempting to populate the absolute ground state, two major problems must be addressed. These also explain why a two-photon process, as depicted in Fig.4.1, is needed instead of a single transition to the ground state.

For all bialkali molecules, the absolute ground state is a singlet state, the $X^1\Sigma^+$ manifold. The weakly bound Feshbach molecules exist mainly in a highly vibrationally excited state of the $a^3\Sigma^+$ manifold and are therefore triplet dominated. As there are no allowed dipole transitions between singlet and triplet states, the intermediate level needs to act as a bridge with singlet and triplet character. Triplet and singlet states couple through spin-orbit interactions. These are quite weak, on the order of a few GHz. Therefore two intermediate states, a singlet and a triplet state, need to be found with an unperturbed energy spacing of the same order.

The other problem arises from the large size of the Feshbach molecule, which can be on the order of 10000 Bohr radii, in comparison to the ground-state molecules with just a few Bohr radii in size [96]. Although there are no selection rules regarding the change of the vibrational quantum number v , a direct coupling of these two states is very weak, due to a small wavefunction overlap $\langle f|i\rangle$, with $|f\rangle$ the wavefunction of the ground state and $|i\rangle$ of the Feshbach state. This is called the Franck-Condon principle that can also be visualized. During an electronic transition, the nuclear spacing R remains almost the same as the atomic nuclei are very inert compared to the electron. For this reason, transitions are preferred where the wavefunctions of the initial and final states have a significant amplitude at the same nuclear distance. Hence, the intermediate wavefunction $|e\rangle$ needs

to have a sufficient overlap with the initial and final state. The Franck-Condon principle is therefore also the reason, why in a first step weakly bound molecules are prepared. This drastically increases the wavefunction overlap with the intermediate state $|e\rangle$, compared to two unbound atoms.

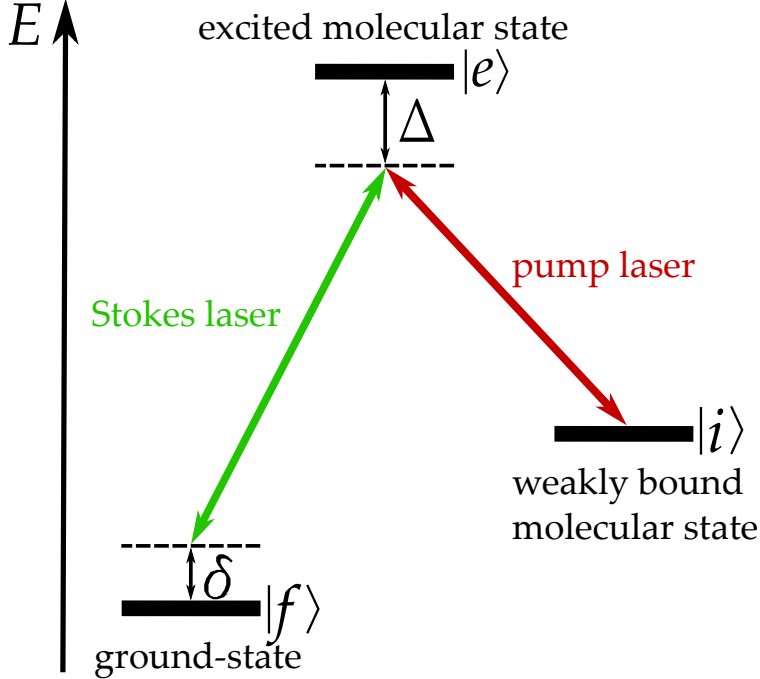


Figure 4.1: Schematic of a two-photon transfer, starting from the initial weakly bound molecular state $|i\rangle$, with an intermediate excited molecular state $|e\rangle$, acting as a bridge to the final ground state $|f\rangle$. The pump laser couples the initial state $|i\rangle$ with the state $|e\rangle$, while the Stokes laser couples $|e\rangle$ with $|f\rangle$. $\Delta = \frac{1}{\hbar}(E_{|e\rangle} - E_{|i\rangle}) - \omega_{\text{pump}}$ denotes the one-photon detuning and $\delta = \frac{1}{\hbar}(E_{|e\rangle} - E_{|f\rangle}) - \omega_{\text{Stokes}} - \Delta$ the two-photon detuning, with $\omega_{\text{pump/Stokes}}$ the carrier frequencies of the respective pump and Stokes laser and $E_{|i\rangle,|e\rangle,|f\rangle}$ the individual state energies.

From a multichannel modelling of two-photon coherent transfer pathways in NaK [97] and together with spectroscopic data from hot beam experiments [98], two possible intermediate levels were identified, the $|B^1\Pi, v = 8\rangle$ and $|c^3\Sigma^+, v = 30\rangle$ manifolds.

In the following paper, hyperfine resolved spectroscopic measurements of the $|B^1\Pi, v = 8\rangle$ and $|c^3\Sigma^+, v = 30\rangle$ manifolds in an external magnetic field are presented, starting from an ultracold atomic mixture of ^{23}Na and ^{39}K , by identifying atomic loss features. Both atomic species are prepared in the $|F = 1, m_F = -1\rangle$ hyperfine state. Note that, as mentioned, the coupling of the atomic state to the intermediate state $|e\rangle$ is very small. However, the high stability and the possibility for long exposure times by the atomic cloud with the pump laser of up to 1.6 s improves the signal-to-noise ratio and reduces the complexity of the experimental sequence, compared to the production of Feshbach molecules.

In addition, the singlet/triplet mixing of the intermediate levels was deduced and the rovibrational

4.1 A pathway to ultracold bosonic $^{23}\text{Na}^{39}\text{K}$ ground state molecules [A4]

ground state was identified using spectroscopic studies of the Autler-Townes splitting. As the splitting between the dressed states is equal to $\hbar\Omega$, with \hbar the reduced Planck constant and Ω the Rabi frequency, the coupling strength of the Stokes laser could be deduced, which is the coupling of the intermediate level $|e\rangle$ to the ground state $|f\rangle$.

Copyright © 2022 The Author(s), Originally published by IOP Publishing Ltd on behalf of the Institute of Physics and Deutsche Physikalische Gesellschaft, CC BY 3.0.

DOI <https://doi.org/10.1088/1367-2630/ab5f31>

PAPER • OPEN ACCESS

A pathway to ultracold bosonic $^{23}\text{Na}^{39}\text{K}$ ground state molecules

To cite this article: Kai K Voges *et al* 2019 *New J. Phys.* **21** 123034

View the [article online](#) for updates and enhancements.

You may also like

- [Effects of Pure Dzyaloshinskii–Moriya Interaction with Magnetic Field on Entanglement in Intrinsic Decoherence](#)
Da-Chuang Li, , Xian-Ping Wang et al.
- [Atomistic modeling of dislocation interactions with twin boundaries in Ti](#)
M S Hooshmand, M J Mills and M Ghazisaeidi
- [Anisotropic elastic properties and ideal uniaxial compressive strength of \$\text{TiB}_2\$ from first principles calculations](#)
Min Sun, , Chong-Yu Wang et al.



PAPER

A pathway to ultracold bosonic $^{23}\text{Na}^{39}\text{K}$ ground state molecules

OPEN ACCESS

RECEIVED

9 September 2019

REVISED

27 November 2019

ACCEPTED FOR PUBLICATION

5 December 2019

PUBLISHED

17 December 2019

Original content from this work may be used under the terms of the [Creative Commons Attribution 3.0 licence](#).

Any further distribution of this work must maintain attribution to the author(s) and the title of the work, journal citation and DOI.



Kai K Voges, Philipp Gersema, Torsten Hartmann, Torben A Schulze, Alessandro Zenesini and Silke Ospelkaus

Institut für Quantenoptik, Leibniz Universität Hannover, D-30167 Hannover, Germany

E-mail: silke.ospelkaus@iqo.uni-hannover.de

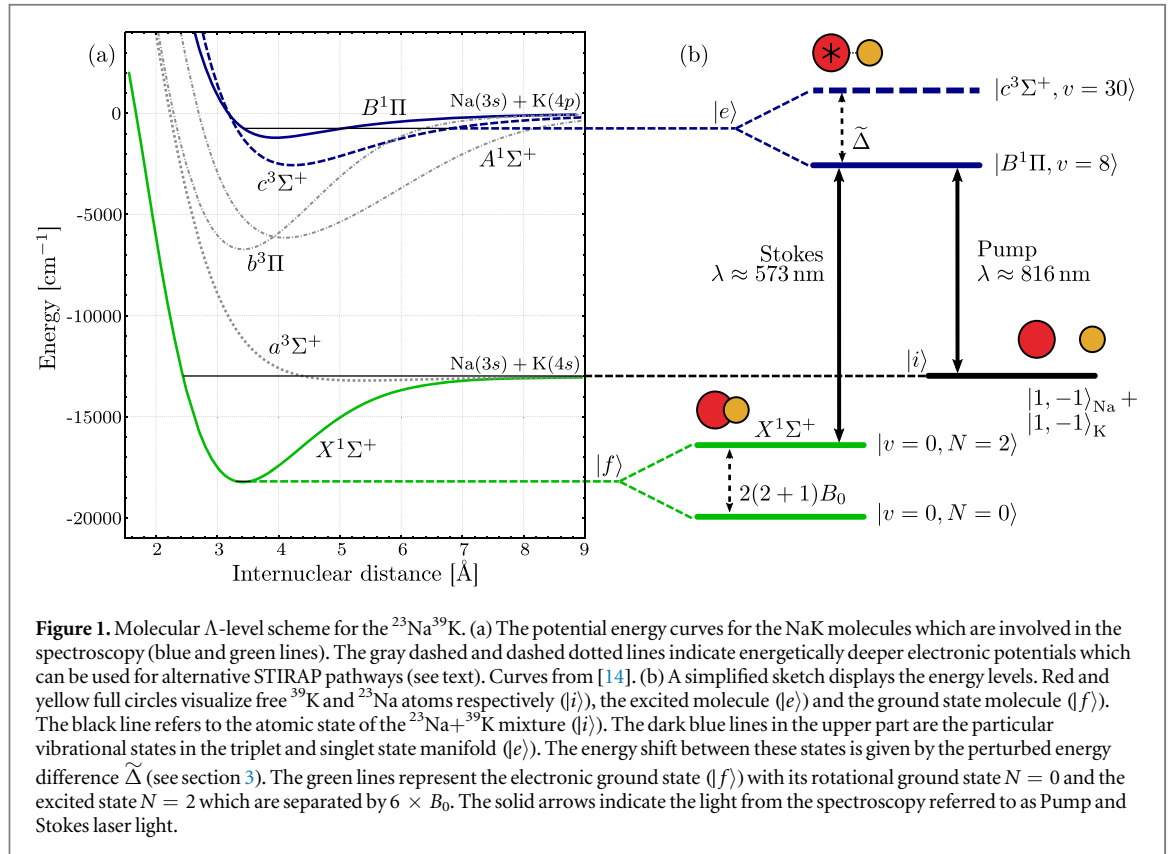
Keywords: STIRAP, molecular spectroscopy, ultracold polar molecules, bosonic quantum gases

Abstract

We spectroscopically investigate a pathway for the conversion of $^{23}\text{Na}^{39}\text{K}$ Feshbach molecules into rovibronic ground state molecules via stimulated Raman adiabatic passage. Using photoassociation spectroscopy from the diatomic scattering threshold in the $a^3\Sigma^+$ potential, we locate the resonantly mixed electronically excited intermediate states $|B^1\Pi, \nu = 8\rangle$ and $|c^3\Sigma^+, \nu = 30\rangle$ which, due to their singlet–triplet admixture, serve as an ideal bridge between predominantly $a^3\Sigma^+$ Feshbach molecules and pure $X^1\Sigma^+$ ground state molecules. We investigate their hyperfine structure and present a simple model to determine the singlet–triplet coupling of these states. Using Autler–Townes spectroscopy, we locate the rovibronic ground state of the $^{23}\text{Na}^{39}\text{K}$ molecule ($|X^1\Sigma^+, \nu = 0, N = 0\rangle$) and the second rotationally excited state $N = 2$ to unambiguously identify the ground state. We also extract the effective transition dipole moment from the excited to the ground state. Our investigations result in a fully characterized scheme for the creation of ultracold bosonic $^{23}\text{Na}^{39}\text{K}$ ground state molecules.

1. Introduction

Quantum gases of ultracold polar molecules offer unprecedented novel opportunities for the investigation of dipolar collisions, quantum chemical processes and quantum many-body systems [1–5]. The new handle in comparison to atomic systems is given by the electric dipole moment of heteronuclear diatomic ground state molecules. The most successful approach to the creation of ultracold ensembles of polar ground state molecules is based on the association of two chemically different ultracold atomic alkali species. This process starts with magneto-association to weakly bound Feshbach molecules and continues with the coherent transfer of the weakly bound molecules to the rovibrational ground state of polar molecules using a STImulated Raman Adiabatic Passage (STIRAP) [6]. For the transfer from the initially magneto-associated molecular state $|i\rangle$ to the final molecular ground state $|f\rangle$, the STIRAP transfer consists of an adiabatic change of the dressed state composition by involving two coherent laser beams referred to as Pump and Stokes laser. The Pump laser couples $|i\rangle$ to a third excited state $|e\rangle$, the Stokes laser $|f\rangle$ to $|e\rangle$, resulting in a typical Λ -level scheme; see figure 1. During the time evolution the intermediate state $|e\rangle$ is not populated and therefore does not contribute to incoherent molecule losses due to spontaneous decay. In the case of bi-alkali molecules, the coupling between $|i\rangle/|f\rangle$ and $|e\rangle$ is governed by the Franck–Condon overlap, the singlet–triplet fraction and the hyperfine composition of the states. For bi-alkali heteronuclear molecules the ground state $|f\rangle$ always belongs to the $X^1\Sigma^+$ potential while a weakly bound dimer state $|i\rangle$ exists mainly in the $a^3\Sigma^+$ potential; see figure 1(a). To act as an efficient coupling bridge, the choice of $|e\rangle$ is crucial. It needs to be chosen to couple well to the initial triplet as well as to the final singlet state. This can be achieved through the careful choice of mixed states in the $^3\Pi/{}^1\Sigma^+$ or $^3\Sigma^+/{}^1\Pi$ potentials; see figure 1(a). Up to now, the production of trapped ground state molecules, either fermionic, such as $^{40}\text{K}^{87}\text{Rb}$ [7], $^{23}\text{Na}^{40}\text{K}$ [8] and $^6\text{Li}^{23}\text{Na}$ [9], or bosonic, such as $^{87}\text{Rb}^{133}\text{Cs}$ [10, 11] and $^{23}\text{Na}^{87}\text{Rb}$ [12] has been reported. NaRb [12] and RbCs [10, 11] ground state molecules have been prepared by using coupled states in the $A^1\Sigma^+$ and $b^3\Pi$ potentials. KRb [7] and fermionic $^{23}\text{Na}^{40}\text{K}$ [8] ground state molecules have been created using states in the $c^3\Sigma^+$ and $B^1\Pi$ potentials. Additionally, ground state molecules for fermionic $^{23}\text{Na}^{40}\text{K}$ have been created using excited states in energetically higher $D^1\Pi$ and $d^3\Pi$ potentials [13]; not shown in figure 1(a).



In the case of $^{23}\text{Na}^{39}\text{K}$, suitable transitions for the creation of ground state molecules have so far only been investigated experimentally in hot beam experiments accessing rotational states with $N \geq 6$ [15]. Moreover, the work [15] does not include hyperfine structure and offset magnetic fields. In addition, previous theory work [16] describes a complete spectrum involving spin–orbit, Coriolis and spin–rotation interactions as well as Franck–Condon factors identifying promising singlet–triplet mixed states. However, the hyperfine structure still remains untreated although it is crucial for a successful STIRAP transfer [13]. In this paper, we present hyperfine resolved spectroscopic investigations of the $^{23}\text{Na}^{39}\text{K}$ molecule at bias magnetic fields for strongly mixed states known from [15, 16].

Using one-photon association spectroscopy, we first locate and characterize the strongly mixed $|B^1\Pi, \nu = 8\rangle$ and $|c^3\Sigma^+, \nu = 30\rangle$ states serving as a bridge between the $a^3\Sigma^+$ and $X^1\Sigma^+$ potentials. A large Zeeman splitting at 150 G enables us to perform hyperfine resolved optical spectroscopy of the excited molecular state manifold. We present a simple model to determine the singlet–triplet admixtures of the excited states. Furthermore, we perform two-photon Autler–Townes spectroscopy [17] to locate the rovibronic ground state, determine the rotational constants and extract effective dipole transition matrix elements from our measurements. Thus, we present and fully characterize a pathway for the creation of rovibronic ($\nu = 0, N = 0$) $^{23}\text{Na}^{39}\text{K}$ ground state molecules for the first time.

In the following, we give an outline of the experimental setup and procedures; see section 2. In section 3.1 we present the model fit for the coupled excited states, and in section 3.2 we detail the spectroscopic one-photon measurements. This is followed by the two-photon ground state spectroscopy which includes the determination of the rotational constant and the transition dipole element of the Stokes transition in section 4.

2. Experimental setup and procedures

The spectroscopic studies presented in this work are based on the preparation of an ultracold mixture of $^{23}\text{Na}+^{39}\text{K}$. A description of the experimental setup can be found in [16, 18, 19]. Details of the experimental procedure can be found in [20, 21]. In the following, we briefly summarize the main experimental steps. First, ^{23}Na and ^{39}K atoms are loaded into a two-color magneto-optical trap, followed by simultaneous molasses cooling of both species. The atoms are optically pumped to the $F = 1$ manifold and loaded into an optically plugged magnetic quadrupole trap, where forced microwave evaporative cooling of ^{23}Na is performed. ^{39}K atoms are sympathetically cooled by ^{23}Na . After both atomic species are transferred into a 1064 nm crossed-beam optical dipole trap (cODT), a homogeneous magnetic field of 150 G is applied to ensure favorable scattering properties in the mixture [20]. The atoms are

prepared in the $|f = 1, m_f = -1\rangle_{\text{Na}} + |f = 1, m_f = -1\rangle_{\text{K}}$ states. Then, forced optical evaporation is performed on both species by lowering the intensity of both beams of the cODT. The forced evaporation process is stopped when the atomic sample has a temperature of about $1 \mu\text{K}$ and a corresponding phase space density ≤ 0.1 for both species. To decrease the differential gravitational sag and assure a significant overlap of the two clouds, the cODT intensity is ramped up again. For the spectroscopy presented in this work, the magnetic field is either set to 130 G or left at 150 G yielding values at which the inter and intra species scattering properties allow for a long lifetime of the sample by minimizing three-body losses. This allows for a sufficiently long interaction time during photoassociation experiments, as required by the expected weak coupling between the atom pair at the scattering threshold and the electronically excited state molecules. The laser light for the Pump and the Stokes transitions at 816 nm and 573 nm respectively is generated by diode laser systems. The 816 nm light is generated by a commercial external-cavity diode laser (ECDL). The generation of the 573 nm light starts from a commercial ECDL operating at 1146 nm. The light is amplified by a tapered amplifier and subsequently frequency doubled in a self-built resonant bow-tie doubling cavity. Both lasers are locked to a commercial ultra-low expansion (ULE) glass cavity by using the Pound–Drever–Hall technique [22]. A sideband locking scheme involving widely tunable electro-optical modulators ensure the tunability of both locked lasers within the free spectral range of the ULE cavity which is 1.499 GHz. The finesse of the ULE cavity is 24 900 and 37 400 for 816 nm and 1146 nm light, respectively. The laser system setup is similar to the one described in [23].

Optical fibers spatially filter the light and ensure high quality beam properties. The polarization is set by a half-wave plate for each wavelength. The foci of the two beams on the atoms are adjusted to $1/e^2$ -beam waists of $35 \mu\text{m}$ for the Pump laser and $40 \mu\text{m}$ for the Stokes laser. The maximum laser power is 25 mW for each laser. With the Pump beam at full power, the Stokes beam is reduced to ≤ 10 mW to avoid a depletion of ^{23}Na atoms in the trap center, originating from a strong repulsive dipole force. The beams are geometrically superimposed and orientated perpendicularly to the applied magnetic field.

3. Excited state spectroscopy

3.1. Local model for the excited state manifold

In our experiment, we are specifically interested in a detailed understanding of the previously located [15] strongly mixed $|B^1\Pi, \nu = 8\rangle$ and $|c^3\Sigma^+, \nu = 30\rangle$ states. Hyperfine splitting and spin–orbit coupling for these two states can be modeled by a simple two-manifold coupled system, when neglecting contributions from other vibrational and rotational levels, from nucleus–nucleus interaction and nucleus–rotation coupling. This allows us to treat the two state manifolds separately in the following spectrally local model.

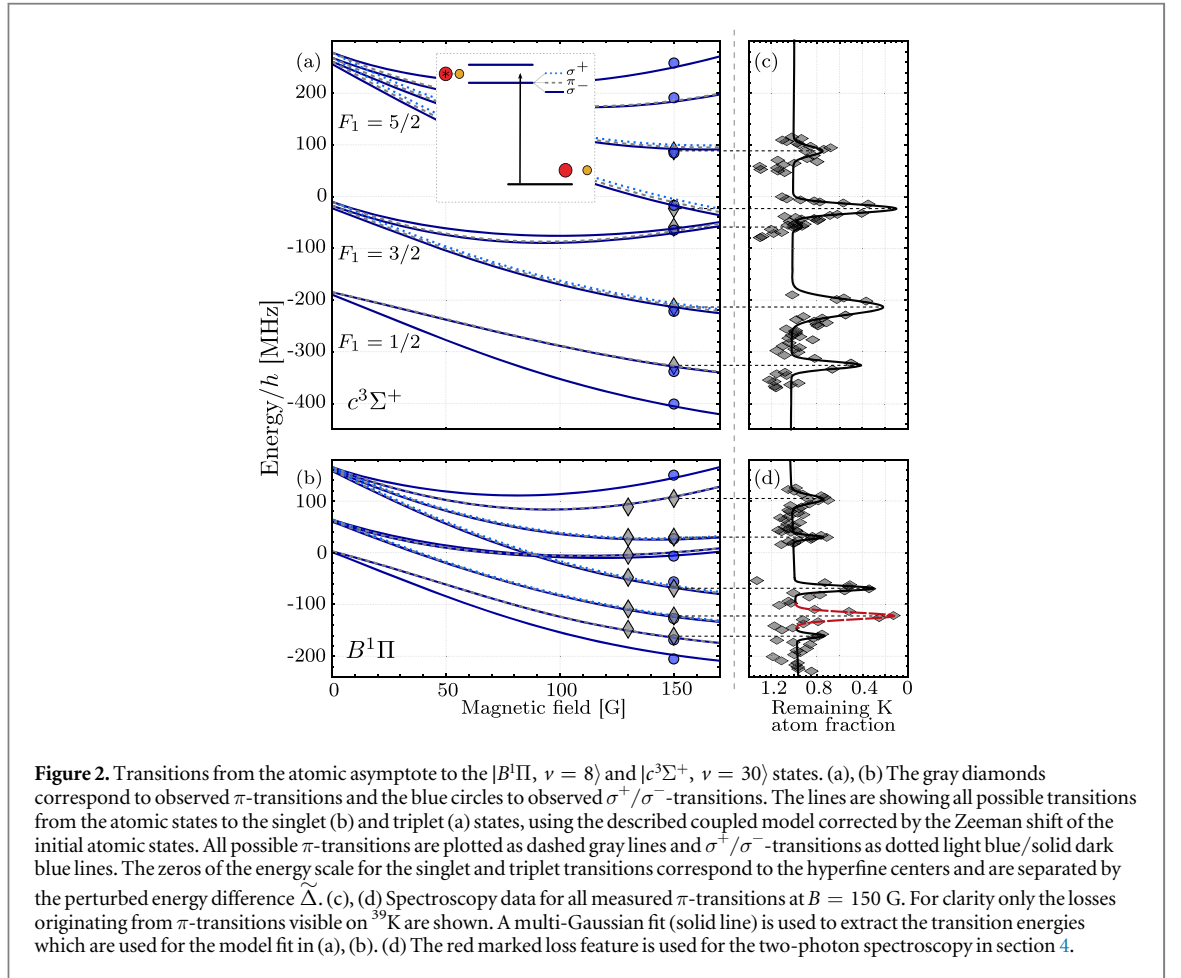
The excited state can be described by Hund’s case (a) and that allows to consider the total angular momentum $J = 1$ as resulting from the coupling of the rotational angular momentum \vec{N} and the spin \vec{S} [24]. ^{23}Na and ^{39}K nuclear spins are $i_{\text{Na}} = i_{\text{K}} = 3/2$ leading to $3 \times 4 \times 4 = 48$ different states in the singlet and triplet channel.

In absence of coupling the Hamiltonians for the investigated states, in the basis of $|B/c, J, m_j, i_{\text{Na}}, m_{i_{\text{Na}}}, i_{\text{K}}, m_{i_{\text{K}}}\rangle$, reads as [25]

$$H^B = \mu_0 g_J^B \vec{J} \cdot \vec{B} \quad (1)$$

$$H^c = \Delta + \vec{J} \cdot (A_{\text{K}} \vec{i}_{\text{K}} + A_{\text{Na}} \vec{i}_{\text{Na}}) + \mu_0 g_J^c \vec{J} \cdot \vec{B}, \quad (2)$$

where A_{K} and A_{Na} are the hyperfine constants, μ_0 the Bohr magneton and \vec{B} the applied magnetic field. The energy Δ corresponds to the unperturbed energy difference between the two states and we neglect the hyperfine term for the singlet state. The ^{23}Na hyperfine coupling A_{Na} is almost two orders of magnitude larger than A_{K} and it was already resolved in previous spectroscopic measurements on cold molecular beams [15]. The hyperfine splitting of ^{39}K is comparable or even smaller than the molecular state linewidth and remains mainly unresolved. At low field this allows to consider $F_1 = |\vec{J} + \vec{i}_{\text{Na}}| = (1/2, 3/2, 5/2)$ as a good quantum number, as visible in figure 2, with three groups of states at low magnetic field. Additionally, one can consider the total angular momentum $\vec{F} = \vec{J} + \vec{i}_{\text{Na}} + \vec{i}_{\text{K}} = \vec{F}_1 + \vec{i}_{\text{K}}$, where the projection on the quantization axes m_F is the only preserved quantity even at large magnetic fields. The Zeeman term of equation (2) neglects nuclear contributions and can be expanded as $\mu_0 m_j g_J B$, where m_j is the projection of \vec{J} on the magnetic field axis and g_J the Landé factor. In absence of coupling between singlet and triplet, one has $g_J^B = g_N = g_L/(J(J+1)) = 1/2$ and $g_J^c = g_s/2 \approx 1$ [25, 26], where g_L and g_s are the known electron orbital and spin g -factors equal to 1 and 2.0023, respectively. Spin–orbit interaction couples singlet and triplet with strength ξ_{Bc} with selection rules $\Delta J = 0$, $\Delta m_{i_{\text{Na}}} = 0$ and $\Delta m_{i_{\text{K}}} = 0$. The coupling also already incorporates the vibrational wavefunction overlap of the two states. Hence, the problem reduces to solving the following $(48 + 48) \times (48 + 48)$ matrix



$$\begin{pmatrix} H^B & \xi_{Bc} \\ \xi_{Bc} & H^c \end{pmatrix}. \quad (3)$$

Note that the coupling ξ_{Bc} shows its effect in two ways:

- As the Zeeman term remains significantly smaller than both the unperturbed singlet–triplet energy difference Δ and of the coupling strength ξ_{Bc} , one finds for strong fields compared to the hyperfine splitting (not shown in the later figure 3) the effective Landé factors $g_{J,\text{eff}}^{B,c}$

$$g_{J,\text{eff}}^{B,c} = \frac{1}{2} \left(g_J^c + g_J^B \mp \Delta \frac{g_J^c - g_J^B}{\sqrt{4\xi_{Bc}^2 + \Delta^2}} \right) \quad (4)$$

$$= g_J^{B,c} \pm \frac{1}{4} \left(1 - \frac{\Delta}{\tilde{\Delta}} \right), \quad (5)$$

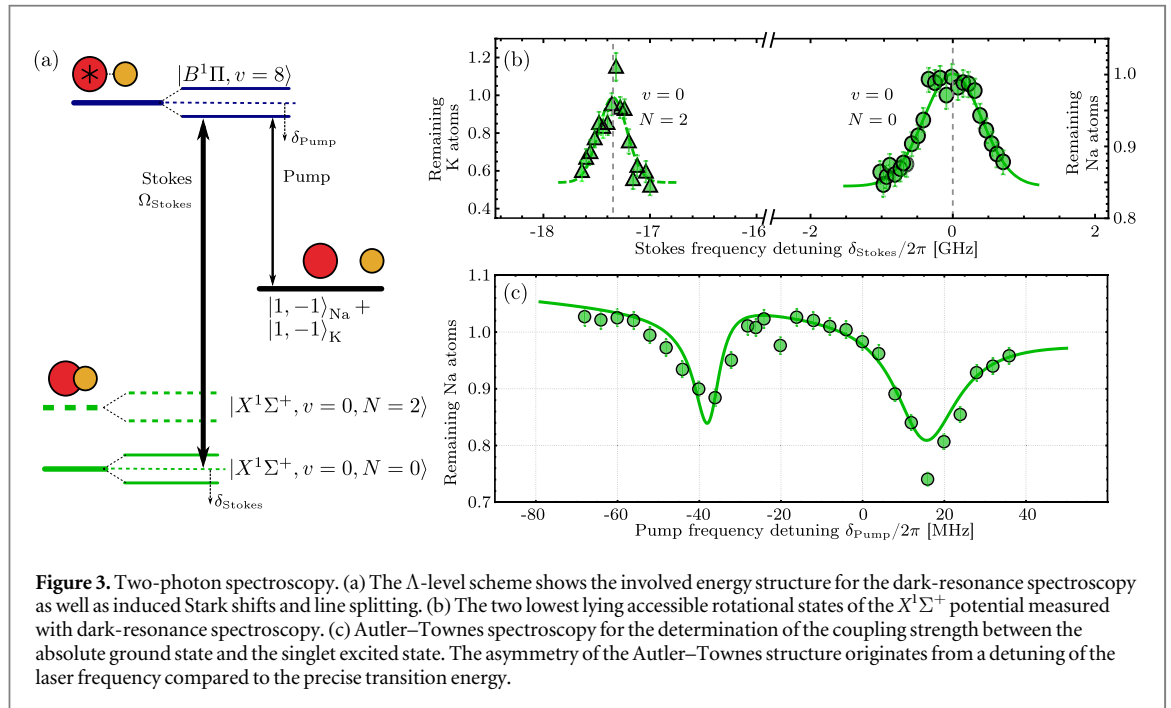
where $\tilde{\Delta} = \sqrt{4\xi_{Bc}^2 + \Delta^2}$ is the energy difference of the hyperfine centers at $B = 0$ in the coupled case.

- The acquired triplet character of the singlet state will lead to a large hyperfine splitting, while the triplet one is decreased.

3.2. One-photon spectroscopy

From spectroscopic investigations [15] the transition energies from the atomic scattering threshold in the $a^3\Sigma^+$ potential to the dominantly $|B^1\Pi, \nu = 8\rangle$ and dominantly $|c^3\Sigma^+, \nu = 30\rangle$ states are expected to be about $12\,242.927\text{ cm}^{-1}$ for the triplet state and about $12\,242.017\text{ cm}^{-1}$ for the singlet state at a magnetic field of 150 G. In the following we will refer to the states with a dominant triplet character as *triplet* and to the ones with dominantly singlet character as *singlet*.

To locate the excited states, we measure the remaining atom number in both species after applying the Pump light for up to 1.6 s for variable detunings from the expected transition frequencies. The atoms associated to



molecules in the excited state collide with the remaining atoms and/or decay to a lower lying molecular state. Both of these effects manifest themselves as a decreased number of atoms in the initial state. The step size for the laser detuning scan is set to a few MHz, which is sufficient to resolve the different structures with an expected linewidth of about $2\pi \times 6$ MHz. The measurements are performed both for polarizations parallel to the magnetic field (which implies π -transitions from the atomic to the molecular state) and perpendicular to it (leading to both σ^+ - and σ^- -transitions). Figures 2(a), (b) shows the positions of the loss features for the triplet and singlet states and π - and σ^+ / σ^- -transitions. In the case of the singlet state, we perform spectroscopic measurements at two different magnetic field strengths to calibrate our model for the Zeeman splitting. Figures 2(c), (d) show the corresponding atom losses from π -transitions measured on ^{39}K .

In the magnetic field range at which our measurements are performed, the energy splitting remains in an intermediate region between pure Zeeman and Paschen–Back regime (see figure 2), where F and F_1 are no good quantum numbers. Selection rules based on the m_F allow to decrease the number of states to 18 observable ones, 6 for π - and 12 (3/9) for σ^+ / σ^- -transitions.

Figures 2(a), (b) contains the complete collection of the observed resonant features with a distance of 27.347 GHz ($\cong 0.913 \text{ cm}^{-1}$) between the manifold zeroes. The lines result from the fit of our model to the experimental observations, where the coupling ξ_{Bc} , the energy difference Δ and the hyperfine coupling constants A_{Na} and A_{K} are used as free parameters. The overall curvature of the lines originates from the atomic state Zeeman effect which is in the intermediate regime for both atoms. From the fit, we obtain $g_{J,\text{eff}}^B = 0.630(8)$ and $g_{J,\text{eff}}^c = 0.870(8)$. The uncertainty comes from the fit and from the ambiguous assignment of few resonances to a precise state, due to the simultaneous presence of σ^+ / σ^- polarized light. The unperturbed energy difference Δ is found to be equal to 13.1(8) GHz ($= 0.437(31) \text{ cm}^{-1}$) and ξ_{Bc} to be equal to 12.0(2) GHz ($= 0.400(8) \text{ cm}^{-1}$). The obtained values correspond to a 26(1)%/74(1)% mixing of singlet and triplet states, which is in agreement with previous predictions [27]. Remarkably the coupling strength ξ_{Bc} is comparable to the unperturbed energy difference Δ . This explains the large mixing. The obtained value for A_{Na} of 307(9) MHz ($\cong 0.0102(3) \text{ cm}^{-1}$) is in good agreement with previous spectroscopic measurements [28]. Our model provides a value for $A_{\text{K}} = 6(9) \text{ MHz}$ ($\cong 2(3) \times 10^{-3} \text{ cm}^{-1}$), compatible with previous predictions and measurements [28, 29].

The amplitudes of the loss features depend on the coupling between the atomic and molecular states and are therefore highly dependent on their hyperfine quantum numbers and the wavefunction overlap. The strong mixing of the wavefunctions in the excited states and the scattering wavefunction of the atoms lead to interference effects altering the effective transition dipole strength. Our calculations do not account for the interference and thus do not provide an accurate description of transition amplitudes [16].

4. Two-photon ground state spectroscopy

Using the located excited state as a bridge, we demonstrate two-photon spectroscopy of the rovibrational ground state $|X^1\Sigma, \nu = 0, N = 0\rangle$; as sketched in figure 1. The energy difference between ground and excited state is well known from spectroscopic data [15] and can be predicted within a precision of $\pm 0.08 \text{ cm}^{-1}$. To exactly determine the energy of the rovibrational ground state, we fixed the Pump laser frequency on the transition with strongest losses from figure 2(d) within the singlet states which is marked with a red dashed curve. The state originates from the combination of two basis states which are labeled by $|B/c, 1, -1, 3/2, -1/2, 3/2, -1/2\rangle$ and $|B/c, 1, 0, 3/2, -1/2, 3/2, -3/2\rangle$ where the quantum numbers are as described in section 3.1.

When the Stokes laser is on resonance, it is inducing a Stark shift on the excited state and a revival of the atom number is expected as sketched in figure 3(a). Figure 3(b) shows this protection when the detuning δ_{Stokes} is scanned with a full width half maximum for the $|X^1\Sigma^+, \nu = 0, N = 0\rangle$ of about 405(35) MHz for a laser power of 5 mW. The observed peak of the transition energy is at $17\,452.826(2) \text{ cm}^{-1}$.

Furthermore, to unambiguously identify the ground state, we performed an atom-loss scan also in the range of frequencies where the second rotationally excited state with $N = 2$ is expected; see figure 3(b). The observed energy difference of $\Delta_{N=0 \rightarrow N=2} = h \times 17.3(3) \text{ GHz}$ allows us to deduct the rotational constant to be $B_{\nu=0} = h \times 2.89(5) \text{ GHz}$ by using the relation $\Delta_{N=0 \rightarrow N=2} = B_0 \times 2(2 + 1)$. This value agrees with the one observed by using microwave spectroscopy [30]. The full width of half maximum for the protection is 133(27) MHz. This is smaller than for the $N = 0$ state, indicating a weaker coupling to the excited states, as expected from theoretical considerations.

To directly determine the coupling strength between the ground and the excited state, we fixed the Stokes laser frequency close to resonance and scanned the Pump laser frequency detuning δ_{pump} . This scan reveals the well-known Autler–Townes splitting [17], the magnitude of which is proportional to the dipole matrix element of the transition. Figure 3(c) shows the measured remaining atom number with the typical double-loss feature. The asymmetric shape of the splitting originates from a residual detuning to the exact transition frequency of the Stokes laser which is determined to be $\delta_{\text{Stokes}} = 2\pi \times -22 \text{ MHz}$. We derive the Rabi frequency $\Omega_{\text{Stokes}} = 2\pi \times 23.5 \text{ MHz}$ for an applied laser power of 5 mW, corresponding to a normalized Rabi frequency of $\tilde{\Omega}_{\text{Stokes}} = 2\pi \times 65.2 \text{ kHz} \times \sqrt{I/(\text{mW cm}^{-2})}$ and an effective transition dipole moment of 0.170 D. Both values, δ_{Stokes} and Ω_{Stokes} are derived from a three-level master equation modeling the line shape shown in figure 3(c).

5. Conclusion and outlook

Within this work, we have characterized a two-photon scheme for the coupling of the diatomic scattering threshold in the $a^3\Sigma^+$ potential to the rovibrational ground state $|X^1\Sigma^+, \nu = 0, N = 0\rangle$. Using photoassociation spectroscopy, we have observed and characterized the excited state hyperfine manifolds of the coupled $|B^1\Pi, \nu = 8\rangle$ and $|c^3\Sigma^+, \nu = 30\rangle$ states in the bosonic $^{23}\text{Na}^{39}\text{K}$ molecules at 130 and 150 G, starting from an ultracold atomic quantum gas mixture in the states $|f = 1, m_f = -1\rangle_{\text{Na}} + |f = 1, m_f = -1\rangle_{\text{K}}$. By applying a spectral local model fit to the measurements, we have extracted the admixture of these states to be 26%/74%. Due to the strong singlet–triplet mixing, this part of the spectrum serves as an ideal bridge from the triplet atomic scattering threshold to the singlet rovibronic ground state molecules. Making use of this bridge, we have identified the rovibrational ground state and the second rotationally excited state in two-photon spectroscopy. From an Autler–Townes measurement we have extracted the Rabi-coupling between the excited and the ground state. Our work results in a fully characterized scheme for the conversion of $^{23}\text{Na}^{39}\text{K}$ Feshbach molecules to rovibrational ground state polar molecules and will allow for the efficient creation of ultracold ensembles of chemically stable bosonic $^{23}\text{Na}^{39}\text{K}$ ground state molecules.

Acknowledgments

We thank Eberhard Tiemann for enlightening discussions and suggestions. We gratefully acknowledge financial support from the European Research Council through ERC Starting Grant POLAR and from the Deutsche Forschungsgemeinschaft (DFG) through CRC 1227 (DQ-mat), project A03 and FOR2247, project E5. KKV and PG thank the Deutsche Forschungsgemeinschaft for financial support through Research Training Group (RTG) 1991.

References

- [1] Ospelkaus S, Ni K K, Wang D, de Miranda M H G, Neyenhuis B, Quéméner G, Julienne P S, Bohn J L, Jin D S and Ye J 2010 *Science* **327** 853–7
- [2] Guo M, Ye X, He J, González-Martínez M L, Vexiau R, Quéméner G and Wang D 2018 *Phys. Rev. X* **8** 041044
- [3] Zuchowski P S and Hutson J M 2010 *Phys. Rev. A* **81** 060703
- [4] Gorshkov A V, Manmana S R, Chen G, Ye J, Demler E, Lukin M D and Rey A M 2011 *Phys. Rev. Lett.* **107** 115301
- [5] Büchler H, Micheli A and Zoller P 2007 *Nat. Phys.* **3** 726–31
- [6] Bergmann K, Theuer H and Shore B W 1998 *Rev. Mod. Phys.* **70** 1003–25
- [7] Ni K K, Ospelkaus S, de Miranda M H G, Peer A, Neyenhuis B, Zirbel J J, Kotochigova S, Julienne P S, Jin D S and Ye J 2008 *Science* **322** 231–5
- [8] Park J W, Will S A and Zwierlein M W 2015 *Phys. Rev. Lett.* **114** 205302
- [9] Rvachov T M, Son H, Sommer A T, Ebadi S, Park J J, Zwierlein M W, Ketterle W and Jamison A O 2017 *Phys. Rev. Lett.* **119** 143001
- [10] Takekoshi T, Reichsöllner L, Schindewolf A, Hutson J M, Le Sueur C R, Dulieu O, Ferlaino F, Grimm R and Nägerl H C 2014 *Phys. Rev. Lett.* **113** 205301
- [11] Molony P K, Gregory P D, Ji Z, Lu B, Köppinger M P, Le Sueur C R, Blackley C L, Hutson J M and Cornish S L 2014 *Phys. Rev. Lett.* **113** 255301
- [12] Guo M, Zhu B, Lu B, Ye X, Wang F, Vexiau R, Bouloufa-Maafa N, Quéméner G, Dulieu O and Wang D 2016 *Phys. Rev. Lett.* **116** 205303
- [13] Seefelberg F, Buchheim N, Lu Z K, Schneider T, Luo X Y, Tiemann E, Bloch I and Gohle C 2018 *Phys. Rev. A* **97** 013405
- [14] Aymar M and Dulieu O 2007 *Mol. Phys.* **105** 1733–42
- [15] Temelkov I, Knöckel H, Pashov A and Tiemann E 2015 *Phys. Rev. A* **91** 032512
- [16] Schulze T A, Temelkov I I, Gempel M W, Hartmann T, Knöckel H, Ospelkaus S and Tiemann E 2013 *Phys. Rev. A* **88** 023401
- [17] Autler S H and Townes C H 1955 *Phys. Rev.* **100** 703–22
- [18] Gempel M W 2016 *PhD Thesis* University of Hannover www.tib.eu/de/suchen/id/TIBKAT%3A853787425/Towards-ultracold-polar-NaK-molecules-and-the-investigation/
- [19] Hartmann T 2018 *PhD Thesis* University of Hannover www.tib.eu/de/suchen/id/datacite%3Aadoi-10.15488%252F4699/An-experiment-apparatus-for-the-production-of-ultracold/
- [20] Schulze T A, Hartmann T, Voges K K, Gempel M W, Tiemann E, Zenesini A and Ospelkaus S 2018 *Phys. Rev. A* **97** 023623
- [21] Hartmann T, Schulze T A, Voges K K, Gersema P, Gempel M W, Tiemann E, Zenesini A and Ospelkaus S 2019 *Phys. Rev. A* **99** 032711
- [22] Drever R W P, Hall J L, Kowalski F V, Hough J, Ford G M, Munley A J and Ward H 1983 *Appl. Phys. B* **31** 97–105
- [23] Gregory P D, Molony P K, Köppinger M P, Kumar A, Ji Z, Lu B, Marchant A L and Cornish S L 2015 *New J. Phys.* **17** 055006
- [24] Ishikawa K 1993 *J. Chem. Phys.* **98** 1916–24
- [25] Townes C H and Schawlow A 1955 *Microwave Spectroscopy* (New York: Dover)
- [26] Semenov M, Yurchenko S N and Tennyson J 2016 *J. Mol. Spectrosc.* **330** 57–62
- [27] Ferber R, Pazyuk E A, Stolyarov A V, Zaitsevskii A, Kowalczyk P, Chen H, Wang H and Stwalley W C 2000 *J. Chem. Phys.* **112** 5740
- [28] Ishikawa K, Kumauchi T, Baba M and Katô H 1992 *J. Chem. Phys.* **96** 6423–32
- [29] Kowalczyk P 1989 *J. Chem. Phys.* **91** 2779–89
- [30] Yamada C and Hirota E 1992 *J. Mol. Spectrosc.* **153** 91

4.2 Ultracold Gas of Bosonic $^{23}\text{Na}^{39}\text{K}$ Ground-State Molecules [A5]

The creation of Feshbach molecules $|f\rangle$, see section 3.3, and the spectroscopic measurements of excited intermediate molecular levels $|e\rangle$, see section 4.1, that can act as a bridge between the Feshbach state and the absolute rovibronic ground state $|g\rangle$ in a two-photon process, pave the way for the production of ultracold $^{23}\text{Na}^{39}\text{K}$ molecules¹. However, for an efficient two-photon transfer, losses need to be minimized. These can, for example, originate from a spontaneous decay of the intermediate level to an energetically lower lying molecular state. The large number of available decay channels of these excited molecular levels lead to natural linewidths of about $\Gamma = 12$ MHz and thus to lifetimes of $\tau = 1/\Gamma \approx 80$ ns. Therefore, the population of the excited molecular state needs to be minimized. This can, for example, be done with a two-photon π pulse, with a large one-photon detuning Δ . However, due to pulse broadening issues and delicate time and laser intensity constraints, a highly efficient and stable transfer is difficult to achieve. For this reason, a STIRAP transfer can be beneficial, which will be described in the next section.

4.2.1 Stimulated Raman adiabatic passage (STIRAP)

In order to explain the STIRAP, let's assume a three-level system with two laser fields, as depicted in Fig.4.1, with time-dependent laser intensities. We can describe the dynamic of this system with the time-dependent Schrödinger equation,

$$i\hbar \frac{d}{dt} \Psi(t) = H(t)\Psi(t), \quad (4.1)$$

where $H(t)$ is the Hamilton operator of the molecule and its interaction with the laser fields. Using the rotating-wave approximation the Hamiltonian can be written as [99]

$$H(t) = \hbar \begin{bmatrix} 0 & \frac{1}{2}\Omega_{\text{pump}}(t) & 0 \\ \frac{1}{2}\Omega_{\text{pump}}(t) & \Delta & \frac{1}{2}\Omega_{\text{Stokes}}(t) \\ 0 & \frac{1}{2}\Omega_{\text{Stokes}}(t) & \delta \end{bmatrix}, \quad (4.2)$$

with the one-photon detuning Δ and the two-photon detuning δ , as shown in Fig. 4.1. Under the condition of $\delta = 0$, the eigenstates of this system are

$$\begin{aligned} |a^+\rangle &= \sin \Theta \sin \Phi |f\rangle + \cos \Phi |e\rangle + \cos \Theta \sin \Phi |g\rangle \\ |a^0\rangle &= \cos \Theta |f\rangle - \sin \Theta |g\rangle \\ |a^-\rangle &= \sin \Theta \cos \Phi |f\rangle - \sin \Phi |e\rangle + \cos \Theta \cos \Phi |g\rangle \end{aligned}, \quad (4.3)$$

¹Note that, the labelling of these states changed between paper [A4] and [A5]. In [A4] they were labelled as initial $|i\rangle$, excited $|e\rangle$ and final state $|g\rangle$, whereas from now on they are labelled as Feshbach $|f\rangle$, excited $|e\rangle$ and ground state $|g\rangle$.

4 From Feshbach molecules to ground-state molecules

with the mixing angles $\tan \Theta = \Omega_{\text{pump}}(t)/\Omega_{\text{Stokes}}(t)$ and $\tan 2\Phi = \sqrt{\Omega_{\text{pump}}(t)^2 + \Omega_{\text{Stokes}}(t)^2}/\Delta$. The eigenstate $|a^0\rangle$ is called the "dark" state, as it does not have any contribution from the excited state $|e\rangle$. Dependent on the mixing angle Θ this state has more or less contributions from the Feshbach state and the ground state. If the pump laser intensity is zero and only the Stokes laser applied, this results in $\Theta = 0$, thus the dark state is equal to the Feshbach state $|f\rangle$. On the other hand in the limit of a vanishing Stokes laser intensity with an applied pump laser, the mixing angle is $\Theta = \pi/2$ and the dark state is equal to the ground state.

Therefore, when the mixing angle is changed from $\Theta = 0$ to $\Theta = \pi/2$ by changing the applied Stokes and pump laser intensities, the Feshbach state can be transferred to the ground state without ever occupying the excited state $|e\rangle$. These intensity ramps can not be arbitrarily fast, as the system needs to be able to follow and therefore stay in the dark state. The adiabaticity criterion is given by

$$\sqrt{\Omega_{\text{pump}}(t)^2 + \Omega_{\text{Stokes}}(t)^2} \gg |\dot{\Theta}|. \quad (4.4)$$

In theory, with slow enough intensity ramps, this transfer can have an efficiency of 100% and is robust against small variations in the laser intensities, ramps speeds and pulse shapes. However, for this to be true, the relative phase of the pump and Stokes laser can be arbitrary, but must be constant during the transfer. Otherwise the system does not remain in the dark state and the excited state is populated, resulting in the loss of a molecule. In the POLAR experiment this relative phase stability is achieved by locking both lasers to an ultra-low expansion and high-finesse cavity. This cavity also reduces the phase noise of both lasers and serves as frequency reference. For a detailed description of the high finesse cavity and its properties, see [58].

The remaining phase noise, peak Rabi frequencies as well as the finite lifetime of the Feshbach molecules of around $300 \mu\text{s}$, determine the optimal intensity ramp speed.

In the following paper the creation of up to 4200 ultracold bosonic $^{23}\text{Na}^{39}\text{K}$ ground-state molecules with a PSD of around 0.14 is shown. The STIRAP is characterized in dependence on the involved molecular levels, Rabi-couplings, pulse lengths and the one- and two-photon detuning. First molecular collisional properties are measured, revealing a large two-body loss rate coefficient close to the universal limit. In addition, collisional properties of atom-molecule mixtures, with the atoms in the $F = 1, m_F = -1$ hyperfine state, are shown, with near universal two-body losses of $^{23}\text{Na}+^{23}\text{Na}^{39}\text{K}$ and an intriguingly low two-body loss rate for $^{39}\text{K}+^{23}\text{Na}^{39}\text{K}$.

After the report of the successful creation of a new ultracold rovibronic molecule in [A5], improvements on the STIRAP pathway as well as the molecule number have been implemented. These are discussed in the following sections.

4.2.2 Preparation of an ultracold atomic $^{23}\text{Na}+^{39}\text{K}$ mixture

In the papers [A3],[A4],[A5] the ultracold atomic mixture of ^{23}Na and ^{39}K is created as described in [90]. After a dual species MOT and Molasses stage and a subsequent evaporation in a magnetic trap, the atoms are transferred to a cODT. Due to the magnetic trap the atoms are spin polarized in the $|F = 1, m_F = -1\rangle$ hyperfine state. At about 150 G one can find favourable intra- and inter-species scattering lengths for a final evaporation stage, see Fig. 4.2. After this evaporation stage the magnetic field is quickly ramped to 199.3 G, across a Feshbach resonance, where the weakly bound molecules are created by a resonant RF pulse. This ramp across the resonance leads to an increased overall loss rate due to three-body-losses and anti-evaporation. Nevertheless, this process yields roughly $6 \cdot 10^4$ potassium and $1.8 \cdot 10^5$ sodium atoms at 300 nK with trap frequencies of $2\pi \cdot \{309, 297, 51\}$ Hz and $2\pi \cdot \{247, 242, 41\}$ Hz, respectively, along the mutually orthogonal x, y, z directions determined by the experimental geometry.

To circumvent the problem of high three-body-losses and anti-evaporation, a new magnetic field range for the cODT evaporation was chosen at around 175 G. At this position, the absolute values of all three scattering lengths are very similar and also strong enough for an efficient evaporation. Note that, due to the negative scattering length of ^{39}K and $^{23}\text{Na}+^{39}\text{K}$ no dual species BEC can be created.

In a first step the roughly $10 \mu\text{K}$ "hot" atomic mixture is ramped to the new target magnetic field of 175 G. Due to the, in comparison, much lower density and therefore much lower three-body loss rates, crossing the Feshbach resonances is less critical. After this evaporation step the magnetic field is ramped to 199.3 G, yielding $9 \cdot 10^4$ potassium and $2.7 \cdot 10^5$ sodium atoms at the same temperature and trap frequencies described above, which enables the creation of up to $1 \cdot 10^4$ Feshbach molecules.

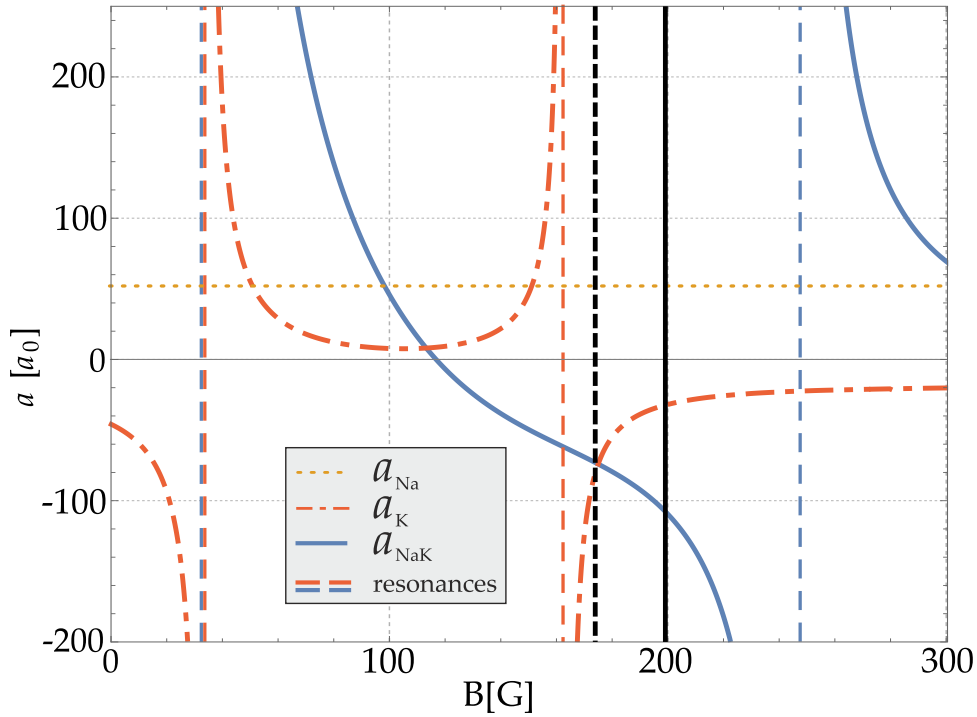


Figure 4.2: Intra- and interspecies scattering lengths of sodium a_{Na} , potassium a_{K} and sodium with potassium a_{NaK} , in yellow, orange and blue respectively, versus the applied external magnetic field strength. The sodium and potassium atoms are both in the $|F = 1, m_F = -1\rangle$ hyperfine state. The black dashed line shows the magnetic field at which the evaporation in the dipole trap is performed. After the evaporation, the magnetic field is ramped to 199.3 G (black solid lines), at which an RF pulse populates the weakly bound molecular state close to the atomic $|F = 1, m_F = -1\rangle_{\text{Na}} + |F = 2, m_F = -2\rangle_{\text{K}}$ scattering channel. This is followed by a STIRAP transfer of the population to the molecular ground state. Image adopted from [17].

4.2.3 Identifying a new intermediate level for a STIRAP pathway

The initially chosen intermediate level $|e\rangle$ has the disadvantage of two additionally coupled excited states $|e_{1,2}\rangle$ that disturb the STIRAP, see [A5]. A new intermediate level with a similar coupling strength for the pump laser transition would therefore be desirable.

In order to find a new intermediate level, some important properties must be considered. At a magnetic field of 200 G, the nuclear spin of potassium i_{K} is decoupled from the electronic momentum for both the excited $|e\rangle$ and the molecular ground state $|g\rangle$. Therefore dipole transitions between these states can not change the potassium nuclear spin projection. For the nuclear spin of sodium i_{Na} this is only true for the molecular ground state, see [A5]. The initial Feshbach state can be written as $\alpha_1 |m_{i_{\text{Na}}} = -3/2, m_{i_{\text{K}}} = -1/2, M_S = -1\rangle + \alpha_2 |m_{i_{\text{Na}}} = -3/2, m_{i_{\text{K}}} = -3/2, M_S = 0\rangle$, where M_S is the total electron spin projection and $\alpha_{1/2}$ represent the state admixtures, see supplemental material of [A5]. This suggests, that intermediate states with either a nuclear spin projection of

$m_{i,\text{K}} = -1/2$ or $m_{i,\text{K}} = -3/2$ should be accessible². However, in contrast to our expectations, but as experimentally demonstrated, only intermediate states with a nuclear spin projection of $m_{i,\text{K}} = -1/2$ have been accessible.

As a result, the number of available intermediate states is drastically reduced. Considering only π transitions for the pump laser, only one excited state can be addressed. This is the old intermediate level $|e\rangle$, see [A5] and the supplemental material. Therefore, a new intermediate level in the $c^3\Sigma^+$ can only be found with a switched pump laser polarization of σ^\pm . With this polarization the model presented in [A4] predicts two potentially accessible intermediate levels. These two levels have been spectroscopically investigated by identifying Feshbach molecule loss features. Note that, for all the following measurements the pump and Stokes laser setup remains unchanged in comparison with the setup explained in the supplemental material of [A5], though in order to populate the same rovibrational ground state, also the polarization of the Stokes laser beam is switched to π polarized light. Thus, only the intermediate state is changed, the initial and ground state remain the same.

These transitions, starting from the Feshbach molecule state at 200 G for a σ^\pm polarized pump laser are shown in Fig. 4.3. Loss rate measurements revealed the one with the strongest coupling strength, which was chosen as the new intermediate level $|e'\rangle$ (top slightly larger grey dot), with a maximum Rabi frequency of $\Omega_{\text{pump}} = 2\pi \cdot 2.9(6)$ MHz. The blue dot marks the old intermediate state $|e\rangle$.

At 200 G the new intermediate level is $|e'\rangle \approx 0.47 |m_{i,\text{Na}} = -1/2, m_{i,\text{K}} = -1/2, M_J = -1, M_F = -2\rangle + 0.88 |m_{i,\text{Na}} = -3/2, m_{i,\text{K}} = -1/2, M_J = 0, M_F = -2\rangle$ and can be accessed with a σ^+ -transition. $m_{i,\text{K}/\text{Na}}$ are the projections on the magnetic field axis of the nuclear spins $i_{\text{K}/\text{Na}}$ of ^{39}K and ^{23}Na . M_J is the projection of the angular momentum \vec{J} , resulting from the coupling of the rotational angular momentum \vec{N} and the spin \vec{S} and finally M_F is the projection of the total angular momentum \vec{F} , with $\vec{F} = \vec{F}_1 + \vec{i}_{\text{K}}$ and $\vec{F}_1 = \vec{J} + \vec{i}_{\text{Na}}$. For a detailed description of the involved quantum numbers and couplings, see [A4].

² i_{K} is decoupled from the electronic momentum, thus the intermediate levels only have a single $m_{i,\text{K}}$ contribution

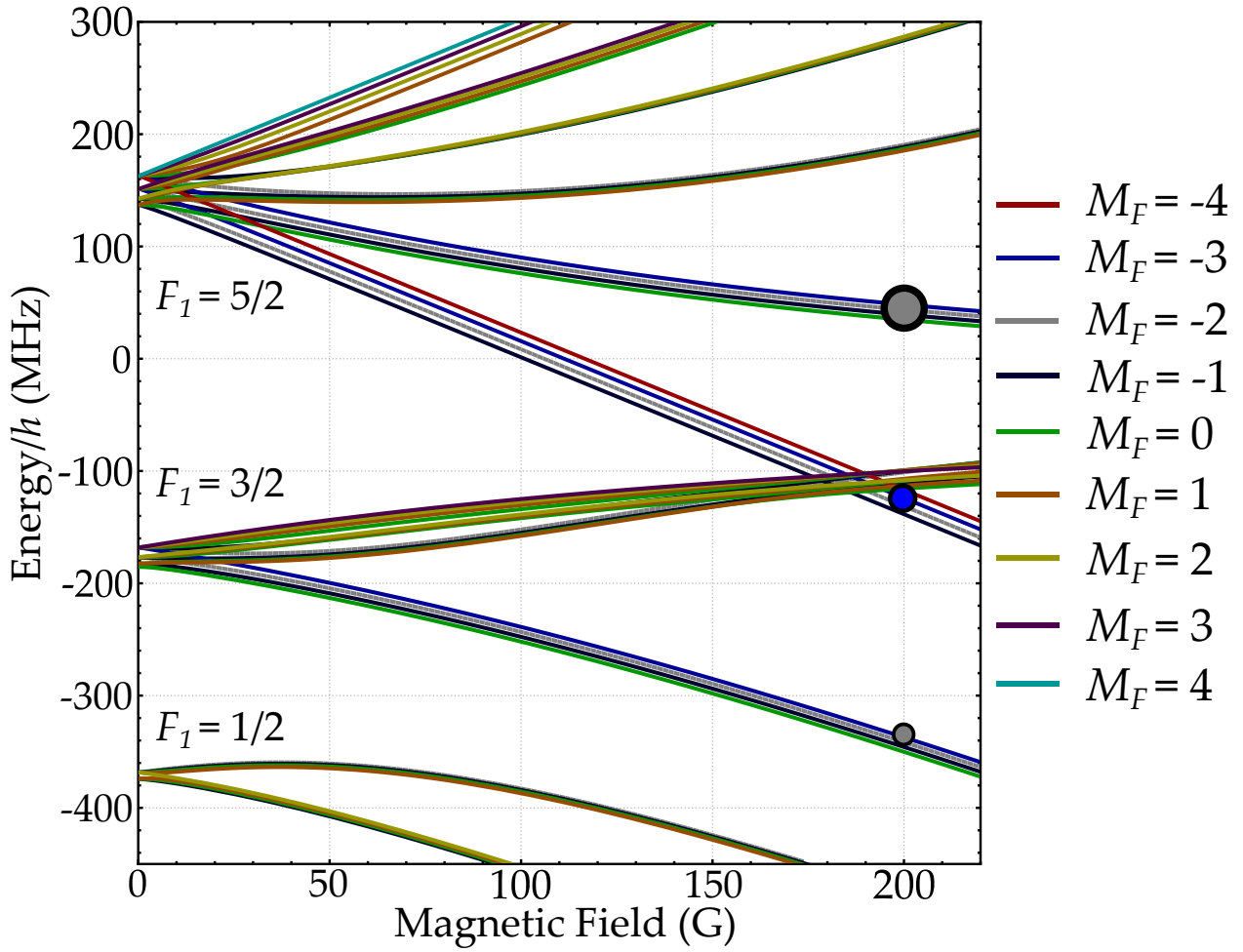


Figure 4.3: Energy levels of the $c^3\Sigma^+$ states in an external magnetic field. The lines show all levels calculated by the model introduced in [A4] and are colour coded with their corresponding total angular momentum projection M_F . The grey dots mark the measured transitions starting from the atomic asymptote $|F = 1, m_F = -1\rangle_{\text{Na}} + |F = 2, m_F = -2\rangle_{\text{K}}$ and were accessible with σ^+ polarized pump laser light. The top slightly larger grey dot shows the newly chosen intermediate level $|e'\rangle$, while the blue dot marks the old intermediate level described in [A5].

To verify that no additional intermediate states disturb the STIRAP, the molecule number was measured as a function of the one-photon detuning Δ of the STIRAP, as shown in Fig. 4.4. The STIRAP pulse shape and laser intensities were kept unchanged for all data points. At zero detuning the maximum single trip efficiency is around 70%, which is the same as described in [A5].

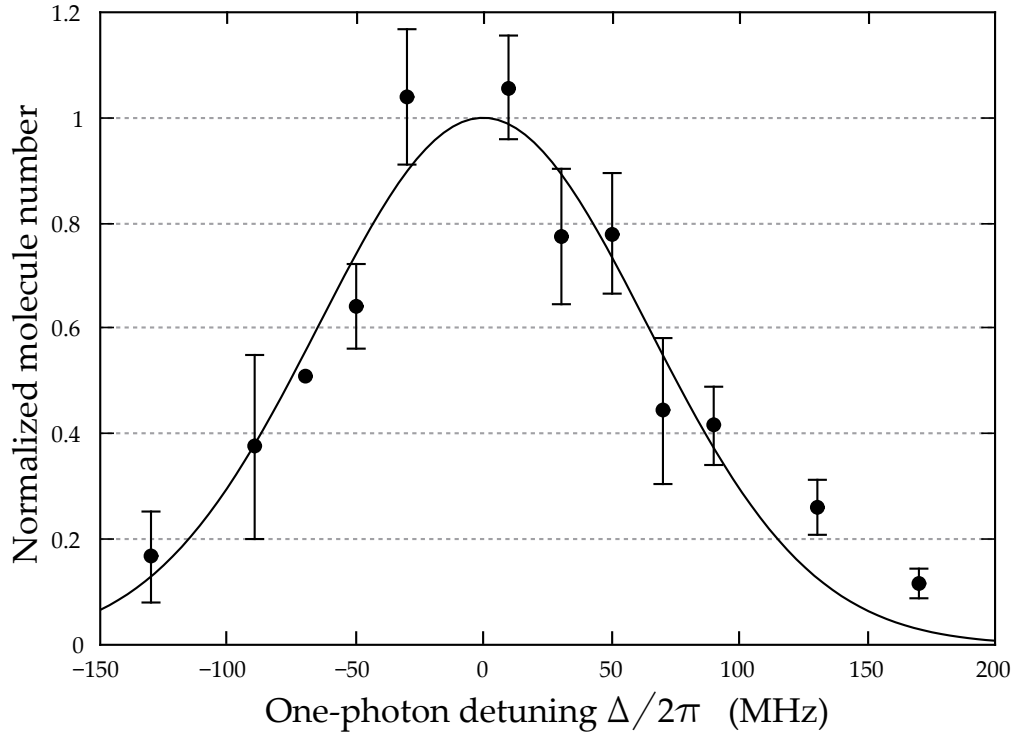


Figure 4.4: Measured normalized number of molecules transferred to the ground state in dependence on the one-photon detuning Δ of the STIRAP, with the new intermediate state $|e'\rangle$. The pulse form and the laser powers were left unchanged during the measurement. The solid line is a phenomenological Gaussian fit to the data. As can be seen, in contrast to [A5], close to the newly chosen intermediate level no interfering intermediate levels are observed and the optimal transfer is achieved at zero detuning. The single trip efficiency at zero detuning is still around 70%.

4 *From Feshbach molecules to ground-state molecules*

Reprinted with permission from Voges *et al.*, Ultracold Gas of Bosonic $^{23}\text{Na}^{39}\text{K}$ Ground-State Molecules, Phys. Rev. Lett. 125, 083401, 2020

Copyright © 2022 by the American Physical Society (APS).

DOI <https://link.aps.org/doi/10.1103/PhysRevLett.125.083401>

Ultracold Gas of Bosonic $^{23}\text{Na}^{39}\text{K}$ Ground-State Molecules

Kai K. Voges^{1,*}, Philipp Gersema¹, Mara Meyer zum Alten Borgloh¹, Torben A. Schulze,¹
Torsten Hartmann¹, Alessandro Zenesini^{1,2} and Silke Ospelkaus^{1,†}

¹*Institut für Quantenoptik, Leibniz Universität Hannover, 30167 Hannover, Germany*

²*INO-CNR BEC Center and Dipartimento di Fisica, Università di Trento, 38123 Povo, Italy*



(Received 27 April 2020; accepted 29 July 2020; published 21 August 2020)

We report the creation of ultracold bosonic dipolar $^{23}\text{Na}^{39}\text{K}$ molecules in their absolute rovibrational ground state. Starting from weakly bound molecules immersed in an ultracold atomic mixture, we coherently transfer the dimers to the rovibrational ground state using an adiabatic Raman passage. We analyze the two-body decay in a pure molecular sample and in molecule-atom mixtures and find an unexpectedly low two-body decay coefficient for collisions between molecules and ^{39}K atoms in a selected hyperfine state. The preparation of bosonic $^{23}\text{Na}^{39}\text{K}$ molecules opens the way for future comparisons between fermionic and bosonic ultracold ground-state molecules of the same chemical species.

DOI: 10.1103/PhysRevLett.125.083401

Heteronuclear polar ground-state molecules have attracted considerable attention in recent years. They serve as a new platform for controlled quantum chemistry [1,2], novel many-body physics [3,4], and quantum simulations [5,6]. Their permanent electric dipole moment gives rise to anisotropic and tunable long-range interactions which can be induced in the lab frame via electric fields or resonant microwave radiation [7,8]. This gives exquisite control over additional quantum degrees of freedom. In recent years there has been continuous progress in the production of ultracold bialkali molecules. Fermionic $^{40}\text{K}^{87}\text{Rb}$ [9], $^{23}\text{Na}^{40}\text{K}$ [10], and $^6\text{Li}^{23}\text{Na}$ [11], as well as bosonic $^{87}\text{Rb}^{133}\text{Cs}$ [12] and $^{23}\text{Na}^{87}\text{Rb}$ [13] molecules have been prepared.

Up to now, not a single molecule has been available both as a bosonic and a fermionic molecular quantum gas, which makes findings among different species and quantum statistics challenging to interpret and to compare. For bialkali molecules only combinations with Li or K offer the possibility to prepare the bosonic and fermionic molecule, as Li and K are the only alkali metals which possess long-lived fermionic and bosonic isotopes. Among these molecules (LiK, LiNa, LiRb, LiCs, NaK, KRb, KCs) all possible combinations with a Li atom as well as the KRb molecule are known to undergo exothermic atom exchange reactions in molecule-molecule collisions [14]. This leaves only NaK and KCs [15] as chemically stable molecules for a comparison of scattering properties of the same molecular species but different quantum statistics.

Both chemically reactive and nonreactive spin-polarized fermionic molecular ensembles have been reported to be long-lived due to the centrifugal p -wave collisional barrier limiting the two-body collisional rate to the tunneling rate [1,10]. The lifetime of bosonic molecular ensembles, however, has been observed to be significantly shorter and limited

by the two-body universal scattering rate [13,16]. Two-body collisions involving molecules can lead to the formation of collisional complexes due to a large density of states. The complexes can either decay to new chemical species for chemically reactive molecules [17] or within the lifetime of the complexes are removed from the trap by light excitation [18–20] or collisions with a third scattering partner [16,21].

In this Letter, we report on the production of ultracold bosonic $^{23}\text{Na}^{39}\text{K}$ rovibrational ground-state molecules. The preparation follows the pioneering experiments for the creation of $^{40}\text{K}^{87}\text{Rb}$ molecules [9] with Feshbach molecule creation and subsequent stimulated Raman adiabatic passage (STIRAP) transfer [22] to a selected hyperfine state in the rovibrational ground-state manifold. We model our STIRAP transfer through an effective five-level master equation model and work out an efficient pathway to create spin-polarized ground-state molecular ensembles. We prepare pure molecular ensembles as well as molecule-atom mixtures and extract the resulting collisional loss rate coefficients. We find the loss rate for the $^{23}\text{Na}^{39}\text{K} + ^{39}\text{K}$ mixture to be drastically suppressed, which opens interesting perspectives for sympathetic cooling.

The experiments start from ultracold weakly bound molecules. As previously described in Ref. [23], we associate $^{23}\text{Na}^{39}\text{K}$ Feshbach dimers by applying a radio frequency pulse to an ultracold mixture of bosonic ^{23}Na and ^{39}K held in a 1064 nm crossed-beam optical dipole trap with temperatures below 350 nK. We create 6×10^3 dimers in the least bound vibrational state $|f\rangle$ with a total angular momentum projection $M_F = -3$ and a binding energy of $h \times 100$ kHz at a magnetic field of 199.3 G. In terms of atomic quantum numbers the state $|f\rangle$ is mainly composed of $\alpha_1 |m_{i,\text{Na}} = -3/2, m_{i,\text{K}} = -1/2, M_S = -1\rangle + \alpha_2 |m_{i,\text{Na}} = -3/2, m_{i,\text{K}} = -3/2, M_S = 0\rangle$. M_S is the total electron spin

projection, $m_{i,\text{Na}}$ and $m_{i,\text{K}}$ are the nuclear spin projections, and $\alpha_{1/2}$ denote the state admixtures. For detection, we use a standard absorption technique of ^{39}K atoms directly from the weakly bound molecular state.

For the STIRAP transfer, we make use of external-cavity diode laser systems as already described in Ref. [24]. Both lasers are referenced simultaneously to a 10-cm-long high-finesse ultra low expansion cavity using a sideband Pound-Drever-Hall locking scheme [25]. The cavity's finesse for the pump and Stokes laser are 24 900 and 37 400, respectively, and the free spectral range is 1.499 GHz. The linewidths of both locked lasers are estimated to be below 5 kHz. Furthermore, the power of the pump laser is amplified by a tapered amplifier. Both lasers, pump and Stokes, are overlapped and focused to the position of the molecules with $1/e^2$ Gaussian beam waists of 35 and 40 μm , respectively. The direction of propagation is perpendicular to the direction of the magnetic field; thus, π ($\sigma^{+/-}$) transitions can be addressed by choosing the polarization parallel (perpendicular) to the magnetic field.

Possible transfer pathways to the ground state have been previously investigated theoretically and experimentally [24,26]. Figure 1(a) summarizes the relevant states involved in the transfer scheme. Starting from the weakly bound dimer state $|f\rangle$ with mainly triplet character, we make use of the triplet-singlet mixed excited state $|e\rangle$ to transfer the molecules into a selected hyperfine state in the rovibrational ground state $|g\rangle$ with pure singlet character. For the excited state $|e\rangle$ we choose the strongly spin-orbit coupled $B^1\Pi|v=8\rangle/c^3\Sigma^+|v=30\rangle$ state manifolds [see Fig. 1(a)], which have a large state admixture of 26%/74% [24]. The hyperfine structure of the $|X^1\Sigma^+, v=0, N=0\rangle$ ground state consists of 16 states with a total angular momentum projection $M_F = m_{i,\text{Na}} + m_{i,\text{K}}$, which group into four branches with different $m_{i,\text{Na}}$ at high magnetic fields [see Fig. 1(b)] [27]. At 199.3 G, where the molecule creation is performed, the ground states are deeply in the Paschen-Back regime. In the excited states the ^{39}K nuclear momenta are also decoupled from the other nuclear and electronic angular momenta [28]. Therefore, dipole transitions only change the latter ones. This limits the number of accessible ground states to three, which are highlighted in Fig. 1(b). Accounting only for π transitions for the pump transition to maximize the coupling strength, only a single state is accessible in the $c^3\Sigma^+$ hyperfine manifold, namely the $|e_0\rangle = |c^3\Sigma^+, m_{i,\text{Na}} = -3/2, m_{i,\text{K}} = -1/2, M_J = -1, M_F = -3\rangle$. The transition yields an energy of $12242.024(3) \text{ cm}^{-1}$ [which corresponds to a wavelength of $816.8584(2) \text{ nm}$] and is shown in Fig. 1(a). The Stokes transition, with an energy of $17453.744(3) \text{ cm}^{-1}$ [$572.94297(10) \text{ nm}$], connects the excited state to the ground state. In our case, we use a σ^- transition to the $|g\rangle = |X^1\Sigma^+, m_{i,\text{Na}} = -3/2, m_{i,\text{K}} = -1/2, M_J = 0, M_i = -2\rangle$ state. Nevertheless, our experimental setup always supports σ^- and σ^+ transitions at

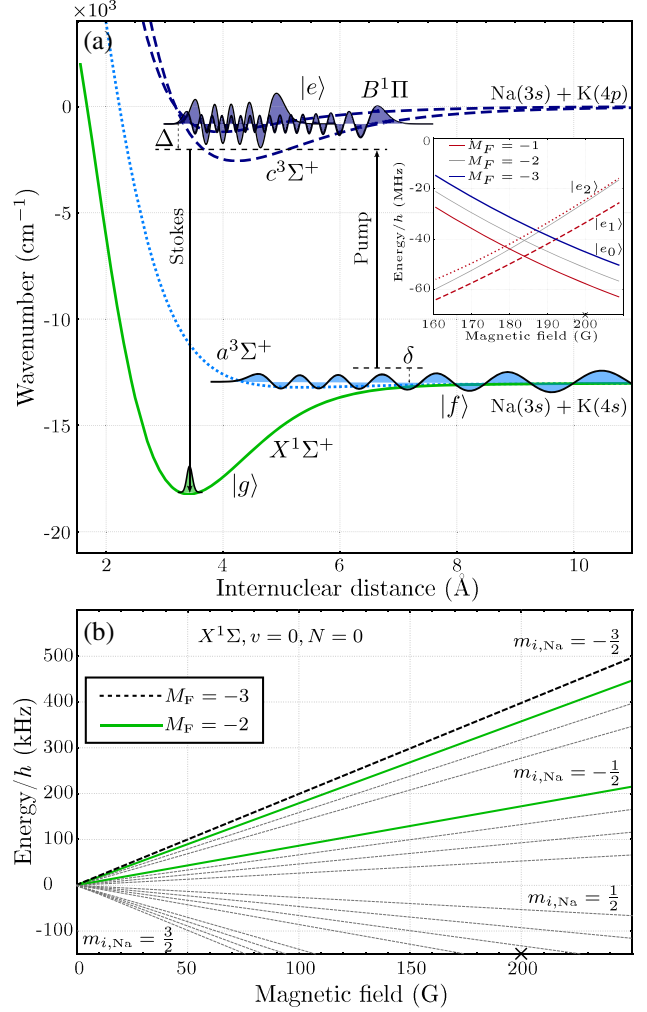


FIG. 1. (a) Potential energy curves of the $^{23}\text{Na}^{39}\text{K}$ molecule. The energy is shown in cm^{-1} as function of the internuclear distance. The solid green curve corresponds to the electronic $X^1\Sigma^+$, the dotted light blue to the $a^3\Sigma^+$, and the dashed lines to the $c^3\Sigma^+$ and $B^1\Pi$ potentials. Wave functions are shown as black lines with the corresponding shading. Amplitudes of the wave functions are not to scale. The black arrows indicate the STIRAP transitions and the one- (Δ) and two- (δ) photon detunings. The inset shows the magnetic field dependence of the pump transition to the excited states from the model in Ref. [24]. (b) Magnetic field dependence of the ground-state hyperfine energy structure. The green lines are the states with $M_F = -2$ and the black dashed line is the one with $M_F = -3$. As the states enter the Paschen-Back regime the four branches for different $m_{i,\text{Na}}$ become visible. The magnetic field, where the molecule creation process is performed, is marked with a cross on the axis.

the same time. Consequently, the ground state is coupled to two additional states $|e_{1,2}\rangle$ through σ^+ transitions [see inset Fig. 1(a)]. For the experiments and for the modeling we thus have to consider an effective five-level system. The details of the model are described in the Supplemental Material [29].

For STIRAP a high degree of phase coherence between the two independent laser sources is imperative. To prove the coherence and to determine the explicit frequencies for the two-photon Raman transition, we perform electromagnetically induced transparency (EIT) experiments on the selected states. For the measurement shown in Fig. 2(a), Rabi frequencies of $\Omega_{\text{pump}} = 2\pi \times 0.63(2)$ MHz and $\Omega_{\text{Stokes}} = 2\pi \times 4.1(2)$ MHz are used. The coherent interaction time is set to $50 \mu\text{s}$. The observed asymmetry of the molecule revival arises from a one-photon detuning $\Delta = 2\pi \times 400(20)$ kHz to the excited state $|e_0\rangle$. EIT relies only on coherent dark state effects and never populates the ground state. A coupling between the ground state and the perturbing excited states $|e_{1,2}\rangle$ does not alter the coupling scheme as the two-photon condition is not fulfilled for these states. Consequently, a three-level scheme is sufficient for its description. Figure 2(a) shows the experimental data and the theoretical prediction (solid black line) using experimentally determined parameters for Rabi frequencies and laser detunings. The errors on the parameters are displayed as dashed lines and gray shaded area. We find very good agreement of our data with the model and consequently good conditions for the STIRAP.

For the creation of ground-state molecules, we perform STIRAP starting from Feshbach molecules. As the Feshbach molecule lifetime is very short, on the order of 0.3 ms [23], STIRAP is completed $25 \mu\text{s}$ after Feshbach molecules creation. The STIRAP process itself takes $11 \mu\text{s}$ so that no significant loss from a decay of the weakly bound dimers is expected. Figure 2(b) shows a typical signal for ground-state molecule creation. The figure includes the STIRAP light pulse sequence (lower panel) and the populations of the Feshbach molecules as well as the ground-state molecules during the pulse sequence calculated by a five-level master equation. Starting with Feshbach molecules at $t = 0$, the molecules are transferred to the ground state at $t = 14 \mu\text{s}$ where the molecules become dark for the imaging light. To image the molecules, we reverse the STIRAP sequence and transfer ground-state molecules back to the Feshbach state. Because of the additional coupling of the ground state to the excited states $|e_{1,2}\rangle$, the STIRAP is highly dependent on the one-photon detuning (see Fig. 3). The states $|e_{1,2}\rangle$ act as loss channels, into which the ground-state molecules are pumped and consequently get lost. On resonance with one of the $|e_{1,2}\rangle$ states, nearly no ground-state molecules revive (see Fig. 3). Clearly, in the vicinity of the $|e_{1,2}\rangle$ states, the STIRAP benefits from fast transfers, which is restricted by the adiabaticity in the limit of small pulse-overlap areas [22]. On the other hand, the pulse-overlap area can be increased by raising the Rabi frequencies of the pulses, which accordingly also increases the undesired coupling to the states $|e_{1,2}\rangle$. We find the best results in our system for a pulse duration of $12 \mu\text{s}$ with a pump pulse delay of $-2 \mu\text{s}$ and resonant Rabi frequencies of $\Omega_{\text{pump}} = 2\pi \times 3.0(1)$ MHz and $\Omega_{\text{Stokes}} = 2\pi \times 2.3(1)$ MHz at a

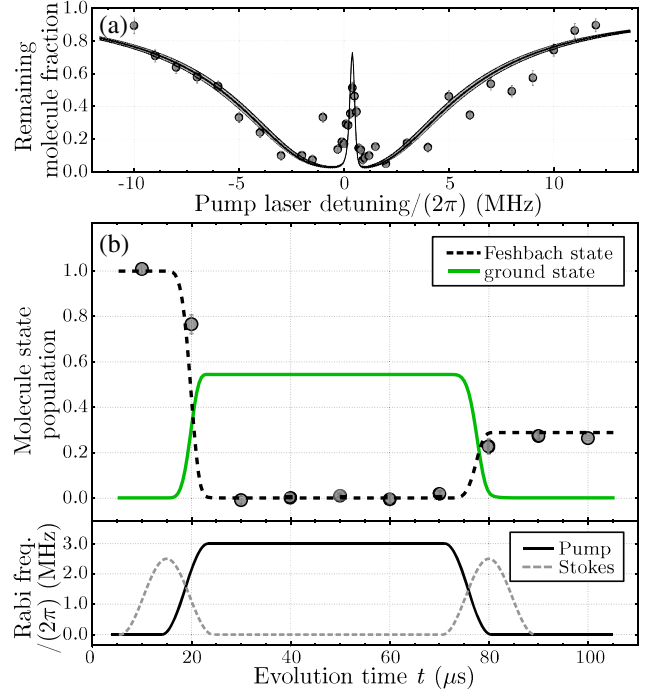


FIG. 2. EIT and time evolution of STIRAP. (a) EIT measurement together with a theory curve. The points are the remaining Feshbach molecule fraction normalized to the initial Feshbach molecule number. The solid black line is the theory curve from a three-level master equation and the dashed lines with the enclosed shaded gray area correspond to the uncertainty of the Rabi frequencies. (b) Time evolution of the Feshbach and ground-state population during a round-trip STIRAP. Data points in the upper panel are the observed Feshbach molecule number normalized to the initial molecule number. The solid green (dashed black) line is a theory curve for the ground-state (Feshbach molecule-state) population using the model described in the text and the pulses from the lower panel. The pulse duration for both lasers is $10 \mu\text{s}$. The ramping-up of the pump pulse starts $1 \mu\text{s}$ before the ramp-down of the Stokes pulse begins. The lower panel shows the pulse sequence of the pump and Stokes laser during the STIRAP. Rabi frequencies are obtained from one-photon loss measurements (not shown here). Error bars are the standard deviation coming from different experimental runs.

one-photon detuning $\Delta = 2\pi \times 8$ MHz to the center position of $|e_0\rangle$. Under these conditions single-trip STIRAP efficiency can get as high as 70%, which corresponds to a ground-state molecule number of about 4200 in a single hyperfine spin state (see inset of Fig. 3). Moreover, we do not observe heating effects of the molecules due to the STIRAP (see Supplemental Material [29]), leading to a phase-space density of up to 0.14. To model the influence of the states $|e_{1,2}\rangle$ on the STIRAP we apply a five-level master equation model fit (solid curve in Fig. 3) and compare it to an ideal three-level one (dashed curve in Fig. 3). The model is described in detail in the Supplemental Material [29]. In the comparison between the five- and three-level model the influence of the states $|e_{1,2}\rangle$ gets clear. It indicates that

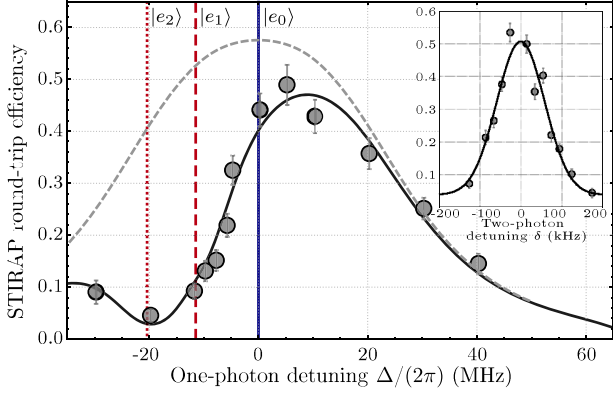


FIG. 3. One- and two-photon detuning for STIRAP. The round-trip efficiency for STIRAP is shown as a function of the one-photon detuning Δ . The pulse sequence and laser intensities for these measurements were kept constant corresponding to the optimal values given in the text. The vertical solid blue (dashed red) [dotted red] line is the position of the $|e_{0(1|2)}\rangle$ state deduced from measurements and the model developed in Ref. [24]. The solid black curve is a fit using the five-level master equation model and the individual couplings of the Stokes laser to the $|e_{1,2}\rangle$ states as free parameters. The dashed gray curve is a theory curve from a three-level model using the same set of parameters. The inset shows the STIRAP round-trip efficiency dependent on the two-photon detuning δ with a phenomenological Gaussian fit. The error bars for both plots are the standard error coming from different experimental cycles.

the STIRAP efficiency can be easily increased by choosing a different excited state, experimental geometric condition, such as laser polarization relative to the magnetic field axis, and larger STIRAP pulse overlap areas, which is discussed in the Supplemental Material [29].

After the transfer to the ground state the molecules are still immersed in a gas of ^{23}Na and ^{39}K atoms remaining from the creation process of the weakly bound dimers. ^{23}Na atoms can be removed by applying a $500\ \mu\text{s}$ resonant light pulse. ^{39}K atoms can be removed by transferring them to the $|f=2, m_f=-2\rangle$ state by a rapid adiabatic passage and a subsequent resonant light pulse for $500\ \mu\text{s}$. By introducing a variable hold time between the atom removals and the reversed STIRAP pulse, we perform loss measurements, which we analyze assuming a two-body decay model to extract the two-body decay rate coefficient. The model is described in the Supplemental Material [29].

First, we investigate the mixture of molecules and atoms. We observe fast losses from $^{23}\text{Na}^{39}\text{K} + ^{23}\text{Na}$ collisions (see Fig. 4). The extracted loss rate coefficient is $1.25(14) \times 10^{-10}\ \text{cm}^3\ \text{s}^{-1}$, which is close to the theoretical prediction of $1.3 \times 10^{-10}\ \text{cm}^3\ \text{s}^{-1}$ taken from Ref. [31]. We assign the saturation of the losses to chemical reactions, in which $^{23}\text{Na}_2$ dimers are formed. Thus, ^{23}Na atoms are generally removed as fast as possible from the trap as the ground-state molecule number suffers from the strong losses.

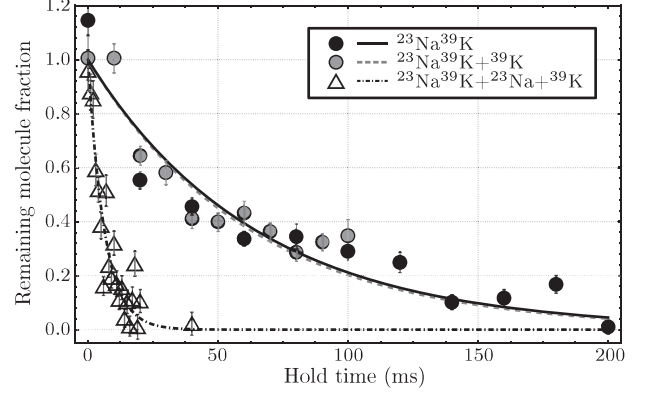


FIG. 4. Loss measurements of pure ground-state molecules and with remaining atoms. The open triangles are measurements without atom removal. The fast loss originates from the chemical reaction with ^{23}Na atoms. The gray circles are measurements with only ^{23}Na removed while still ^{39}K atoms remain in the trap. The solid circles are measurements performed with a pure molecular ensemble. The data are normalized to the molecule number without holding time obtained from the individual fits. The curves are fits using a coupled differential equation system for modeling the losses. For the corresponding loss rate coefficients, see text. All error bars are the standard deviation resulting from different experimental runs.

In a next step, we measure losses in a pure molecular ensemble (see Fig. 4). The two-body loss rate coefficient is measured to be $4.49(1.18) \times 10^{-10}\ \text{cm}^3\ \text{s}^{-1}$. This loss rate coefficient is comparable to the universal limit [32] and is possibly resulting from sticky collisions [21] and subsequent removal of the tetramers from the trap. Comparable observations have been made in experiments with other bosonic ground-state molecules, such as $^{87}\text{Rb}^{133}\text{Cs}$ and $^{23}\text{Na}^{87}\text{Rb}$ [12,13]. However, the loss rate coefficient for the fermionic counterpart $^{23}\text{Na}^{40}\text{K}$ is $6 \times 10^{-11}\ \text{cm}^3\ \text{s}^{-1}$ [10]. The difference can be assigned to the absence of the centrifugal barrier in bosonic s -wave collisions.

Next, we investigate collisions between the molecules and ^{39}K atoms. Surprisingly, even a high density of ^{39}K atoms in the nonstretched $|f=1, m_f=-1\rangle_{\text{K}}$ state colliding with $^{23}\text{Na}^{39}\text{K}$ in the nonstretched hyperfine ground state does not increase the molecular loss (compare Fig. 4), although sticky collisions with trimer formation are also expected in mixtures of $^{23}\text{Na}^{39}\text{K} + ^{39}\text{K}$ [33]. In these collisional trimer complexes nuclear spin transitions can occur leading to subsequent loss of molecules from the prepared hyperfine state. We analyze the observed decay of the molecular cloud using the model fit described in the Supplemental Material [29]. We find the loss rate coefficient for the two-body $^{23}\text{Na}^{39}\text{K} + ^{39}\text{K}$ collisions to be consistent with zero with an upper limit of $1.5 \times 10^{-14}\ \text{cm}^3\ \text{s}^{-1}$. The corresponding universal limit is calculated by using the prediction from Refs. [33,34] and parameters from Ref. [35] and results in $1.3 \times 10^{-10}\ \text{cm}^3\ \text{s}^{-1}$. Note that this corresponds to a

suppression of the two-body decay in comparison to the universal limit by more than 3 orders of magnitude. This is in contrast to experiments reported for fermionic molecules in collisions with bosonic atoms ($^{40}\text{K}^{87}\text{Rb} + ^{87}\text{Rb}$ [1]) and fermionic atoms ($^{23}\text{Na}^{40}\text{K} + ^{40}\text{K}$ [36]), where such suppression of losses far below the universal limit has not been observed for sticky molecule-atom collisions. The only experiment describing such a suppression has been performed in a mixture of the fermionic molecule $^6\text{Li}^{23}\text{Na}$ with the bosonic atom ^{23}Na with both particles in their lowest stretched hyperfine states [37]. Here, we now report collisions in nonstretched states with loss rates far below the universal limit, which might result from a low density of resonant states [33]. Individual resonances might thus be resolvable in this system and demand for further investigations of loss rates in other spin channels and magnetic fields. Moreover, with the low loss rate between $^{23}\text{Na}^{39}\text{K}$ molecules and ^{39}K atoms in the named hyperfine state it might be possible to use ^{39}K atoms as a coolant for bosonic $^{23}\text{Na}^{39}\text{K}$ molecules to further increase the molecular phase-space density [37].

In conclusion, we have reported the first creation of an ultracold high phase-space density gas of bosonic $^{23}\text{Na}^{39}\text{K}$ ground-state molecules. We have investigated the creation process and find very good agreement with our five-level model. The spin-polarized molecular ensemble yields up to 4200 molecules and is chemically stable. We extract the two-body decay coefficient for the bosonic $^{23}\text{Na}^{39}\text{K}$ molecules. For molecule-atom collisions, we find a significant suppression of the two-body decay rate in collisions between $^{23}\text{Na}^{39}\text{K}$ molecules and ^{39}K atoms in nonstretched states. This unexpected result demands further experiments including the analysis of collisions between molecules and atoms in different hyperfine states and as a function of magnetic field to identify possible scattering resonances. These experiments can be extended to a detailed comparison of collision properties between same species molecules of different quantum statistics.

We thank M. Siercke for enlightening comments and discussions and the group of P. O. Schmidt, PTB Brunswick, for providing scientific material for the Raman laser system. We gratefully acknowledge financial support from the European Research Council through ERC Starting Grant POLAR and from the Deutsche Forschungsgemeinschaft (DFG) through CRC 1227 (DQ-mat), project A03, and FOR 2247, project E5. P. G. thanks the DFG for financial support through RTG 1991.

*voges@iqo.uni-hannover.de

†silke.ospelkaus@iqo.uni-hannover.de

[1] S. Ospelkaus, K.-K. Ni, D. Wang, M. H. G. de Miranda, B. Neyenhuis, G. Quéméner, P. S. Julienne, J. L. Bohn, D. S. Jin, and J. Ye, *Science* **327**, 853 (2010).

- [2] M. Guo, X. Ye, J. He, M. L. González-Martínez, R. Vexiau, G. Quéméner, and D. Wang, *Phys. Rev. X* **8**, 041044 (2018).
- [3] S. A. Moses, J. P. Covey, M. T. Miecnikowski, D. S. Jin, and J. Ye, *Nat. Phys.* **13**, 13 (2016).
- [4] L. De Marco, G. Valtolina, K. Matsuda, W. G. Tobias, J. P. Covey, and J. Ye, *Science* **363**, 853 (2019).
- [5] D. DeMille, *Phys. Rev. Lett.* **88**, 067901 (2002).
- [6] B. Yan, S. Moses, B. Gadway, J. Covey, K. Hazzard, A. Rey, D. Jin, and J. Ye, *Nature (London)* **501**, 521 (2013).
- [7] M. H. G. de Miranda, A. Chotia, B. Neyenhuis, D. Wang, G. Quéméner, S. Ospelkaus, J. L. Bohn, J. Ye, and D. S. Jin, *Nat. Phys.* **7**, 502 (2011).
- [8] S. A. Will, J. W. Park, Z. Z. Yan, H. Loh, and M. W. Zwierlein, *Phys. Rev. Lett.* **116**, 225306 (2016).
- [9] K.-K. Ni, S. Ospelkaus, M. H. G. de Miranda, A. Peer, B. Neyenhuis, J. J. Zirbel, S. Kotochigova, P. S. Julienne, D. S. Jin, and J. Ye, *Science* **322**, 231 (2008).
- [10] J. W. Park, S. A. Will, and M. W. Zwierlein, *Phys. Rev. Lett.* **114**, 205302 (2015).
- [11] T. M. Rvachov, H. Son, A. T. Sommer, S. Ebadi, J. J. Park, M. W. Zwierlein, W. Ketterle, and A. O. Jamison, *Phys. Rev. Lett.* **119**, 143001 (2017).
- [12] T. Takekoshi, L. Reichsöllner, A. Schindewolf, J. M. Hutson, C. R. Le Sueur, O. Dulieu, F. Ferlaino, R. Grimm, and H.-C. Nägerl, *Phys. Rev. Lett.* **113**, 205301 (2014).
- [13] M. Guo, B. Zhu, B. Lu, X. Ye, F. Wang, R. Vexiau, N. Bouloufa-Maafa, G. Quéméner, O. Dulieu, and D. Wang, *Phys. Rev. Lett.* **116**, 205303 (2016).
- [14] P. S. Żuchowski and J. M. Hutson, *Phys. Rev. A* **81**, 060703 (R) (2010).
- [15] M. Gröbner, P. Weinmann, E. Kirilov, H.-C. Nägerl, P. S. Julienne, C. R. Le Sueur, and J. M. Hutson, *Phys. Rev. A* **95**, 022715 (2017).
- [16] P. D. Gregory, M. D. Frye, J. A. Blackmore, E. M. Bridge, R. Sawant, J. M. Hutson, and S. L. Cornish, *Nat. Commun.* **10**, 3104 (2019).
- [17] M.-G. Hu, Y. Liu, D. D. Grimes, Y.-W. Lin, A. H. Gheorghe, R. Vexiau, N. Bouloufa-Maafa, O. Dulieu, T. Rosenband, and K.-K. Ni, *Science* **366**, 1111 (2019).
- [18] A. Christianen, M. W. Zwierlein, G. C. Groenenboom, and T. Karman, *Phys. Rev. Lett.* **123**, 123402 (2019).
- [19] P. D. Gregory, J. A. Blackmore, S. L. Bromley, and S. L. Cornish, *Phys. Rev. Lett.* **124**, 163402 (2020).
- [20] Y. Liu, M.-G. Hu, M. A. Nichols, D. D. Grimes, T. Karman, H. Guo, and K.-K. Ni, *arXiv:2002.05140*.
- [21] M. Mayle, G. Quéméner, B. P. Ruzic, and J. L. Bohn, *Phys. Rev. A* **87**, 012709 (2013).
- [22] N. V. Vitanov, A. A. Rangelov, B. W. Shore, and K. Bergmann, *Rev. Mod. Phys.* **89**, 015006 (2017).
- [23] K. K. Voges, P. Gersema, T. Hartmann, T. A. Schulze, A. Zenesini, and S. Ospelkaus, *Phys. Rev. A* **101**, 042704 (2020).
- [24] K. K. Voges, P. Gersema, T. Hartmann, T. A. Schulze, A. Zenesini, and S. Ospelkaus, *New J. Phys.* **21**, 123034 (2019).
- [25] R. W. P. Drever, J. L. Hall, F. V. Kowalski, J. Hough, G. M. Ford, A. J. Munley, and H. Ward, *Appl. Phys. B* **31**, 97 (1983).
- [26] T. A. Schulze, I. I. Temelkov, M. W. Gempel, T. Hartmann, H. Knöckel, S. Ospelkaus, and E. Tiemann, *Phys. Rev. A* **88**, 023401 (2013).

- [27] J. Aldegunde and J. M. Hutson, *Phys. Rev. A* **96**, 042506 (2017).
- [28] I. Temelkov, H. Knöckel, A. Pashov, and E. Tiemann, *Phys. Rev. A* **91**, 032512 (2015).
- [29] See Supplemental Material at <http://link.aps.org/supplemental/10.1103/PhysRevLett.125.083401> for details about the five-level STIRAP model, the alternative STIRAP pathways, the temperature measurements of molecules, and the models for the calculations of the molecule-atom and molecule-molecule loss rate coefficients, which includes Ref. [30].
- [30] H. J. Carmichael, *Statistical Methods in Quantum Optics I: Master Equations and Fokker-Planck Equations* (Springer-Verlag, Berlin, 1999).
- [31] H. Li, M. Li, C. Makrides, A. Petrov, and S. Kotochigova, *Atoms* **7**, 36 (2019).
- [32] P. S. Julienne, T. M. Hanna, and Z. Idziaszek, *Phys. Chem. Chem. Phys.* **13**, 19114 (2011).
- [33] M. Mayle, B. P. Ruzic, and J. L. Bohn, *Phys. Rev. A* **85**, 062712 (2012).
- [34] G. Quéméner, J. L. Bohn, A. Petrov, and S. Kotochigova, *Phys. Rev. A* **84**, 062703 (2011).
- [35] B. E. Londoño, J. E. Mahecha, E. Luc-Koenig, and A. Crubellier, *Phys. Rev. A* **82**, 012510 (2010).
- [36] H. Yang, D.-C. Zhang, L. Liu, Y.-X. Liu, J. Nan, B. Zhao, and J.-W. Pan, *Science* **363**, 261 (2019).
- [37] H. Son, J. J. Park, W. Ketterle, and A. O. Jamison, *Nature (London)* **580**, 197 (2020).

Supplemental Material: An ultracold gas of bosonic $^{23}\text{Na}^{39}\text{K}$ ground-state molecules

Kai K. Voges,^{1,*} Philipp Gersema,¹ Mara Meyer zum Alten Borgloh,¹
Torben A. Schulze,¹ Torsten Hartmann,¹ Alessandro Zenesini,^{1,2} and Silke Ospelkaus^{1,†}

¹*Institut für Quantenoptik, Leibniz Universität Hannover, 30167 Hannover, Germany*

²*INO-CNR BEC Center and Dipartimento di Fisica, Università di Trento, 38123 Povo, Italy*

(Dated: July 30, 2020)

In this supplement, we provide additional details on the 5-level STIRAP model, alternative STIRAP pathways for the $^{23}\text{Na}^{39}\text{K}$ molecules and the temperature measurements of the molecules. Furthermore, we detail on the loss model used for the determination of the two-body decay loss coefficients for molecule-molecule and molecule-atom collisions.

5-level STIRAP model

STIMulated Raman Adiabatic Passage (STIRAP) for the transfer of weakly bound Feshbach molecules to the ground state, and vice versa, is typically performed in a pure 3-level Λ -system [1]. In our case, the Feshbach molecule state is named $|f\rangle$, the ground state $|g\rangle$ and the excited states are named $|e_i\rangle$. The laser beams for the Pump and the Stokes transitions are copropagating and perpendicular to the magnetic field. For both beams, linear polarizations parallel (\parallel) to the magnetic field access π -transitions in the molecules and linear polarizations perpendicular (\perp) to the magnetic field access always both σ^+ - and σ^- -transitions.

The molecular starting state $|f\rangle$ can be described as a composed state of $\alpha_1 |m_{i,\text{Na}} = -3/2, m_{i,\text{K}} = -1/2, M_S = -1\rangle + \alpha_2 |m_{i,\text{Na}} = -3/2, m_{i,\text{K}} = -3/2, M_S = 0\rangle$, where M_S is the total electron spin projection and $\alpha_{1/2}$ represent state admixtures. With the goal of maximizing the Rabi frequency $\Omega_{\text{P(ump)}}$, we choose excited states from the triplet hyperfine manifold of the coupled triplet-singlet states $|c^3\Sigma^+, v = 30\rangle$ and $|B^1\Pi, v = 8\rangle$ [2, 3]. Moreover, we choose the polarization of the Pump beam to be \parallel . The only possible accessible excited state is the $|e_0\rangle = |m_{i,\text{Na}} = -3/2, m_{i,\text{K}} = -1/2, M_J = -1, M_F = -3\rangle$.

Using \perp polarization for the Stokes laser, we reach the $|g\rangle = |m_{i,\text{Na}} = -3/2, m_{i,\text{K}} = -1/2, M_J = 0, M_i = -2\rangle$ ground state with a σ^- -transition. Other states in the ground state cannot be reached, because the ground state manifold has pure singlet character and is deeply in the Paschen-Back regime. Thus, nuclear and electronic spins are decoupled so that only the electronic spin projection can be changed by an optical transition.

At the same time σ^+ -transitions couple the state $|g\rangle$ to the excited state $|e_{1,2}\rangle$ which have both state contributions in the atomic base from $|m_{i,\text{Na}} = -3/2, m_{i,\text{K}} = -1/2, M_J = 1, M_F = -1\rangle$. Note that the Pump beam does not couple the state $|f\rangle$ to the states $|e_{1,2}\rangle$ due to $\Delta M_F = 2$.

In summary, the experimental situation requires to extend the typical 3-level Λ -system (for the state $|f\rangle$, $|e_0\rangle$ and $|g\rangle$) to a 5-level system (for the states $|f\rangle$, $|e_0\rangle$,

$|g\rangle$ and $|e_{1,2}\rangle$). The model Hamilton operator $H(t)$ for the light-molecule interaction and the molecular energies in the rotating-wave-approximation is

$$\hbar \begin{bmatrix} 0 & \Omega_{\text{P}}(t)/2 & 0 & 0 & 0 \\ \Omega_{\text{P}}(t)/2 & \Delta_{\text{P}} & \Omega_{\text{S}}(t)/2 & 0 & 0 \\ 0 & \Omega_{\text{S}}(t)/2 & \Delta_{\text{P}} - \Delta_{\text{S}} & \Omega_{\text{S},1}(t)/2 & \Omega_{\text{S},2}(t)/2 \\ 0 & 0 & \Omega_{\text{S},1}(t)/2 & \Delta_{\text{P}} - \Delta_{\text{S},1} & 0 \\ 0 & 0 & \Omega_{\text{S},2}(t)/2 & 0 & \Delta_{\text{P}} - \Delta_{\text{S},2} \end{bmatrix}.$$

The time dependent state vector is represented by $(c_f(t), c_{e_0}(t), c_g(t), c_{e_1}(t), c_{e_2}(t))^T$, where c_i is the probability amplitude of the corresponding state $|i\rangle$. $\Omega_{\text{P}}(t)$ is the Rabi frequency for the Pump transition and $\Omega_{\text{S}(\text{tokes})}(t)$, $\Omega_{\text{S},1}(t)$ and $\Omega_{\text{S},2}(t)$ are the Rabi frequencies for the Stokes transition to the excited states $|e_0\rangle, |e_1\rangle$ and $|e_2\rangle$, respectively. Note, that all Rabi frequencies are time dependent and real. Δ_{P} and Δ_{S} are the detunings of the Pump and Stokes laser frequency to the respective molecular transition. The relative positions of the excited states $|e_{1,2}\rangle$ to $|e_0\rangle$ are $\Delta_{\text{S},1} = 2\pi \times (-10)$ MHz and $\Delta_{\text{S},2} = 2\pi \times (-21)$ MHz, respectively, at 199.3 G and are taken from our excited state model presented in [3]. To additionally model losses of the molecules from the excited states, a sixth state $|l\rangle$ is introduced, which is not directly coupled to any other state. This is important for the numerical calculation, as it keeps the population normalized during the evaluation. The dynamics of the system can be modeled by solving the master equation in Lindblad representation with the density matrix $\rho(t)$

$$\dot{\rho}(t) = -\frac{i}{\hbar}[H(t), \rho(t)] + \sum_k \gamma_k D[A_k]\rho(t). \quad (1)$$

The second term denotes the losses from the system, where γ_k are the decay rates of the excited states which we set for all three states to $\gamma_0 = \gamma_1 = \gamma_2 = 2\pi \times 11$ MHz and $D[A_k]$ are the corresponding Lindblad superoperators with the jump operator A_k from the excited state $|e_k\rangle$ to the loss state $|l\rangle$ [4].

For the fit of the experimental data in Fig. 3 we use this model with the Rabi frequencies $\Omega_{\text{S},1}$ and $\Omega_{\text{S},2}$ as free parameters as well as the STIRAP Rabi frequencies Ω_{P} and Ω_{S} constrained to their experimentally determined uncertainties. We assign the optimum of the fit within

these constrains, confirming the consistency of our data. Furthermore, this model was used to also calculate the STIRAP time dynamics of Fig. 2(b).

The 5-level model can be reduced to a 3-level one by setting the coupling to the excited state $|e_{1,2}\rangle$ to zero. We use this to calculate the theoretical electromagnetically induced transparency curve in Fig. 2(a) and the optimal curve for the one-photon detuning (gray dashed line) in Fig. 3.

Alternative STIRAP pathways

Alternative STIRAP pathways using states from the $c^3\Sigma^+$ potential may be possible with either another STIRAP beam alignment, for example parallel to the magnetic field direction, and/or with other polarizations. In case of a perpendicular alignment, as it is described above, alternative STIRAP pathways to the ground state $|g\rangle$ are possible when switching the laser polarizations, using now \perp polarization for the Pump and \parallel polarization for the Stokes beam; see Fig.S1.

We identify two additional states $|e_{a,1}\rangle$ and $|e_{a,2}\rangle$ suiting these pathways, both yielding state contributions from the $|m_{i,\text{Na}} = -3/2, m_{i,\text{K}} = -1/2, M_J = 0, M_F = -2\rangle$ in the atomic base. Their transitions are +189 and -146 MHz detuned from the original one $|e_0\rangle$ and do not possess neighboring states close by which may be populated through σ^- -transitions to the state $|f\rangle$. The additional STIRAP pathways are identified based on the model of the excited states [3]. Simulations, utilizing the model described above suggest round-trip efficiencies of more than 80%. These states will be object of future investigation.

Loss coefficients

Two-body loss coefficients for molecule-molecule and molecule-atom collisions are extracted from the decay of the $^{23}\text{Na}^{39}\text{K}$ ground-state molecule ensemble.

In a pure molecular ensemble, losses can be assigned to two-body losses with tetramer formation and subsequent removal or loss of the tetramers, see [5]. We obtain an analytic solution for the two-body loss of the ground-state molecule number $N_{\text{NaK}}(t)$ [6]

$$N_{\text{NaK}}(t) = \frac{N_{\text{NaK},0}}{\left(1 + \frac{11}{8} \epsilon k_{\text{NaK},2} t\right)^{8/11}}, \quad (2)$$

where $N_{\text{NaK},0}$ is the initial ground-state molecule number, $k_{\text{NaK},2}$ the molecular two-body loss coefficient and $\epsilon = (m_{\text{NaK}}\bar{\omega}/(2\pi k_B))^{3/2}$ with $\bar{\omega}$ the average trap frequency and k_B the Boltzmann constant. $N_{\text{NaK},0}$ and $k_{\text{NaK},2}$ were used as free parameters for the fit. For the model of the loss from molecule-atom collisions

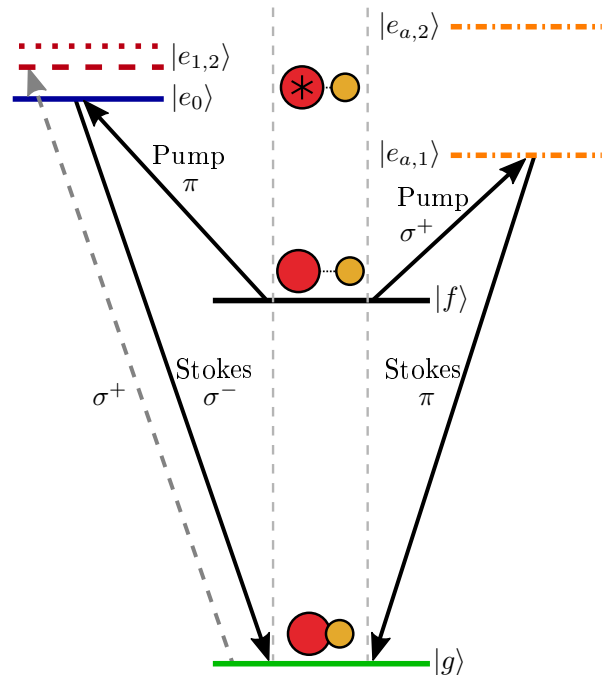


FIG. S1. STIRAP pathways. This figure shows the current (left) and the alternative (right) STIRAP pathway. Pathways start from the Feshbach molecule state $|f\rangle$ (black solid line) and end in the ground state $|g\rangle$ (green solid line). The excited states $|e_i\rangle$ are the ones described in the text. For the current STIRAP the Pump beam drives π -transitions and the Stokes beam σ^- -transitions, displayed as solid arrows. On contrary, the Stokes beam couples also with σ^+ -transition to the excited states $|e_{1,2}\rangle$ (dashed arrow). The alternative STIRAP pathways use σ^+ -transitions for the Pump and π -transitions for the Stokes beam. The states $|e_{a,1,2}\rangle$ are shown as orange dashed-dotted lines.

we use the coupled differential equation system:

$$\begin{aligned} \dot{N}_{\text{NaK}}(t) &= -\epsilon k_{\text{NaK},2} \frac{N_{\text{NaK}}(t)^2}{T_{\text{NaK}}(t)^{3/2}} - \eta k_a N_{a,0} N_{\text{NaK}}(t) \\ \dot{T}_{\text{NaK}}(t) &= \epsilon k_{\text{NaK},2} \frac{N_{\text{NaK}}(t)}{4\sqrt{T_{\text{NaK}}(t)}}. \end{aligned} \quad (3)$$

η is the density overlap between molecules and atoms, k_a the loss coefficient for the molecule-atom collision, $N_{a,0}$ the initial atom number and T_{NaK} the temperature of the ground-state molecules.

Note, that in the model anti-evaporation effects may be considered for molecules only, or for both, molecules and atoms. The difference of these two cases is smaller than our experimental uncertainties. The presented data only consider effects on molecules.

Temperature measurement for molecular clouds

Temperature measurements for atomic clouds are typically done through time-of-flight (TOF) measurements after releasing them from the trap and fitting a temperature dependent expansion curve to the clouds width. For ground-state molecules, this technique is limited by the free expansion time, as the molecules might leave the region of the STIRAP laser beams which is needed to transfer the ground-state molecules back to the Feshbach state for imaging. In our experiment, the STIRAP beam foci have $1/e^2$ radii of 35 and 40 μm , respectively, allowing for almost no free expansion time of the molecules before leaving the STIRAP beam area.

To still measure the temperature of the ground-state molecule ensemble we reverse the entire molecule creation process, by means of STIRAP and Feshbach molecule dissociation, before performing the TOF and imaging on the dissociated atoms. Note, that for our Feshbach molecules, imaging normally takes place from the Feshbach molecule state itself, as the linewidth of the imaging transition in ^{39}K is larger than the binding energy of the weakly bound dimers [7]. A temperature measurement in TOF with Feshbach molecules is also not possible, because the Feshbach molecule lifetime is very short, about 1 ms in a pure molecular ensemble, and an appropriate signal would be lost very fast. A complete dissociation within 600 μs using a resonant radio frequency of 210.0 MHz to the $|f = 1, m_f = -1\rangle_{\text{Na}} + |f = 1, m_f = -1\rangle_{\text{K}}$ is performed immediately after the

backwards STIRAP. Temperature TOF measurements are then performed on the long living atomic ensemble. All atoms involved in the temperature measurement come originally from deeply bound molecules.

The extracted temperature from the atoms show the same temperature as the initial atoms measured before the molecule creation happened. Consequently, all transfers in between (Feshbach molecule creation, STIRAPs, atom state preparations and removals, Feshbach molecule dissociation) do not heat the molecule ensemble.

* voges@iqo.uni-hannover.de

† silke.ospelkaus@iqo.uni-hannover.de

- [1] N. V. Vitanov, A. A. Rangelov, B. W. Shore, and K. Bergmann, *Rev. Mod. Phys.* **89**, 015006 (2017).
- [2] T. A. Schulze, I. I. Temelkov, M. W. Gempel, T. Hartmann, H. Knöckel, S. Ospelkaus, and E. Tiemann, *Phys. Rev. A* **88**, 023401 (2013).
- [3] K. K. Voges, P. Gersema, T. Hartmann, T. A. Schulze, A. Zenesini, and S. Ospelkaus, *New Journal of Physics* **21**, 123034 (2019).
- [4] H. J. Carmichael, Springer-Verlag Berlin Heidelberg 10.1007/978-3-662-03875-8 (1999).
- [5] P. D. Gregory, M. D. Frye, J. A. Blackmore, E. M. Bridge, R. Sawant, J. M. Hutson, and S. L. Cornish, *Nature Communications* **10** (2019).
- [6] The derivation of the analytical solution will be presented in a future publication.
- [7] K. K. Voges, P. Gersema, T. Hartmann, T. A. Schulze, A. Zenesini, and S. Ospelkaus, *Phys. Rev. A* **101**, 042704 (2020).

5 Molecule-molecule and atom-molecule collisions

Within this chapter, I describe our recent studies of molecule-molecule [A6] and atom-molecule [A7] collisions. The experiments have revealed astonishing collisional properties which are, at the current point, far from understood and have initiated lively theoretical discussions and novel experiments.

5.1 Probing photoinduced two-body losses [A6]

As briefly mentioned in the introduction (see section 1.3), the observation of rapid two-body losses near the universal scattering rate, even for chemically stable molecules, was against the expectations. $^{23}\text{Na}^{39}\text{K}$ ground-state molecules are no exception to this, as shown in [A5]. A possible explanation was introduced by Mayle *et al.* by the concept of long-lived four body complexes that form during a collision, so-called sticky collisions. [78]. In this model the long lifetime of these metastable tetramers originates from the high density of ro-vibrationally excited tetramer states, that are close to the energy of the scattering channel. As the two molecules approach each other, they ergodically explore the energetically permissible tetramer states. Eventually they will split back into two separate molecules, with their initial quantum numbers conserved. This is crucial as the molecules can only be detected in the experiment after they were successfully transferred back to the Feshbach molecule state. This is done by another STIRAP pulse, which is state-sensitive. The lifetime of these complexes (or in other words the average time delay until the molecules separate again) τ_C can be calculated using the Rice-Ramsperger-Kassel-Marcus (RRKM) theory

$$\tau_C = \frac{2\pi\hbar\rho}{N_0}, \quad (5.1)$$

where ρ is the density of resonant tetramer states and N_0 the number of available exit channels [79]. In ultracold chemically stable molecular collisions this number can be as low as $N_0 = 1$.

Mayle *et al.* calculated that the lifetime of the complexes is on the order of many milliseconds and long enough to make it likely for the complex to collide with another molecule, resulting in the loss of all three molecules [78].

In 2019 Christianen *et al.* estimated the density of states (DOS) to be much lower. Due to the resulting lower lifetime of the complex, in the region of only a few microseconds, the collision of a complex with another molecule became unlikely. Therefore, they proposed a different loss mech-

anism that is photoexcitation of the complex to an electronically excited tetramer state through light from the optical dipole trap [79]. Even though the typically used ODT wavelengths, such as 1064 nm or 1550 nm, are far off-resonant to the next nearest excited dimer states, this is no longer true for the tetramer states. Christianen *et al.* calculated a laser excitation lifetime τ_{Laser} of $0.3 \mu\text{s}$ for a Na_2K_2 complex at an ODT trap depth of $10 \mu\text{K}$. This is much lower than the estimated complex lifetime for the bosonic $^{23}\text{Na}^{39}\text{K}$ molecule, $\tau_{\text{C,NaK}} = 6 \mu\text{s}$. Shortly thereafter, the idea of testing this hypothesis with ultracold molecules in a stroboscopic/chopped ODT emerged, where the ODT light is periodically turned on (bright) and off (dark). If the loss is indeed dominated by photoexcitations of the complexes, molecular decay should come to a halt in a dark environment, leading to a longer lifetime dependent on the ratio between the dark time t_d and the complex lifetime τ_C as well as the ratio between dark and bright time. As a chopped trap might lead to additional heating and consequently to an overall higher loss rate which would diminish possible lifetime enhancements, the experiments were also performed in direct comparison between two chopped traps, one with an additional "killing" beam, see [A6]. The implementation of the chopped cODT can be found in the supplemental material of [A6].

To our surprise and in stark contrast to the theoretical expectations, no significant enhancement was observed, even though at the same time Gregory *et al.* have been successful, with measured complex lifetimes close to the theoretical expectations [80]. Soon after a direct observation of K_2Rb_2 complexes has been achieved, also with good theoretical and experimental agreement [81]. However, simultaneously performed experiments on fermionic NaK or bosonic NaRb also showed no evidence of photoexcitation. This makes systematic experimental errors unlikely as the source of the observed discrepancy. To corroborate the experimental findings, we collaborated with the NaRb group in Hong Kong led by Prof. Dr. D. Wang. Simultaneously the fermionic NaK group in Munich also published their results [82]. After the publication of our findings in [A6], the Durham group of Simon Cornish carried out further investigations of the loss rates of their RbCs molecules in a chopped ODT, this time in non-stretched molecular hyperfine states. Interestingly they observed a diminished suppression of losses, which could be attributed to higher complex lifetimes due to a higher DOS or inelastic losses that happen during a collision [100].

These results emphasize, that the collisional processes between two molecules are to date not well understood. A possible oversight in the simulation of complex formation might be due to issues with the application of RRKM theory to ultracold collisions between $^{23}\text{Na}^{87}\text{Rb}$ and $^{23}\text{Na}^{39}\text{K}$. The predicted DOS is less than $\frac{1}{k_B \mu\text{K}}$ [79], where k_B is the Boltzmann constant, resulting in a low number of accessible resonant states. The RRKM theory can be applied in scattering processes with a high DOS and treats them in a statistical manner, so that one does not need to consider individual resonances, which might not be justified in our molecular system [78, 101]. The predicted lifetime is also only of value if the molecules can actually explore all possible states ergodically, although for alkali molecules this is assumed to be true [102]. Due to these concerns Croft *et al.* had a more detailed view at the case of ultracold non-reactive molecules. They draw the conclusion

that a statistical approach should be valid, due to for example overlapping resonances, and that the RRKM theory just gives an upper bound for the complex decay rate, especially for only one open channel. As this is the case for ultracold non-reactive molecules, this might lead to a higher complex lifetime.

Another possible explanation for a longer lifetime might be the occurrence of nuclear spin changes, that drastically increase the DOS. In experiments with KRb molecules it was verified, that the nuclear spin is conserved even after inelastic processes [77]. Jachymski *et al.* [103] propose that this is only due to the relatively high number of open channels in such reactive collisions, as this presumably prevents spin-changing processes. This could be completely different for $^{23}\text{Na}^{87}\text{Rb}$ and $^{23}\text{Na}^{39}\text{K}$, where the nuclear spin might not be conserved during complex formation, resulting in a drastically increased DOS.

In 2021 Kłos *et al.* used a different technique to study molecular collisions, which does not utilize a statistical approach. This was done through real-time simulations of the time-dependent classical collision trajectories [104]. These computations, done for $^{23}\text{Na}^{87}\text{Rb}$, also showed evidence for long-lived collisional complexes that are subsequently excited through the 1064 nm ODT light with near unity probability. Still these results can not explain the absence of a decrease of the molecular loss rate in a modulated trap [104].

In summary, these results make it clear that promising work has already been done to better understand ultracold molecular collisions, but that further experiments are needed to confirm these hypotheses and answer open questions.

In the following paper photoinduced two-body loss processes of ultracold bosonic $^{23}\text{Na}^{87}\text{Rb}$ and $^{23}\text{Na}^{39}\text{K}$ are probed utilizing a chopped optical dipole trap. Measurements with different chopping frequencies, duty cycles (the ratio between bright and dark times), killing beam intensities and wavelengths have been performed and compared to theoretical expectation. Together with the group of Prof. D. Wang from Hong Kong working with $^{23}\text{Na}^{87}\text{Rb}$ the results show no evidence of photoexcitations of tetramer complexes, that might form after a two-body collision.

5 *Molecule-molecule and atom-molecule collisions*

Reprinted with permission from Gersema, Voges, Lin, He *et al.*, Probing Photoinduced Two-Body Loss of Ultracold Nonreactive Bosonic $^{23}\text{Na}^{87}\text{Rb}$ and $^{23}\text{Na}^{39}\text{K}$ Molecules, *Phys. Rev. Lett.* 127, 163401, 2021

Copyright © 2022 by the American Physical Society (APS).

DOI <https://link.aps.org/doi/10.1103/PhysRevLett.127.163401>

Probing Photoinduced Two-Body Loss of Ultracold Nonreactive Bosonic $^{23}\text{Na}^{87}\text{Rb}$ and $^{23}\text{Na}^{39}\text{K}$ Molecules

Philipp Gersema¹, Kai K. Voges¹, Mara Meyer zum Alten Borgloh¹, Leon Koch¹, Torsten Hartmann¹,
Alessandro Zenesini^{1,2} and Silke Ospelkaus^{1,*}

¹*Institut für Quantenoptik, Leibniz Universität Hannover, 30167 Hannover, Germany*

²*INO-CNR BEC Center, Dipartimento di Fisica, Università di Trento and TIFPA-INFN, 38123 Povo, Italy*

Junyu Lin[†], Junyu He[†], and Dajun Wang[†]

Department of Physics, The Chinese University of Hong Kong, Hong Kong, China

 (Received 2 March 2021; accepted 16 September 2021; published 11 October 2021)

We probe photoinduced loss for chemically stable bosonic $^{23}\text{Na}^{87}\text{Rb}$ and $^{23}\text{Na}^{39}\text{K}$ molecules in chopped optical dipole traps, where the molecules spend a significant time in the dark. We expect the effective two-body decay to be significantly suppressed due to the small expected complex lifetimes of about 13 and 6 μs for $^{23}\text{Na}^{87}\text{Rb}$ and $^{23}\text{Na}^{39}\text{K}$, respectively. However, instead we do not observe any suppression of the two-body loss in parameter ranges where large loss suppressions are expected. We believe these unexpected results are most probably due to drastic underestimation of the complex lifetime by at least 1–2 orders of magnitude.

DOI: [10.1103/PhysRevLett.127.163401](https://doi.org/10.1103/PhysRevLett.127.163401)

The field of ultracold heteronuclear molecules has gained a lot of attention in recent years [1]. Nowadays, full simultaneous control over the molecules' external and rich internal structure including electronic, vibrational, rotational, and hyperfine degrees of freedom is within reach. This is opening many new research opportunities, such as quantum simulation of new many-body states with tunable anisotropic long-range interactions [2–4], the possibility for quantum-state controlled chemistry [5,6], quantum computation [7], and precision measurements [8,9].

Currently, the most advanced experimental molecular system is given by ultracold gases of alkali rovibrational ground-state polar molecules. The first creation of an ultracold ensemble of polar ground-state molecules with high phase-space density has been achieved with the fermionic $^{40}\text{K}^{87}\text{Rb}$ molecules at JILA [5,10]. Ultracold clouds of these molecules suffered from strong two-body losses at the universal limit, which were later explained by an exothermic chemical reaction taking place during the collision between two molecules, $2\text{KRb} \rightarrow \text{K}_2 + \text{Rb}_2$ [5,11–13]. Since then considerable effort has been devoted to the production of chemically stable ground-state molecules. Molecules such as $^{87}\text{Rb}^{133}\text{Cs}$ [14,15], $^{23}\text{Na}^{87}\text{Rb}$ [16], and fermionic $^{23}\text{Na}^{40}\text{K}$ [17,18], as well as bosonic $^{23}\text{Na}^{39}\text{K}$ [19] have been successfully prepared in the laboratory. However, in all of these experiments, molecular two-body losses close to the universal loss limit have been observed [14,16,17,19].

The most accepted mechanism underlying these unexpected losses is the so-called sticky collision introduced by

Mayle *et al.* in 2013 [20]. They predicted the formation of long-lived four-atom complexes in the two-body collision between chemically nonreactive ground-state molecules due to enormously dense nonresolvable resonances [20,21]. Eventually the complexes are expected to dissociate back to molecules in their initial quantum states. Unless the complexes get lost during their sticking time, this process should not result in molecular losses. However, different loss mechanisms have been discussed in the literature. Mayle *et al.* calculated the complex lifetime to be long enough for a collision of the complex with another molecule during the sticking time to occur. This would result in an effective loss of three molecules [20]. In 2019 Christianen *et al.* estimated a 2–3 orders of magnitudes shorter complex lifetime, making the collisional loss of complexes far less likely [22]. Instead they proposed photoinduced complex excitation to excited tetramer states by light of the optical dipole trap (ODT) as the dominant loss mechanism [22]. The complex excitation has been estimated to be much faster than the complex dissociation. Consequently, the two-body loss rate of molecules in the ODT is dominated by the complex formation rate.

Recently, the complex excitation hypothesis has been supported by experiments with bosonic $^{87}\text{Rb}^{133}\text{Cs}$ molecules confined in a modulated (chopped) ODT [23]. The Rb_2Cs_2 complex lifetime has been measured to be $\tau_{c,\text{RbCs}} = 0.53(6)$ ms, which is just about twice the value of 0.253 ms predicted by Christianen *et al.* [24]. Additionally, the complex lifetime estimate has also been confirmed with the chopped ODT technique in the

chemically reactive $^{40}\text{K}^{87}\text{Rb}$ system by probing the K_2Rb_2 complex directly with a sensitive ion detection method [25]. It is of great interest to expand the investigation of chopped ODT measurements to different chemically non-reactive molecular species. This allows one to validate that the light excitation of complexes in the ODT is indeed the dominant loss mechanism, to measure the complex lifetimes, and therefore the density of resonant states, and to compare these to the theoretical predictions.

In this Letter, we probe photoinduced collisional loss of ultracold chemically stable bosonic $^{23}\text{Na}^{87}\text{Rb}$ and $^{23}\text{Na}^{39}\text{K}$ ground-state molecules using chopped ODTs. Given the short predicted complex lifetimes of 13 and 6 μs for $^{23}\text{Na}^{87}\text{Rb}$ and $^{23}\text{Na}^{39}\text{K}$, respectively [24], it is easy to enter a regime where the dark time t_d of the chopped traps is more than 10 times longer than the expected complex lifetime τ_c . Assuming that photoinduced two-body loss is indeed the dominating decay mechanism, this should result in a largely suppressed two-body decay in chopped traps.

Surprisingly, and in stark contrast to our expectations, we do not find such a strong suppression. Our data are instead consistent with near-universal loss even at the lowest modulation frequencies f_{mod} and largest t_d we can probe and thus inconsistent with the short predicted complex lifetimes. This suggests that the recent picture of dominant loss through complex formation and photoinduced loss and/or the predicted complex lifetime is still incomplete.

Assuming the dominant loss mechanism for ultracold chemically nonreactive molecules to be sticky collisions followed by photoinduced complex excitation, we can model the loss dynamics of molecules in continuous-wave (cw) and chopped ODTs [23],

$$\begin{aligned} \dot{n}_m &= -k_2 n_m^2 + \frac{2}{\tau_c} n_c, \\ \dot{n}_c &= +\frac{1}{2} k_2 n_m^2 - \frac{1}{\tau_c} n_c - k_l I(t) n_c, \end{aligned} \quad (1)$$

where n_m is the molecule density, n_c is the complex density, k_2 is the two-body loss rate coefficient measured in a continuously operated ODT, and k_l is the excitation rate of the complexes per unit intensity $I(t)$ of the applied laser field. We assume that $k_l I(t)$ is much larger than $1/\tau_c$ in the cw ODT [22].

In a first step, we apply the model to calculate the decay dynamics of molecules with the predicted τ_c of 6 μs (12.9 μs) for $^{23}\text{Na}^{39}\text{K}$ ($^{23}\text{Na}^{87}\text{Rb}$) and initial peak densities of $n_0 = 2 \times 10^{12} \text{ cm}^{-3}$ at $t = 0$, $k_2 = 4.49 \times 10^{-10} \text{ cm}^3 \text{ s}^{-1}$, and $k_l = 3.9 \times 10^2 \text{ s}^{-1} / \text{W cm}^{-2}$ [22]. Figure 1(a) shows the simulated loss curves for $^{23}\text{Na}^{39}\text{K}$ molecules in the cw ODT and ODTs modulated with a frequency $f_{\text{mod}} = 5 \text{ kHz}$ and two different duty cycles η of 0.25 and 0.5. The modulation results in $t_d = (1 - \eta) \times 1/f_{\text{mod}}$ in which the ODT intensity is zero and the photoinduced loss term k_l thus vanishes. As expected, the molecular loss slows down significantly with decreasing η .

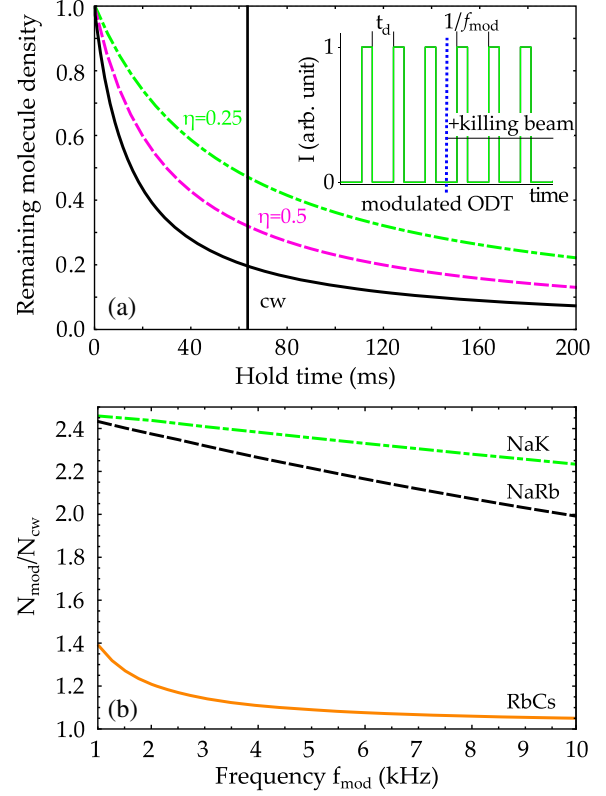


FIG. 1. (a) Simulated $^{23}\text{Na}^{39}\text{K}$ two-body decay dynamics in the cw ODT (black solid curve) in comparison to ODTs modulated with frequency $f_{\text{mod}} = 5 \text{ kHz}$ and duty cycles η of 0.5 (purple dashed curve) and 0.25 (green dash-dotted curve). The time-averaged intensity of the modulated ODTs is the same as the intensity of the cw ODT. Inset: sketch of the ODT modulation sequence with and without an additional killing beam. (b) Comparison of $N_{\text{mod}}/N_{\text{cw}}$ versus f_{mod} for $^{23}\text{Na}^{39}\text{K}$ (green dash-dotted curve), $^{23}\text{Na}^{87}\text{Rb}$ (black dashed curve), and $^{87}\text{Rb}^{133}\text{Cs}$ (orange solid curve). All three curves are calculated with $\eta = 0.25$ and at a hold time when 20% of the initial density is left in the cw ODT.

Figure 1(b) presents the simulated ratio of the remaining number of molecules in the chopped ODT (N_{mod}) to that in the cw ODT (N_{cw}) after 60 ms hold time in the trap as a function of f_{mod} with η fixed at 0.25. Here, larger and above one $N_{\text{mod}}/N_{\text{cw}}$ values signal an increasingly large suppression of loss in the chopped trap in comparison to the cw trap. For comparison, curves for $^{23}\text{Na}^{39}\text{K}$, Na^{87}Rb , and $^{87}\text{Rb}^{133}\text{Cs}$ are included. In the range of selected modulation parameters, due to their shorter estimated τ_c , the expected loss suppressions for both $^{23}\text{Na}^{87}\text{Rb}$ and $^{23}\text{Na}^{39}\text{K}$ are much larger than that for the $^{87}\text{Rb}^{133}\text{Cs}$ case [23]. Thus, the suppression of loss should be much easier to be observed for these two species.

To test the theoretical expectations, we measure the loss of $^{23}\text{Na}^{87}\text{Rb}$ (in Hong Kong) and $^{23}\text{Na}^{39}\text{K}$ (in Hannover) molecules in chopped ODTs. Both ensembles of molecules are prepared using Feshbach molecule association [26,27]

and transfer of the Feshbach molecules to a specific hyperfine state of the $v = 0, J = 0$ rovibrational level of the $X^1\Sigma^+$ ground state using stimulated Raman adiabatic passage [16,19]. The $^{23}\text{Na}^{87}\text{Rb}$ molecules are in the lowest hyperfine state of the rovibrational ground-state manifold $|J = 0, M_J = 0, m_{i,\text{Na}} = 3/2, m_{i,\text{Rb}} = 3/2\rangle$ [16], with a typical temperature of 500 nK and a peak density of $5 \times 10^{11} \text{ cm}^{-3}$, where J is the total molecular electronic spin and M_J is its projection, and $m_{i,a}$ is the respective atomic nuclear spin projections. The $^{23}\text{Na}^{39}\text{K}$ experiments are performed with molecules in $|J = 0, M_J = 0, m_{i,\text{Na}} = -3/2, m_{i,\text{K}} = -1/2\rangle$ state, with a temperature of about 300 nK and a peak density of $2 \times 10^{12} \text{ cm}^{-3}$. Both ensembles are trapped in crossed ODTs operating at about 1064 nm.

For both species, we implemented the chopped ODT with two methods. (i) We used double-passed acousto-optic modulator (AOM) configurations to vary f_{mod} and η arbitrarily, only limited by the rise and fall time of the AOM's resonance circuit. However, in this case, the light extinction during t_d is not complete. We measured a leakage at the level of 100 ppb (10 ppb) for the $^{23}\text{Na}^{87}\text{Rb}$ ($^{23}\text{Na}^{39}\text{K}$) experiment. This corresponds to an intensity of $<5 \text{ mW/cm}^2$ for the typical ODT intensity in use. For both the $^{87}\text{Rb}^{133}\text{Cs}$ [23] and the $^{40}\text{K}^{87}\text{Rb}$ [25] systems, such a low intensity causes nearly no loss of the complexes. We also ruled out leakages from other lasers, as well as radio and microwave sources. (ii) We used an optical chopper wheel to totally block the light during t_d . However, the drawback is a somewhat restricted f_{mod} and η .

As a first measurement, Fig. 2 shows a direct comparison of the molecule number losses in the cw and chopped ODT for $^{23}\text{Na}^{87}\text{Rb}$. In this experiment, the chopped ODT is modulated by the optical chopper at $\eta = 0.33$. The chosen f_{mod} of 1 and 2 kHz ensures that t_d is much longer than the predicted $\tau_{c\text{NaRb}} = 12.9 \mu\text{s}$ of Na_2Rb_2 [24,28], which should allow the complex dissociation to happen. The initial sample conditions are nearly the same for the three measurements. However, we do not observe any sign of loss reduction. This is in contrast to the theoretical predictions (inset of Fig. 2) calculated with the same initial sample conditions, which show a clear suppression of the two-body decay in the chopped trap. $\tau_{c\text{NaRb}} = 12.9 \mu\text{s}$, $k_2 = 4.0 \times 10^{-10} \text{ cm}^3 \text{ s}^{-1}$ [29], and $k_l = 4 \times 10^2 \text{ s}^{-1} / \text{Wcm}^{-2}$ (similar to $^{87}\text{Rb}^{133}\text{Cs}$ [23] and $^{40}\text{K}^{87}\text{Rb}$ [25]) are used in the calculation.

A caveat for this direct comparison is the unavoidable heating and also possible one-body loss induced by the modulation, which change the sample conditions in the chopped ODT. These side effects, which have been ignored in the simulation, can already modify the loss dynamics in the chopped ODT and thus make the loss suppression signal obscure. To avoid these complications, for the following measurements, we mimic the loss in the cw trap

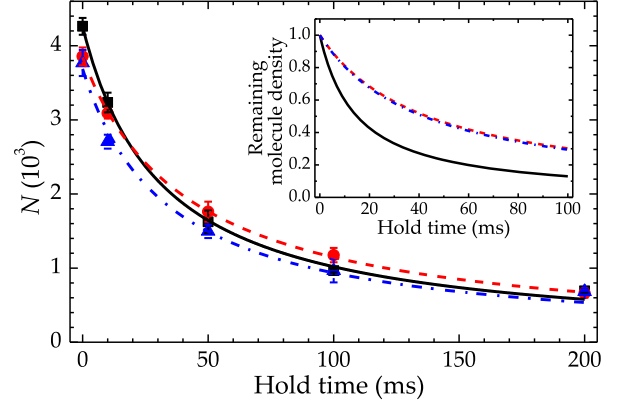


FIG. 2. Loss of $^{23}\text{Na}^{87}\text{Rb}$ in the cw ODT (black squares) and chopped ODTs modulated at 1 kHz (red dots) and 2 kHz (blue triangles) using the optical chopper with a fixed η of 33%. The black solid, red dashed, and blue dash-dotted curves are corresponding two-body loss fittings for the three ODT configurations. Error bars represents one standard error. Inset: simulated $^{23}\text{Na}^{87}\text{Rb}$ loss curves in the cw (solid black curve) and chopped traps with $\eta = 33\%$, $f_{\text{mod}} = 1 \text{ kHz}$ (red dashed curve), and $f_{\text{mod}} = 2 \text{ kHz}$ (blue dash-dotted curve).

by adding an additional cw “killing beam” of variable intensities to the chopped trap without significantly perturbing the confinement [inset of Fig. 1(a)]. The killing beam should excite the complex during the dark time and induce increasingly larger loss for increasing intensities, while the side effects (such as heating) caused by the chopping are the same in the “mimicked cw” and the chopped trap. We then compare the remaining number of molecules in the mimicked cw ($N_{\text{mod+kill}}$) and the chopped (N_{mod}) trap after a fixed hold time. The ratio $N_{\text{mod}}/N_{\text{mod+kill}}$ should be above one if there is suppression of molecular loss in the chopped trap in comparison to the mimicked cw trap.

First, we measure $N_{\text{mod}}/N_{\text{mod+kill}}$ at different killing beam intensities with f_{mod} at 1 kHz (5 kHz), η at 0.33 (0.5), and the hold time at 80 ms (60 ms) for $^{23}\text{Na}^{87}\text{Rb}$ ($^{23}\text{Na}^{39}\text{K}$). These parameters are chosen such that $N_{\text{mod}}/N_{\text{mod+kill}}$ is nearly maximized according to the simulation. We take at least 30 shots, with and without the killing beam, and calculate $N_{\text{mod}}/N_{\text{mod+kill}}$ with the averaged numbers for each case. Figures 3(a) and 4(a) summarize the measurements for $^{23}\text{Na}^{87}\text{Rb}$ and $^{23}\text{Na}^{39}\text{K}$, respectively. For $^{23}\text{Na}^{87}\text{Rb}$, $N_{\text{mod}}/N_{\text{mod+kill}}$ is observed to be consistent with one independent of the chopping technique [chopper wheel (red dots)/AOM (blue squares)]. The same is true for $^{23}\text{Na}^{39}\text{K}$, using the chopper wheel technique.

We also measure the dependence of $N_{\text{mod}}/N_{\text{mod+kill}}$ on f_{mod} . For both species, relatively high killing beam intensities are used to maximize the expected $N_{\text{mod}}/N_{\text{mod+kill}}$. These data are shown in Figs. 3(b) and 4(b) for $^{23}\text{Na}^{87}\text{Rb}$ and $^{23}\text{Na}^{39}\text{K}$, respectively. However, for both cases, we observe no f_{mod} and thus t_d dependence.

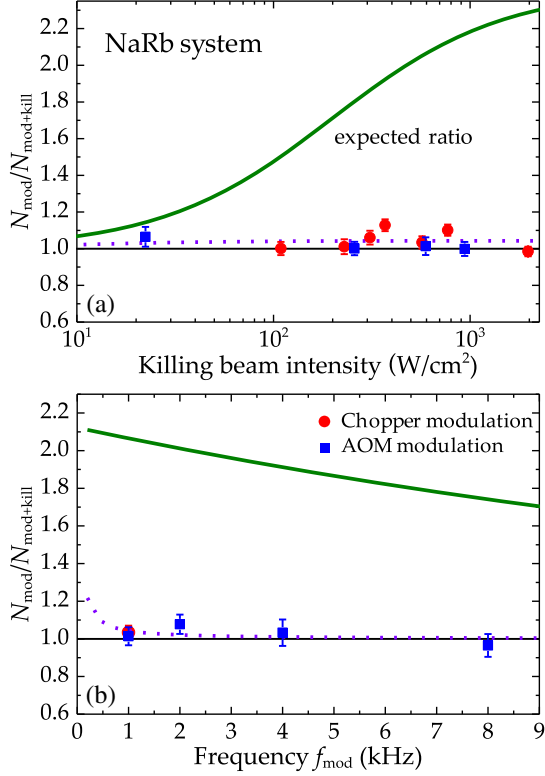


FIG. 3. Probing photoinduced loss of NaRb molecules comparing loss in a chopped ODT to a mimicked cw ODT (see text). (a) $N_{\text{mod}}/N_{\text{mod+kill}}$ after a hold time of 80 ms versus the killing intensity. The trap is modulated at $f_{\text{mod}} = 1$ kHz and $\eta = 0.33$ with the two different methods. The killing beam wavelength is 1064.4 nm, the same as for the ODT light. The green solid and purple dotted lines show the expected $N_{\text{mod}}/N_{\text{mod+kill}}$ as a function of cw killing intensity for different complex lifetimes $\tau_{c\text{NaRb}}$ of 12.9 μs and 4.6 ms, respectively. (b) $N_{\text{mod}}/N_{\text{mod+kill}}$ as a function of f_{mod} and thus t_d with a fixed killing intensity of 0.6 kW/cm². The curves show the expected $N_{\text{mod}}/N_{\text{mod+kill}}$ for the $\tau_{c\text{NaRb}}$ in (a). The theoretical curves are calculated with $k_l = 4 \times 10^2 \text{ s}^{-1}/\text{W cm}^{-2}$ (similar to $^{87}\text{Rb}^{133}\text{Cs}$ [23] and $^{40}\text{K}^{87}\text{Rb}$ [25]). Error bars indicate 1 σ standard errors.

Instead, $N_{\text{mod}}/N_{\text{mod+kill}}$ is constant over the whole frequency range and again consistent with one. For the $^{23}\text{Na}^{39}\text{K}$ experiment, this even remains true when η is varied from 0.5 (purple points) to 0.25 (green points)—again contrary to our expectations.

We also performed experiments on the $^{23}\text{Na}^{87}\text{Rb}$ molecule with another killing beam wavelength of 1248 nm and on the $^{23}\text{Na}^{39}\text{K}$ molecule with killing beam wavelengths of 950 and 816 nm. The results are similar to those in Figs. 3 and 4 with no clear loss suppression observed. These measurements excluded wavelength dependence of the complex excitation and thus an unexpected weak complex excitation at 1064 nm as the cause of the zero signal.

As can be seen from the simulated curves in Figs. 3 and 4, at the selected experimental parameters, a drastic

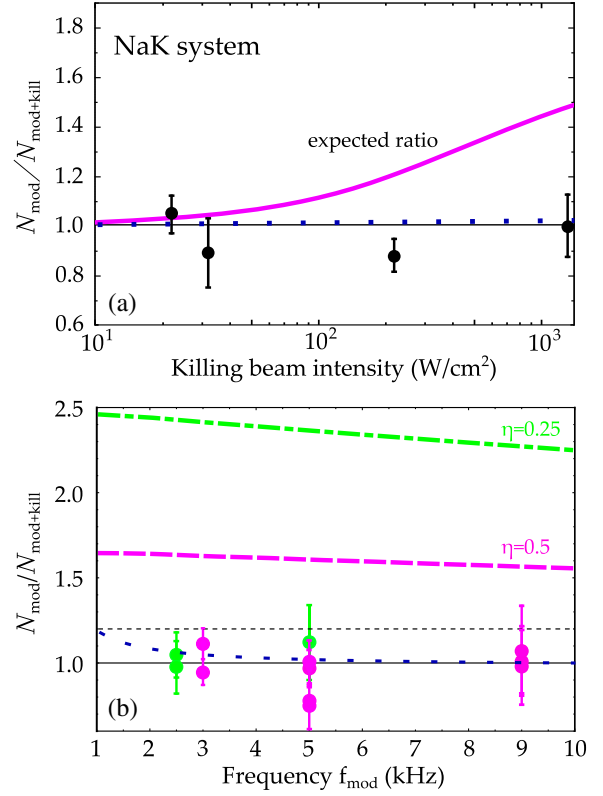


FIG. 4. Probing photoinduced loss of NaK molecules comparing loss in a chopped ODT to a mimicked cw ODT (see text). (a) $N_{\text{mod}}/N_{\text{mod+kill}}$ at 20% remaining density versus the killing beam intensity. The killing beam wavelength is 1064.5 nm, the same as the ODT light. The trap is modulated via the chopper wheel at a frequency of $f_{\text{mod}} = 5$ kHz and a duty cycle $\eta = 0.5$. The purple solid (blue dotted) line shows the expected number ratio for a complex lifetime of 6 μs (1 ms) at the best estimated k_l (see text). (b) $N_{\text{mod}}/N_{\text{mod+kill}}$ as a function of modulation frequency for two different duty cycles $\eta = 0.5$ (purple) or $\eta = 0.25$ (green points). The value of all data points is expected to be above the horizontal dashed line and below the corresponding theoretical gain, which should be resolvable for our experiments. The killing beam intensity is > 0.2 kW/cm². The purple dashed and green dash-dotted curves show the expected ratio $N_{\text{mod}}/N_{\text{mod+kill}}$ for a $\tau_{c\text{NaK}} = 6 \mu\text{s}$ with η of 0.5 and 0.25. The blue dotted curve shows the expected ratio for a $\tau_{c\text{NaK}}$ of 1 ms with $\eta = 0.25$. Note that measurements using the AOM technique are not marked on purpose for clarity. Error bars show 1 σ standard errors.

increase in molecule number in a purely chopped trap in comparison to any kind of mimicked cw trap is expected and the signal should be too obvious to miss. The experimental results are thus very surprising and cannot be explained by our current knowledge. Assuming complex excitation from the ODT is still the dominant loss mechanism, we can provide a lower bound for the complex lifetime: taking the largest measured $N_{\text{mod}}/N_{\text{mod+kill}}$ from the $^{23}\text{Na}^{39}\text{K}$ data, we extract a $\tau_{c\text{NaK}} = 0.35$ ms. For

$^{23}\text{Na}^{87}\text{Rb}$, this is 1.2 ms. If we, on the other hand, consider all measurements to be equal, this would force $\tau_{c\text{NaK}} > 1$ and $\tau_{c\text{NaRb}} > 4$ ms, as dotted curves in Figs. 4 and 3 show. Either way, these complex lifetimes are much longer than those from currently known quantum chemistry calculations [22,24,28].

Given the very reasonable agreements between the measured and the calculated complex lifetimes in the $^{87}\text{Rb}^{133}\text{Cs}$ [23] and $^{40}\text{K}^{87}\text{Rb}$ [25], our findings here are rather unexpected. Furthermore, in parallel to our work, similar results have also been found in experiments with fermionic $^{23}\text{Na}^{40}\text{K}$ by the Munich group [30]. Together, these results indicate that, contrary to what is believed, our understanding of the two-body loss of bialkali molecules is still not complete. To us, the most suspicious point is the accuracy of the theoretical complex lifetimes. Currently, the best-known complex lifetimes are determined using the Rice-Ramsperger-Kassel-Marcus (RRKM) theory with the near-threshold four-atom density of states (DOS) obtained from advanced quantum chemistry calculations [22,24,28]. While the latest DOS calculation method is well established and deviations by orders of magnitude seems hard to imagine, the application of the RRKM theory to ultracold conditions may not be fully justified [31]. For $^{23}\text{Na}^{87}\text{Rb}$ and $^{23}\text{Na}^{39}\text{K}$, for example, the estimated DOS is less than $1/\mu\text{K}$ [24]. At our sample temperatures, on average less than 0.5 four-atom states can be sampled during the two-body molecular collision. This is a clear violation of the statistical assumption of the RRKM theory. This peculiar situation, which should be considered as yet another distinct feature of ultracold molecules, calls for a thorough and immediate investigation.

The Hanover group thanks Leon Karpa for stimulating discussions and Jule Heier for laboratory assistance. The group gratefully acknowledges financial support from the Deutsche Forschungsgemeinschaft (DFG) through the collaborative research centre SFB 1227 DQ-mat, the Research Unit 2247 project E05 and Germanys Excellence Strategy—EXC-2123/1 QuantumFrontiers. P. G. thanks the DFG for financial support through RTG 1991. The Hong Kong team thanks Hua Guo and Daiqian Xie for the new complex lifetime calculation, and Guanghua Chen and Mucan Jin for laboratory assistance. The team was supported by the Hong Kong RGC General Research Fund (grants 14301119, 14301818 and 14301815) and the Collaborative Research Fund C6005-17G.

P. G., K. K. V., J. L., and J. H. contributed equally to this work.

Note added.—Recently, a new preprint by the Harvard group appeared on arXiv in which a much longer $^{40}\text{K}^{87}\text{Rb}_2$ complex lifetime than predicted is reported [32].

*silke.ospelkaus@iqo.uni-hannover.de

†djwang@cuhk.edu.hk

- [1] J. L. Bohn, A. M. Rey, and J. Ye, *Science* **357**, 1002 (2017).
- [2] S. A. Moses, J. P. Covey, M. T. Miecnikowski, D. S. Jin, and J. Ye, *Nat. Phys.* **13**, 13 (2017).
- [3] L. De Marco, G. Valtolina, K. Matsuda, W. G. Tobias, J. P. Covey, and J. Ye, *Science* **363**, 853 (2019).
- [4] B. Yan, S. Moses, B. Gadway, J. Covey, K. Hazzard, A. Rey, D. Jin, and J. Ye, *Nature (London)* **501**, 521 (2013).
- [5] S. Ospelkaus, K.-K. Ni, D. Wang, M. H. G. de Miranda, B. Neyenhuis, G. Quemener, P. S. Julienne, J. L. Bohn, D. S. Jin, and J. Ye, *Science* **327**, 853 (2010).
- [6] M. Guo, X. Ye, J. He, M. L. González-Martínez, R. Vexiau, G. Quémener, and D. Wang, *Phys. Rev. X* **8**, 041044 (2018).
- [7] D. DeMille, *Phys. Rev. Lett.* **88**, 067901 (2002).
- [8] J. Baron, W. C. Campbell, D. DeMille, J. M. Doyle, G. Gabrielse, Y. V. Gurevich, P. W. Hess, N. R. Hutzler, E. Kirilov, I. Kozyryev, B. R. O’Leary, C. D. Panda, M. F. Parsons, E. S. Petrik, B. Spaun, A. C. Vutha, and A. D. West, *Science* **343**, 269 (2014).
- [9] V. Andreev, D. G. Ang, D. DeMille, J. M. Doyle, G. Gabrielse, J. Haefner, N. Hutzler, Z. Lasner, C. Meisenhelder, B. O’Leary, C. Panda, A. West, E. West, and X. Wu, *Nature (London)* **562**, 355 (2018).
- [10] K.-K. Ni, S. Ospelkaus, M. H. G. de Miranda, A. Pe’er, B. Neyenhuis, J. J. Zirbel, S. Kotochigova, P. S. Julienne, D. S. Jin, and J. Ye, *Science* **322**, 231 (2008).
- [11] P. S. Żuchowski and J. M. Hutson, *Phys. Rev. A* **81**, 060703 (R) (2010).
- [12] E. R. Meyer and J. L. Bohn, *Phys. Rev. A* **82**, 042707 (2010).
- [13] M.-G. Hu, Y. Liu, D. D. Grimes, Y.-W. Lin, A. H. Gheorghe, R. Vexiau, N. Bouloufa-Maafa, O. Dulieu, T. Rosenband, and K.-K. Ni, *Science* **366**, 1111 (2019).
- [14] T. Takekoshi, L. Reichsöllner, A. Schindewolf, J. M. Hutson, C. R. Le Sueur, O. Dulieu, F. Ferlaino, R. Grimm, and H.-C. Nägerl, *Phys. Rev. Lett.* **113**, 205301 (2014).
- [15] P. K. Molony, P. D. Gregory, Z. Ji, B. Lu, M. P. Köppinger, C. R. Le Sueur, C. L. Blackley, J. M. Hutson, and S. L. Cornish, *Phys. Rev. Lett.* **113**, 255301 (2014).
- [16] M. Guo, B. Zhu, B. Lu, X. Ye, F. Wang, R. Vexiau, N. Bouloufa-Maafa, G. Quémener, O. Dulieu, and D. Wang, *Phys. Rev. Lett.* **116**, 205303 (2016).
- [17] J. W. Park, S. A. Will, and M. W. Zwierlein, *Phys. Rev. Lett.* **114**, 205302 (2015).
- [18] F. Seeßelberg, N. Buchheim, Z.-K. Lu, T. Schneider, X.-Y. Luo, E. Tiemann, I. Bloch, and C. Gohle, *Phys. Rev. A* **97**, 013405 (2018).
- [19] K. K. Voges, P. Gersema, M. Meyer zum Alten Borgloh, T. A. Schulze, T. Hartmann, A. Zenesini, and S. Ospelkaus, *Phys. Rev. Lett.* **125**, 083401 (2020).
- [20] M. Mayle, G. Quémener, B. P. Ruzic, and J. L. Bohn, *Phys. Rev. A* **87**, 012709 (2013).
- [21] M. Mayle, B. P. Ruzic, and J. L. Bohn, *Phys. Rev. A* **85**, 062712 (2012).
- [22] A. Christianen, M. W. Zwierlein, G. C. Groenenboom, and T. Karman, *Phys. Rev. Lett.* **123**, 123402 (2019).
- [23] P. D. Gregory, J. A. Blackmore, S. L. Bromley, and S. L. Cornish, *Phys. Rev. Lett.* **124**, 163402 (2020).

- [24] A. Christianen, T. Karman, and G. C. Groenenboom, *Phys. Rev. A* **100**, 032708 (2019).
- [25] Y. Liu, M.-G. Hu, M. A. Nichols, D. D. Grimes, T. Karman, H. Guo, and K.-K. Ni, *Nat. Phys.* **16**, 1132 (2020).
- [26] F. Wang, X. He, X. Li, B. Zhu, J. Chen, and D. Wang, *New J. Phys.* **17**, 035003 (2015).
- [27] K. K. Voges, P. Gersema, T. Hartmann, T. A. Schulze, A. Zenesini, and S. Ospelkaus, *Phys. Rev. A* **101**, 042704 (2020).
- [28] By courtesy of Hua Guo and Daiqian Xie, a new Na_2Rb_2 complex lifetime of $\tau_{c\text{NaRb}} = 65.7 \mu\text{s}$ is obtained from a latest quantum chemistry calculation. However, this slightly longer complex lifetime is not enough to explain our observation.
- [29] X. Ye, M. Guo, M. L. González-Martínez, G. Quéméner, and D. Wang, *Sci. Adv.* **4**, eaaq0083 (2018).
- [30] R. Bause, A. Schindewolf, R. Tao, M. Duda, X.-Y. Chen, G. Quéméner, T. Karman, A. Christianen, I. Bloch, and X.-Y. Luo, *Phys. Rev. Research* **3**, 033013 (2021).
- [31] M. Frye and J. Hutson (private communication).
- [32] M. A. Nichols, Y.-X. Liu, L. Zhu, M.-G. Hu, Y. Liu, and K.-K. Ni, [arXiv:2105.14960](https://arxiv.org/abs/2105.14960).
- [33] See Supplemental Material at <http://link.aps.org/supplemental/10.1103/PhysRevLett.127.163401> for an explanation of the modulated trap setup and the selection of the experimental parameters.

Supplemental Materials

Probing photoinduced two-body loss of ultracold non-reactive bosonic $^{23}\text{Na}^{87}\text{Rb}$ and $^{23}\text{Na}^{39}\text{K}$ molecules

Modulated Trap Setup

For both species, we implemented the chopped ODT with two methods.

(i) We used a double-passed AOM configuration to vary f_{mod} and η arbitrarily, only limited by the rise and fall time of the AOM's resonance circuit. The double pass configuration ensures high suppression of leakage light, measured to be at the level of 100 ppb (10 ppb) for the $^{23}\text{Na}^{87}\text{Rb}$ ($^{23}\text{Na}^{39}\text{K}$) experiment.

The Feshbach molecules are produced in a 1064 nm cw crossed-ODT (XODT), formed by two individual beams. After the molecules are transferred to the ground state, the cw XODT is switched to the AOM-modulated trap by switching the trapping beams alternately on/off with the AOM. After that the molecules are hold for a specific time with or without a cw killing beam.

For the $^{23}\text{Na}^{87}\text{Rb}$ AOM-modulated data shown in Fig. 3, the trap frequencies are $2\pi \times (106, 143, 189)$ Hz. For the $^{23}\text{Na}^{39}\text{K}$ experiment, the chopped ODTs have the same average intensities as in the cw case with trap frequencies of $2\pi \times (226, 226, 33)$ Hz .

(ii) We used an optical chopper wheel to totally block the light during t_d , for the case of a much higher k_l coefficient than theoretically anticipated. However, the drawback is a somewhat restricted f_{mod} and η .

For $^{23}\text{Na}^{87}\text{Rb}$ a XODT is formed with a single beam in a bow-tie configuration, allowing both arms to be modulated by one chopper. To avoid interference between two arms, the second arm passed an AOM for a frequency shift.

For $^{23}\text{Na}^{39}\text{K}$ the 1064 nm laser light is separated into two different beams. One passes a chopper wheel and is afterwards overlapped with the other beam at a beam splitter. After the beam splitter the 1064 nm light is split up into the two ODT beams. In the normal cw XODT operation a mechanical shutter blocks the chopped XODT beam path. After the creation of ground state molecules we switch between the cw and the chopped XODT by closing a shutter in the cw beam path and opening the chopped beam path.

Data shown in Fig. 2 is measured in a chopper-modulated trap, with trap frequencies $2\pi \times (84, 127, 130)$ Hz. For chopper-modulated data shown in Fig. 3, trap frequencies are $2\pi \times (87, 132, 135)$ Hz.

Selection of Experimental Parameters

All the parameters chosen are expected to result in a significant gain, which can be distinguished from the fluctuation of our system. Briefly speaking, the principle is that the dark time in the modulated trap should be longer than the complex lifetime, and as long as possible in one cycle.

Here, we take the case of $^{23}\text{Na}^{87}\text{Rb}$ as an example to illustrate the selection of experimental parameters, with simulation parameters $\tau_{c,\text{NaRb}} = 12.9 \mu\text{s}$, $k_2 = 4.0 \times 10^{-10} \text{ cm}^3\text{s}^{-1}$, $k_l = 4 \times 10^2 \text{ s}^{-1}/\text{Wcm}^{-2}$ and initial peak density as $n(0) = 5 \times 10^{11} \text{ cm}^{-3}$.

Fig. S1(a) shows a simulation of the molecule density of $^{23}\text{Na}^{87}\text{Rb}$ in a modulated trap with different modulation frequencies $f_{\text{mod}} = 0.5 \text{ kHz}$, 2 kHz , 10 kHz and 100 kHz with a fixed duty cycle $\eta = 0.5$. Compared with the cw case, a strong two-body loss suppression occurs for $f_{\text{mod}} \ll 1/\tau_{c,\text{NaRb}}$, as a result of the dissociation of complexes. For low f_{mod} , like 0.5 kHz , the loss behavior is similar to 2 kHz , indicating that even lower f_{mod} will not help to enhance the suppression effect. Thus, a modulation frequency f_{mod} of a few kHz is good enough to observe the suppression of losses. This is also true for the $^{23}\text{Na}^{39}\text{K}$ case.

Fig. S1(b) shows the relative gain $N_{\text{mod}}/N_{\text{mod+kill}}$ for duty cycles $\eta = 0.1, 0.3, 0.5$ and 0.7 , with a killing beam intensity of 2.0 kW/cm^2 and $f_{\text{mod}} = 1 \text{ kHz}$. As we expected, for a fixed holding time, a lower duty cycle gives a higher gain. The selection for the hold time is dependent on the duty cycle we choose for the experiment. For example, with $\eta = 0.5$ (purple dotted curve), a hold time of 60 ms is long enough, as a further increment will not significantly increase the relative gain.

Furthermore, the experimental limitations should be taken into account. With decreasing duty cycle, a higher trap laser intensity should be used to keep the same trap depth experienced by the molecules. Limiting by the total output power of our ODT laser, there is a lowest duty cycle we could reach. In addition, all the molecules experience free fall during the dark time and will be heated or dropped out of the trap once the dark time is too long.

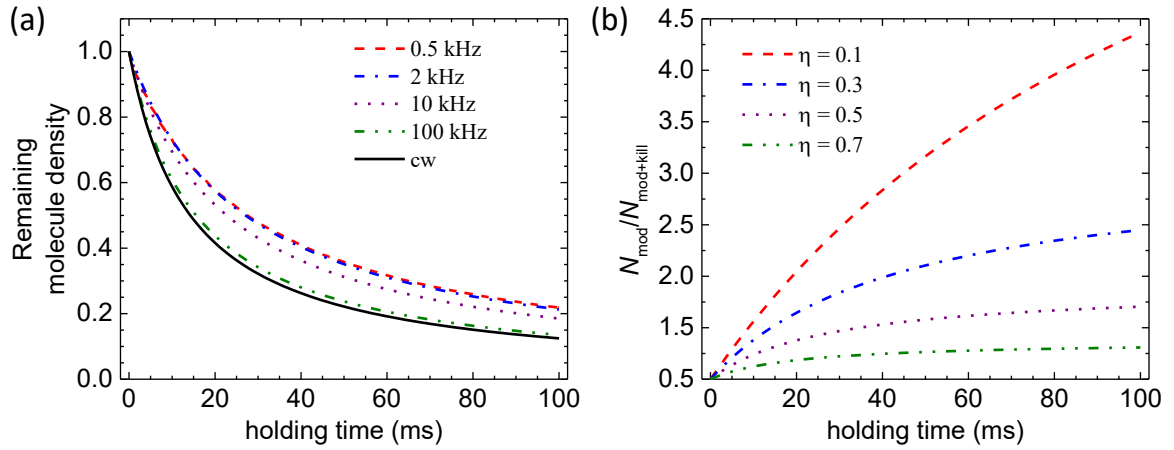


FIG. S1. Selection of experimental parameters on the example of $^{23}\text{Na}^{87}\text{Rb}$. (a) Remaining molecule density evolution in a modulation trap with $f_{\text{mod}} = 0.5$ kHz (red dashed), 2 kHz (blue dash-dotted), 10 kHz (purple dotted) and 100 kHz (green dash-dot-dot). The black solid curve shows a cw trap. (b) Relative gain for different hold times, with duty cycles $\eta = 0.1$ (red dashed), 0.3 (blue dash-dotted), 0.5 (purple dotted) and 0.7 (green dash-dot-dot). The killing beam intensity is set to 2.0 kW/cm^2 , while $f_{\text{mod}} = 1$ kHz.

For both $^{23}\text{Na}^{87}\text{Rb}$ and $^{23}\text{Na}^{39}\text{K}$ experiments, we choose the experimental parameters considering all factors mentioned above. It should allow us to have a large enough gain, which can be distinguished from the density fluctuation of molecules in our system.

5.2 Spin dependent atom-molecule collisions [A7]

Not only the scattering properties of molecule-molecule mixtures, but also of atom-molecule mixtures are of great interest, since they are still not well understood and could, for example, be used to sympathetically cool molecules, to generate trimer states or to probe trimer complexes. Collisional studies observed losses in atom-molecule mixtures governed by two-body processes [35, 105]. The formation of trimer complexes was detected with complex lifetimes of $^{40}\text{K}^{87}\text{Rb}_2$ in the milliseconds range [106]. This is $\approx 10^5$ longer than expected from RRKM theory and raises the question if trimer complex formation plays a role in the observed two-body loss processes. Experiments with $^6\text{Li}^{23}\text{Na}$ molecules in a mixture with ^{23}Na showed that sympathetic cooling through elastic atomic collisions is possible, even in an environment where exothermic reactions can occur [107]. Magnetic field dependent resonant behaviour of atom-molecule collisions was discovered in $^{23}\text{Na}^{40}\text{K}+^{40}\text{K}$ which was attributed to trimer Feshbach resonances [73, 108], however with resonance spacings that do not match theoretical predictions [101, 109]. Shortly thereafter, this led to the first evidence of triatomic Feshbach molecules [110]. Recently, Feshbach resonances have been observed in reactive collisions of $^6\text{Li}^{23}\text{Na}+^{23}\text{Na}$ that enabled tunable loss rates by more than a factor of a hundred [74]. Up to now, no complete picture is available to explain these different experimental observations.

In the POLAR experiment another startling atom-molecule property was observed. Immediately after the STIRAP, the sodium atoms must be removed from the ODT as they can enter into reactive collisions with the molecules and therefore rapid losses are observed [57]. Surprisingly, the molecular lifetime did not depend on whether the potassium atoms still remained in the trap or not [A5]. The observed losses were so low that only an upper limit for the two-body loss rate coefficient could be derived. This is particularly striking since the potassium density is more than an order of magnitude higher than the molecular density and as the potassium atoms are in a non-stretched hyperfine state [57]. This intriguing behaviour called for a more thorough investigation of $^{39}\text{K}+^{23}\text{Na}^{39}\text{K}$ mixtures in different hyperfine states of ^{39}K , see [A7]. This was done together with a newly derived analytical solution, that can describe loss dynamics with an arbitrary number of involved particles, for example one-, two- or three-body loss processes.

Copyright © 2022 The Author(s), Originally published by arXiv, CC BY 4.0.

DOI <https://arxiv.org/abs/2109.03605v2>, accepted in Phys. Rev. Res.

Hyperfine dependent atom-molecule loss analyzed by the analytic solution of few-body loss equations

Kai K. Voges,^{1,*} Philipp Gersema,^{1,*} Torsten Hartmann,¹ Silke Ospelkaus,^{1,†} and Alessandro Zenesini^{1,2}

¹*Institut für Quantenoptik, Leibniz Universität Hannover, 30167 Hannover, Germany*

²*INO-CNR BEC Center, Dipartimento di Fisica, Università di Trento
and TIFPA-INFN, 38123 Povo, Italy*

(Dated: May 12, 2022)

We prepare mixtures of ultracold ^{39}K atoms in various hyperfine spin states with $^{23}\text{Na}^{39}\text{K}$ molecules in an optical dipole trap at a fixed magnetic field and study inelastic two-body atom-molecule collisions. We observe atom-molecule losses that are hyperfine dependent with a two-body loss rate far below the universal limit. We analyze the two-body loss dynamics based on the derivation of general and easy applicable analytic solutions for the differential equations describing the loss of an arbitrary number γ of particles in a single collisional event.

I. INTRODUCTION

Quantum gas experiments rely on the scattering properties of the neutral particles [1]. Their collisions are crucial for example in rethermalization during evaporative cooling [2] or Bose-Einstein condensation [3]. The control of the collisions by means of Feshbach resonances [4] can lead to the selective emergence or collapse of Bose-Einstein condensates [5, 6], formation of liquid quantum droplets [7, 8] or creation of ultracold dimer molecules [9]. However, short-range collisions are often accompanied by losses. Especially resonant scattering conditions can enhance the losses from the ultracold ensemble. The loss dynamics itself offer valuable clues to the origin of these losses, for example the number of involved particles, the loss mechanisms or the density of resonant states [10].

A prominent and timely example for few-body losses are ultracold heteronuclear ground-state molecular gases. In all so far created ground-state molecular many-particle gases two-body associated losses have been detected [11–17], where the particular loss rate coefficients are close to the universal scattering limit [18, 19]. In the case of chemically unstable molecules, such as the KRb molecule, those losses originate mainly from two-body exothermic exchange reactions [19–21]. In contrast to that, chemically stable ground-state molecules, such as NaK, NaRb and RbCs are not affected by exothermic reactions [20], but still suffer from nearly universal loss in collisions [12–15, 17]. This is suspected to be due to sticky collisions [22, 23]. Due to the high density of states in molecular collisions long-lived tetramer complexes form and might get excited by light from the optical dipole trap [24] such that both molecules get lost. This has been detected in the relatively heavy KRb and RbCs molecules [25, 26], but remains elusive in the light weight molecular systems of NaK and NaRb. Indeed, experiments with these molecules suggest complex life-

time several orders of magnitude larger than calculated [27] or even additional unexplained loss mechanisms [28]. The same kind of investigation recently expands to ensembles of molecule-atom systems, in which also sticky trimer complexes can form in collisions of a single dimer molecule with a single atom. Near universal losses due to light excitation have already been observed in KRb+Rb collisions [29], likewise for an unexpected high complex lifetime. Again, in contrast to the heavy systems, the light weight systems LiNa+Na and NaK+K have observed deviations from that behaviour, where losses can be suppressed [17, 30] or even be tuned by means of external magnetic fields [31, 32]. The complex formation and the loss mechanisms are not fully understood and require further fundamental investigations towards few- and many-body quantum physics and chemistry. The data analysis of the loss dynamics involves the relatively complicated use of sets of differential equations modeling the loss of the particles and the associated temperature evolution in the trap. Numerical solving and fitting routines make a fast analysis of the data inconvenient and less intuitive.

In this paper, we report the observation of hyperfine dependent atom-molecule loss in mixtures of ^{39}K atoms prepared in various hyperfine spin states of the electronic ground state and bosonic $^{23}\text{Na}^{39}\text{K}$ molecules in a single but fixed hyperfine state of the rovibronic ground state. We observe the atom-molecule two-body loss rate to be dependent on the hyperfine spin state of the ^{39}K atoms and far below the universal limit. We analyze the two-body loss dynamics based on the derivation of analytic solutions to the differential equation system for the time evolution of particle number and temperature in a γ -body loss process.

In Sec. II we describe the general coupled differential equation system for loss dynamics resulting from a γ -body loss process and the derivation of the analytic solutions to this problem. Sec. III reports about our experimental work. First, we summarize the preparation of atom-molecule mixtures of ^{39}K atoms in various hyperfine spin states and $^{23}\text{Na}^{39}\text{K}$ molecules in our experimental apparatus. We then discuss the hyperfine spin de-

* These authors contributed equally to this work.
voges@iqo.uni-hannover.de

† silke.ospelkaus@iqo.uni-hannover.de

pendent loss measurements and their analysis using the analytic solution from Sec. II for the two-body decay ($\gamma = 2$). Finally, we discuss our results in Sec. IV.

II. ANALYTICAL MODEL FOR THE γ -BODY LOSS PROBLEM

The loss dynamics in pure molecular ensembles and atom-molecule mixtures presented in this paper follow typical two-body losses. This is described by a set of nonlinear differential equations where the loss rate coefficient k_2 is used as a fit parameter. Nevertheless, such a set of equations can be generally applied to the case of a γ -body problem, where γ is the number of particles interacting with each other during a single scattering event. This is a universal problem in many fields of physics.

The typical approach to apply these systems to experimental data is to laboriously fit numerically deduced solutions of the differential equation system. The application of analytic solutions thus will be much more convenient and facilitate the analysis of experimental data drastically. In the following we derive these solutions for the loss problem in general with γ involved particles. This makes our solutions applicable for a broad range of applications.

We consider a system of $N(t)$ particles of temperature $T(t)$ trapped in a harmonic potential $U(x, y, z)$ with trapping frequency ω_i for the direction i . Following the Boltzmann statistics, the size of the ensemble is given by a Gaussian profile with width $\sigma_i(t) = \sqrt{k_B T(t)/m\omega_i^2}$ [33], where m is the mass of the particle and k_B is the Boltzmann constant. The density of the ensemble is given by

$$n(t, x, y, z) = N(t) \prod_{i=x,y,z} \frac{e^{-i^2/(2\sigma_i(t)^2)}}{\sqrt{2\pi}\sigma_i(t)}. \quad (1)$$

If we limit the derivation to one- and γ -body particle loss processes in the system, with loss rates k_1 and k_γ , the particle number $N(t)$ and the temperature $T(t)$, assuming re-thermalization, result from a system of coupled equations

$$\begin{aligned} \dot{N}(t) &= -k_\gamma \langle n(t)^\gamma \rangle_V - k_1 N(t), \\ \dot{T}(t) &= + \frac{\Gamma_\gamma(t)}{3k_B N(t)} k_\gamma \langle n(t)^\gamma \rangle_V, \end{aligned} \quad (2)$$

where the $\langle n(t)^\gamma \rangle_V$ is the volume integral of the γ -body density $n(t, x, y, z)^\gamma$. The anti-evaporation is described by the quantity $\Gamma_\gamma(t)$ and corresponds to the mean potential energy

$$\Gamma_\gamma(t) = \frac{3}{2} k_B T(t) - \langle U(x, y, z) n(t, x, y, z)^\gamma \rangle_V. \quad (3)$$

$\Gamma_\gamma(t)$ depends on time both through the temperature and the density. Note that the one-body loss process does not contribute to the anti-evaporation as it is not density-dependent.

By explicitly integrating the volume integrals over the Gaussian density profiles, one reaches the following system of equations

$$\begin{aligned} \dot{N}(t) &= -\frac{k_\gamma C^{\gamma-1}}{\gamma^{3/2}} \frac{N(t)^\gamma}{T(t)^{(3/2)(\gamma-1)}} - k_1 N(t), \\ \dot{T}(t) &= \frac{k_\gamma C^{\gamma-1}}{\gamma^{3/2}} \left(\frac{\gamma-1}{2\gamma} \right) \frac{N(t)^{\gamma-1}}{T(t)^{(3\gamma-5)/2}}, \end{aligned} \quad (4)$$

where C is $(m\omega^2/(2\pi k_B))^{(3/2)}$ and ω is the average trap frequency of the trapping potential $\omega = (\omega_x \omega_y \omega_z)^{1/3}$. Note that we use the same conventions as used in [23].

The first step to an analytic solution for $N(t)$ and $T(t)$ consists in substituting $N(t)$ with $M(t)e^{-(\gamma-1)k_1 t}$ to hide the one-body term

$$\begin{aligned} \dot{M}(t) &= -\frac{k_\gamma C^{\gamma-1}}{\gamma^{3/2}} \frac{M(t)^\gamma}{T(t)^{(3/2)(\gamma-1)}} e^{-(\gamma-1)k_1 t}, \\ \dot{T}(t) &= \frac{k_\gamma C^{\gamma-1}}{\gamma^{3/2}} \frac{\gamma-1}{2\gamma} \left(\frac{M(t)^{\gamma-1}}{T(t)^{(3\gamma-5)/2}} \right) e^{-(\gamma-1)k_1 t}. \end{aligned} \quad (5)$$

By dividing the first line by the second one in Eq. 5 we have:

$$\frac{\dot{M}(t)}{\dot{T}(t)} = -\frac{2\gamma}{\gamma-1} \frac{M(t)}{T(t)}, \quad (6)$$

which leads to

$$\frac{M(t)}{N_0} = \left(\frac{T(t)}{T_0} \right)^{-\frac{2\gamma}{\gamma-1}}, \quad (7)$$

where $N_0 = N(0) = M(0)$ and $T_0 = T(0)$ are the initial atom number and the initial temperature. By introducing $M(t)$ and N_0 in the first equation in Eq. 5, we get

$$\frac{\dot{M}(t)}{N_0} = -N_0^{\gamma-1} \frac{k_\gamma C^{\gamma-1}}{\gamma^{3/2}} \frac{(M(t)/N_0)^\gamma}{T(t)^{(3/2)(\gamma-1)}} e^{-(\gamma-1)k_1 t}, \quad (8)$$

where $M(t)/N_0$ can be substituted using Eq. 7:

$$\begin{aligned} \frac{d}{dt} \left[\left(\frac{T(t)}{T_0} \right)^{-\frac{2\gamma}{\gamma-1}} \right] &= \\ -\frac{k_\gamma (N_0 C)^{\gamma-1}}{\gamma^{3/2}} \frac{\left(\left(\frac{T(t)}{T_0} \right)^{-\frac{2\gamma}{\gamma-1}} \right)^\gamma}{T(t)^{(3/2)(\gamma-1)}} e^{-(\gamma-1)k_1 t}. \end{aligned} \quad (9)$$

This differential equation for $T(t)$ has the solution

$$\frac{T(t)}{T_0} = \left(1 + k_\gamma \frac{\eta}{\alpha} \left(\frac{1 - e^{-(\gamma-1)k_1 t}}{(\gamma-1)k_1} \right) \right)^\beta, \quad (10)$$

where η contains the starting conditions and trapping parameters

$$\eta = \frac{1}{\gamma^{3/2}} \left(\frac{C N_0}{T_0^{3/2}} \right)^{\gamma-1}. \quad (11)$$

The two constants α and β depend only on γ and can be written as

$$\alpha = \frac{4\gamma}{(\gamma-1)(7\gamma-3)}, \quad (12)$$

$$\beta = \frac{2}{7\gamma-3}. \quad (13)$$

The solution for $N(t)$ is then obtained by combining Eq. 7 and Eq. 10.

$$\frac{N(t)}{N_0} = \frac{e^{-k_1 t}}{\left(1 + k_\gamma \frac{\eta}{\alpha} \left(\frac{1 - e^{-(\gamma-1)k_1 t}}{(\gamma-1)k_1}\right)\right)^\alpha}. \quad (14)$$

For $\gamma = 1$, this solution collapses to the known exponential decay. The solutions for $\gamma = 2, 3, 4, 5$ have the following α and β :

γ	α	β
2	8/11	2/11
3	1/3	1/9
4	16/75	2/25
5	5/32	1/16

Note that the case $\gamma = 3$ corresponds to the solution already presented by Kraemer [34] although the solution of $T(t)$ in the thesis manuscript has a typo on η . The limit for negligible one-body losses ($k_1 \rightarrow 0$) can be obtained just by noticing that $\lim_{k_1 \rightarrow 0} \left(\frac{1 - e^{-(\gamma-1)k_1 t}}{(\gamma-1)k_1}\right) = t$, which leads to:

$$\begin{aligned} T(t)/T_0 &= \left(1 + k_\gamma \frac{\eta}{\alpha} t\right)^\beta, \\ N(t)/N_0 &= \left(1 + k_\gamma \frac{\eta}{\alpha} t\right)^{-\alpha}. \end{aligned} \quad (15)$$

In the following, we use our newly derived analytic solutions to analyze the hyperfine dependent atom-molecule loss observed in our experiments.

III. HYPERFINE DEPENDENT ATOM-MOLECULE LOSS

A. Preparation of atom-molecule mixtures

The ground-state molecule creation starts from mixtures of about 1.8×10^5 ultracold ^{23}Na and 0.6×10^5 ^{39}K atoms trapped in a 1064 nm crossed beam optical dipole trap (cODT) with temperatures of 300 nK. The cODT frequencies are measured by trap oscillations of the respective particles. For ^{39}K atoms the trap frequencies are $\omega_{\text{K},(x,y,z)} = 2\pi \times (375.8(8.6), 375.8(8.6), 60.8(6.4))$ Hz. The trap frequencies for ^{23}Na atoms are scaled by a factor of about 0.62 due to different dynamical polarizability and mass. The atoms are initially prepared in the states $|f=1, m_f=-1\rangle_{\text{Na}} + |f=1, m_f=-1\rangle_{\text{K}}$

for which the inter- and intra-species scattering properties are well known [35]. Feshbach molecules are formed close to a Feshbach resonance at about 200 G in the atomic $|f=1, m_f=-1\rangle_{\text{Na}} + |f=2, m_f=-2\rangle_{\text{K}}$ states [36]. The bound molecular state is populated by a short radio frequency pulse of 400 μs . Immediately after molecule formation the transfer to the ground state takes place. This is done within 12 μs via a stimulated Raman adiabatic passage (STIRAP) to a single rovibrational hyperfine state $|m_{i,\text{Na}}=-3/2, m_{i,\text{K}}=-1/2, M_J=0, M_{i,\text{NaK}}=-2\rangle$ [17]. For detection of molecules the STIRAP is reversed and ^{39}K atoms from the Feshbach molecule state are imaged via a cycling transition. Typically, about 4000 ground-state molecules are generated per experimental cycle. The determined trap frequencies of the $^{23}\text{Na}^{39}\text{K}$ molecules are $\omega_{\text{NaK},(x,y,z)} = 2\pi \times (195.6(8.3), 195.6(8.3), 33.1(1.3))$ Hz. The temperature of the $^{23}\text{Na}^{39}\text{K}$ molecules is measured by a time-of-flight measurement on the ^{39}K atoms after STIRAP reversal and Feshbach molecule dissociation [17]. The temperature of the remaining ^{39}K atoms is still 300 nK, from which we conclude that neither molecule association nor dissociation lead to heating of the molecules. After ground-state transfer the molecules are still embedded in a bath of remaining atoms. ^{23}Na atoms are usually removed as fast as possible since the molecules undergo a chemical reaction with ^{23}Na atoms. This is done by a 500 μs resonant light pulse, which pushes the atoms out of the cODT. To prevent optical pumping and thus incomplete removal of the ^{23}Na atoms, two resonant frequencies are used connecting the excited state $|f=2, m_f=-2\rangle_{\text{Na}}$ to the corresponding low field ground states $|1, -1\rangle_{\text{Na}}$ and $|2, -1\rangle_{\text{Na}}$. The notation is given in the basis of the Zeeman regime with $|f, m_f\rangle$, where f is the hyperfine number and m_f its projection. After the removal of the ^{23}Na atoms, the molecules are left in a gas of ^{39}K atoms in the $|1, -1\rangle$ hyperfine state. Fortunately, this atomic state leads to very little losses of the molecules [17], which is favorable for all further state manipulations of the mixture; see Fig. 1. For the preparation of a pure molecular cloud ^{39}K atoms are removed from the trap by a rapid adiabatic passage (RAP) to the $|2, -2\rangle$ state followed by a 500 μs resonant light pulse. For the study of atom-molecule loss with ^{39}K atoms in various spin states, the hyperfine state of the ^{39}K atoms is manipulated using RAPs and rf pulses. In our experiment, we prepare six different ^{39}K hyperfine states: $|1, 1\rangle, |1, 0\rangle, |1, -1\rangle, |2, -2\rangle, |2, -1\rangle$ and $|2, 0\rangle$, where the states are written in the basis $|f, m_f\rangle$.

B. Atom-molecule two-body loss coefficients

Atom-molecule collisions between $^{23}\text{Na}^{39}\text{K}$ molecules in the $|m_{i,\text{Na}}=-3/2, m_{i,\text{K}}=-1/2, M_J=0, M_{i,\text{NaK}}=-2\rangle$ state [17] and ^{39}K atoms in one of the six different

hyperfine states mentioned above are studied in the optical dipole trap at a fixed magnetic field of 200 G in the vicinity of the used Feshbach resonance. Apart from losses due to two-body atom-molecule collisions, the decay dynamics of an atom-molecule mixture is also affected by the two-body losses due to molecule-molecule collisions, and it is therefore important to first understand in detail the two-body decay of a pure molecular cloud.

Pure molecular collisions between $^{23}\text{Na}^{39}\text{K}$ molecules have already been studied in our previous work [17]. One-body background losses for example from vacuum background gas collisions [35] or photo-excitation of bialkali molecules are negligible [37] and the dominating loss is observed to result from two-body molecule-molecule collisions. We thus analyse the decay of a pure molecular cloud using the analytic solution from Eq. 15 with $\gamma = 2$. Accordingly, α is 8/11 and the constant η contains the parameters of the particles and the trap, which are the initial particle number and temperature as well as trap frequencies; see Sec. III A. We fit this model to the decay of a pure molecular cloud and extract the two-body loss rate coefficient $k_2 = 4.49(1.18) \times 10^{-10} \text{ cm}^3\text{s}^{-1}$ at 200 G close to the universal limit and consistent with the value reported in [17] (see Fig. 1).

Knowing the background two-body loss resulting from collisions of two ground-state molecules we can investigate ultracold collisions of molecules with ^{39}K atoms in various hyperfine states. We therefore prepare different atom-molecule mixtures of ^{39}K atoms in one of the six different hyperfine states and $^{23}\text{Na}^{39}\text{K}$ molecules; see Sec. III A. We measure the decay of the molecular cloud as a function of time for each of the six different atom-molecule mixtures and analyze loss dynamics using solutions from Sec. II, in particular Eq. 14.

To apply Eq. 14 to this problem, one needs to include potassium losses into the analytical model. Given that the density of the ^{39}K gas is one to two orders of magnitude larger than the density of the molecular gas, we can safely assume that the atomic density does not change during the decay of the molecular cloud. Therefore one can treat this like losses from vacuum background collisions, although that does not account for possible re-thermalization of the molecules with the potassium cloud. This results in a molecular two-body decay with an additional exponential one-body decay on top, originating from a two-body atom-molecule loss.

We thus analyze the loss dynamics of the molecular cloud considering molecule-molecule collisions with the obtained k_2 and modeling atom-molecule loss as a one-body (molecule) loss part with k_1 from Eq. 14 expressed as

$$k_1 = k_{2,K}n_K, \quad (16)$$

where n_K is the initial ^{39}K density and $k_{2,K}$ the actual two-body loss rate coefficient, including spatial density overlap of the atomic and molecular cloud in the ODT,

for the atom-molecule collision.

Note that, within the experimental and statistical uncertainties, the obtained values of k_1 , found with the solutions in Sec. II, are compatible with the ones calculated for a system where the atoms and molecules thermalize and therefore remain at a fixed temperature.

We extract the $k_{2,K}$ loss rate coefficients for the atom-molecule collision for the six different hyperfine states of the ^{39}K atoms. The results are shown in Fig. 1 in the left panel. All state combinations show a loss rate coefficient much smaller than the calculated universal limit [38], with one state even showing a drastic suppression of the loss rate coefficient of several orders of magnitude [17]. For comparison, we include the calculated universal scattering limit as a solid black line in Fig. 1, the two-body loss rate coefficient for $^{23}\text{Na}^{39}\text{K}+^{23}\text{Na}$ (Fig. 1, middle panel) as well as the molecule-molecule two-body loss rate coefficient (right panel). The lower part of Fig. 1 shows the number of available energetically allowed loss channels due to hyperfine changing collisions with and without preserved M_F (left and right axes, respectively). The loss rate coefficient for $^{23}\text{Na}^{39}\text{K}+^{23}\text{Na}$ collisions obtained by mean of our model is in agreement with the universal limit and with the fact that for a chemical unstable reaction, all collisions lead to loss of the involved atom and molecule. This is consistent with the large losses observed during the sample preparation and the aforementioned necessity to remove ^{23}Na as quickly as possible from the trap. The numerical agreement also allows us to verify that the applied model gives reasonable output.

IV. DISCUSSION

Without including hyperfine interactions and possible coupling to trimer states, the endoergic nature of the $^{23}\text{Na}^{39}\text{K}+^{39}\text{K}$ system [20] would result in stable and long-lived mixtures, as there are no two-body losses from chemical exchange reactions.

However, near-universal decay which has been attributed to the coupling to a large density of trimer states has been observed in various atom-molecule systems with the exception of $^{40}\text{K}^{87}\text{Rb}+^{87}\text{Rb}$ mixtures when both atoms and molecules have been prepared in their lowest stretched states [19] and in $^6\text{Li}^{23}\text{Na}+^{23}\text{Na}$ with both particles in their highest stretched states [30]. In other state combinations of both examples losses consistent with the universal limit have been reported [16, 19]. Meanwhile, for $^{23}\text{Na}^{40}\text{K}+^{40}\text{K}$ collisions numerous magnetic field tuneable Feshbach resonances in different hyperfine states have been found and assigned to long-range states [32]. In fact, in these experiments collisional resonances have been identified as an enhancement of the loss rate coefficient in the vicinity of a resonance starting from a near-universal background loss [31].

In contrast, for the bosonic $^{23}\text{Na}^{39}\text{K}+^{39}\text{K}$ case we do report suppression of losses far below the universal limit

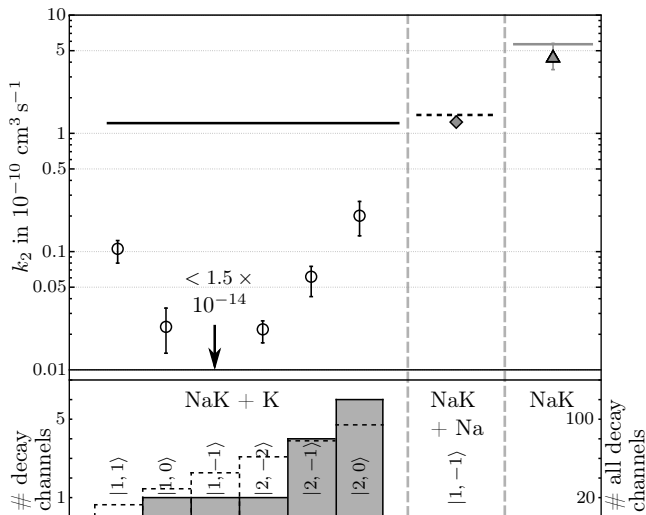


FIG. 1. Loss in atom-molecule mixtures. The upper part shows the two-body loss rate coefficients for the different molecular systems. The left panel includes the loss rate coefficients for the $^{23}\text{Na}^{39}\text{K}+^{39}\text{K}$ mixture with different hyperfine states for ^{39}K atoms (open circles). The values for $^{23}\text{Na}^{39}\text{K}+^{23}\text{Na}$ (gray diamond, middle panel) and $^{23}\text{Na}^{39}\text{K}$ (gray triangle, right panel) are shown for comparison. Note, that the value for the $|1, -1\rangle$ state is so small, that it is not shown in the graph. All measurements were performed at a temperature of 300 nK. The horizontal lines represent the respective universal limit, calculated also for 300 nK. The solid gray bar diagram in the lower part shows the number of available loss channels (left axes) due to hyperfine changing collisions for the $^{23}\text{Na}^{39}\text{K}+^{39}\text{K}$ mixture with the total $M_F = M_{i,\text{NaK}} + m_{f,\text{K}}$ preserved. The dashed bar diagram indicates the number of all energetically possible decay channels (right axes), if one assumes that M_F is not preserved.

where neither the molecules nor the atoms are in their stretched states at the same time, see Fig. 1. Although for the bosonic case $^{23}\text{Na}^{39}\text{K}+^{39}\text{K}$ no magnetic field dependent measurements have been done so far, still the change of the loss rate coefficient for different spin channels suggests a hyperfine dependent Feshbach structure, which is similarly tuneable as in fermionic $^{23}\text{Na}^{40}\text{K}+^{40}\text{K}$ collisions.

The effect of the changed loss rate coefficients and the loss of the particles remains elusive. We rule out, that the losses of molecules originate from hyperfine changing collisions between atoms and molecules with preserved total M_F of the atom-molecule system. For this purpose we determine the Zeeman structure of the lowest hyperfine states of the $^{23}\text{Na}^{39}\text{K}+^{39}\text{K}$ at the magnetic field of 200 G, including hyperfine structure of the molecule in the Paschen-Back and for the atom in the intermediate regime and compare the number of possible $M_F = M_{i,\text{NaK}} + m_{f,\text{K}}$ preserving inelastic loss channels for atom-molecule mixture with the measured loss rate coefficients. The results are shown in the lower panel in Fig. 1. The number of available hyperfine changing loss

channels does not correlate with the loss rate coefficients. This indicates that the observed loss is not dominated by hyperfine changing collisional processes.

In dipolar collisions, hyperfine changing processes can also lead to a non-preserved total angular momentum projection M_F [39, 40]. The dipolar angular momentum of the $^{23}\text{Na}^{39}\text{K}$ molecule in absence of an externally applied electric field is zero. Moreover, the only dipole moments in our $^{23}\text{Na}^{39}\text{K}$ system are the nuclear ones, which are only relevant at short range. Since we cannot exclude the possibility that some resonant processes amplify the influence of the nuclear dipoles, we give in Fig. 1 the number of all energetically possible decay channels even when M_F is not preserved. We find that this number does not correlate with the loss rate coefficients, thus we can rule out a role of hyperfine changing processes just based on possible decay channels.

One other possibility of losses from a collisional system are light-induced losses of long-lived trimer complexes [24, 29], for example from the light of the optical trap. Estimations of rovibrational as well as the hyperfine spacing for the $^{23}\text{Na}^{39}\text{K}+^{39}\text{K}$ complex give evidence for resolvable photo-excitation resonances which might explain the increased loss rate coefficient in certain hyperfine states of ^{39}K atoms [41].

V. CONCLUSION

In summary we investigated atom-molecule two-body loss in a mixture of ultracold $^{23}\text{Na}^{39}\text{K}$ molecules and ^{39}K atoms in six different hyperfine states prepared in an optical dipole trap at a fixed magnetic field of around 200 G. We observed atom-molecule loss that is hyperfine dependent with a two-body loss rate far below the universal limit. We analyzed the two-body loss dynamics based on the derivation of general and easily applicable analytic solutions for the differential equations describing the loss of γ particles in a single collisional event, which are easily implementable in data analysis. In contrast to the numerous atom-molecule mixtures studied to date, in which losses predominantly near or at the universal limit have been observed, the light NaK+K system exhibits interesting properties that require further investigation. Feshbach resonances and hyperfine-dependent collisions have been observed and are far from being understood. New theory insight will be required to understand the physical mechanisms underlying the observed phenomena. Such insight will help to develop a complete understanding of atom-molecule collisions and associated trimer formation and should ultimately be applicable also to molecule-molecule collisions. Detailed understanding of both molecule-molecule and atom-molecule collisions is crucial for further advancement in the production of molecular gases close to quantum degeneracy and associated research opportunities in quantum chemistry, quantum simulation, quantum information and precision

measurements.

ACKNOWLEDGEMENTS

We thank Goulven Quéméner for enlightening comments and Jeremy Hutson and Matthew Frye for insightful conceptions. We gratefully acknowledge financial

support from the European Research Council through ERC Starting Grant POLAR and from the Deutsche Forschungsgemeinschaft (DFG) through CRC 1227 (DQ-mat), project A03 and FOR2247, project E5. P.G. thanks the Deutsche Forschungsgemeinschaft for financial support through Research Training Group 1991. A.Z. thanks Provincia Autonoma di Trento for financial support.

-
- [1] J. Weiner, V. S. Bagnato, S. Zilio, and P. S. Julienne, Experiments and theory in cold and ultracold collisions, *Rev. Mod. Phys.* **71**, 1 (1999).
- [2] H. F. Hess, Evaporative cooling of magnetically trapped and compressed spin-polarized hydrogen, *Phys. Rev. B* **34**, 3476 (1986).
- [3] M. H. Anderson, J. R. Ensher, M. R. Matthews, C. E. Wieman, and E. A. Cornell, Observation of Bose-Einstein Condensation in a Dilute Atomic Vapor, *Science* **269**, 198 (1995).
- [4] C. Chin, R. Grimm, P. Julienne, and E. Tiesinga, Feshbach resonances in ultracold gases, *Rev. Mod. Phys.* **82**, 1225 (2010).
- [5] C. C. Bradley, C. A. Sackett, and R. G. Hulet, Bose-Einstein Condensation of Lithium: Observation of Limited Condensate Number, *Phys. Rev. Lett.* **78**, 985 (1997).
- [6] G. Roati, M. Zaccanti, C. D’Errico, J. Catani, M. Modugno, A. Simoni, M. Inguscio, and G. Modugno, ^{39}K Bose-Einstein Condensate with Tunable Interactions, *Phys. Rev. Lett.* **99**, 010403 (2007).
- [7] D. S. Petrov, Quantum Mechanical Stabilization of a Collapsing Bose-Bose Mixture, *Phys. Rev. Lett.* **115**, 155302 (2015).
- [8] C. R. Cabrera, L. Tanzi, J. Sanz, B. Naylor, P. Thomas, P. Cheiney, and L. Tarruell, Quantum liquid droplets in a mixture of Bose-Einstein condensates, *Science* **359**, 301–304 (2018).
- [9] E. A. Donley, N. R. Claussen, S. T. Thompson, and C. E. Wieman, Atom–molecule coherence in a Bose–Einstein condensate, *Nature* **417**, 529–533 (2002).
- [10] M. Mayle, B. P. Ruzic, and J. L. Bohn, Statistical aspects of ultracold resonant scattering, *Phys. Rev. A* **85**, 062712 (2012).
- [11] K.-K. Ni, S. Ospelkaus, M. H. G. de Miranda, A. Peer, B. Neyenhuis, J. J. Zirbel, S. Kotochigova, P. S. Julienne, D. S. Jin, and J. Ye, A High Phase-Space-Density Gas of Polar Molecules, *Science* **322**, 231 (2008).
- [12] T. Takekoshi, L. Reichsöllner, A. Schindewolf, J. M. Hutson, C. R. Le Sueur, O. Dulieu, F. Ferlaino, R. Grimm, and H.-C. Nägerl, Ultracold Dense Samples of Dipolar RbCs Molecules in the Rovibrational and Hyperfine Ground State, *Phys. Rev. Lett.* **113**, 205301 (2014).
- [13] P. K. Molony, P. D. Gregory, Z. Ji, B. Lu, M. P. Köpinger, C. R. Le Sueur, C. L. Blackley, J. M. Hutson, and S. L. Cornish, Creation of Ultracold $^{87}\text{Rb}^{133}\text{Cs}$ Molecules in the Rovibrational Ground State, *Phys. Rev. Lett.* **113**, 255301 (2014).
- [14] J. W. Park, S. A. Will, and M. W. Zwierlein, Ultracold Dipolar Gas of Fermionic $^{23}\text{Na}^{40}\text{K}$ Molecules in Their Absolute Ground State, *Phys. Rev. Lett.* **114**, 205302 (2015).
- [15] M. Guo, B. Zhu, B. Lu, X. Ye, F. Wang, R. Vexiau, N. Bouloufa-Maafa, G. Quéméner, O. Dulieu, and D. Wang, Creation of an Ultracold Gas of Ground-State Dipolar $^{23}\text{Na}^{87}\text{Rb}$ Molecules, *Phys. Rev. Lett.* **116**, 205303 (2016).
- [16] T. M. Rvachov, H. Son, A. T. Sommer, S. Ebadi, J. J. Park, M. W. Zwierlein, W. Ketterle, and A. O. Jamiison, Long-Lived Ultracold Molecules with Electric and Magnetic Dipole Moments, *Phys. Rev. Lett.* **119**, 143001 (2017).
- [17] K. K. Voges, P. Gersema, M. Meyer zum Alten Borgloh, T. A. Schulze, T. Hartmann, A. Zenesini, and S. Ospelkaus, Ultracold Gas of Bosonic $^{23}\text{Na}^{39}\text{K}$ Ground-State Molecules, *Phys. Rev. Lett.* **125**, 083401 (2020).
- [18] P. S. Julienne, T. M. Hanna, and Z. Idziaszek, Universal ultracold collision rates for polar molecules of two alkali-metal atoms, *Phys. Chem. Chem. Phys.* **13**, 19114 (2011).
- [19] S. Ospelkaus, K.-K. Ni, D. Wang, M. H. G. de Miranda, B. Neyenhuis, G. Quemener, P. S. Julienne, J. L. Bohn, D. S. Jin, and J. Ye, Quantum-State Controlled Chemical Reactions of Ultracold Potassium-Rubidium Molecules, *Science* **327**, 853 (2010).
- [20] P. S. Żuchowski and J. M. Hutson, Reactions of ultracold alkali-metal dimers, *Phys. Rev. A* **81**, 060703 (2010).
- [21] M.-G. Hu, Y. Liu, D. D. Grimes, Y.-W. Lin, A. H. Gheorghe, R. Vexiau, N. Bouloufa-Maafa, O. Dulieu, T. Rosenband, and K.-K. Ni, Direct observation of bimolecular reactions of ultracold KRb molecules, *Science* **366**, 1111–1115 (2019).
- [22] M. Mayle, G. Quéméner, B. P. Ruzic, and J. L. Bohn, Scattering of ultracold molecules in the highly resonant regime, *Phys. Rev. A* **87**, 012709 (2013).
- [23] P. D. Gregory, M. D. Frye, J. A. Blackmore, E. M. Bridge, R. Sawant, J. M. Hutson, and S. L. Cornish, Sticky collisions of ultracold RbCs molecules, *Nature Communications* **10**, 3104 (2019).
- [24] A. Christianen, M. W. Zwierlein, G. C. Groenenboom, and T. Karman, Photoinduced Two-Body Loss of Ultracold Molecules, *Phys. Rev. Lett.* **123**, 123402 (2019).
- [25] Y. Liu, M.-G. Hu, M. A. Nichols, D. D. Grimes, T. Karman, H. Guo, and K.-K. Ni, Photo-excitation of long-lived transient intermediates in ultracold reactions, *Nature Physics* **16**, 1132–1136 (2020).
- [26] P. D. Gregory, J. A. Blackmore, S. L. Bromley, and S. L. Cornish, Loss of Ultracold $^{87}\text{Rb}^{133}\text{Cs}$ Molecules via Optical Excitation of Long-Lived Two-Body Collision Complexes, *Phys. Rev. Lett.* **124**, 163402 (2020).

- [27] P. Gersema, K. K. Voges, M. Meyer zum Alten Borghlo, L. Koch, T. Hartmann, A. Zenesini, S. Ospelkaus, J. Lin, J. He, and D. Wang, Probing Photoinduced Two-Body Loss of Ultracold Nonreactive Bosonic $^{23}\text{Na}^{87}\text{Rb}$ and $^{23}\text{Na}^{39}\text{K}$ Molecules, *Phys. Rev. Lett.* **127**, 163401 (2021).
- [28] R. Bause, A. Schindewolf, R. Tao, M. Duda, X.-Y. Chen, G. Quémener, T. Karman, A. Christianen, I. Bloch, and X.-Y. Luo, Collisions of ultracold molecules in bright and dark optical dipole traps, *Phys. Rev. Research* **3**, 033013 (2021).
- [29] M. A. Nichols, Y.-X. Liu, L. Zhu, M.-G. Hu, Y. Liu, and K.-K. Ni, Detection of Long-Lived Complexes in Ultracold Atom-Molecule Collisions (2021), arXiv:2105.14960 [physics.atom-ph].
- [30] H. Son, J. J. Park, W. Ketterle, and A. O. Jamison, Collisional cooling of ultracold molecules, *Nature* **580**, 197–200 (2020).
- [31] H. Yang, D.-C. Zhang, L. Liu, Y.-X. Liu, J. Nan, B. Zhao, and J.-W. Pan, Observation of magnetically tunable Feshbach resonances in ultracold $^{23}\text{Na}^{40}\text{K} + ^{40}\text{K}$ collisions, *Science* **363**, 261 (2019).
- [32] X.-Y. Wang, M. D. Frye, Z. Su, J. Cao, L. Liu, D.-C. Zhang, H. Yang, J. M. Hutson, B. Zhao, C.-L. Bai, and J.-W. Pan, Magnetic Feshbach resonances in collisions of $^{23}\text{Na}^{40}\text{K}$ with ^{40}K (2021), arXiv:2103.07130 [physics.atom-ph].
- [33] Note, we define 2σ as the distance, where the density drops to $\frac{1}{e^2} \cdot n(0, 0, 0)$.
- [34] P.-T. Kraemer, Few-body interactions in an ultracold gas of cesium atoms (2006).
- [35] T. A. Schulze, T. Hartmann, K. K. Voges, M. W. Gempel, E. Tiemann, A. Zenesini, and S. Ospelkaus, Feshbach spectroscopy and dual-species Bose-Einstein condensation of $^{23}\text{Na}-^{39}\text{K}$ mixtures, *Phys. Rev. A* **97**, 023623 (2018).
- [36] K. K. Voges, P. Gersema, T. Hartmann, T. A. Schulze, A. Zenesini, and S. Ospelkaus, Formation of ultracold weakly bound dimers of bosonic $^{23}\text{Na}^{39}\text{K}$, *Phys. Rev. A* **101**, 042704 (2020).
- [37] S. Y. Buhmann, M. R. Tarbutt, S. Scheel, and E. A. Hinds, Surface-induced heating of cold polar molecules, *Phys. Rev. A* **78**, 052901 (2008).
- [38] Y.-P. Bai, J.-L. Li, G.-R. Wang, Z.-B. Chen, B.-W. Si, and S.-L. Cong, Simple analytical model for high-partial-wave ultracold molecular collisions, *Phys. Rev. A* **101**, 063605 (2020).
- [39] J. Söding, D. Guéry-Odelin, P. Desbiolles, G. Ferrari, and J. Dalibard, Giant spin relaxation of an ultracold cesium gas, *Phys. Rev. Lett.* **80**, 1869 (1998).
- [40] S. Hensler, U. J. Werner, A. Griesmaier, P. Schmidt, A. Görlitz, T. Pfau, S. Giovanazzi, and K. K. Rzazewski, Dipolar relaxation in an ultra-cold gas of magnetically trapped chromium atom, *Appl. Phys. B* **77**, 765–772 (2003).
- [41] J. M. Hutson and M. D. Frye, private communication (2021).

6 Conclusion and outlook

Within this dissertation, a new molecular species with high phase-space density in the rovibronic ground state was added to the few of already existing ultracold polar molecules. This was made possible, by spectroscopic studies of the molecular manifolds $|B^1\Pi, v = 8\rangle$ and $|c^3\Sigma^+, v = 30\rangle$, which exhibit strong singlet/triplet mixing and sufficient Franck-Condon factors, the measurement of previously unknown $^{23}\text{Na}^{39}\text{K}$ Feshbach resonances and the subsequent generation of weakly bound molecules. This new molecular platform enabled collisional studies that contributed to the ongoing efforts to understand ultracold molecular ensembles. To this end, the photoexcitation of molecular tetramer complexes was studied. The results show much longer complex lifetimes than predicted by RRKM theory or hint to a different loss mechanism. They therefore partially call into question what was previously considered to be a complete picture of complex formation and subsequent excitation of these complexes by light from the optical dipole trap.

The POLAR laboratory can also be used for experiments with ultracold ^{39}K atoms. Three new potassium d -wave Feshbach resonances have been measured. These refined the interatomic potassium potentials and showed that corrections beyond the Born-Oppenheimer approximation are necessary for an accurate description.

In addition atom-molecule mixtures have been investigated. The results revealed spin-dependent scattering properties and, especially intriguing, a strong suppression of the two-body loss-rate coefficient in the non-stretched hyperfine state $|F = 1, m_F = -1\rangle$, roughly four orders of magnitude below the universal limit. Such a strong suppression has not been observed to date.

These measurements leave many possibilities for future experiments in the POLAR laboratory.

To avoid the currently unknown loss mechanisms of $^{23}\text{Na}^{39}\text{K}$ in the ODT, one could use shielding techniques, e.g. optical shielding [86]. This technique requires a blue-detuned laser relative to the transition from the rovibronic ground state in the $X^1\Sigma^+$ manifold, to a rotationally excited state of the lowest electronically excited triplet manifold $b^3\Pi$. Spectroscopic measurements are currently in preparation to determine the precise energy levels, transition strengths, and linewidths of this state. Furthermore, these results can be utilized to perform spectroscopic measurements of trimer $^{23}\text{Na}^{39}\text{K}_2$ states, below the energetically lowest lying $b^3\Pi$ manifold. With a successful implementation of shielding, evaporative cooling of the molecules should be possible. In particular it could be especially interesting to try to sympathetically cool the molecules with potassium atoms in the $|F = 1, m_F = -1\rangle$ hyperfine state. If this low two-body loss rate is corresponding to a high elastic and low inelastic collision rate, one could apply a magnetic field gradient, which does not affect

6 Conclusion and outlook

the molecules, while lowering the potential by slowly increasing the gradient. With this almost no molecules should be lost and therefore this cooling method could be highly efficient.

The investigation of spin-dependent losses in atom-molecule mixtures can be further extended by magnetic field scans. This would allow the study of magnetic field-dependent loss rates and potential Feshbach resonances. For the success of these measurements, it is important to study the scattering properties of the molecules in the first few milliseconds after their formation, since the dynamics of the two-body decay is fastest at the beginning and slows down afterwards, when only a few molecules remain. This fast initial loss demands fast magnetic field ramps, which in turn induce Eddy currents in the experimental chamber. Pre-emphasis magnetic field ramps allow to circumvent this problem [108]. It is therefore planned to implement this technique in the future. To complete the picture, it is desirable to change not only the hyperfine state of the potassium atoms, but also the nuclear spin of the molecules in the ground state. This can be done for example with MW pulses, that couple to the first excited rotational state [111].

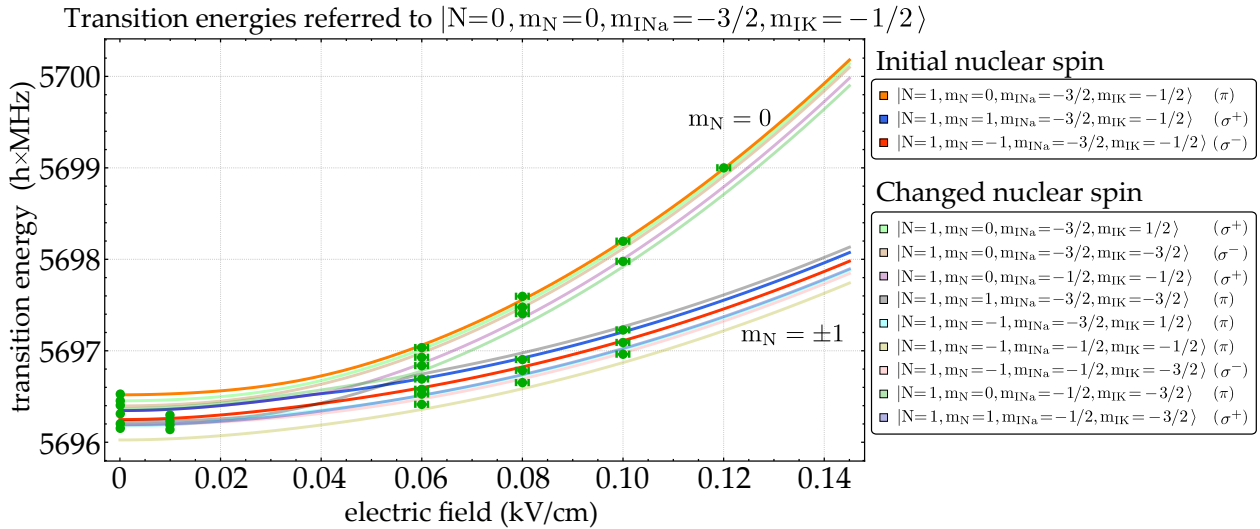


Figure 6.1: Preliminary $^{23}\text{Na}^{39}\text{K}$ microwave spectroscopy results of the first excited rotational state starting from the rovibronic ground state with nuclear spin projections $|m_{I,Na} = -3/2, m_{I,K} = -1/2\rangle$ in an external electric field. The upper legend shows the levels with the same nuclear spin as in the rovibronic ground state, the lower one the levels with changed nuclear spin. The levels are denoted in the limit of high electric fields. Green dots mark the positions of found MW transitions. In future measurements these transitions will allow for the manipulation of the nuclear spin state of the ground-state molecules, by a consecutive MW pulse back to a different rovibronic ground state.

MW spectroscopy measurements inside an external electric field have already been performed. Preliminary results can be found in Fig. 6.1. The legend denotes the states with the same or different nuclear spin compared to the initial state in the limit of a high external electric field. N is the molecular rotation quantum number, m_N its projection along the electric field axis and

$m_{I,\text{Na}}$ and $m_{I,\text{K}}$ the projections of the nuclear spins. The external electric field is applied through indium tin oxide (ITO) electrodes on the main windows of the experimental chamber. A detailed description can be found in [33].

Finally, the POLAR experiment has the capability to include a three-dimensional lattice and a high resolution objective, with the ability of single site resolved imaging [33]. In a first step of the lattice implementation, a one-dimensional standing wave could be introduced. Together with a strong external electric field, with its axis aligned along the lattice beam paths, collisional shielding could be achieved due to the anisotropic nature of the DDIs, similarly to KRb [61]. This might allow forced evaporation inside the dipole trap. In Fig. 6.2 the Stark shift of the rovibronic ground state is measured, together with the induced dipole moment, shown in the inset.

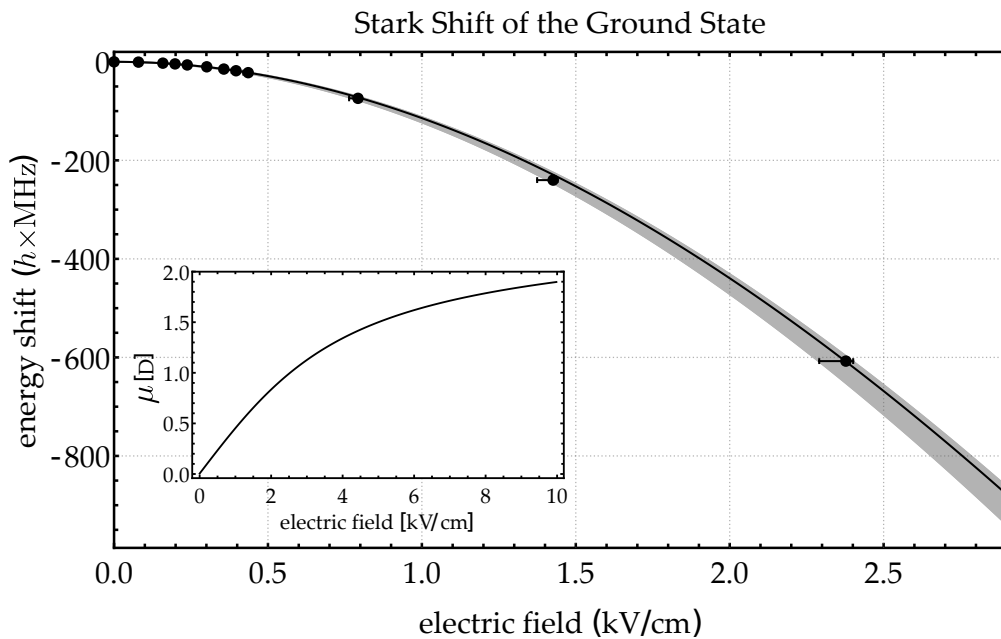


Figure 6.2: Stark shift of the rovibronic ground state in an external electric field generated using the electrode configuration described in [33], with the induced dipole moment in the inset. The black solid line represents a fit with a dipole moment of $\mu = 2.80^{+0.10}_{-0.03}$ Debye, consistent with the value given in [112]. This dipole moment is only reached in the limit of infinitely strong electric fields. Image adopted from [95].

Bibliography

- [1] T. H. Maiman. Stimulated Optical Radiation in Ruby. *Nature*, 187:493–494, August 1960.
- [2] M. A. Lombardi. A Historical Review of U.S. Contributions to the Atomic Redefinition of the SI Second in 1967. *Journal of Research of the National Institute of Standards and Technology*, 122:29:4, June 2017.
- [3] S. Bravyi, D. Gosset, and R. König. Quantum advantage with shallow circuits. *Science*, 362(6412):308–311, October 2018.
- [4] K. B. Davis, M. O. Mewes, M. R. Andrews, N. J. van Druten, D. S. Durfee, D. M. Kurn, and W. Ketterle. Bose-Einstein Condensation in a Gas of Sodium Atoms. *Physical Review Letters*, 75:3969–3973, November 1995.
- [5] M. H. Anderson, J. R. Ensher, M. R. Matthews, C. E. Wieman, and E. A. Cornell. Observation of Bose-Einstein Condensation in a Dilute Atomic Vapor. *Science*, 269(5221):198–201, July 1995.
- [6] C. C. Bradley, C. A. Sackett, J. J. Tollett, and R. G. Hulet. Evidence of Bose-Einstein Condensation in an Atomic Gas with Attractive Interactions. *Physical Review Letters*, 75:1687–1690, August 1995.
- [7] B. DeMarco and D. S. Jin. Onset of Fermi Degeneracy in a Trapped Atomic Gas. *Science*, 285(5434):1703–1706, 1999.
- [8] C. A. Regal, C. Ticknor, J. Bohn, and D. S. Jin. Creation of ultracold molecules from a Fermi gas of atoms. *Nature*, 424:47–50, July 2003.
- [9] M. W. Zwierlein, C. A. Stan, C. H. Schunck, S. M. F. Raupach, A. J. Kerman, and W. Ketterle. Condensation of pairs of fermionic atoms near a feshbach resonance. *Physical Review Letters*, 92:120403, March 2004.
- [10] C. A. Regal, M. Greiner, and D. S. Jin. Observation of resonance condensation of fermionic atom pairs. *Physical Review Letters*, 92:040403, January 2004.
- [11] I. Bloch. Ultracold quantum gases in optical lattices. *Nature Physics*, 1:23–30, Oktober 2005.

Bibliography

- [12] M. Greiner, O. Mandel, T. Esslinger, T. W. Hänsch, and I. Bloch. Quantum phase transition from a superfluid to a mott insulator in a gas of ultracold atoms. *Nature*, 415:194197, January 2002.
- [13] X.-Y. Luo, Y.-Q. Zou, L.-N. Wu, Q. Liu, M.-F. Han, M. K. Tey, and L. You. Deterministic entanglement generation from driving through quantum phase transitions. *Science*, 355(6325):620–623, 2017.
- [14] J. Pesie, I. Kruse, K. Lange et al., B. Lücke, L. Pezzè, J. Arlt, W. Ertmer, K. Hammerer, L. Santos, A. Smerzi, and C. Klempt. Satisfying the einstein-podolsky-rosen criterion with massive particles. *Nature Communications*, 6, November 2015.
- [15] T. Lahaye, C. Menotti, L. Santos, M. Lewenstein, and T. Pfau. The physics of dipolar bosonic quantum gases. *Reports on Progress in Physics*, 72(12):126401, November 2009.
- [16] N. Šibalić and C. S. Adams. *Rydberg Physics*. 2399-2891. IOP Publishing, 2018.
- [17] T. A. Schulze. Quantum degenerate mixtures of ^{23}Na - ^{39}K and coherent transfer paths in NaK molecules. *PhD thesis, Leibniz Universität Hannover*, May 2018.
- [18] A. Griesmaier, J. Werner, S. Hensler, J. Stuhler, and T. Pfau. Bose-einstein condensation of chromium. *Physical Review Letters*, 94:160401, April 2005.
- [19] M. Lu, N. Q. Burdick, S. H. Youn, and B. L. Lev. Strongly dipolar bose-einstein condensate of dysprosium. *Physical Review Letters*, 107:190401, October 2011.
- [20] K. Aikawa, A. Frisch, M. Mark, S. Baier, A. Rietzler, R. Grimm, and F. Ferlaino. Bose-einstein condensation of erbium. *Physical Review Letters*, 108:210401, 2012.
- [21] E. T. Davletov, V. V. Tsyganok, V. A. Khlebnikov, D. A. Pershin, D. V. Shaykin, and A. V. Akimov. Machine learning for achieving bose-einstein condensation of thulium atoms. *Physical Review A*, 102:011302, July 2020.
- [22] L. Chomaz, R.M.W. van Bijnen, D. Petter et al., G. Faraoni, S. Baier, F. Wächtler L. Santos J. H. Becher, M. J. Mark, and F. Ferlaino. Observation of roton mode population in a dipolar quantum gas. *Nature Physics*, 14:442–446, March 2018.
- [23] I. Ferrier-Barbut, H. Kadau, M. Schmitt, M. Wenzel, and T. Pfau. Observation of quantum droplets in a strongly dipolar bose gas. *Physical Review Letters*, 116:215301, May 2016.
- [24] H. Kadau, M. Schmitt, Wenzel et al., M., C. Wink, T. Maier, I. Ferrier-Barbut, and T. Pfau. Observing the rosenweig instability of a quantum ferrofluid. *Nature*, 530:194–197, February 2016.

- [25] M.A. Norcia, C. Politi, L. Klaus, M. Sohmen E. Poli, M. J. Mark, R. N. Bisset, L. Santos, and F. Ferlaino. Two-dimensional supersolidity in a dipolar quantum gas. *Nature*, 596:357–361, August 2021.
- [26] T. F. Gallagher and P. Pillet. Dipole-Dipole Interactions of Rydberg Atoms. In *Advances in Atomic, Molecular, and Optical Physics*, volume 56, pages 161–218. Academic Press, 2008.
- [27] C. S. Adams, J. D. Pritchard, and J. P. Shaffer. Rydberg atom quantum technologies. *Journal of Physics B: Atomic, Molecular and Optical Physics*, 53(1):012002, December 2019.
- [28] E. Urban, T. Johnson, T. Henage., L. Isenhower, D. D. Yavuz, T. G. Walker, and M. Saffman. Observation of rydberg blockade between two atoms. *Nature Physics*, 5:110–114, January 2009.
- [29] T. Wilk, A. Gaëtan, C. Evellin, J. Wolters, Y. Miroshnychenko, P. Grangier, and A. Browaeys. Entanglement of two individual neutral atoms using rydberg blockade. *Physical Review Letters*, 104:010502, January 2010.
- [30] A. Omran, H. Levine, A. Keesling, G. Semeghini, T. T. Wang, S. Ebadi, H. Bernien, A. S. Zibrov, H. Pichler, S. Choi, J. Cui, M. Rossignolo, P. Rembold, S. Montangero, T. Calarco, M. Endres, M. Greiner, V. Vuleti, and M. D. Lukin. Generation and manipulation of schrödinger cat states in rydberg atom arrays. *Science*, 365(6453):570–574, 2019.
- [31] T. Niederprüm, O. Thomas, T. Eichert, C. Lippe, C. H. Greene J. Pérez-Ríos, and H. Ott. Observation of pendular butterfly rydberg molecules. *Nature Communications*, 7:12820, October 2016.
- [32] M. W. Gempel, T. Hartmann, T. A. Schulze, K. K. Voges, A. Zenesini, and S. Ospelkaus. Versatile electric fields for the manipulation of ultracold NaK molecules. *New Journal of Physics*, 18(4):045017, April 2016.
- [33] M. W. Gempel. Towards Ultracold Polar NaK Molecules and the Investigation of Dipolar Quantum Gases. *PhD thesis, Leibniz Universität Hannover*, February 2018.
- [34] H. J. Metcalf and P. van der Straten. Laser cooling and trapping. *Optics & Photonics News-OPT PHOTONICS NEWS*, 11, 2000.
- [35] S. Ospelkaus, K.-K. Ni, D. Wang, M. H. G. de Miranda, B. Neyenhuis, G. Quéméner, P. S. Julienne, J. L. Bohn, D. S. Jin, and J. Ye. Quantum-state controlled chemical reactions of ultracold potassium-rubidium molecules. *Science*, 327(5967):853–857, 2010.
- [36] S. Moses, J. Covey, M. Miecnikowski, D. S. Jin, and J. Ye. New frontiers for quantum gases of polar molecules. *Nature Physics*, 530:194–197, February 2016.

Bibliography

- [37] L. W. Cheuk, L. Anderegg, B. L. Augenbraun, Y. Bao, S. Burchesky, W. Ketterle, and J. M. Doyle. Λ -enhanced imaging of molecules in an optical trap. *Physical Review Letters*, 121:083201, August 2018.
- [38] H. Son, J. J. Park, W. Ketterle et al., and Jamison A. O. Collisional cooling of ultracold molecules. *Nature*, 580:197–200, April 2020.
- [39] N. R. Hutzler, H.-I Lu, and J. M. Doyle. The buffer gas beam: An intense, cold, and slow source for atoms and molecules. *Chemical Reviews*, 112(9):4803–4827, 2012. PMID: 22571401.
- [40] H. L. Bethlem and G. Meijer. Production and application of translationally cold molecules. *International Reviews in Physical Chemistry*, 22(1):73–128, 2003.
- [41] E. Narevicius, A. Libson, C. G. Parthey, I. Chavez, J. Narevicius, U. Even, and M. G. Raizen. Stopping supersonic beams with a series of pulsed electromagnetic coils: An atomic coilgun. *Physical Review Letters*, 100:093003, March 2008.
- [42] B. L. Augenbraun, A. Frenett, H. Sawaoka, C. n Hallas, N. B. Vilas, A. Nasir, Z. D. Lasner, and J. M. Doyle. Zeeman-sisyphus deceleration of molecular beams. *Physical Review Letters*, 127:263002, December 2021.
- [43] S. Chervenkov, X. Wu, J. Bayerl, A. Rohlfes, T. Gantner, M. Zeppenfeld, and G. Rempe. Continuous centrifuge decelerator for polar molecules. *Physical Review Letters*, 112:013001, January 2014.
- [44] J. Barry, D. McCarron, E. Norrgard, M. H. Steinecker, and D. DeMille. Magneto-optical trapping of a diatomic molecule. *Nature*, 512:286–289, August 2014.
- [45] M. Petzold, P. Kaebert, P. Gersema, M. Siercke, and S. Ospelkaus. A zeeman slower for diatomic molecules. *New Journal of Physics*, 20(4):042001, April 2018.
- [46] Y. Wu, J. J. Burau, K. Mehling, J. Ye, and S. Ding. High phase-space density of laser-cooled molecules in an optical lattice. *Physical Review Letters*, 127.
- [47] N. V. Vitanov, A. A. Rangelov, B. W. Shore, and K. Bergmann. Stimulated raman adiabatic passage in physics, chemistry, and beyond. *Reviews of Modern Physics*, 89:015006, March 2017.
- [48] S. Ospelkaus, A. Pèer, K.-K. Ni, J. J. Zirbel, B. Neyenhuis, S. Kotochigova, P. S. Julienne, J. Ye, and D. S. Jin. Efficient state transfer in an ultracold dense gas of heteronuclear molecules. *Nature Physics*, 4:622–626, June 2008.
- [49] J. J. Zirbel, K.-K. Ni, S. Ospelkaus, T. L. Nicholson, M. L. Olsen, P. S. Julienne, C. E. Wieman, J. Ye, and D. S. Jin. Heteronuclear molecules in an optical dipole trap. *Physical Review A*, 78:013416, July 2008.

- [50] J. W. Park, S. A. Will, and M. W. Zwierlein. Ultracold Dipolar Gas of Fermionic $^{23}\text{Na}^{40}\text{K}$ Molecules in Their Absolute Ground State. *Physical Review Letters*, 114:205302, May 2015.
- [51] J. Rui, H. Yang, L. Liu, D.-C. Zhang, Y.-X. Liu, J. Nan, Y.-A. Chen, B. Zhao, and J.-W. Pan. Controlled state-to-state atom-exchange reaction in an ultracold atom-dimer mixture. *Nature Physics*, 13:699–703, April 2017.
- [52] F. Seeßelberg, N. Buchheim, Z.-K. Lu, T. Schneider, X.-Y. Luo, E. Tiemann, I. Bloch, and C. Gohle. Modeling the adiabatic creation of ultracold polar $^{23}\text{Na}^{40}\text{K}$ molecules. *Physical Review A*, 97:013405, January 2018.
- [53] T. Takekoshi, L. Reichsöllner, A. Schindewolf, Jeremy M. Hutson, C. R. Le Sueur, O. Dulieu, F. Ferlaino, R. Grimm, and H.-C. Nägerl. Ultracold dense samples of dipolar rbc molecules in the rovibrational and hyperfine ground state. *Physical Review Letters*, 113:205301, November 2014.
- [54] P. K. Molony, P. D. Gregory, Z. Ji, B. Lu, M. P. Köppinger, C. R. Le Sueur, C. L. Blackley, J. M. Hutson, and S. L. Cornish. Creation of Ultracold $^{87}\text{Rb}^{133}\text{Cs}$ Molecules in the Rovibrational Ground State. *Physical Review Letters*, 113:255301, December 2014.
- [55] M. Guo, B. Zhu, B. Lu, X. Ye, F. Wang, R. Vexiau, N. Bouloufa-Maafa, G. Quéméner, O. Dulieu, and D. Wang. Creation of an Ultracold Gas of Ground-State Dipolar $^{23}\text{Na}^{87}\text{Rb}$ Molecules. *Physical Review Letters*, 116:205303, May 2016.
- [56] W. B. Cairncross, J. T. Zhang, L. R. B. Picard, Y. Yu, K. Wang, and K.-K. Ni. Assembly of a rovibrational ground state molecule in an optical tweezer. *Physical Review Letters*, 126:123402, March 2021.
- [57] K. K. Voges, P. Gersema, M. Meyer zum Alten Borgloh, T. A. Schulze, T. Hartmann, A. Zenesini, and S. Ospelkaus. Ultracold gas of bosonic $^{23}\text{Na}^{39}\text{K}$ ground-state molecules. *Physical Review Letters*, 125:083401, August 2020.
- [58] K. K. Voges. An Ultracold Gas of Bosonic $^{23}\text{Na}^{39}\text{K}$ Ground-State Molecules. *PhD thesis, Leibniz Universität Hannover*, October 2018.
- [59] B. Yan, S. Moses, B. Gadway, J. P. Covey, K. R. A. Hazzard, A. M. Rey, D. S. Jin, and J. Ye. Observation of dipolar spin-exchange interactions with lattice-confined polar molecules. *Nature*, 501:521–525, September 2013.
- [60] J. He, X. Ye, J. Lin, M. Guo, G. Quéméner, and D. Wang. Observation of resonant dipolar collisions in ultracold $^{23}\text{Na}^{87}\text{Rb}$ rotational mixtures. *Physical Review Research*, 3:013016, January 2021.

Bibliography

- [61] G. Valtolina, K. Matsusada, W.G. Tobias, J.-R. Li, L. De Marco, and J. Ye. Dipolar evaporation of reactive molecules to below the fermi temperature. *Nature*, 588:239–243, December 2020.
- [62] L. De Marco, G. Valtolina, K. Matsuda, W. G. Tobias, J. P. Covey, and J. Ye. A degenerate fermi gas of polar molecules. *Science*, 363(6429):853–856, 2019.
- [63] A. Schindewolf, R. Bause, X.-Y. Chen, M. Duda, T. Karman, I. Bloch, and Xin-Yu Luo. Evaporation of microwave-shielded polar molecules to quantum degeneracy, 2022.
- [64] S. Ospelkaus, K.-K. Ni, D. Wang, M. H. G. de Miranda, B. Neyenhuis, G. Quéméner, P. S. Julienne, J. L. Bohn, D. S. Jin, and J. Ye. Quantum-state controlled chemical reactions of ultracold potassium-rubidium molecules. *Science*, 327(5967):853–857, 2010.
- [65] P. S. Julienne, T. M. Hanna, and Z. Idziaszek. Universal ultracold collision rates for polar molecules of two alkali-metal atoms. *Physical Chemistry Chemical Physics*, 13:19114–19124, 2011.
- [66] P. S. Żuchowski and J. M. Hutson. Reactions of ultracold alkali-metal dimers. *Physical Review A*, 81:060703, June 2010.
- [67] E. R. Meyer and J. L. Bohn. Product-state control of bi-alkali-metal chemical reactions. *Physical Review A*, 82:042707, October 2010.
- [68] P. D. Gregory, M.D. Frye, J. A. Blackmore, E. M. Bridge, R. Sawant, J. M. Hutson, and S. L. Cornish. Sticky collisions of ultracold rbc molecules. *Nature Communications*, 10:3104, July 2019.
- [69] X. Ye, M. Guo, M. L. González-Martínez, G. Quéméner, and D. Wang. Collisions of ultracold $^{23}\text{Na}^{87}\text{Rb}$ molecules with controlled chemical reactivities. *Science Advances*, 4(1):eaq0083, January 2018.
- [70] K.-K. Ni, S. Ospelkaus, D. Wang, G. Quéméner, B. Neyenhuis, M. H. G. de Miranda, J. L. Bohn, J. Ye, and D. S. Jin. Dipolar collisions of polar molecules in the quantum regime. *Nature*, 464:1324–1328, April 2010.
- [71] M. Guo, X. Ye, J. He, M. L. González-Martínez, R. Vexiau, G. Quéméner, and D. Wang. Dipolar collisions of ultracold ground-state bosonic molecules. *Physical Review X*, 8:041044, December 2018.
- [72] G. Quéméner, J. F. E. Croft, and J. L. Bohn. Electric field dependence of complex-dominated ultracold molecular collisions. *Physical Review A*, 105:013310, January 2022.
- [73] X.-Y. Wang, M. D. Frye, Z. Su, J. Cao, L. Liu, D.-C. Zhang, H. Yang, J. M. Hutson, B. Z., C.-L. Bai, and J.-W. Pan. Magnetic Feshbach resonances in collisions of $^{23}\text{Na}^{40}\text{K}$ with ^{40}K . *New Journal of Physics*, 23(11):115010, November 2021.

- [74] Y.-K. Lu, A. O. Jamison, T. Karman, H. Son, J. J. Park and W. Ketterle. Control of reactive collisions by quantum interference, September 2021.
- [75] J. Rui, H. Yang, L. Liu, D.-C. Zhang, Y.-X. Liu, J. Nan, Y.-A. Chen, B. Zhao, and J.-W. Pan. Controlled state-to-state atom-exchange reaction in an ultracold atom-dimer mixture. *Nature Physics*, 13:699–703, April 2017.
- [76] M.-G. Hu, Y. Liu, D. D. Grimes, Y.-W. Lin, A. H. Gheorghe, R. Vexiau, N. Bouloufa-Maafa, O. Dulieu, T. Rosenband, and K.-K. Ni. Direct observation of bimolecular reactions of ultracold KRb molecules. *Science*, 366(6469):1111–1115, November 2019.
- [77] M.-G. Hu, Y. Liu, M. A. Nichols, L. Zhu, G. Quéméner, O. Dulieu, and K.-K. Ni. Nuclear spin conservation enables state-to-state control of ultracold molecular reactions. *Nature Chemistry*, 13:434–440, December 2021.
- [78] M. Mayle, G. Quéméner, B. P. Ruzic, and J. L. Bohn. Scattering of ultracold molecules in the highly resonant regime. *Physical Review A*, 87:012709, January 2013.
- [79] A. Christianen, M. W. Zwierlein, G. C. Groenenboom, and T. Karman. Photoinduced two-body loss of ultracold molecules. *Physical Review Letters*, 123:123402, September 2019.
- [80] P. D. Gregory, J. A. Blackmore, S. L. Bromley, and S. L. Cornish. Loss of ultracold $^{87}\text{Rb}^{133}\text{Cs}$ molecules via optical excitation of long-lived two-body collision complexes. *Physical Review Letters*, 124:163402, April 2020.
- [81] Y. Liu, M.-G. Hu, M. A. Nichols, D. D. Grimes, T. Karman, H. Guo, and K.-K. Ni. Photo-excitation of long-lived transient intermediates in ultracold reactions. *Nature Physics*, 16(11):11321136, July 2020.
- [82] Roman Bause, Andreas Schindewolf, Renhao Tao, Marcel Duda, Xing-Yan Chen, Goulven Quéméner, Tijds Karman, Arthur Christianen, Immanuel Bloch, and Xin-Yu Luo. Collisions of ultracold molecules in bright and dark optical dipole traps. *Phys. Rev. Research*, 3:033013, July 2021.
- [83] P. Gersema, K. K. Voges, M. Meyer zum Alten Borgloh, L. Koch, T. Hartmann, A. Zenesini, S. Ospelkaus, J. Lin, J. He, and D. Wang. Probing photoinduced two-body loss of ultracold nonreactive bosonic $^{23}\text{Na}^{87}\text{Rb}$ and $^{23}\text{Na}^{39}\text{K}$ molecules. *Physical Review Letters*, 127:163401, October 2021.
- [84] G. Wang and G. Quéméner. Tuning ultracold collisions of excited rotational dipolar molecules. *New Journal of Physics*, 17(3):035015, March 2015.
- [85] T. Karman and J. M. Hutson. Microwave shielding of ultracold polar molecules. *Physical Review Letters*, 121:163401, October 2018.

Bibliography

- [86] T. Xie, M. Lepers, R. Vexiau, A. Orbán, O. Dulieu, and N. Bouloufa-Maafa. Optical shielding of destructive chemical reactions between ultracold ground-state narb molecules. *Physical Review Letters*, 125:153202, October 2020.
- [87] J. R. Li, W.G. Tobias, K. Matsusada, C. Miller, G. Valtolina, L. De Marco, R. R. W. Wang, L. Lassablière, G. Quéméner, J. L. Bohn, and J. Ye. Tuning of dipolar interactions and evaporative cooling in a three-dimensional molecular quantum gas. *Nature Physics*, 17:1144–1148, September 2021.
- [88] L. Anderegg, S. Burchesky, Y. Bao, S. S. Yu, T. Karman, E. Chae, K.-K. Ni, W. Ketterle, and J. M. Doyle. Observation of microwave shielding of ultracold molecules. *Science*, 373(6556):779–782, August 2021.
- [89] T. Hartmann. An experiment apparatus for the production of ultracold bosonic dipolar ground state $^{23}\text{Na}^{39}\text{K}$ molecules and Feshbach spectroscopy in a cold mixture of ^{23}Na and ^{39}K . *PhD thesis, Leibniz Universität Hannover*, November 2018.
- [90] T. A. Schulze, T. Hartmann, K. K. Voges, M. W. Gempel, E. Tiemann, A. Zenesini, and S. Ospelkaus. Feshbach spectroscopy and dual-species Bose-Einstein condensation of ^{23}Na – ^{39}K mixtures. *Physical Review A*, 97:023623, February 2018.
- [91] C. Chin, R. Grimm, P. Julienne, and E. Tiesinga. Feshbach resonances in ultracold gases. *Review of Modern Physics*, 82:1225–1286, Apr 2010.
- [92] J. L. Roberts, N. R. Claussen, S. L. Cornish, E. A. Donley, E. A. Cornell, and C. E. Wieman. Controlled collapse of a bose-einstein condensate. *Physical Review Letters*, 86:4211–4214, May 2001.
- [93] S. B. Papp and C. E. Wieman. Observation of heteronuclear feshbach molecules from a ^{85}Rb – ^{87}Rb gas. *Physical Review Letters*, 97:180404, Oct 2006.
- [94] Y.-M. Yang, B. Xiao, W.-C. Ji, X.-K. Wang, H.-N. Dai, Y.-A. Chen, Z.-S. Yuan, and X. Jiang. A battery-powered floating current source of 100 a for precise and fast control of magnetic field. *AIP Advances*, 10(12):125207, 2020.
- [95] M. Meyer zum Alten Borgloh. Präparation ultrakalter $^{23}\text{Na}^{39}\text{K}$ Grundzustandsmoleküle mit induziertem Dipolmoment. *Master thesis, Leibniz Universität Hannover*, February 2021.
- [96] L. D. Carr and J. Ye. Focus on cold and ultracold molecules. *New Journal of Physics*, 11 055009, 2009.
- [97] T. A. Schulze, I. I. Temelkov, M. W. Gempel, T. Hartmann, H. Knöckel, S. Ospelkaus, and E. Tiemann. Multichannel modeling and two-photon coherent transfer paths in nak. *Physical Review A*, 88:023401, Aug 2013.

- [98] I. Temelkov, H. Knöckel, A. Pashov, and E. Tiemann. Molecular beam study of the $a^3\Sigma^+$ state of NaK up to the dissociation limit. *Physical Review A*, 91:032512, Mar 2015.
- [99] Nikolay V. Vitanov, Andon A. Rangelov, Bruce W. Shore, and Klaas Bergmann. Stimulated raman adiabatic passage in physics, chemistry, and beyond. *Review of Modern Physics*, 89:015006, Mar 2017.
- [100] P. D. Gregory, J. A. Blackmore, Frye M. D., L. M. Fernley, S. L. Bromley, J. M. Hutson, and S. L. Cornish. Molecule-molecule and atom-molecule collisions with ultracold RbCs molecules. *New Journal of Physics*, 23(12):125004, December 2021.
- [101] Michael Mayle, Brandon P. Ruzic, and John L. Bohn. Statistical aspects of ultracold resonant scattering. *Physical Review A*, 85:062712, June 2012.
- [102] J. F. E. Croft and J. L. Bohn. Long-lived complexes and chaos in ultracold molecular collisions. *Physical Review A*, 89(1), January 2014.
- [103] K. Jachymski, M. Gronowski, and M. Tomza. Collisional losses of ultracold molecules due to intermediate complex formation, October 2021.
- [104] J. Klos, Q. Guan, H. Li, M. Li, E. Tiesinga, and S. Kotochigova. Roaming pathways and survival probability in real-time collisional dynamics of cold and controlled alkali molecules. *Scientific Reports*, 11:10589, April 2021.
- [105] Timur M. Rvachov, Hyungmok Son, Ariel T. Sommer, Sepehr Ebadi, Juliana J. Park, Martin W. Zwierlein, Wolfgang Ketterle, and Alan O. Jamison. Long-Lived Ultracold Molecules with Electric and Magnetic Dipole Moments. *Phys. Rev. Lett.*, 119:143001, Oct 2017.
- [106] Matthew A. Nichols, Yi-Xiang Liu, Lingbang Zhu, Ming-Guang Hu, Yu Liu, and Kang-Kuen Ni. Detection of Long-Lived Complexes in Ultracold Atom-Molecule Collisions, 2021.
- [107] Hyungmok Son, Juliana J. Park, Wolfgang Ketterle, and Alan O. Jamison. Collisional cooling of ultracold molecules. *Nature*, 580(7802):197200, April 2020.
- [108] Huan Yang, De-Chao Zhang, Lan Liu, Ya-Xiong Liu, Jue Nan, Bo Zhao, and Jian-Wei Pan. Observation of magnetically tunable Feshbach resonances in ultracold $^{23}\text{Na}^{40}\text{K} + ^{40}\text{K}$ collisions. *Science*, 363(6424):261–264, 2019.
- [109] M. D. Frye and J. M. Hutson. Complexes formed in collisions between ultracold alkali-metal diatomic molecules and atoms. *New Journal of Physics*, 23(12):125008, December 2021.
- [110] H. Yang, X.-Y. Wang, Z. Su, J. Cao, D.-C. Zhang, J. Rui, B. Zhao, C.-L. Bai, and J.-W. Pan. Evidence for association of triatomic molecule in ultracold $^{23}\text{Na}^{40}\text{K}$ and ^{40}K mixture, April 2021.

Bibliography

- [111] S. Ospelkaus, K.-K. Ni, G. Quéméner, B. Neyenhuis, D. Wang, M. H. G. de Miranda, J. L. Bohn, J. Ye, and D. S. Jin. Controlling the hyperfine state of rovibronic ground-state polar molecules. *Physical Review Letters*, 104:030402, January 2010.
- [112] A. Gerdes, O. Dulieu, H. Knöckel, and E. Tiemann. Stark effect measurements on the NaK molecule. *The European Physical Journal D*, 65:105–111, June 2011.

List of publications (complete)

- Philipp Gersema. Characterization of a high resolution imaging system for sodium atoms. Leibniz Universität Hannover, Institut für Quantenoptik (2014)
- Philipp Gersema. A cooling laser system for Zeeman deceleration of potassium atoms on the D1 line and first cooling experiments. Leibniz Universität Hannover, Institut für Quantenoptik (2017)
- Maurice Petzold, Paul Kaebert, Philipp Gersema, Mirco Siercke and Silke Ospelkaus. A Zeeman slower for diatomic molecules. *New J. Phys.* 20 042001 (2018)
- Maurice Petzold, Paul Kaebert, Philipp Gersema, Timo Poll, Niklas Reinhardt, Mirco Siercke and Silke Ospelkaus. Type-II Zeeman slowing: Characterization and comparison to conventional radiative beam-slowing schemes. *Phys. Rev. A* 98, 063408 (2018)
- Torsten Hartmann, Torben A. Schulze, Kai K. Voges, Philipp Gersema, Matthias W. Gempel, Eberhard Tiemann, Alessandro Zenesini, and Silke Ospelkaus. Feshbach resonances in $^{23}\text{Na}+^{39}\text{K}$ mixtures and refined molecular potentials for the NaK molecule. *Phys. Rev. A* 99, 032711 (2019)
- Kai K. Voges, Philipp Gersema, Torsten Hartmann, Torben A. Schulze, Alessandro Zenesini, and Silke Ospelkaus. A pathway to ultracold bosonic $^{23}\text{Na}^{39}\text{K}$ ground-state molecules. *New J. Phys.* 21 123034 (2019)
- Kai K. Voges, Philipp Gersema, Torsten Hartmann, Torben A. Schulze, Alessandro Zenesini, and Silke Ospelkaus. Formation of ultracold weakly bound dimers of bosonic $^{23}\text{Na}^{39}\text{K}$. *Phys. Rev. A* 101, 042704 (2020)
- Eberhard Tiemann, Philipp Gersema, Kai K. Voges, Torsten Hartmann, Alessandro Zenesini, and Silke Ospelkaus. Beyond Born-Oppenheimer approximation in ultracold atomic collisions. *Phys. Rev. Research* 2, 013366 (2020)

- Kai K. Voges, Philipp Gersema, Mara Meyer zum Alten Borgloh, Torben A. Schulze, Torsten Hartmann, Alessandro Zenesini, and Silke Ospelkaus. Ultracold Gas of Bosonic $^{23}\text{Na}^{39}\text{K}$ Ground-State Molecules. *Phys. Rev. Lett.* 125, 083401 (2020)
- Philipp Gersema, Kai K. Voges, Mara Meyer zum Alten Borgloh, Leon Koch, Torsten Hartmann, Alessandro Zenesini, Silke Ospelkaus, Junyu Lin, Junyu He, and Dajun Wang. Probing Photoinduced Two-Body Loss of Ultracold Nonreactive Bosonic $^{23}\text{Na}^{87}\text{Rb}$ and $^{23}\text{Na}^{39}\text{K}$ Molecules. *Phys. Rev. Lett.* 127, 163401 (2021)
- Kai K. Voges, Philipp Gersema, Torsten Hartmann, Silke Ospelkaus and Alessandro Zenesini. Hyperfine dependent atom-molecule loss analyzed by the analytic solution of few-body loss equations. arXiv:2109.03605v2. accepted in *Phys. Rev. Research*

Curriculum Vitae

Personal Details

Name **Philipp Gersema**
Date of birth **29.05.1992**
Place of birth **26655 Westerstede**

Education

Studies

- Mar. 2011 **Allgemeine Hochschulreife (Abitur)**
Lothar-Meyer-Gymnasium Varel, Germany
- Oct. 2011- Dec. 2014 **Bachelor of Science (Physics)**
Leibniz Universität Hannover
- Mar. 2014- Dec. 2014 **Bachelor Thesis, *Characterization of a high resolution imaging system for sodium atoms***
Institut für Quantenoptik, Leibniz Universität Hannover
Group POLAR, Prof. Dr. S. Ospelkaus
- Oct. 2014- Mar. 2017 **Master of Science (Physics)**
Leibniz Universität Hannover
- Feb. 2016- Feb. 2017 **Master Thesis, *A cooling laser system for Zeeman deceleration of potassium atoms on the D1 line and first cooling experiments***
Institut für Quantenoptik, Leibniz Universität Hannover
Group SLOMO, Prof. Dr. S. Ospelkaus

Research

- Apr. 2017- Today **Doctoral studies**
Institut für Quantenoptik, Leibniz Universität Hannover
Group POLAR, Prof. Dr. S. Ospelkaus
- March. 2018 **Visiting scientist**
Physikalisches Institut, Universität Heidelberg
Li-Cs experiment, Prof. Dr. M. Weidemüller

